

AD-A088 571

PENNSYLVANIA STATE UNIV UNIVERSITY PARK MATERIALS RE--ETC F/6 7/4
MECHANISMS OF EROSION.(U)
AUG 80 N H MACMILLAN

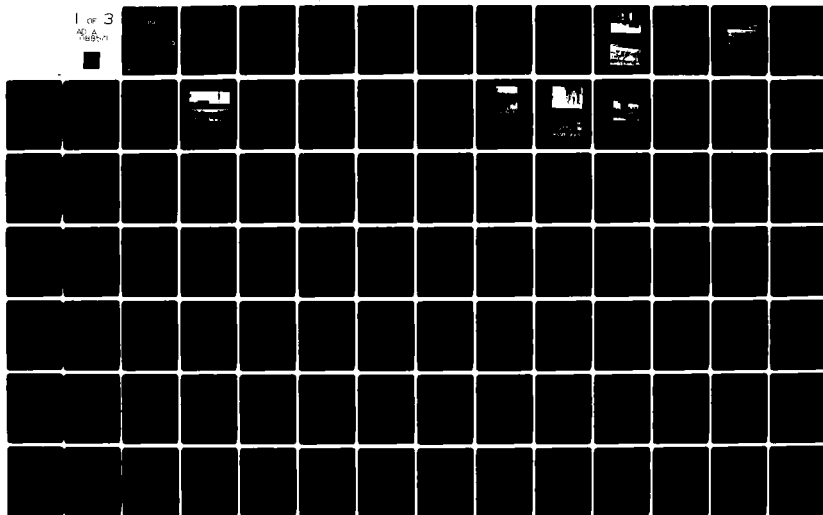
DAA629-79-C-0104

UNCLASSIFIED

ARO-14084.13-MS

NL

1 of 3
NO A
REASON



AD A088571

DDC FILE COPY

UNCLASSIFIED
SECURITY CLASSIFICATION OF THIS PAGE (When Data Entered)

REPORT DOCUMENTATION PAGE		READ INSTRUCTIONS BEFORE COMPLETING FORM
1. REPORT NUMBER 14084.13-MS	2. GOVT ACCESSION NO. AD-A088571	3. RECIPIENT'S CATALOG NUMBER
4. TITLE (and Subtitle) Mechanisms of Erosion,		5. TYPE OF REPORT & PERIOD COVERED Final Report 1 Apr 77 - 31 May 80
6. AUTHOR(s) Norman H. Macmillan		7. CONTRACT OR GRANT NUMBER(s) DAAG29-77-G-0100 DAAG29-78-G-0056 DAAG29-79-C-0104
8. PERFORMING ORGANIZATION NAME AND ADDRESS Materials Research Laboratory The Pennsylvania State University University Park, PA 16802		9. PROGRAM ELEMENT, PROJECT, TASK AREA & WORK UNIT NUMBERS 12 224
10. CONTROLLING OFFICE NAME AND ADDRESS U. S. Army Research Office Post Office Box 12211 Research Triangle Park, NC 27709		11. REPORT DATE August 1980
12. MONITORING AGENCY NAME & ADDRESS (if different from Controlling Office)		13. NUMBER OF PAGES 212
		14. SECURITY CLASS. (of this report) Unclassified
		15. DECLASSIFICATION/DOWNGRADING SCHEDULE
16. DISTRIBUTION STATEMENT (of this Report) Approved for public release; distribution unlimited.		
17. DISTRIBUTION STATEMENT (of the abstract entered in Block 20, if different from Report) NA		
18. SUPPLEMENTARY NOTES The view, opinions, and/or findings contained in this report are those of the author(s) and should not be construed as an official Department of the Army position, policy, or decision, unless so designated by other documentation.		
19. KEY WORDS (Continue on reverse side if necessary and identify by block number) gas gun, whirling arm apparatus, erosion, magnesium oxide, aluminum, lithium fluoride, single crystal, polycrystals, single impact, multiple impacts.		
20. ABSTRACT (Continue on reverse side if necessary and identify by block number) A single stage gas gun and a whirling arm rig have been used to study the erosion of mono- and poly-crystalline MgO and Al and mono-crystalline LiF targets by millimeter scale steel and WC - 6% Co spheres. Both single and multiple impact studies were variously performed as functions of impact angle, impact velocity, particle size, method of surface preparation and (in the case of mono-crystalline targets) surface orientation. The resultant damage was variously studied by optical and scanning electron microscopy, (continued on reverse side)		

DD FORM 1 JAN 73 1473 EDITION OF 1 NOV 63 IS OBSOLETE

UNCLASSIFIED

SECURITY CLASSIFICATION OF THIS PAGE (When Data Entered)

80 8 25 141

(Abstract continued)

dislocation etching and surface profilometry, and the corresponding mass losses were determined gravimetrically. In addition, a computer model of oblique impact was developed and tested against the experimental observations. The results show that the variation of impact crater dimensions with impact conditions can generally be explained satisfactorily, but that it is difficult to relate mass loss to crater geometry in quantitative terms under either single or multi-particle impact conditions. They also suggest that the erosion of semi-brittle materials is determined primarily by the intersection of the lateral and median (or radial) cracks formed about the impact craters, and that ductile materials erode by the detachment of thin platelets formed by extrusion of piled-up material between subsequently arriving particles and the underlying substrate.

Accession For	
NTIS GRA&I	<input checked="checked" type="checkbox"/>
DDC TAB	<input type="checkbox"/>
Unannounced	<input type="checkbox"/>
Justification _____	
By _____	
Distribution/ _____	
Availability Codes	
Dist	Avail and/or special
A	

MECHANISMS OF EROSION

Final Report on Work Carried Out Between

April 1, 1977 and May 31, 1980

by

N. H. Macmillan

August 1980

U. S. Army Research Office
Grants Nos. DAAG29-77-G-0100,
-78-G-0056 and -79-C-0104

Materials Research Laboratory
The Pennsylvania State University
University Park, PA 16802

Approved for Public Release;
Distribution Unlimited

The view, opinions, and/or findings contained in this report are those of the author and should not be construed as an official Department of the Army position, policy or decision, unless so designated by other documentation.

TABLE OF CONTENTS

Abstract

I INTRODUCTION

II SUMMARY OF RESULTS

(a) Apparatus

(b) Single Particle Impact Studies

(c) Multiple Particle Impact Studies

III LIST OF PUBLICATIONS

IV PARTICIPATING SCIENTIFIC PERSONNEL

V ADVANCED DEGREES AWARDED

Appendix I The Effect of Crystallographic Orientation on Damage in MgO Due to Spherical Particle Impact

Appendix II Observations on the Hardness Anisotropy in MgO and LiF

Appendix III The Hardness of Cubic Single Crystals by Spherical Indentation

Appendix IV Mechanisms of Solid Particle Erosion in Crystalline Materials

Appendix V The Influence of Particle Properties on Impact Damage in LiF

Appendix VI Basic Mechanisms of Erosion in Ceramics

Appendix VII The Erosion of Aluminum by Solid Particle Impingement at Normal Incidence

Appendix VIII On the Oblique Impact of a Rigid Sphere Against a Rigid-Plastic Solid

Appendix IX The Effect of Approach Direction on Damage in MgO Due to Spherical Particle Impact

Appendix X The Erosion of MgO by Solid Particle Impingement at Normal Incidence

Appendix XI The Erosion of Aluminum by Solid Particle Impingement at Oblique Incidence

Appendix XII Erosion of Aluminum and Magnesium Oxide by Spherical Particles

Abstract

A single stage gas gun and a whirling arm rig have been used to study the erosion of mono- and poly-crystalline MgO and Al and mono-crystalline LiF targets by millimeter scale steel and WC - 6% Co spheres. Both single and multiple impact studies were variously performed as functions of impact angle, impact velocity, particle size, method of surface preparation and (in the case of mono-crystalline targets) surface orientation. The resultant damage was variously studied by optical and scanning electron microscopy, dislocation etching and surface profilometry, and the corresponding mass losses were determined gravimetrically. In addition, a computer model of oblique impact was developed and tested against the experimental observations. The results show that the variation of impact crater dimensions with impact conditions can generally be explained satisfactorily, but that it is difficult to relate mass loss to crater geometry in quantitative terms under either single or multi-particle impact conditions. They also suggest that the erosion of semi-brittle materials is determined primarily by the intersection of the lateral and median (or radial) cracks formed about the impact craters, and that ductile materials erode by the detachment of thin platelets formed by extrusion of piled-up material between subsequently arriving particles and the underlying substrate.

I. INTRODUCTION

This report describes the results of an investigation of the mechanisms of solid particle erosion at subsonic velocities that has been carried out by the present author in collaboration with Dr. David G. Rickerby over the past three years. Almost all of these results have already been published or submitted for publication in the form of eleven papers (Nos. 1 to 11 in the list of publications below), and the remainder will shortly be presented in two further papers (Nos. 12 and 13 on the same list). Accordingly, the bulk of this report consists of twelve appendices containing the texts of the first eleven papers and the abstract from the twelfth, the text of which is not yet complete.* The remaining material consists only of Section II, which summarizes these appendices and presents some experimental information that does not appear in them, and the very brief Sections III, IV and V, which are self-explanatory.

It should also be noted that four of the papers in the list of publications (Nos. 1, 4, 5 and 6) include contributions by one or other of two of the author's graduate students, who carried out related work under National Science Foundation sponsorship during the first 18 months or so of this project. Accordingly, these four papers carry an acknowledgement of both sources of support.

* Paper No. 13 remains to be written.

II. SUMMARY OF RESULTS

(a) Apparatus

In the early stages of this project two major pieces of equipment were designed and built--a single stage gas gun and a "whirling arm" erosion rig.

The five main components of the gas gun are shown in Figure 1. These are: (i) a 2.3 l steel gas cylinder that acts as a reservoir for the propellant gas; (ii) a three-part brass breech, Figure 2, incorporating a dual "bursting diaphragm" trigger mechanism, Figure 3; (iii) an external gas supply system with its associated high pressure lines, control valves, gauges, etc., Figure 3; (iv) a 16 mm caliber steel barrel fitted with a steel muzzle block (and interchangeable with a square (12.7 x 12.7 mm) cross-section barrel); and (v) a demountable, three-stage, photo-electric time-of-flight velocity measurement system, Figures 4 to 6, that can be attached to the muzzle end of either barrel.

To prepare for firing at a pressure p_f , the chosen erosive particle--which may be of any shape or size that will fit inside the barrel--is loosely mounted in a recess in the front face of a 25 mm long nylon sabot of the appropriate cross-section. Then, this sabot and diaphragms having bursting pressures in the range $0.5 p_f$ to p_f are installed in the breech, and the gas reservoir and the space between the diaphragms are pressurized to p_f and $0.5 p_f$, respectively. Firing is then accomplished by de-pressurizing the space between the diaphragms, thereby sequentially raising the pressure differential across each to p_f and causing them to rupture in turn. The gas thereby released propels the loaded sabot down the barrel past the three equally spaced, short rise-time ($\sim 1 \mu s$) phototransistors that control the velocity measurement system. At the muzzle the sabot is stopped by the muzzle block, and the projectile continues freely onwards to impact with a target several centimeters beyond.

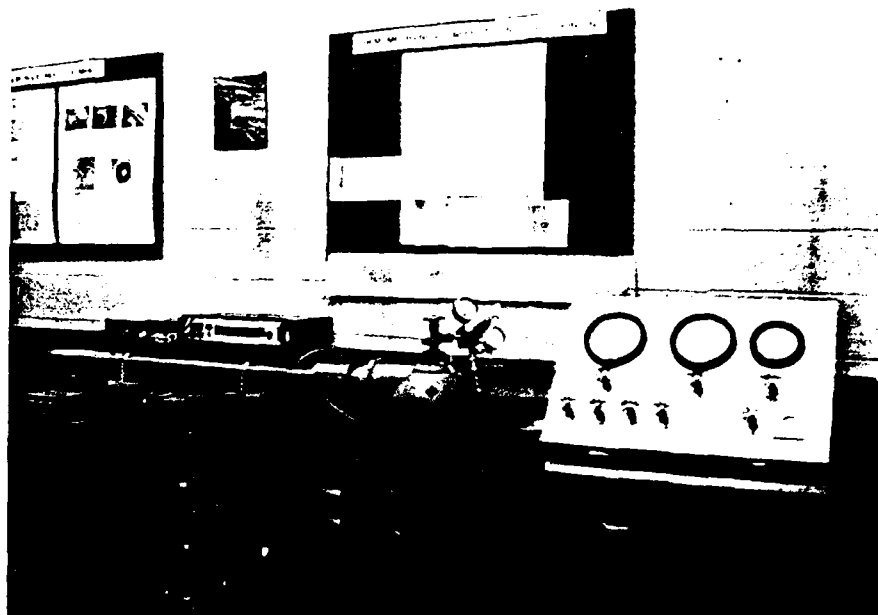


Figure 1 General arrangement of the gas gun

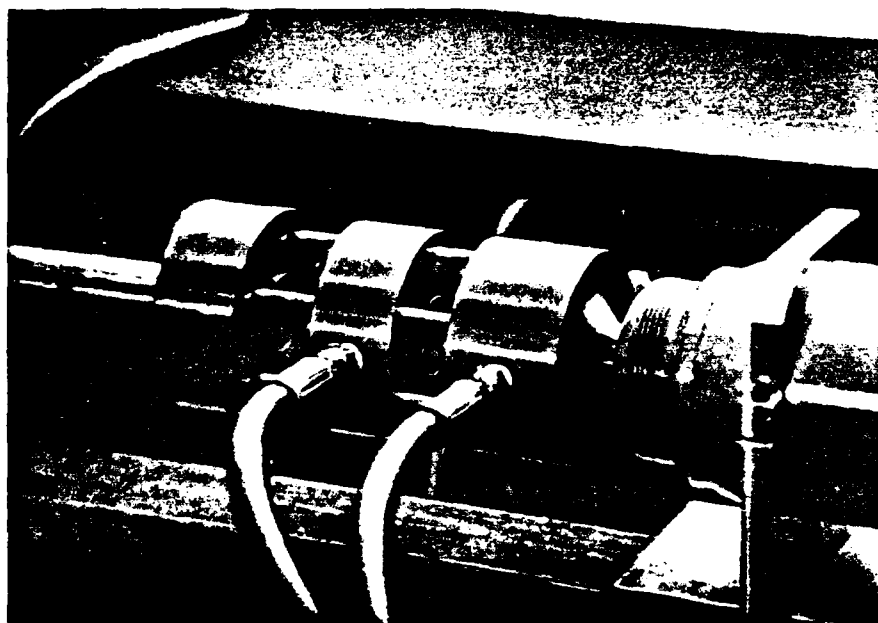


Figure 2 The construction of the breech

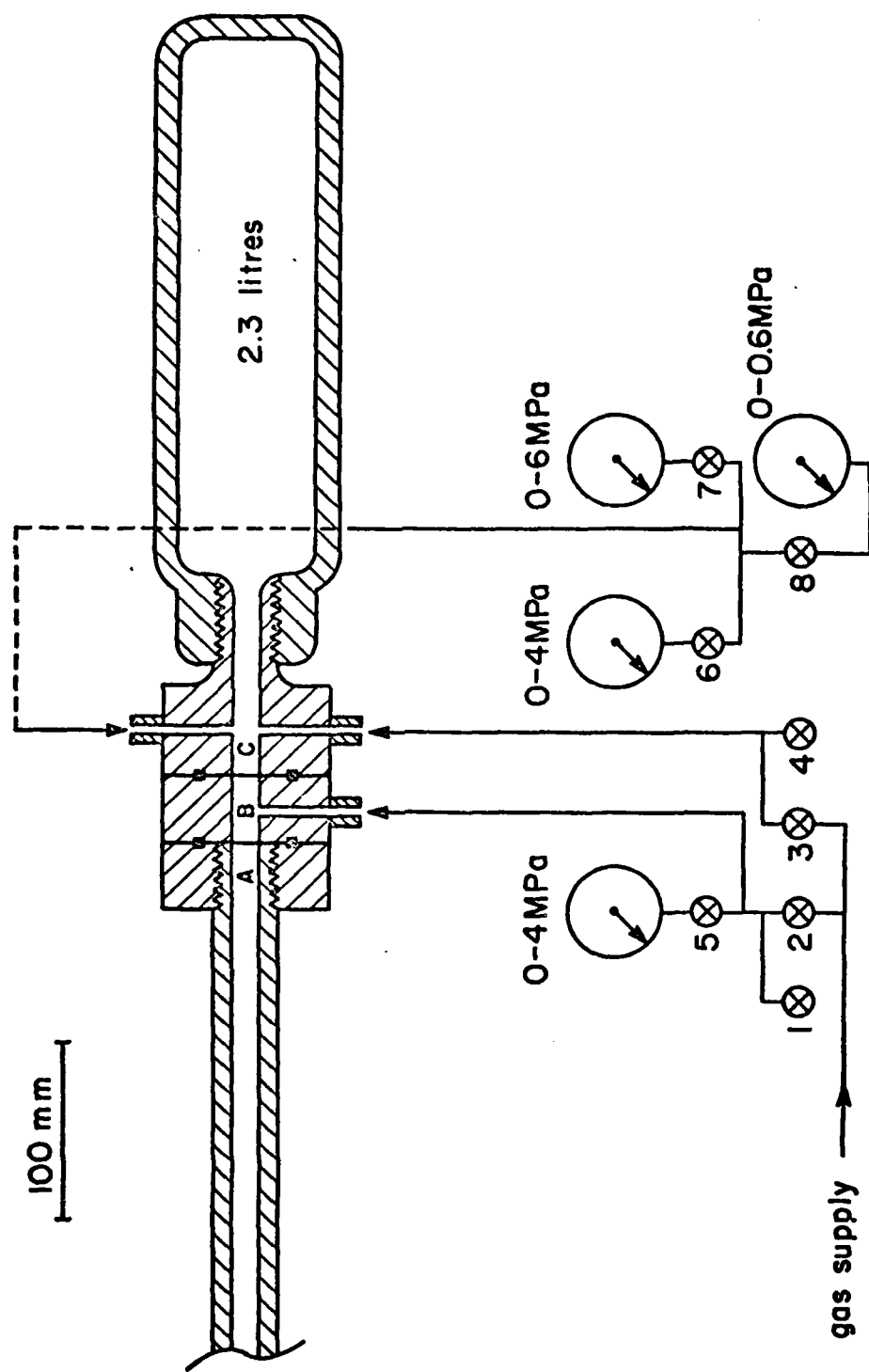


Figure 3 Schematic diagram of trigger mechanism and gas supply system

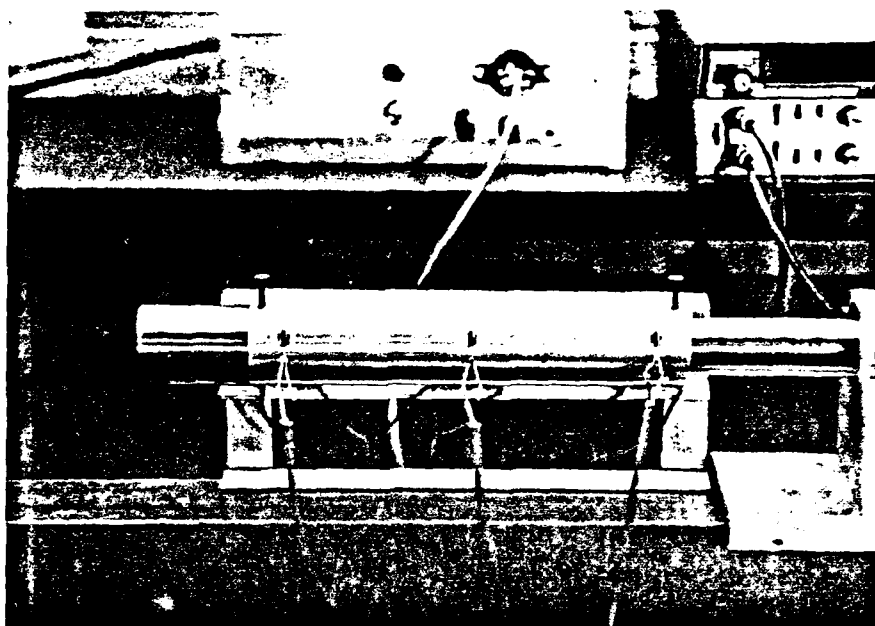


Figure 4 Construction of the time-of-flight velocity measurement system.

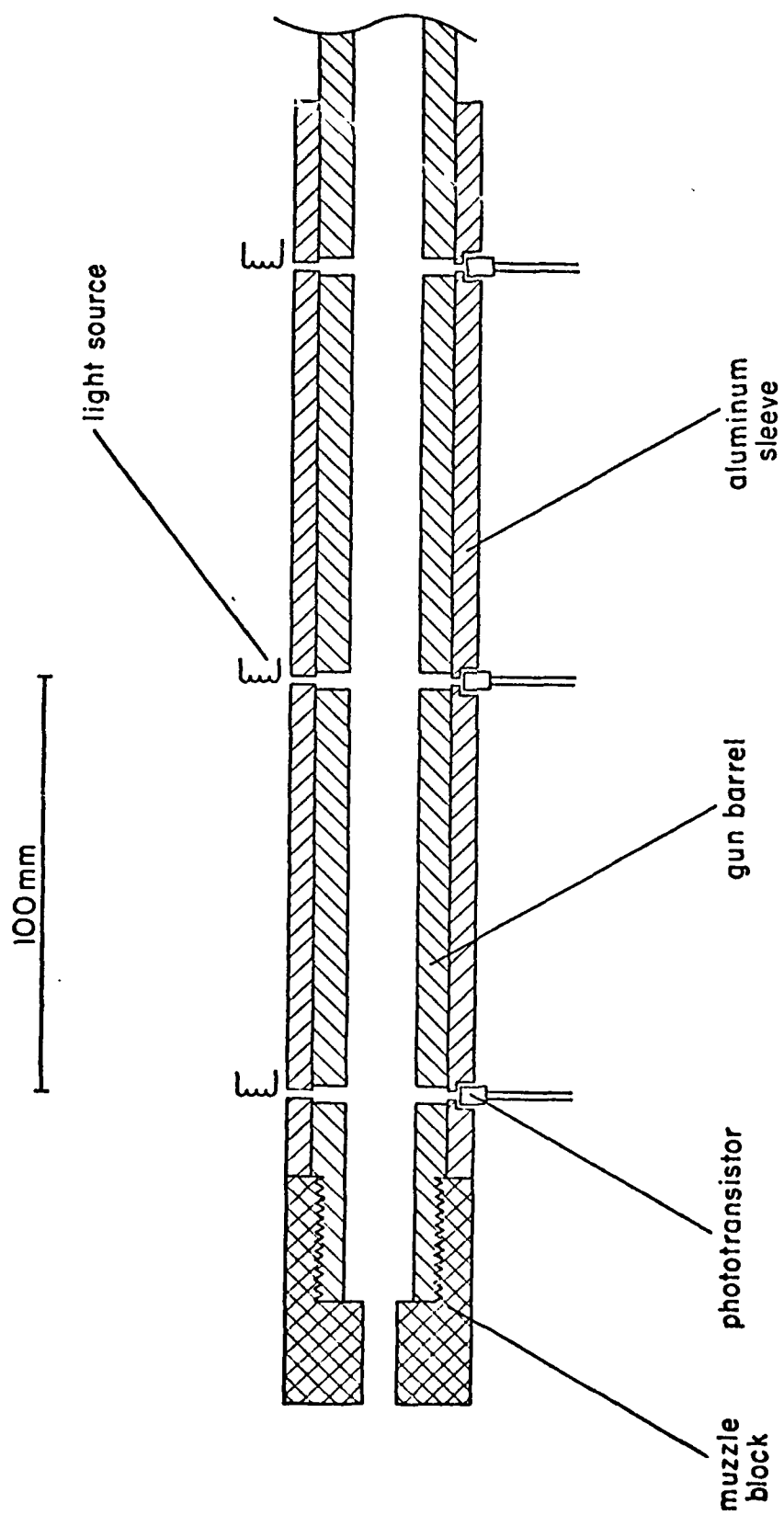


Figure 5 Schematic diagram of the time-of-flight velocity measurement system

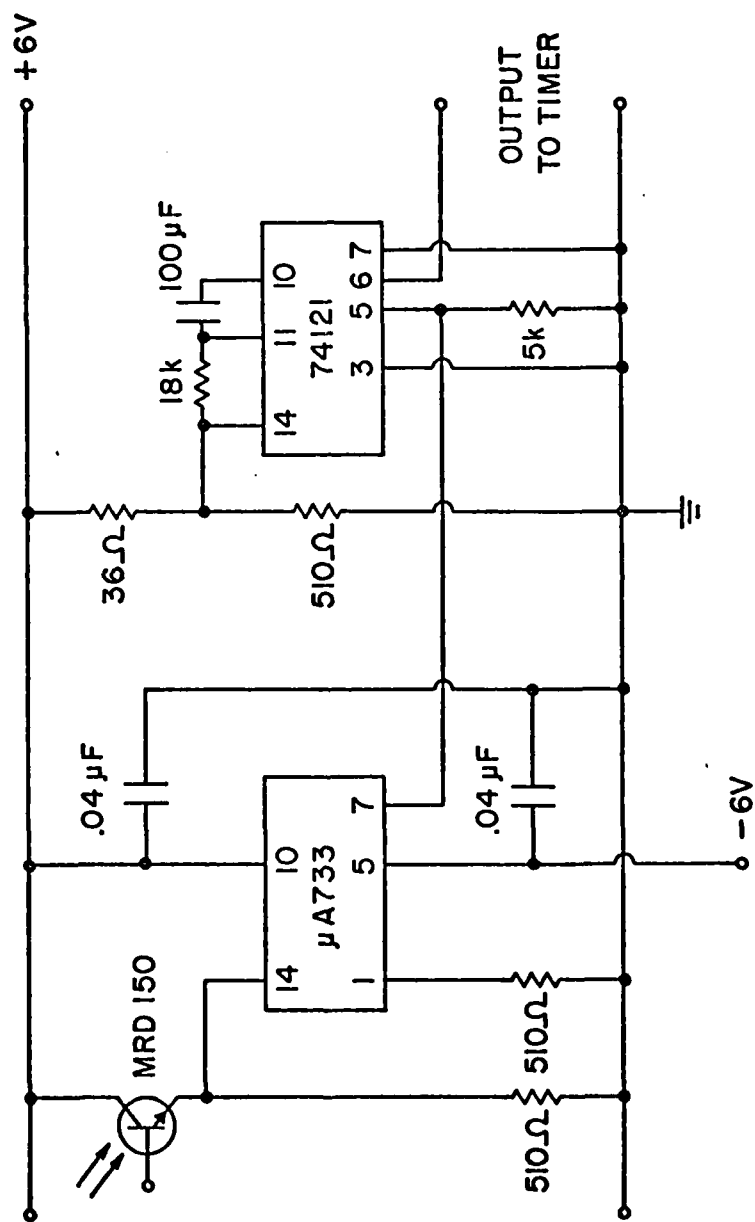


Figure 6 Circuit for time-of-flight velocity measurement system

To confirm that an erosive particle launched in this fashion strikes the target with a velocity equal to that measured by the photoelectronic time-of-flight system, a series of high speed photographic measurements were made. The experimental set-up is illustrated in Figure 7. A double pulse ruby laser provided the illumination, and a dual image of the particle was recorded by a 35 mm camera. Triggering of the laser was achieved by inserting a wire through a small hole in the side of the muzzle block, so that the arrival of the sabot made a contact between the wire and the block and thereby applied a potential to the trigger input of the laser control system. The interval between the two laser pulses typically was 500 μ s.

Two of the photographs obtained in this manner are reproduced as Figure 8. They reveal that at higher velocities the particle is accompanied in its flight by a certain amount of nylon debris resulting from partial break-up of the sabot when it strikes the muzzle block. In general, however, this debris travels somewhat more slowly than the projectile. It also has a much lower density than the steel and WC particles used in most of this work. And hence it contributes only slightly to the impact damage. Measurements of the particle velocity v_p obtained from such photographs are plotted against the corresponding (photoelectronically determined) sabot velocity v_s in Figure 9, together with the straight line $v_p = v_s$. It is apparent that v_p is a little less than v_s at velocities less than $\sim 70 \text{ m s}^{-1}$, but that no large errors result from assuming $v_p = v_s$.

Calibration of the gun, Figures 10 and 11, shows that, when N_2 is used as the propellant, impact velocities of up to $\sim 400 \text{ m s}^{-1}$ can be obtained from the 1.22 m long, round cross-section barrel, while the shorter (1 m long), square cross-section barrel conveniently provides for firing particles in pre-determined orientations at velocities up to $\sim 350 \text{ m s}^{-1}$. For both barrels the velocity is

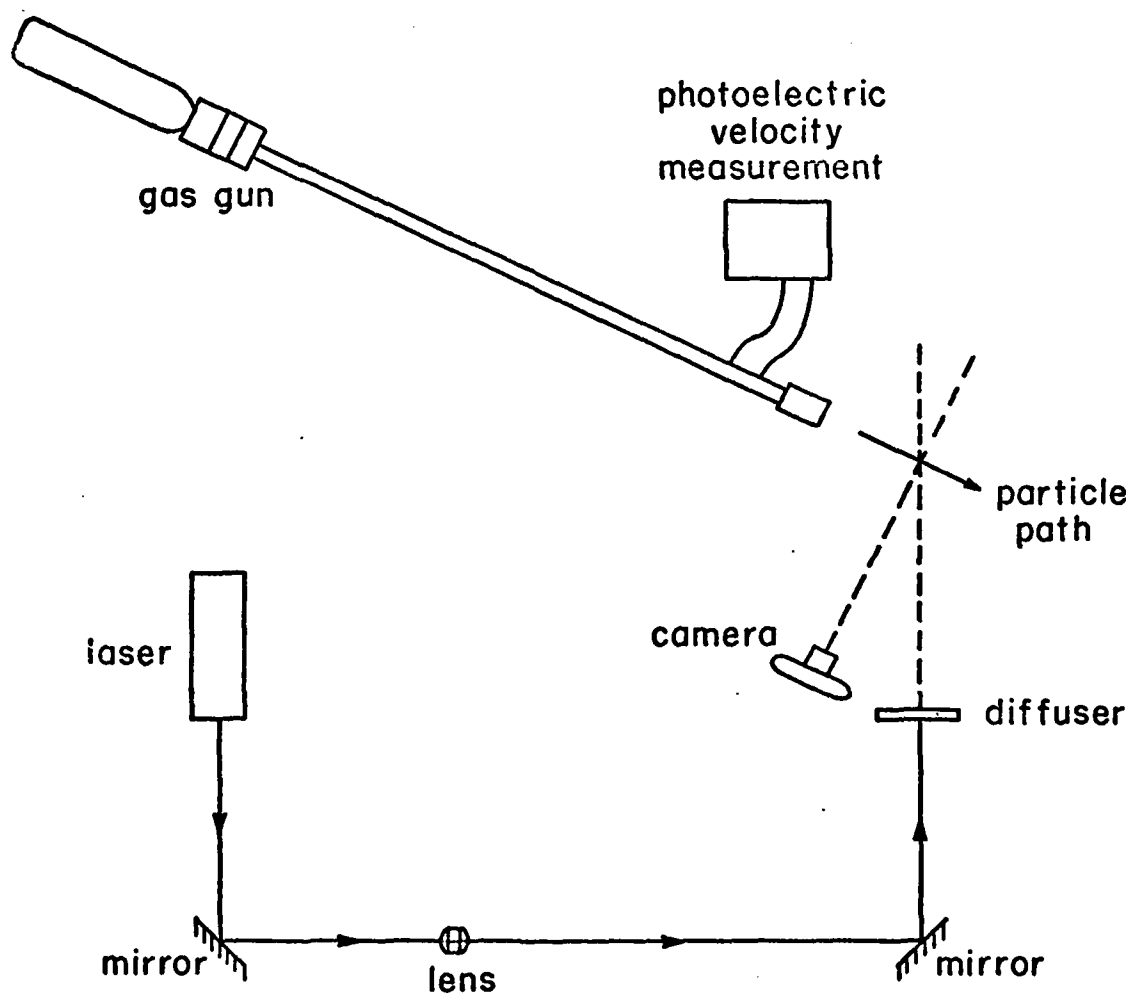
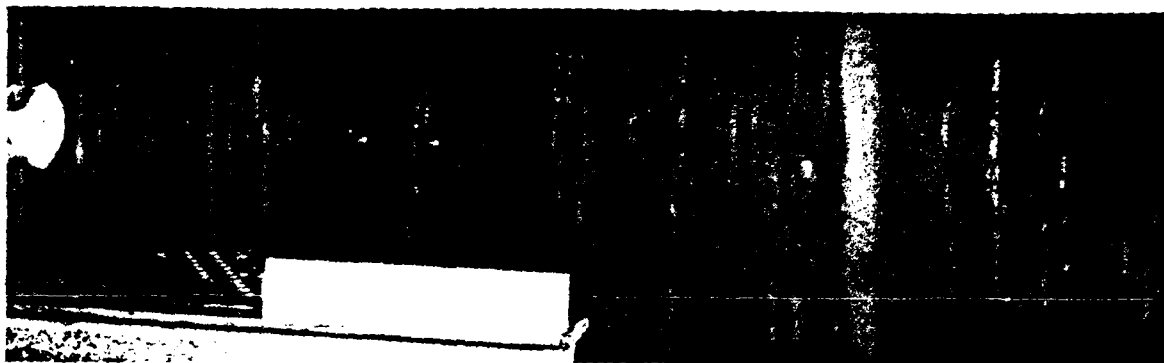


Figure 7 Schematic diagram of the experimental arrangement used to confirm the correct operation of the time-of-flight velocity measurement system

(a)



(b)

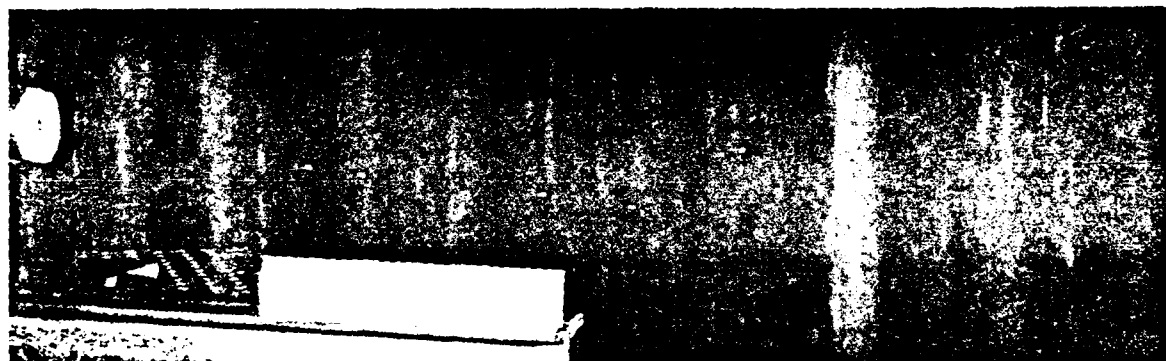


Figure 8 Double pulse laser photographs of erosive particles in free flight

(a) $v_p = 76.4 \text{ m s}^{-1}$, $v_s = 79.2 \text{ m s}^{-1}$, (b) $v_p = 134.8 \text{ m s}^{-1}$, $v_s = 134.6 \text{ m s}^{-1}$

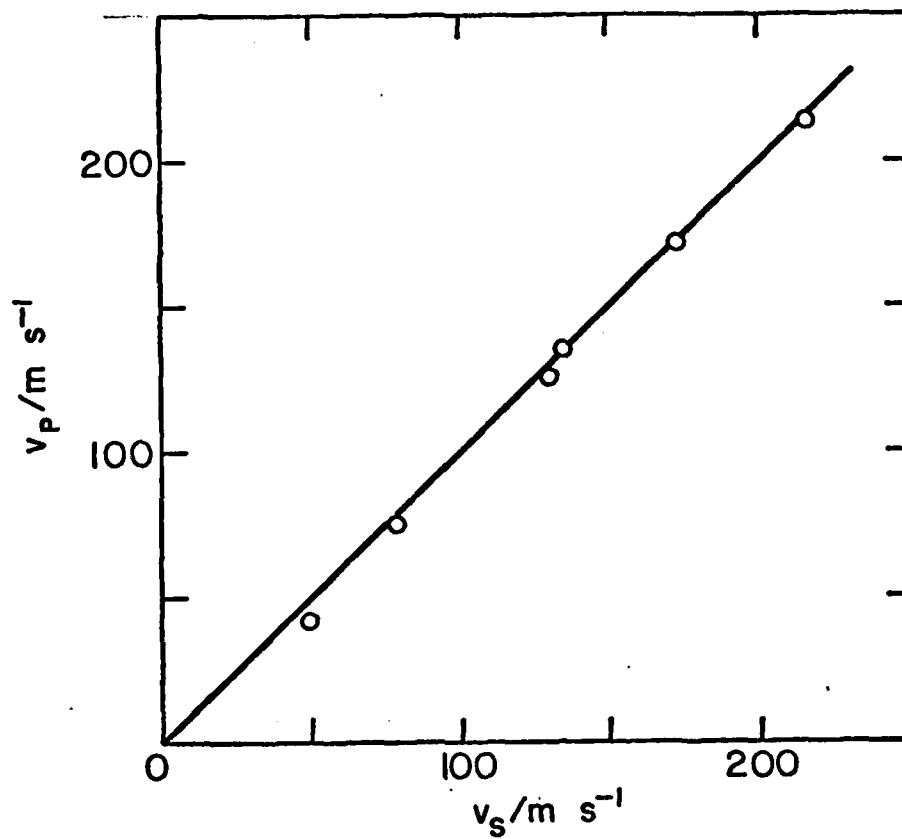


Figure 9 Comparison between experimental measurements of projectile and sabot velocities

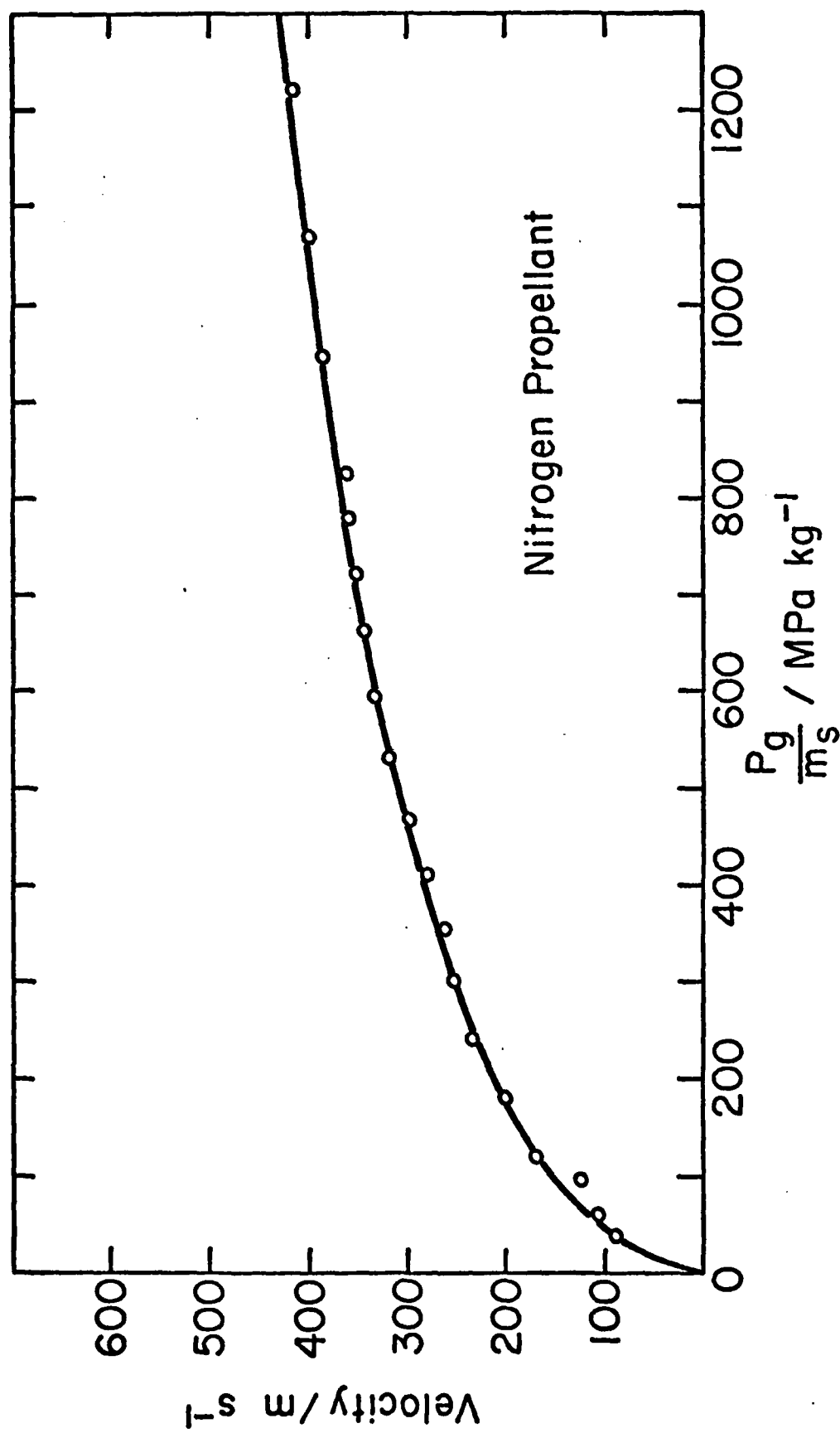


Figure 10 Velocity calibration curve for the round cross-section barrel version of the gas gun

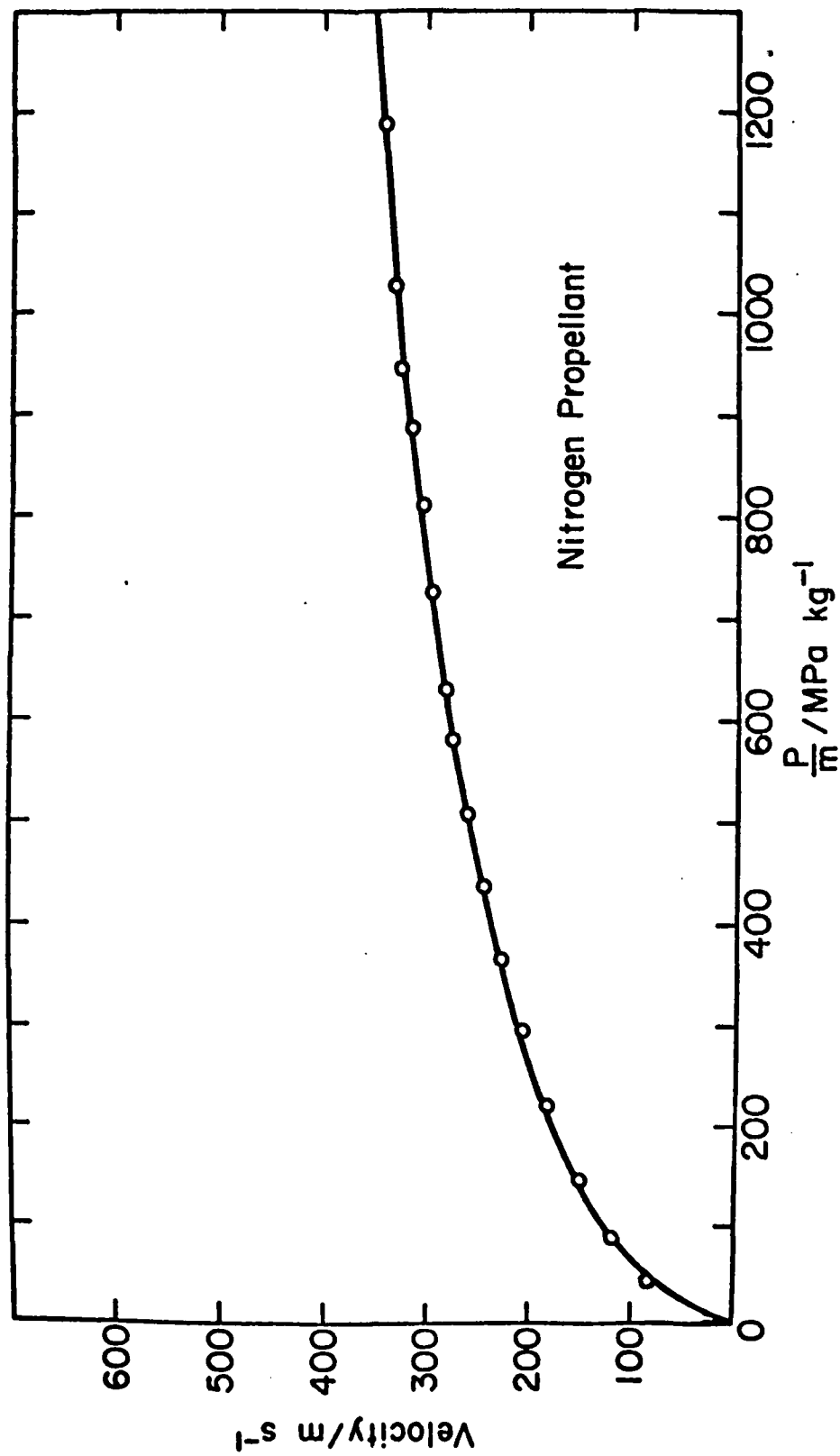


Figure 11 Velocity calibration curve for the square cross-section barrel version of the gas gun

reproducible to $\pm 1\%$ at any given firing pressure and the acceleration of the sabot immediately prior to impact with the muzzle block is $\sim 1\%$ of the velocity.

The complementary multiple particle impact capability was provided by the whirling arm rig shown in Figures 12 to 14. This consists of an electrically driven, counter-balanced rotor arm which carries a specimen through a continually re-established, free-falling "curtain" of millimeter size or smaller particles, Figure 15, at velocities up to $\sim 150 \text{ m s}^{-1}$. The arm is mounted inside a steel tank that can be evacuated to ~ 1 torr by a rotary vacuum pump, thereby making it possible to eliminate any possible aerodynamic influences on the particle trajectories. Further details of this apparatus appear in Paper No. 7, and its calibration is discussed extensively in Papers Nos. 7, 10, 11 and 12.

(b) Single Particle Impact Studies

The gas gun was first used to study the damage resulting from single, normal impacts of 1.59 mm diameter steel or WC - 6% Co spheres against chemically polished {100}, {110} and {111} and mechanically polished {100} and {110} surfaces of MgO single crystals at velocities ranging from 50 to 350 m s^{-1} [1].* The resultant damage was studied by optical and scanning electron microscopy, dislocation etching and surface profilometry, and the mass losses were determined gravimetrically. Subsequently, essentially similar studies were carried out on mechanically polished {100} oriented LiF [5] and {100}, {110} and {111} oriented Al single crystals [4], and an investigation was also made of the damage resulting from oblique, single impacts against chemically polished {100} oriented MgO single crystals [9].

The damage resulting from normal impacts of single spheres against MgO invariably consists of a central crater, formed by combination of primary glide and modes II and III cleavage fracture, and a surrounding zone of brittle

* Numbers in square brackets refer to the papers in the list of publications.

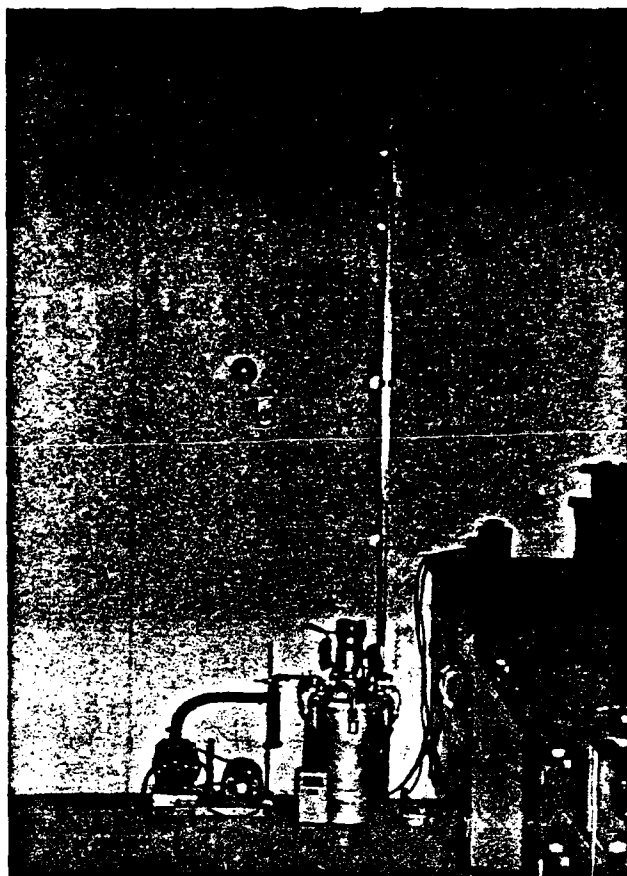


Figure 12 General arrangement of the whirling-arm rig

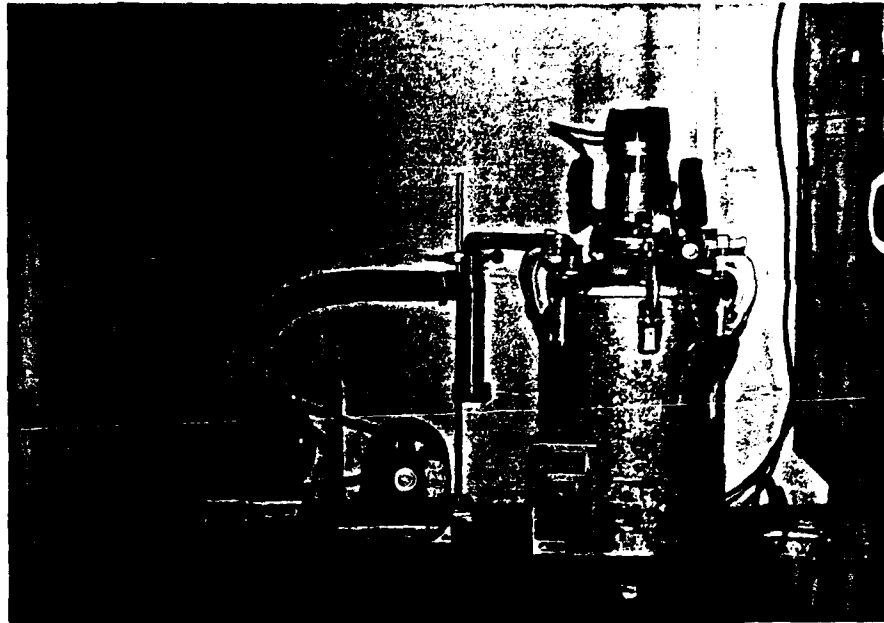


Figure 13 Close-up of whirling arm rig

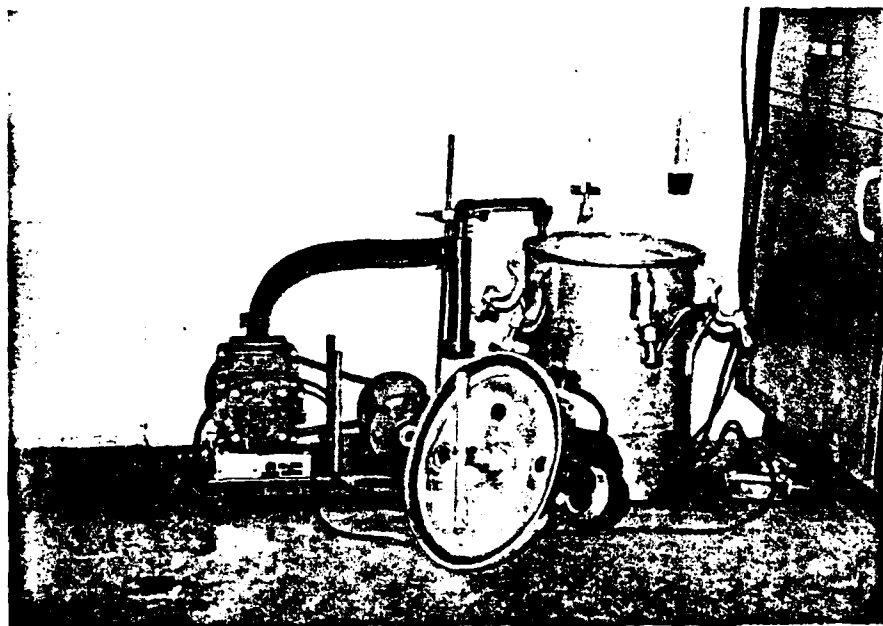


Figure 14 Whirling-arm rig partly disassembled to show the rotor arm.

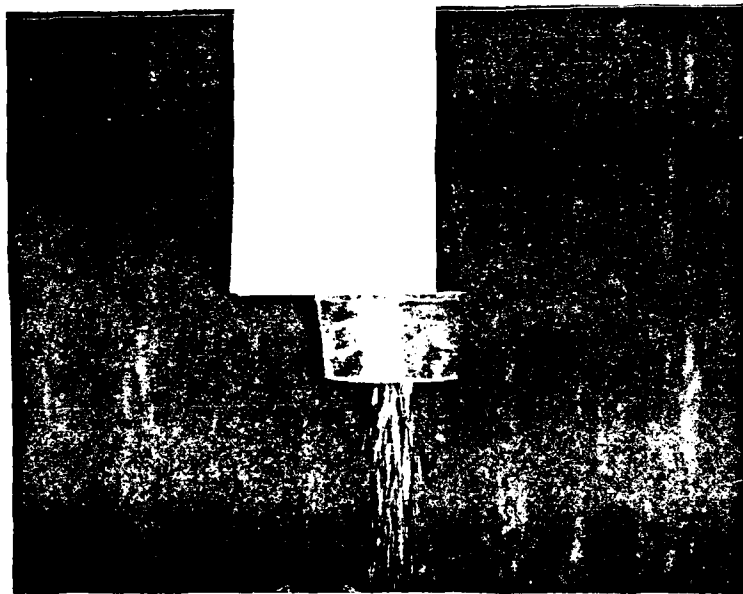


Figure 15 The "curtain" of free-falling erosive particles,
as seen by a target mounted on the rotor arm

fracture from which mass loss occurs by intersection of {100} and {110} cleavage cracks with the free surface and with one another. Below the level of the original surface the shape of the crater conforms closely to that of the spent sphere, regardless of whether this deforms plastically during the impact or not; but the shape of the crater rim is determined by the sinking-in and piling-up resulting from extensive dislocation motion on the primary glide planes, and thus reflects the symmetry of the target surface. The dimensions of the crater are sensitive to crystal orientation and insensitive to the method of target surface preparation, but the mass loss is sensitive to both of these variables. And both crater volume and mass loss are proportional to the square of the impact velocity.

At first glance, the craters formed in LiF look very similar. However, the profilometry studies reveal that post-impact elastic recovery reduces the crater diameter to a proportionally greater extent than the depth, resulting in an indentation with a radius of curvature smaller than that of the indenter that created it. Since the extent of such recovery increases with impact velocity, crater volume is no longer precisely proportional to the square of this velocity. However, the corresponding proportionality between mass loss and the square of the impact velocity persists.

In the case of Al (and also Ni, which was studied in a related program) the damage consists simply of a crater formed by primary glide, and such small mass losses as do occur result from the tearing away of minute, ragged lips from the raised portions of the crater rim, apparently as a result of extrusion of material between the erosive particle and the work-hardened target. These mass losses were too small and irreproducible for it to be possible to determine either if or how they varied with impact velocity, and it may be that their magnitude is determined primarily by (say) the surface roughness or any slight rotation of the erosive particle. More extensive piling-up and sinking-in occurred around

the rims of craters in Al (or Ni) than in MgO or LiF, but the post-impact elastic recovery of both metals was much the same as for LiF.

Since it is possible to solve analytically the equation of motion governing the normal impact of a rigid sphere against an ideal rigid-plastic half-space [1], this model of the impact event was used to obtain from all of the preceding experiments values of the dynamic hardness (at a strain rate $\sim 10^5 \text{ s}^{-1}$) that could be compared with the quasi-static Meyer ball hardness (typically measured at a strain rate $\sim 10^{-2}$ - 10^{-3} s^{-1}) [3]. For MgO and Al, the dynamic hardness showed no obvious velocity dependence and essentially the same anisotropy as the Meyer ball hardness. Thus, both parameters were isotropic (to within the experimental uncertainty) for Al, and both increased by $\sim 50\%$ for $\{111\}$ oriented MgO specimens as compared to $\{100\}$ or $\{110\}$ oriented specimens. And, when the same kind of sphere and size of indentation was used in the measurement of both parameters, the ratio of the dynamic hardness to the Meyer ball hardness was ~ 5 for MgO and LiF and ~ 2 for Al. It was also found, however, that the value of the dynamic hardness depends on the type of indenter used to measure it. Thus, because they deform plastically when they impact MgO, steel spheres produce smaller craters and correspondingly larger values of the dynamic hardness. Similarly, the dynamic hardness for LiF appears to be velocity independent when steel erosive spheres are used, but to decrease as the impact velocity increases when WC - 6% Co spheres are employed. At any given impact velocity, these latter spheres also produce a greater mass loss per unit mass of impacting material. These differences are attributed to the greater elastic mismatch of the WC - 6% Co spheres with the target. Neither hardness parameter could be correlated with mass loss in any obvious, general fashion.

The oblique single impact studies performed on chemically polished $\{100\}$ MgO surfaces with the WC - 6% Co spheres [9] revealed that reducing the angle of impact tended to concentrate the mass loss about the exit end of the crater

and produce more cracking within the crater as the crater got longer. They also revealed surprisingly little effect of hardness anisotropy on either the shape of the craters or the mass losses produced by particles approaching from different directions at the same impact angle, even though the slip line patterns formed around such craters can be quite different. Mass loss varied with impact angle in the same fashion as is usually observed in multi-particle impact studies of brittle or semi-brittle targets. As in all of the normal impact studies, there was no evidence of melting during the impact event; nor did any appreciable amount of target material adhere to the spent erosive particles.

Interpretation of these oblique impact experiments was based on the same model of a rigid sphere striking an ideal rigid-plastic half-space, but in this case the equation of motion of the particle had to be computed numerically by an iterative procedure [8,9,11,12]. The model successfully predicted [9] not only the observed crater dimensions and the measured rebound velocities, but also the value of the exponent (2.2) that characterizes the observed velocity dependence of the mass loss at velocities less than $\sim 200 \text{ m s}^{-1}$. At higher impact velocities, however, this exponent appears to increase, perhaps because frictional effects contribute to the mass loss by causing the erosive particle to drag material out of the impact crater. From the few data collected at normal and near-normal incidence in these oblique impact experiments, it is also apparent that the MgO crystals used were $\sim 25\%$ softer and suffered $\sim 40\%$ less mass loss under any given erosive conditions than those used in the normal impact studies reported above. Hence, because the (admittedly only semi-quantitative) spectroscopic analyses performed on the two sets of crystals revealed no large differences in impurity content, it is inferred that the mechanical behavior of MgO may be markedly more impurity-sensitive at high strain rates than low.

The same computer model has also been shown to explain satisfactorily the dependence of crater volume on impact angle observed by Hutchings et al. in

their studies of the impact of hardened steel spheres against mild steel targets [8]; and it is now being tested more extensively [13] by comparing its predictions of the relationships between such parameters as crater volume, impact angle and velocity, rebound angle and velocity, and energy loss per unit volume of crater formed with the appropriate experimental data from Hutchings' work. Furthermore, when a power law representation of work hardening was incorporated into the model [11], it also predicted successfully the variation of crater depth and volume with impact angle and velocity in the case of polycrystalline Al. For this material, however, the model was less successful at predicting crater length at the shallow impact angles and high impact velocities that produced the greatest pile-up of displaced material about the exit end of the crater.

(c) Multiple Particle Impact Studies

The multi-particle impact (erosion) studies performed with the whirling arm rig [7,10,11,12] used mechanically polished, polycrystalline specimens of Al and MgO as targets. In the case of Al the grain size was 4-5 μm ; and the MgO, which was a 99.5% dense hot-pressed material, had a grain size $\sim 10 \mu\text{m}$. The former material was eroded at velocities up to 150 m s^{-1} with the same 1.59 mm diameter WC - 6% Co spheres under conditions of both normal and oblique incidence; and the latter was eroded at normal incidence by 1.59, 1.14 and 0.35 mm diameter spheres of the same material, using impact velocities in the range $10\text{-}90 \text{ m s}^{-1}$.

An important feature of the studies on Al was that they fully documented for the first time the inception and evolution of the process of erosion on an initially relatively undamaged surface as a function of impact angle and velocity [7,11]. In particular, they showed that the threshold number of impacts per unit area required to initiate erosion (i.e., produce the minimum measurable mass loss) varies roughly as the inverse of the steady-state erosion when the impact angle is varied at some fixed impact velocity and as the impact velocity

raised to the powers -2.67 and -2.5 at impact angles of 30° and 90° (normal incidence), respectively. They also showed that the exponent relating the erosion to the impact velocity decreases monotonically throughout the incubation period--from 5.7 to 3.3 at normal incidence, and from 3.6 to 3.0 at an impact angle of 30°.

The accompanying scanning electron microscopy studies of the eroded target surfaces suggested that the same mechanism of material removal dominates at all angles of impact [11]. Specifically, they suggested that Al erodes via the detachment of thin platelets formed by extrusion of piled-up material between subsequently arriving particles and the underlying substrate. In this view, the role of ploughing deformation (or of cutting deformation when angular erosive particles are involved) is two-fold: first, it creates the piled-material for subsequent particles to extrude; and second, in so doing, it so reconfigures the target surface that a disproportionately large number of impact events take place against elements of surface area oriented more nearly perpendicular to the particle velocity vector than the original target surface.

In the case of the polycrystalline MgO targets [10], scanning electron microscopy revealed the damage to consist of a central crater surrounded by the sort of array of (transgranular) radial and/or median and lateral cracks characteristic of an elastic-plastic impact. However, although the crater had a thin lining of plastically deformed material, it appeared to have been formed primarily by localized transgranular and intergranular fracture processes, suggesting that any mode of irreversible deformation in the contact region will suffice to produce the changeover from Hertzian cracking to radial, median and lateral cracking. Various reports to the contrary notwithstanding, the accompanying gravimetric studies showed that mass loss--which occurred primarily by intersection of lateral cracks with radial and/or median cracks--increased threefold during the short incubation period in which the as-received surface

evolved into its steady-state eroded condition. Also, during this period the exponent relating erosion to impact velocity decreased monotonically to a value (2.1) less than that predicted by any of the current theories of erosion in the elastic or elastic-plastic impact regimes. Nor are these theories any more successful at explaining either the observation that the erosion of polycrystalline MgO varies as the particle diameter raised to the power 0.6 or the differences in the way in which the static and dynamic hardnesses of monocrystalline and polycrystalline MgO vary with strain rate [1,3,9,10].

III. LIST OF PUBLICATIONS

1. D. G. Rickerby, B. N. Pramila Bai and N. H. Macmillan, The Effect of Crystallographic Orientation on Damage in MgO Due to Spherical Particle Impact, J. Mater. Sci., 14, 1807-16 (1979).
2. D. G. Rickerby, Observations on the Hardness Anisotropy in MgO and LiF, J. Am. Ceram. Soc., 62, 222 (1979).
3. D. G. Rickerby and N. H. Macmillan, The Hardness of Cubic Single Crystals by Spherical Indentation, Mater. Sci. and Eng., 40, 251-9 (1979).
4. D. G. Rickerby and N. H. Macmillan, Mechanisms of Solid Particle Erosion in Crystalline Materials, in Erosion by Liquid and Solid Impact, pp. 29/1-6, Cavendish Laboratory, Cambridge (1979).
5. D. G. Rickerby, B. N. Pramila Bai and N. H. Macmillan, The Influence of Particle Properties on Impact Damage in LiF, J. Mater. Sci., 14, 3006-8 (1979).
6. D. G. Rickerby, B. N. Pramila Bai and N. H. Macmillan, Basic Mechanisms of Erosion in Ceramics, in Energy and Ceramics, P. Vincenzini, Editor, pp. 752-67, Elsevier, Amsterdam (1980).
7. D. G. Rickerby and N. H. Macmillan, The Erosion of Aluminum by Solid Particle Impingement at Normal Incidence, Wear, 60, 369-82 (1979).
8. D. G. Rickerby and N. H. Macmillan, On the Oblique Impact of a Rigid Sphere Against a Rigid-Plastic Solid, Int. J. Mech. Sci., in press.
9. D. G. Rickerby and N. H. Macmillan, The Effect of Approach Direction on Damage in MgO Due to Spherical Particle Impact, J. Mater. Sci., in press.
10. D. G. Rickerby and N. H. Macmillan, The Erosion of MgO by Solid Particle Impingement at Normal Incidence, submitted to J. Mater. Sci.
11. D. G. Rickerby and N. H. Macmillan, The Erosion of Aluminum by Solid Particle Impingement at Oblique Incidence, submitted to Wear.
12. D. G. Rickerby and N. H. Macmillan, Erosion of Aluminum and Magnesium Oxide by Spherical Particles, accepted for presentation at the 3rd International Conference on Wear of Materials (to be published by ASME in 1981).
13. I. M. Hutchings, D. G. Rickerby and N. H. Macmillan, Further Studies on the Oblique Impact of a Rigid Sphere Against a Ductile Solid, to be prepared for submission to Int. J. Mech. Sci.

Paper No. 4 was presented at the 5th International Conference on Erosion by Liquid and Solid Impact, Cambridge, England, 3-6 September 1979; and Paper No. 6 was presented at the 4th International Meeting on Modern Ceramics Technologies, Saint-Vincent, Italy, 28-31 May 1979. Paper No. 12 will be presented in San Francisco in April 1981.

IV. PARTICIPATING SCIENTIFIC PERSONNEL

Principal Investigator:

Prof. N. H. Macmillan, Associate Professor of Metallurgy and Materials Research

Project Associate:

Dr. D. G. Rickerby

V. ADVANCED DEGREES AWARDED

None sought.

Appendix I

The effect of crystallographic orientation on damage in MgO due to spherical particle impact

D. G. RICKERBY, B. N. PRAMILA BAI, N. H. MACMILLAN

Materials Research Laboratory, The Pennsylvania State University, University Park, PA 16802, USA

A single stage gas gun has been used to fire spherical chrome steel and WC particles at variously oriented and prepared MgO single crystals at velocities of up to 350 m sec^{-1} . The resultant damage has been studied by optical and scanning electron microscopy, dislocation etching and surface profilometry, and mass losses have been determined gravimetrically. The measured crater dimensions and the mass loss data have been compared with the predictions of a simple analytical model of the impact event.

1. Introduction

The erosion of materials by solid particle impingement is a serious problem in many industrial and aerospace systems. Yet, despite a growing technical literature on the subject, only relatively few attempts have been made to understand the fundamental mechanisms involved [1, 2]. As a result, little or nothing is yet known about the effect of even such a basic parameter as crystallographic orientation on the rate of material loss. It has, however, become clear that single impact studies are a useful means of investigating this and other questions about the mechanisms of erosion [3, 4]. This is because material removal during erosion occurs as the result of a series of essentially independent impact events. Moreover, it has also been recognized that, even though erosive particles are usually random in shape, a spherical particle in many cases can provide a reasonable simulation of a typical impact event [4].

At the present level of understanding, this is ample justification for using spherical particles and taking advantage of the experimental reproducibility and theoretical tractability that derive from doing so. In particular, when the impact direction is normal to the target surface, spherical geometry allows an analytical solution to the equation of motion of the particle to be obtained. It is for these reasons that the experimental work reported herein has been restricted to single normal impacts of spherical particles against surfaces

of different crystallographic orientation. MgO was chosen as the target material because: (i) it is available in the form of large monocrystals, (ii) it is cubic and therefore easily oriented, (iii) its elastic and plastic properties are well understood, (iv) its chemical polishing and dislocation etching characteristics are well established, and (v) it is relatively easy to handle without introducing extraneous damage.

2. Experimental

A 16 mm bore gas gun, developed from a design by Hutchings and Winter [5, 6], was used to fire the erosive particles at the requisite velocities. These particles were mounted on nylon sabots for firing, and were separated from them at the muzzle by means of a steel muzzle block which stopped the sabot virtually instantaneously but allowed the particle to pass on through a small hole. Sabot velocities were determined immediately before reaching the muzzle by a photoelectric time-of-flight device. These measurements were estimated to be accurate to within $\pm 1\%$, and the velocities attained at a given firing pressure were generally reproducible to better than $\pm 5\%$.

The targets were mechanically and/or chemically polished 10 mm \times 10 mm monocrystalline MgO slabs about 5 mm thick. Those slabs oriented parallel to {100} were first rough-shaped by cleavage, and those parallel to {110} or {111} by cutting with a water-cooled diamond saw. Thereafter, all

slabs were successively mechanically polished on wet 240, 320, 400 and 600 grit SiC papers and Buehler Texmet* cloths loaded with aqueous slurries of 1, 0.3 and 0.05 μm Al_2O_3 particles. Some specimens then received a further chemical polish in boiling aqueous H_3PO_4 to which a small amount of concentrated H_2SO_4 or HNO_3 had been added [7, 8]. The optimum solution concentration (which determined the boiling temperature) and polishing time varied with surface orientation [9]; but in each case it was shown by successively polishing and etching (by immersion in boiling concentrated HNO_3 for 10 sec [8]) that all mechanical damage had been removed. Finally, to facilitate subsequent handling, the polished slabs were flush mounted in standard sized cylinders of Kold-mount self-curing resin.† X-ray Laue diffraction studied showed that the polished and mounted target surfaces were typically within 2° of the desired crystallographic orientation.

Two types of crystal, hereinafter referred to as A and B,‡ were used in the experiments. The former were colourless, whereas the latter varied from an almost colourless to a pronouncedly yellow appearance, indicating a variable impurity content. Emission spectroscopic studies of one crystal of type A and several of type B produced the results summarized in Table I, and etch pit counts on chemically polished and etched {100} surfaces indicated that both types of crystal had initial dislocation densities $\sim 10^5 \text{ cm}^{-2}$.

Two kinds of erosive particles were employed. WC spheres weighing $30 \pm 1 \text{ mg}$, and of nominal diameter $1.575 \pm 0.025 \text{ mm}$ and Vickers hardness number (VHN) $\sim 2000 \text{ kg mm}^{-2}$ [10], were fired at surfaces of all three orientations; and precision manufactured chrome steel spheres weighing 16.2 mg, having a diameter of 1.5875 mm and a sphericity§ of 0.00065 mm, and having a Rockwell C hardness of 60 to 66,¶ were used to impact {100} surfaces in order to investigate the effect of particle hardness.

The impact craters formed were examined by surface profilometry and by optical and scanning electron microscopy (SEM). The first of these instruments provided cross-sectional profiles of the

TABLE I Semi-quantitative spectrochemical analyses of MgO crystals (p.p.m.)

Element	Crystal type	
	A	B
Ca	200	100-200
Al	40	40-100
Mn	50	50
Fe	100	100-200
Si	50	50
Ti	50	20

craters at equidistant ($50 \mu\text{m}$) intervals, allowing the determination of crater volume by the trapezoidal rule. In addition, crater depth and diameter were determined from the profile of a diametral section, which was assumed to be the section having the largest area below the original, undisturbed surface level.

Lastly, in order to determine the mass loss associated with impact damage (typically $\sim 10^{-3} \text{ g}$), each specimen was weighed before and after it was impacted. These measurements were reproducible to within $\sim \pm 5 \times 10^{-5} \text{ g}$, and this scatter was attributed to changes in the water content of the slightly hygroscopic Koldmount resin employed to mount the specimens.

3. Theoretical model of the impact

Following Tabor [11] and Andrews [13], consider a rigid sphere of radius r and mass m impacting normally on an ideal plastic-rigid half-space. At some instant during the impact the situation is as illustrated in Fig. 1, i.e. the projectile is moving

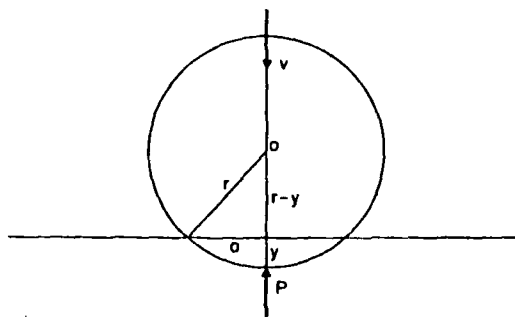


Figure 1 Schematic diagram of a spherical particle impacting normally on a half space.

* Buehler Ltd., 2120 Greenwood Street, Evanston, Illinois, USA.

† Vernon-Benshoff Co., 413 North Pearl Street, Albany 1, NY, USA.

‡ Supplied by: (A) A. Clauer, Battelle Memorial Laboratories, Columbus, OH; and (B) R. C. DeVries, General Electric Research and Development Center, Schenectady, NY, USA.

§ Difference between maximum and minimum diameters.

¶ Various reported as equivalent to VHN's of 765 to 960 kg mm^{-2} [11] and 700 to 860 kg mm^{-2} [12].

with a velocity v against a resistive force P , the radius of contact is a , and the depth of penetration is y . If it is assumed that the indentation pressure, or dynamic hardness, p_d is constant throughout the impact and is independent of the particle velocity,* it follows that $P = \pi a^2 p_d$, and that the equation of motion of the particle is

$$m\ddot{y} = -\pi a^2 p_d. \quad (1)$$

The solution of this equation is

$$v^2 = v_0^2 - \frac{2\pi p_d}{m}(ry^2 - y^3/3), \quad (2)$$

where v_0 is the initial impact velocity. If the sphere comes to rest at $y = l$, this gives

$$p_d = \frac{mv_0^2}{2\pi l^2(r - l/3)}, \quad (3)$$

where l is related to the crater diameter d by

$$l = r - (r^2 - d^2/4)^{1/2}. \quad (4)$$

Equations 1 to 4 are derived on the assumption that there is neither deformation of the particle during impact nor elastic recovery of the surface afterwards, whereas either or both of these may affect the situation significantly in practice. It has been reported that elastic recovery tends to reduce l , but to have little or no effect on d [11]. If plastic deformation of the particle occurs, it can be expected to absorb energy that would otherwise be used in further deforming the target, and to thereby decrease the crater volume V , cause concomitant reductions in both d and l , and affect crater sphericity, with the result that the relation between d and l will no longer be that given in Equation 4. In either event, therefore, the measured crater depth, hereinafter designated l' , may differ from the depth l implied by the theoretical model. However, only when the impacting particle deforms plastically does it seem likely that there will be any significant deviation of the crater diameter from the predicted value of d ; and such a deviation can be detected by conducting parallel experiments with particles of different hardness. It is therefore assumed initially that the measured values of d are consistent with the predictions of the original model and may be used in calculating first l and then p_d . Furthermore, it is also assumed that plastic deformation of the target occurs as a radial outflow of material without any piling up above the level of the original surface. In practice,

pile-up does occur, and so for consistency all measurements of crater dimensions were made relative to the original level of the undisturbed surface.

It should also be noted that, since the volume of a spherical cap of radius r and depth l is $\pi l^2(r - l/3)$, Equation 3 can be rewritten as

$$p_d V = \frac{1}{2} m v_0^2. \quad (5)$$

This expression, which is valid for any shape of crater when p_d is constant, is a statement of the energy balance implicit in the proposed model – namely, that all of the kinetic energy of the impacting particle is consumed in deforming the target plastically during crater formation, and that none is dissipated by plastic deformation of the particle or elastic recovery of the target. Equation 3 can also be rearranged as

$$l = \left[\frac{mv_0^2}{2\pi p_d(r - l/3)} \right]^{1/2}, \quad (6)$$

and then solved iteratively to obtain l in terms of p_d , the first iteration being

$$l \approx \left[\frac{mv_0^2}{2\pi p_d r} \right]^{1/2}. \quad (7)$$

And similarly, Equation 4 can be rearranged as

$$d = 2(2rl - l^2)^{1/2} \quad (8)$$

to give d in terms of l .

Finally, it is useful to make an order of magnitude estimate of the plastic strain rate during an impact event. This can be done straightforwardly for the present model of an ideal plastic-rigid target struck normally by a rigid sphere, for Tabor [11] has shown that: (i) a "representative value" of the strain ϵ in the complex strain field generated in the impact zone is

$$\epsilon \approx 0.1d/r, \quad (9)$$

and (ii) the impact duration t is independent of particle velocity and given by

$$t = \frac{\pi}{2} \left(\frac{m}{2\pi p_d r} \right)^{1/2}. \quad (10)$$

It follows that the mean strain rate $\dot{\epsilon}$ during the impact is

$$\dot{\epsilon} \approx 0.16d \left(\frac{p_d}{rm} \right)^{1/2} \approx 0.064 \frac{dv_0}{rl} \quad (11)$$

* Note also that p_d is, in general, larger than the static hardness p_s [22].

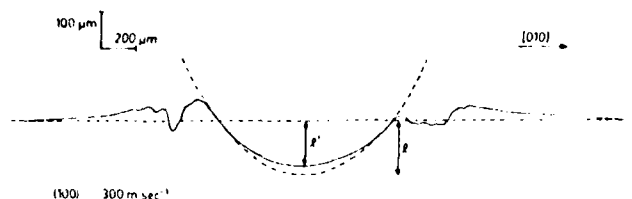


Figure 2 A diametral profile of a crater in a {100} MgO surface produced by the impact of a steel sphere. The broken lines indicate the original surface level and the outline of the sphere.

(from Equation 7). In the present work, typical values of t and $\dot{\epsilon}$ were $\sim 1 \mu\text{sec}$ and $\sim 10^5 \text{ sec}^{-1}$, respectively.

4. Results

4.1. Impacts using steel particles

Figs. 2 to 5 summarize the results obtained by firing single steel spheres at chemically polished {100} surfaces of A-type crystals at velocities of up to $\sim 350 \text{ m sec}^{-1}$.

The first of these figures shows (at a 2:1 ratio of vertical to horizontal magnification) a diametral profilometer trace through a crater created by a 300 m sec^{-1} impact. Superimposed on this profile is the diametral profile of a pristine steel sphere. It is apparent that the two profiles do not correspond and, in particular, that the measured depth is less than that predicted. Profilometry and SEM studies of spent spheres revealed that this discrepancy could be attributed to flattening of the spheres by plastic deformation during impact, at least at higher impact velocities.

Figs. 3 to 5 show the variation with impact velocity of the measured crater diameter, depth and volume, respectively. The values of the dynamic hardness calculated from the individual data points in Fig. 3 by means of Equations 3 and 4 reveal no systematic variation with velocity, but are distributed about a mean value of 1450 kg mm^{-2} with a

standard deviation of 210 kg mm^{-2} . In comparison, the static VHN was measured as 875 kg mm^{-2} , with a standard deviation of 19 kg mm^{-2} . The solid line drawn through the data of Fig. 3 was calculated from the mean value of the dynamic hardness and Equations 6 to 8. The good fit of this line to the experimental data implies, however, only that the scatter in the calculated values of the dynamic hardness is random in nature and limited in extent. In contrast, although the solid lines superimposed on the data for crater depth and volume shown in Figs. 4 and 5 also were obtained from this same value of the dynamic hardness (by means of Equations 6 and 7 in the case of Fig. 4, and Equation 5 in the case of Fig. 5), it is seen that the experimental points systematically diverge from both lines as the impact velocity increases. In

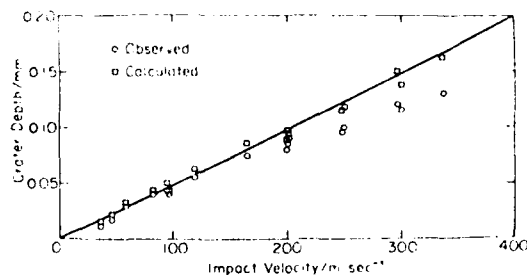


Figure 4 Depths of craters produced by the impact of steel spheres on {100} surfaces.

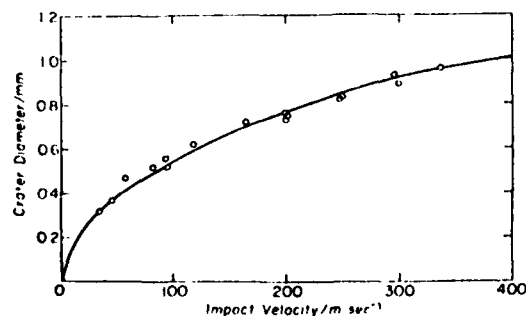


Figure 3 Diameters of craters produced by the impact of steel spheres on {100} surfaces.

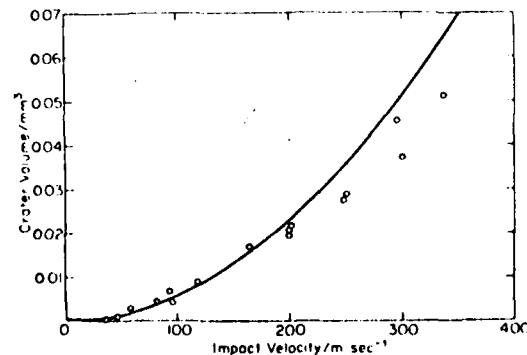


Figure 5 Volumes of craters produced by the impact of steel spheres on {100} surfaces.

the case of Fig. 4 this trend is confirmed by comparison of the experimental data with the points calculated from the measured crater diameters by means of Equation 4.

4.2. Impacts using WC particles

This section presents the results of a similar series of experiments in which single WC spheres were fired at variously polished $\{100\}$, $\{110\}$ and $\{111\}$ surfaces of B-type crystals, again using velocities of up to 350 m sec^{-1} . These spheres exhibited negligible plastic deformation during impact.

Figs. 6a to c show scanning electron micrographs of three craters resulting from impacts against chemically polished $\{100\}$, $\{110\}$ and

$\{111\}$ surfaces. It is clear from the very different patterns of $\{100\}$ and $\{110\}$ cleavage cracks and $\{110\}$ slip traces surrounding these three craters that the mode of material removal due to impact is markedly sensitive to crystallographic orientation. On a $\{100\}$ surface, as noted by Hooker and Adler [14], a roughly square eroded region is formed around a central plastic crater by intersection of $\{100\}$ and $\{110\}$ cleavage cracks. This region is deepest along its $\langle 110 \rangle$ diagonals, and the crater rim is most extensively chipped away in these directions also. In the $\{110\}$ case, the first material lost is that broken out along the $\langle 111 \rangle$ directions in the impact surface by intersection of $\{110\}$ cleavage cracks. At higher impact velocities this

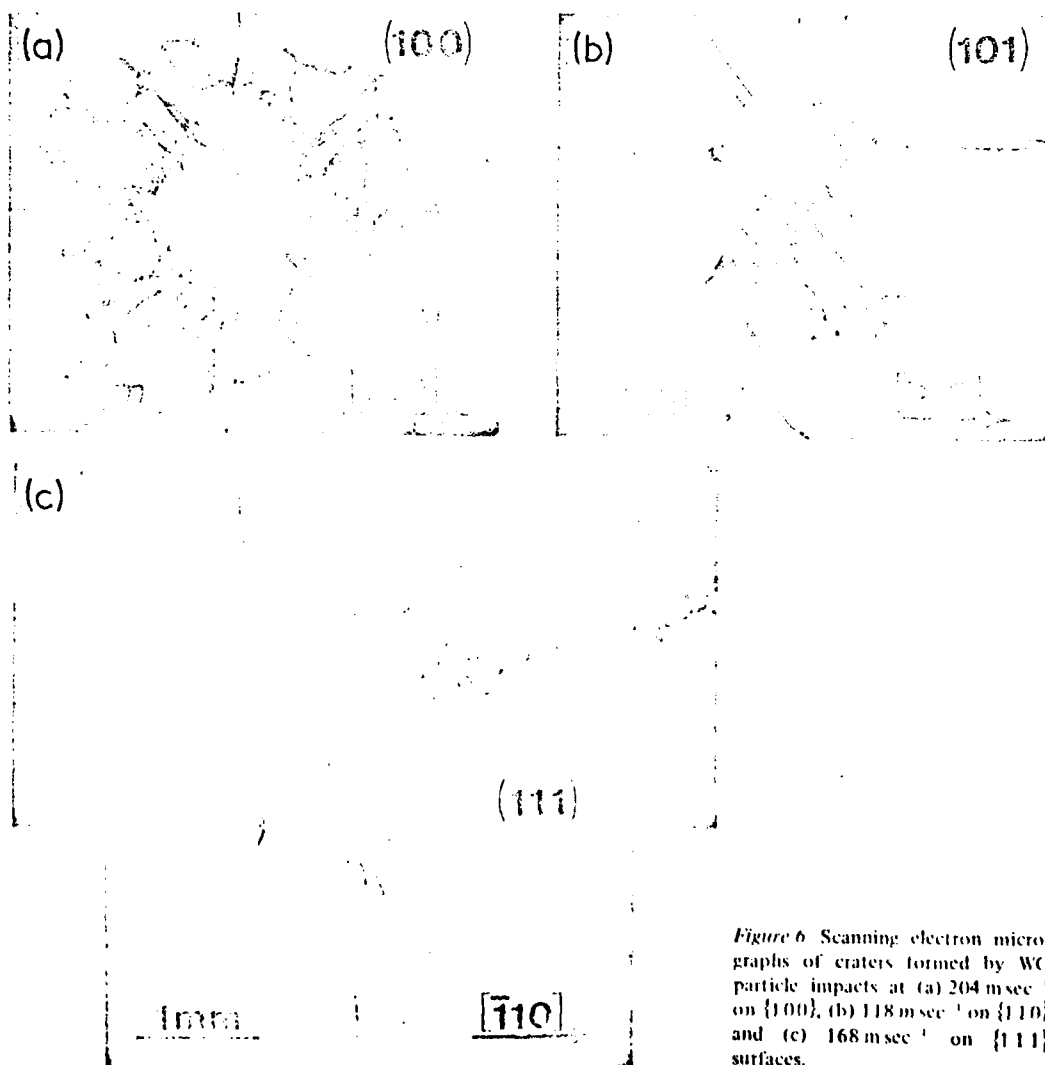


Figure 6 Scanning electron micrographs of craters formed by WC particle impacts at (a) 204 msec^{-1} on $\{100\}$, (b) 118 msec^{-1} on $\{110\}$ and (c) 168 msec^{-1} on $\{111\}$ surfaces.

process is augmented by chipping due to intersection of these same cracks either with subsurface $\{110\}$ cracks lying parallel to the impact surface and/or with $\{100\}$ cleavage cracks lying at 45° to it. There is also a tendency in this orientation for long thin triangular prism-shaped fragments to be broken out along the $\langle 100 \rangle$ direction in the impact surface by intersection of two $\{100\}$ cracks with this surface. The damage arising from impact against a $\{111\}$ surface exhibits strongly the three-fold symmetry of this surface, with material loss occurring primarily by $\{100\}$ cleavage from three petal-shaped areas ("wings") that extend along $\langle 211 \rangle$ directions. Fig. 7, which shows a crater formed at a lower impact velocity, reveals that the material in these wings is not detached when this velocity is small, but is merely raised above the original surface. Detachment begins only when the impact velocity exceeds $\sim 100 \text{ msec}^{-1}$, and occurs over an ever increasing area as this velocity increases, with the wings coalescing to form a continuous eroded region completely surrounding the central plastic crater at velocities around 200 to 300 msec^{-1} . In this velocity regime the damage bears some superficial resemblance to that occurring in polycrystalline ceramics [15], although the detailed fracture processes involved in the two cases are rather different.

Profilometer traces through diametral sections of craters in chemically polished specimens of the same three orientations are shown in Figs. 8a to c

at a 2:1 ratio of vertical to horizontal magnification. These traces were obtained by traversing the profilometer stylus across the impact regions in the particular crystallographic directions noted in the figures*. Several features of these traces are worthy of note. First, each exhibits a central plastic crater that is complete and can be measured accurately. This feature is usually lost at higher impact velocities due to encroachment of the surrounding eroded region into the central crater. Second, below the level of the original surface, each trace is (i) symmetrical and (ii) of the same curvature as the WC sphere that created it. Moreover, traces of other diametral sections obtained by traversing the impact zone in different crystallographic directions reveal the same features. It follows that both plastic deformation of the WC particle and elastic recovery of the target in the central crater region are negligible, and this implies that the difference between the measured and the predicted crater depths observed when steel particles were used can be attributed almost entirely to plastic deformation of these particles during the impact event. A third significant feature of the various diametral traces obtained from different directions of traverse is that most are not symmetrical above the level of the undisturbed surface. This asymmetry, which can be seen in Fig. 8c, for example, arises from material in the vicinity of the crater rim piling up by slip on the active slip planes in the active slip directions. The resultant crater rims exhibit four-, three- and two-fold symmetries in the cases of $\{100\}$, $\{111\}$ and $\{110\}$ target surfaces, respectively.

Figs. 9 and 10 show the variation with impact velocity of the measured crater diameter and depth, respectively, for impacts on chemically polished $\{100\}$ surfaces. The mean value of the dynamic hardness was first calculated from the individual data points in Fig. 9 and then used to obtain the theoretical lines shown in the figures exactly as in the previous section. The important point to note is that, while there is random scatter in the individual data points in Fig. 10, there is no systematic deviation from the theoretical line of the sort seen when steel particles are used. The corresponding crater volumes are shown in Fig. 11, together with those measured on chemically polished $\{110\}$ and $\{111\}$ surfaces.

Mass loss data for the same series of impacts are plotted in Fig. 12, and superimposed on these data

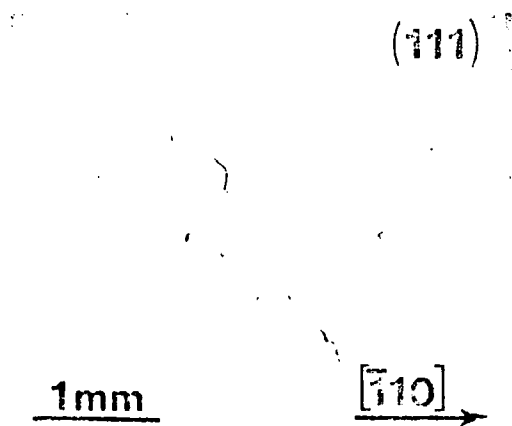


Figure 7 Scanning electron micrograph of a crater formed by the impact of a WC particle at 89 msec^{-1} on a $\{111\}$ surface.

* Quantitative measurements of crater dimensions were always made in these same directions.

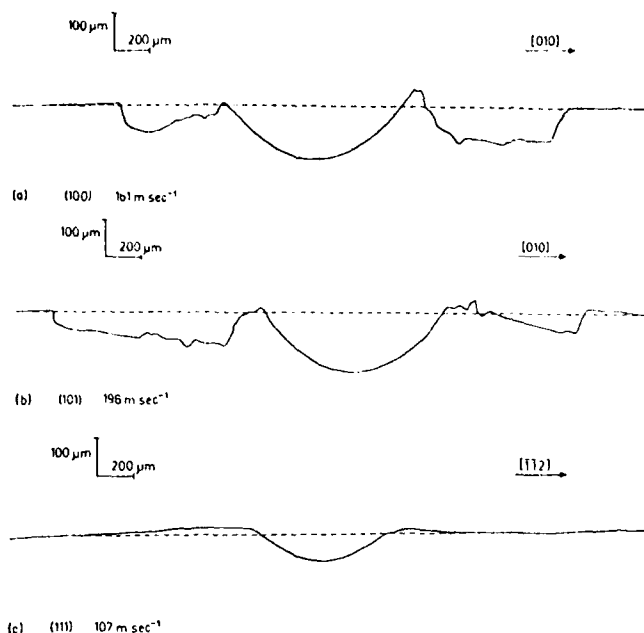


Figure 8 A comparison between diametral traces through impact craters made by WC particles in MgO surfaces of different orientations.

by the least-squares method are parabolas of the form

$$m_1 = kmv_0^2, \quad (12)$$

where m_1 is the mass loss and k is a constant dependent on the crystallographic orientation of the target. The good fit suggests that it is not unreasonable to suppose that, for a single impact, the mass loss depends on the kinetic energy of the impacting particle. It will be noted that, in comparison with {100} surfaces impacted at the same velocity, {110} surfaces yield a comparable crater volume and ~ 3 times the mass loss, while {111} surfaces give rise to a crater of about half the volume and about double the mass loss.

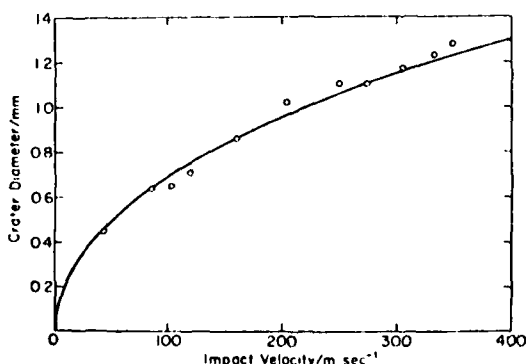


Figure 9 Diameters of craters due to impacts by WC spheres on chemically polished {100} surfaces.

In order to examine the influence of target surface condition on the impact event, further experiments using WC particles were carried out on {100} and {110} surfaces that had been given only

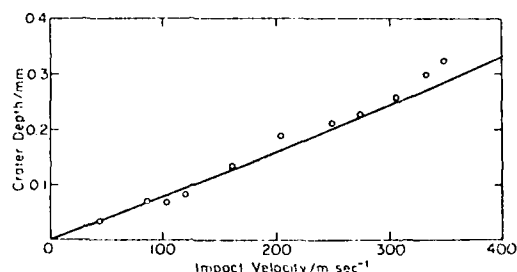


Figure 10 Depths of craters due to impacts by WC spheres on chemically polished {100} surfaces.

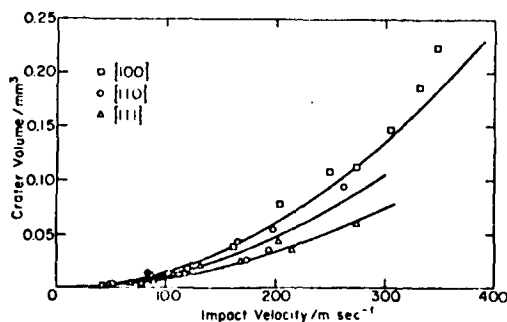


Figure 11 Volumes of craters due to impacts by WC spheres on chemically polished MgO surfaces.

TABLE II Summary of the results of impact experiments with WC particles.

Surface orientation	Polish	$p_d(\text{kg mm}^{-2})^*$	$p_s(\text{kg mm}^{-2})^*$		
			(M_V)	(M_B)	$k \times 10^7 (\text{m}^{-2} \text{sec}^{-1})$
{100}	chemical	1030 ± 180	995 ± 24	185 ± 23	2.02
{100}	mechanical	1170 ± 240	1013 ± 28	213 ± 47	3.71
{110}	chemical	1310 ± 310	972 ± 29	236 ± 34	5.80
{110}	mechanical	1090 ± 240	1014 ± 30	223 ± 75	7.18
{111}	chemical	1860 ± 470	999 ± 20	329 ± 59	3.96

* The figures given are mean values \pm one standard deviation.

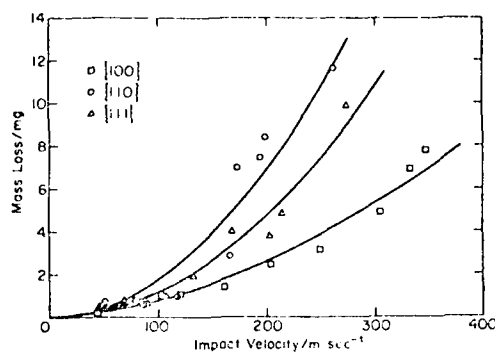


Figure 12 Mass loss data for impacts by WC spheres on chemically polished MgO surfaces.

the mechanical polish. The results indicated that this inferior finish exerted little influence on the size of the central plastic crater formed, but caused a significant increase in the mass loss.

The results of all five sets of dynamic hardness and mass loss measurements made using WC particles are summarized in Table II, together with corresponding values of the static Meyer-Vickers hardness M_V and Meyer ball hardness M_B [16]. The Meyer-Vickers hardness was measured using a conventional Vickers diamond pyramid indenter and a load of 300 g, but calculated as the load divided by the projected rather than the actual area of contact, and is thus related to the VHN by

$$M_V = \text{VHN}/0.927. \quad (13)$$

In a similar manner, the Meyer ball hardness was determined from the ratio of the load to the projected area of contact when one of the WC spheres used in the impact experiment was pressed quasi-statically into the target surface with a load of 50 kg (which gave an indentation comparable in size to a crater formed at an impact velocity $\sim 100 \text{ m sec}^{-1}$). These particular indicators of static hardness were selected because the dynamic hardness

was also calculated on the basis of the projected rather than the actual area of contact.

It is clear from Table II that the dynamic hardness and the Meyer ball hardness both have an essentially similar dependence on (i) surface finish and (ii) surface orientation. Specifically, neither parameter is significantly affected by surface finish, and both are substantially larger for {111} surfaces than for {100} surfaces. In contrast, the Meyer-Vickers hardness is not significantly affected by either surface finish or surface orientation. But the more significant conclusion from Table II is that there is no simple correlation between the mass loss coefficient and any hardness parameter.

5. Discussion

In a semi-brittle crystal such as MgO there is a complex interaction between flow and fracture. Dislocation glide at once promotes fracture by nucleating cracks at blocked slip bands and retards it by relaxing the applied stresses, thereby reducing the forces available to propagate these cracks. Glide may also cause crack tip blunting. This complexity is clearly apparent in the confusing arrays of cracks and slip bands revealed, as in Fig. 13, by etching a crystal after impact. Nevertheless, certain features of the results presented in the preceding section can be explained in terms of the established flow and fracture properties of MgO.

To begin with, it seems clear that the relatively greater anisotropy of the dynamic and Meyer ball hardnesses as compared to the Meyer-Vickers hardness stems simply from the difference in indenter geometry. In particular, because dislocations in MgO glide on {110} planes and have $\langle 110 \rangle$ Burgers vectors, they have no tendency to move as a result of uniaxial stresses directed along $\langle 111 \rangle$ directions, but are readily activated by such stresses acting parallel to $\langle 100 \rangle$ or $\langle 110 \rangle$. Hence, "blunt" spherical indenters, which in the early

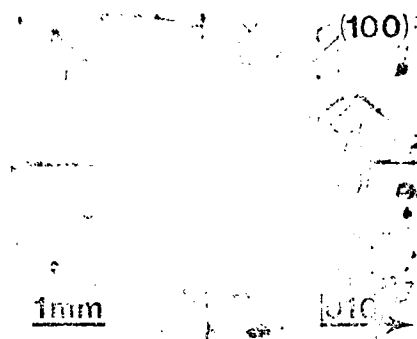


Figure 13 An impact crater on a {100} surface. The surface has been etched to reveal dislocation arrays.

stages of contact exert relatively larger compressive stresses and smaller shear stresses than a "sharper" pyramidal indenter, may be expected to give rise to a pronounced hardness maximum on {111}, as is in fact observed.

Secondly, it is possible to explain semi-quantitatively the difference between the dynamic hardness at a strain rate $\sim 10^5 \text{ sec}^{-1}$ and the Meyer ball hardness at a strain rate $\sim 10^{-3} \text{ sec}^{-1}$ in terms of the known dislocation stress-velocity relationship for MgO [17]. Specifically, because strain rate is proportional to dislocation velocity at constant (mobile) dislocation density (i.e., when the strain, the indenter geometry and the slip geometry are held constant) [18], the ratio p_d/M_B of these hardnesses should be equal to the stress multiplication factor required to speed up dislocation motion by a factor $\sim 10^8 \times$. Linear extrapolation of the data of Singh and Coble [17] gives a limiting value for this factor of 6 to 7 for both edge and screw dislocations, in reasonable agreement with the values of 5 to 6 for p_d/M_B reported in Table II. It is also interesting to note that dividing the longest dimension of the dislocation array seen in Fig. 13 by the impact duration time as given by Equation 10 suggests that dislocations may reach velocities as high as $2.5 \times 10^3 \text{ m sec}^{-1}$ during a typical impact. This is about half the {110}<110> shear wave velocity, and thus about half the maximum theoretical dislocation velocity.

The lack of any simple correlation between either static or dynamic hardness and mass loss is of practical interest because it demonstrates the futility of trying to relate erosion resistance to a single mechanical property. The reason for this lack is, of course, the complexity of the inter-

related flow and fracture processes occurring more or less simultaneously in the impact zone during the impact event. Thus, although the flow processes that absorb most of the impact energy undoubtedly begin, and for the most part take place, beneath the impacting particles, fracture propagation is prevented by the large compressive stresses present in this region. As a result, there is produced instead a well-defined central plastic crater, the size of which defines the hardness; and cracks nucleate only at points around the crater where the hoop stress below the target surface changes from compressive to tensile. Mass loss, in contrast, is determined by the orientation dependent interaction of these cracks with one another and with the free surface as they propagate outwards from the central crater, and is thus difficult to relate to the hardness. Nevertheless, the fact that both crater volume and mass loss appear to be proportional to the kinetic energy indicates that there is some relationship between these quantities. Presumably this relationship is an expression of the frequency and the nature of the dislocation interactions leading to fracture initiation at the edge of the central plastic crater, and is obscured by the complex dependence of this process on slip line length, slip line spacing, dislocation density, and a host of other parameters.

In conclusion, it is cautioned that neither the value of the mass loss coefficients, k , listed in Table II nor the velocity exponent of two used in Equation 12 should be expected to carry over to the multiple impact situation in which the further complication of interaction of cracks from adjacent impacts arises.

Acknowledgements

Work supported jointly by the National Science Foundation under Grant No. DMR-76-02733 and the U.S. Army Research Office under Grant No. DAAG29-77-G-0100.

References

1. C. M. PRELUT and N. H. MACMILLAN, *Ann. Rev. Mat. Sci.* 7 (1977) 95.
2. I. FINNIE, *Wear* 19 (1972) 81.
3. I. M. HUTCHINGS and R. E. WINTER, *J. Phys. D: Appl. Phys.* 8 (1975) 8.
4. I. M. HUTCHINGS, R. E. WINTER and J. E. FIELD, *Proc. Roy. Soc. Lond. A* 348 (1976) 379.
5. I. M. HUTCHINGS, Ph.D. Dissertation, University of Cambridge (1974).
6. I. M. HUTCHINGS and R. E. WINTER, *J. Phys. E: Sci. Instrum.* 8 (1975) 84.

7. R. J. STOKES, T. L. JOHNSTON and C. H. LI, *Trans. AIME* **215** (1959) 437.
8. G. W. GROVES, Ph.D. Dissertation, University of Cambridge (1962).
9. B. N. PRAMILA BAI and N. H. MACMILLAN, *J. Mater. Sci.* **14** (1979) 494.
10. E. K. STORMS, "The Refractory Carbides" (Academic Press, New York, 1967).
11. D. TABOR, "The Hardness of Metals" (Oxford University Press, London, 1951).
12. "Standard Hardness Conversion Tables for Metals", ASTM Standard No. E140-72.
13. J. P. ANDREWS, *Phil. Mag.* **9** (1930) 593.
14. S. V. HOOKER and W. F. ADLER, "Fracture Mechanics of Ceramics", Vol. 3, edited by R. C. Bradt, *et al.* (Plenum Press, New York, 1978).
15. A. G. EVANS, M. E. GULDEN and M. ROSENBLATT, *Proc. Roy. Soc. Lond.* **A361** (1978) 343.
16. F. A. McCLINTOCK and A. S. ARGON, "The Mechanical Behavior of Metals" (Addison-Wesley, Reading, Mass., 1966) Ch. 13.
17. R. N. SINGH and R. L. COBLE, *J. Appl. Phys.* **45** (1974) 990.
18. A. H. COTTRELL, "Dislocations and Plastic Flow in Crystals" (Oxford University Press, London, 1953).

Received 19 July 1978 and accepted 5 January 1979.

Appendix II

Table I. Effective Resolved Shear Stress Factors and Measured Hardness Numbers

Indenter orientation	$\frac{1}{2} \cos \lambda \cos \phi (\cos \psi + \sin \gamma)$		MgO		LiF	
	Vickers	Knoop	VHN	KHN	VHN	KHN
<100>	0.110	0.304	922	400	124	96
<110>	0.360	0.149	765	780	99	103

*Ref. 3.

nated $\{110\}_{45}$ and $\{110\}_{90}$, respectively. The quoted factors refer to the $\{110\}_{45}$ planes, since these are the ones for which the effective resolved shear stress is greatest and on which slip will thus initiate. Although slip will subsequently occur on the $\{110\}_{90}$ planes as well, the analysis used in deriving Eq. (2) is based on the initial yielding condition. There is clearly an inverse correlation between the theoretical factors and the experimental hardness values. Hence the observed anisotropies for both Vickers and Knoop indentation are compatible with the theory of Brookes *et al.*³ and the apparent anomaly is resolved.

Acknowledgment: The writer thanks N. H. Macmillan for useful comments and suggestions.

Observations on the Hardness Anisotropy in MgO and LiF

D. G. RICKERBY

It has been proposed¹ that the Vickers hardness number (VHN) and the Knoop hardness number (KHN) are related by

$$\text{VHN}_\theta = \frac{1}{2}(\text{KHN}_\theta + \text{KHN}_{\theta+90^\circ}) \quad (1)$$

where θ is any arbitrary orientation of the indenter axis. This expression implies that both types of hardness measurement should show similar anisotropies on the (001) surface of MgO and LiF. The fact that they actually exhibit opposite anisotropies has been ascribed, for MgO, to differences in the local work-hardening behavior around the indenter due to changes in its geometry and orientation.²

However, there is an alternative explanation based on the analysis of hardness anisotropy presented by Brookes *et al.*,³ which states that the effective resolved shear stress τ_r on the operative slip plane is given by

$$\tau_r = \frac{1}{2}(F/A) \cos \lambda \cos \phi (\cos \psi + \sin \gamma) \quad (2)$$

where F is the tensile force acting parallel to the line of maximum slope in the indenter facet, A the area over which F is acting, λ the angle between the axis of F and the slip direction, ϕ the angle between the axis of F and the normal to the slip plane, ψ the angle between the line in the indenter facet perpendicular to the axis of F and the axis of rotation for a given slip system, and γ the angle between this same line in the facet and the slip direction. The angular factor in this expression should vary inversely with the relative magnitude of the hardness, a result which these workers confirmed qualitatively by measuring the hardness anisotropies of various crystals.

Experimental values of VHN and KHN for MgO and LiF are given in Table I, together with the corresponding effective resolved shear stress factors computed from Eq. (2). The primary slip system in both crystals is $\{110\}\langle 110 \rangle$ and there are thus two possible orientations of the slip planes with respect to the (001) surface, either at 45° to or perpendicular to it. These slip planes are dis-

¹ R. W. Armstrong and A. C. Raghuram, pp. 174-85 in *The Science of Hardness Testing and Its Research Applications*, Edited by J. H. Westbrook and H. Conrad, American Society for Metals, Metals Park, Ohio, 1973.

² R. W. Armstrong and C. M. Wu, "Lattice Misorientation and Displaced Volume for Microhardness Indentations in MgO Crystals," *J. Am. Ceram. Soc.*, **61** [3-4] 102-106 (1978).

³ C. A. Brookes, J. B. O'Neill, and B. A. W. Redfern, "Anisotropy in the Hardness of Single Crystals," *Proc. R. Soc. London, Ser. A*, **322** [1548] 73-88 (1971).

Appendix III

The Hardness of Cubic Single Crystals by Spherical Indentation

D. G. RICKERBY and N. H. MACMILLAN

Materials Research Laboratory, The Pennsylvania State University, University Park, Pa. 16802 (U.S.A.)

(Received February 22, 1979; in revised form May 4, 1979)

SUMMARY

Spherical indenters have been used to study the effect of indentation diameter on the hardnesses of variously oriented surfaces of ductile and semi-brittle cubic single crystals. The results are discussed in terms of the elastic recovery, the initial yield, the strain hardening and the crack nucleation processes occurring around and beneath the indenter.

1. INTRODUCTION

During the past several years it has become widely recognized that hardness tests represent a useful means of studying various mechanical properties of solids [1, 2]. In particular, the Knoop test has been employed extensively in investigations of plastic anisotropy. One reason for this is that the elongated shape of the Knoop indenter renders this measure of hardness particularly sensitive to indenter orientation about the normal to the plane of indentation. Indeed, Garfinkle and Garlick [3] have found that the Knoop hardness of LiF and of various f.c.c. and b.c.c. metal single crystals depends primarily on the orientation of the long axis of the indenter relative to the crystal lattice rather than on the plane of indentation. A second reason is that the faceted shape of the indenter gives rise to an indentation strain field (and hence a strain hardening contribution to the hardness) that is independent of load. Finally, the Knoop test is attractive for its geometrical simplicity which facilitates the task of relating this measure of hardness to such fundamental parameters as the critical resolved shear stress and the rate of strain hardening. As a result Daniels and Dunn [4]

and Brookes *et al.* [5] have been able to develop geometric arguments to relate Knoop hardness anisotropy to the onset of yielding on the most favorably oriented slip plane or planes, Armstrong *et al.* [6 - 8] have succeeded in extending such arguments to take account of strain hardening and Wonsiewicz and Chin [9, 10] have succeeded in relating this anisotropy to strain hardening by means of a theory that takes into consideration the total crystallographic shear occurring around and beneath the indenter [11].

In contrast, a spherical indenter produces a measure of hardness that is independent of the orientation of the indenter relative to the crystal lattice but sensitive to both the orientation of the indented surface and the applied load. The spherical indentation test is therefore complementary to the Knoop test and of particular value as a means of studying anisotropy in strain hardening; as such it has been used in a variety of studies of single-crystal plasticity [12 - 26]. The present paper extends this previous work in systematic fashion by using spherical indenters to study the effects of load and orientation of the indented surface on the hardness of both ductile (nickel and aluminum) and semi-brittle (LiF and MgO) single crystals.

2. EXPERIMENTAL

2.1. Specimen preparation and characterization

{100}, {110} and {111} oriented slabs of nickel, aluminum and LiF approximately 1 cm × 1 cm × 1 cm in size were sawn from larger single crystals, were rough ground on wet 240, 320, 400 and 600 grit SiC papers,

were polished on Buehler Texmet* cloth with aqueous slurries of 1, 0.3 and 0.05 μm Al_2O_3 abrasives and were mounted in Koldmount** resin. The corresponding MgO specimens were similarly prepared except that they received a final chemical polish in boiling aqueous H_3PO_4 [27, 28] prior to mounting. X-ray Laue diffraction studies showed that the mounted and polished specimens were typically within 2° of the desired orientation.

Because aliovalent impurities can markedly influence dislocation mobility in ionic crystals [29], semiquantitative spectrochemical analyses were performed on the LiF and MgO specimens. The results are shown in Table 1.

TABLE 1

Impurity element	Concentration (ppm)	
	MgO	LiF
Ca	100 - 200	100 - 200
Al	40 - 100	40
Mn	50	—
Fe	100 - 200	100
Si	50	50
Ti	20	—
Mg	—	2 - 5
Cu	—	5 - 20

The suppliers' data indicated that the aluminum and nickel crystals were 99.998% and 99.97% pure respectively. At these levels, impurities should not significantly affect the critical resolved shear stress of these f.c.c. metals [30].

2.2. Indentation tests

An Instron universal testing machine fitted with a spherical WC-6% Co indenter 1.59 mm in diameter was used to make indentations with diameters in the range 0.1 - 1 mm in MgO specimens of all three orientations; the corresponding indentations in nickel, aluminum and LiF were made in similar fashion with a spherical steel indenter 1.58 mm in diameter. The indenters had Vickers hardness numbers (VHNs) of about 2000 and 700 - 860 kgf mm^{-2} respectively, and the harder of

the two was used in the experiments with MgO to minimize any complication due to indenter plasticity [12]. In all tests the rate of indenter penetration was chosen so that the maximum load was reached in 15 - 25 s; the indenter was then held stationary for a further 15 s prior to unloading.

The diameters of the resultant indentations were measured along all the crystallographic directions of each type listed in Table 2 on {100} and {110} surfaces and along any two randomly selected {211} directions on {111} surfaces. The measurements were made by means of an optical microscope fitted with a micrometer eyepiece and focused on the surrounding undisturbed surface, with ancillary oblique illumination being used to highlight the crater rim; in every case the hardness was calculated from the average of the applicable set of diameter measurements. Diametral traces were also made through a number of indentations by means of a surface profilometer.

TABLE 2

Material	Surface orientation	Directions of measurement
Al, Ni	{100}	{100}, {110}
LiF, MgO	{100}	{100}
Al, Ni, LiF, MgO	{110}	{100}, {110}
Al, Ni, LiF, MgO	{111}	{211}

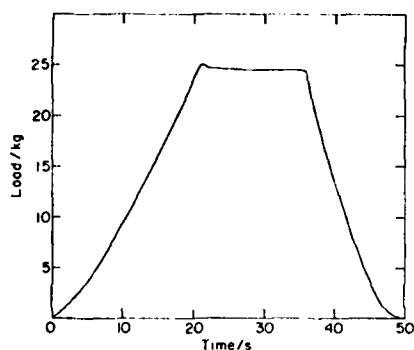
3. RESULTS

Figure 1 shows two typical load-time records from the Instron machine. The one for the nickel specimen has a smooth profile whereas that for the MgO specimen exhibits "spikes" associated with the formation of cracks during loading. This cracking, which was accompanied by an audible "clicking" sound, occurred more extensively at high loads than at low loads and was more extensive in MgO than in LiF. Both records show also that the load relaxed by a few per cent during the 15 s that the indenter was held stationary.

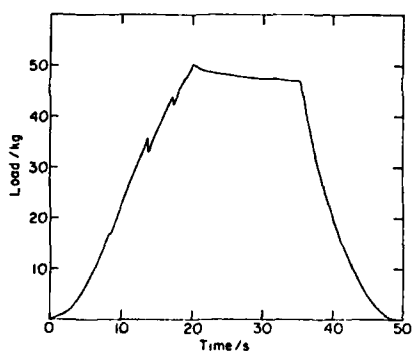
The micrographs in Figs. 2 and 3 show indentations made at both high and low loads in {100}, {110} and {111} surfaces of ductile (nickel) and semi-brittle (LiF) crystals

*Supplied by Buehler Ltd., 2120 Greenwood St., Evanston, Ill. 60201.

**Supplied by Vernon-Benshoff Co., 413 N. Pearl St., Albany, N.Y. 12201.



(a)



(b)

Fig. 1. Load-time records for indentations in {100} surfaces of (a) nickel and (b) MgO.

respectively. It will be noted that none of the indentations made at high loads are wholly in focus but appear as ill-defined and (particularly in the case of nickel) oddly shaped black regions completely lacking in contrast. The lack of definition comes about because the microscope lacked the depth of focus to accommodate the deeper impressions and more extensive piling-up and sinking-in of surrounding material produced by the higher loads; the loss of contrast occurs because the steeper surface slopes in and around impressions produced at higher loads reflected more of the normally incident illumination used for the photomicrography outside the cone of acceptance of the microscope objective. Therefore it should not be inferred from Figs. 2 and 3 that the shapes of indentations formed at different loads differ markedly. On the contrary, as revealed by the surface profilometry studies and the oblique illumination technique used when measuring indentation diameters, the shape of the impression formed in any given surface by a given indenter changes relatively little as the applied load increases. These same sorts of measurements also showed that for a given load and indenter the deviation of the rim of the impression from circularity is greater for nickel and aluminum than for LiF and MgO,

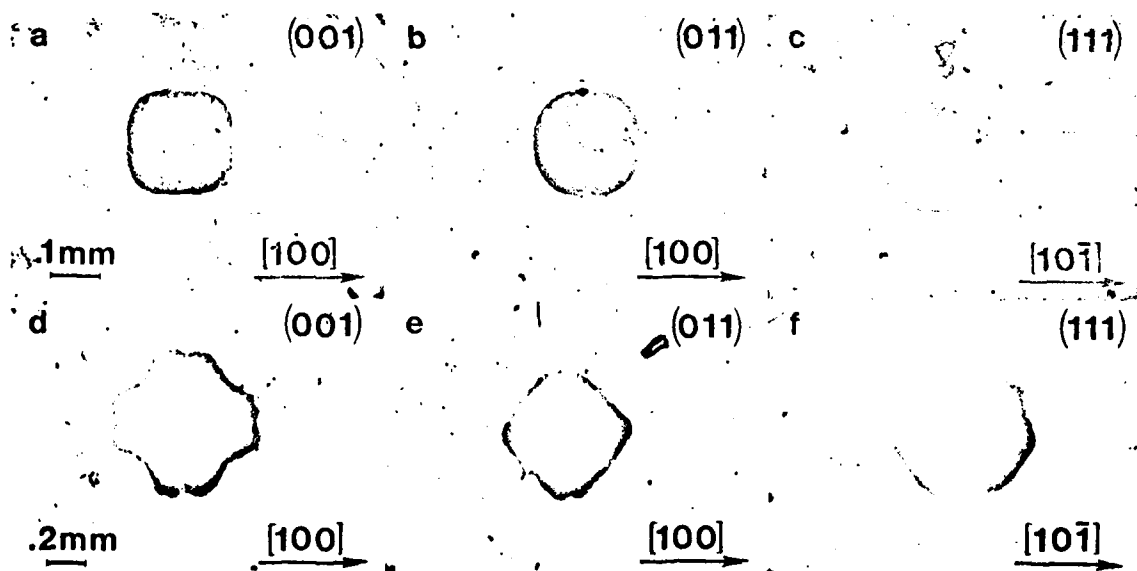


Fig. 2. The appearance of indentations in nickel single crystals for (a), (b), (c) a 2 kgf load and (d), (e), (f) a 25 kgf load.

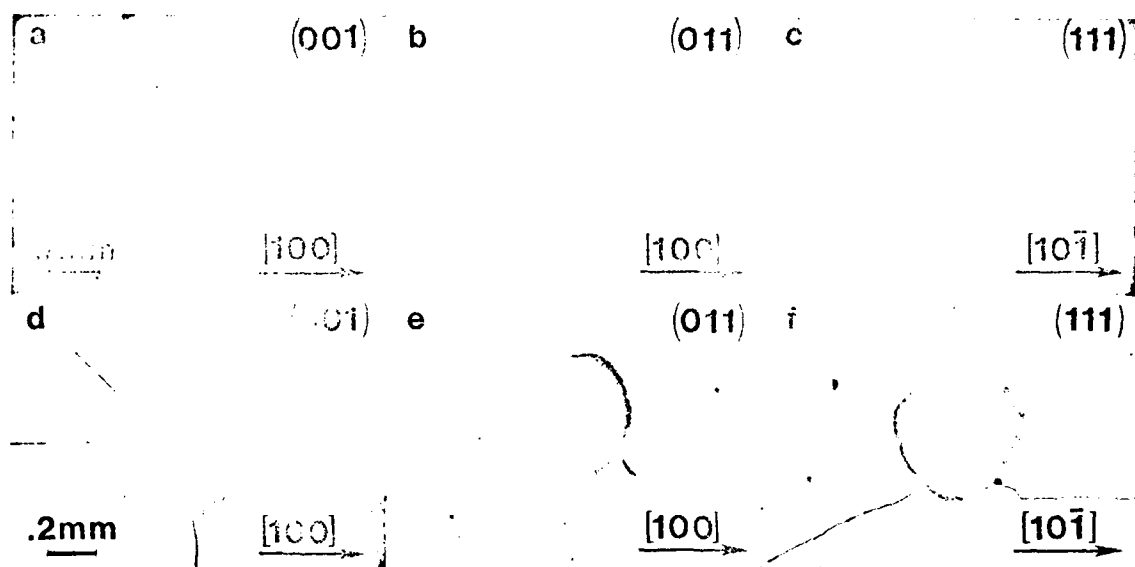


Fig. 3. The appearance of indentations in LiF single crystals for (a), (b), (c) a 5 kgf load and (d), (e), (f) a 20 kgf load.

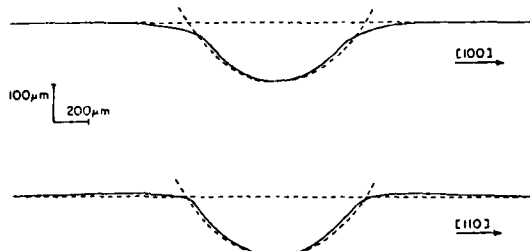


Fig. 4. Diametral surface profiles through an indentation made in nickel at a 50 kgf load. The broken lines indicate the indenter profile and the undisturbed surface.

i.e. that slip produces greater surface displacements than does cracking.

Comparison of the shape of the indenter with surface profilometer traces across different indentation diameters (such as those shown in Fig. 4) revealed negligible elastic recovery below the level of the original surface at low loads. However, for indentations with a diameter greater than about one-half the indenter diameter, elastic recovery resulted in a net reduction of the indentation diameter relative to its depth. This recovery was more pronounced in nickel than in aluminum, and in LiF than in MgO.

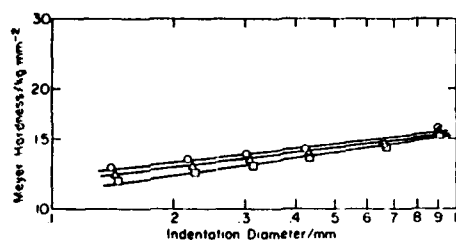
For spherical indenters, Meyer [31] has shown empirically that the load P is related to the indentation diameter d by

$$P = kd^n$$

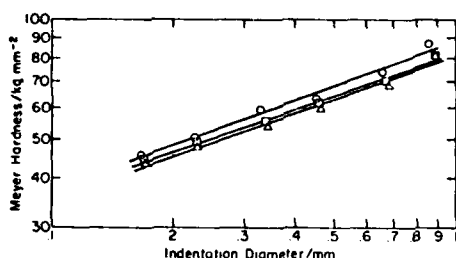
where k and n are material-dependent constants. Further, because the Meyer hardness M is defined [31] as the load divided by the projected area of contact $\pi d^2/4$ it follows that

$$M = k_1 d^{n-2}$$

and $n - 2$ can be found from the slope of a plot of $\log M$ versus $\log d$ when Meyer's law is obeyed. Figures 5 and 6 show such plots for all three surface orientations of the ductile and semi-brittle specimens respectively. Each data point represents the average from nine hardness tests. For each surface of each material a good fit to the data can be obtained by linear regression, showing that Meyer's law is closely obeyed. The values of $n - 2$ obtained from these lines are listed in Table 3 together with the extrapolated hardness values M^* corresponding to an indentation diameter equal to the indenter diameter. It should be noted that, whereas nickel, aluminum and LiF all exhibit hardnesses that vary little with the orientation of the surface and increase with increasing indentation diameter, the hardness of MgO both shows greater anisotropy and decreases as the indentation diameter increases.

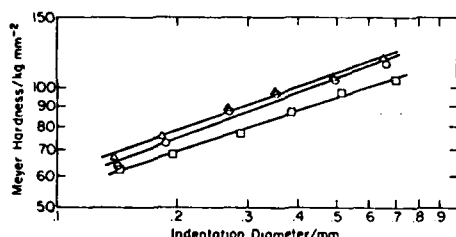


(a)

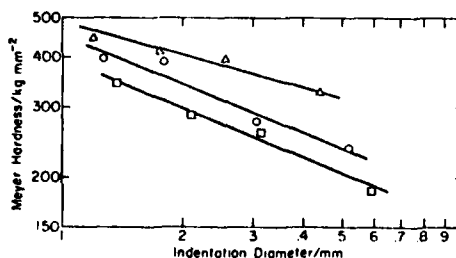


(b)

Fig. 5. The variation of Meyer hardness with indentation diameter and surface orientation in (a) aluminum and (b) nickel: \square , {100}; \circ , {110}; \triangle , {111}.



(a)



(b)

Fig. 6. The variation of Meyer hardness with indentation diameter and surface orientation in (a) LiF and (b) MgO: \square , {100}; \circ , {110}; \triangle , {111}.

4. DISCUSSION

The appearance of the indentations formed in nickel and aluminum is in almost all respects consistent with the descriptions given by earlier workers in this field. In particular,

TABLE 3

Crystal	$n - 2$			M^* (kgf mm ⁻²)		
	{100}	{110}	{111}	{100}	{110}	{111}
Al	0.15	0.12	0.13	16.4	16.6	16.5
Ni	0.35	0.38	0.36	95.9	105.2	95.4
LiF	0.34	0.38	0.36	139.8	165.1	164.6
MgO	-0.41	-0.41	-0.27	126.8	147.9	229.6

there is substantial piling-up and sinking-in around the crater rim, as reported long ago by O'Neill [14, 15] and others [13, 17, 18]. Consequently, as was first pointed out by Carpenter and Elam [13], it is difficult to define the crater diameter unambiguously. As in the case of the dynamic normal impact of a spherical particle [32] the piling-up and sinking-in can be explained in terms of primary {111}⟨110⟩ glide alone, as might be expected in materials having five independent primary slip systems.

The sinking-in and piling-up is much less for the semi-brittle materials LiF and MgO which have only two independent primary slip systems. However, definition of the crater rim is still no easier because extensive fracturing occurs on {100} and {110} planes. Nor is there any evidence of secondary slip about any of the indentations made in LiF and MgO in the present work. The same is true in the dynamic situation at a strain rate about seven orders of magnitude greater [32]. Lack of evidence of secondary slip is not, of course, conclusive proof that such deformation did not take place. However, the observation that cracking occurs more extensively around indentations in MgO than in LiF supports this contention, for the work of Buerger [33] and Mueller [34] implies that secondary slip should occur more easily in relation to primary in MgO, and it must be supposed that such slip would have an inhibiting effect on crack propagation. Apparently the extensive fragmentation occurring around and beneath the indenter permits all the additional deformation necessary to accommodate the shape change imposed by the indenter.

The present results also (i) confirm the previous observations that spherical indenters produce indentations that are circularly symmetric about the surface normal below

the level of the original surface under both quasistatic [35] and dynamic conditions [32] and (ii) reveal that only for the larger indentations does the shape of the residual impression differ measurably from that of the indenter (Fig. 4). For all four materials this difference in shape takes the same form as it does under dynamic conditions, i.e. a proportionally greater reduction in indentation diameter than in depth. As a result the radii of curvature of the larger indentations are less than the radius of the indenter. It follows that this difference in shape between indenter and indentation is the result of elastic recovery of the material indented rather than of flattening of the indenter by plastic deformation [32]. It also follows from (i) not only that anisotropic elastic recovery plays little part in determining the shape of the impression but also that the distortion of the outlines of the indentations seen in Figs. 2 and 3 results primarily from surface displacement by slip.

From Hertz's analysis of the problem of elastic contact between two isotropic elastic spheres [36], the relation between the indentation diameter d , the radius of curvature r_1 of the indenter and the radius of curvature r_2 of the residual impression is

$$d = \left\{ \frac{6Pr_1r_2}{r_2 - r_1} \left(\frac{1 - \nu_1^2}{E_1} + \frac{1 - \nu_2^2}{E_2} \right) \right\}^{1/3}$$

where ν_1 and ν_2 are the Poisson's ratios, and E_1 and E_2 are the Young's moduli, of the indenter and specimen respectively. Tabor [12] has noted that this equation is applicable only if the effect of elastic recovery on indentation diameter is negligible and has reported data confirming that the radius of curvature of the indentation is greater than the indenter radius by the predicted amount for relatively shallow indentations in polycrystalline metals. However, data obtained by Foss and Brumfield [35] indicate that as the indentation becomes deeper the theoretical expression tends increasingly to overestimate the observed radius of curvature of the impression.

In the present work the indenters were about an order of magnitude smaller in diameter than those used in both these previous studies. The product of r_1 and r_2 is thus about two orders of magnitude

smaller, so the difference between them must decrease by a corresponding factor for geometrically similar indentations. It is for this reason that no elastic recovery was observed in indentations made at low loads in the present work. Moreover, the seemingly anomalous recovery observed in the deeper impressions cannot be attributed to the monocrystalline and therefore anisotropic nature of the materials indented, for it was also observed in polycrystalline nickel with a grain diameter of about 0.045 mm. Instead, it appears that the increasing amount of piling-up and sinking-in that occurs as the indenter penetrates deeper sufficiently distorts the surface around the indentation to cause breakdown of the Hertz-Tabor analysis, and this produces a proportionately greater and greater reduction in the diameter of the impression compared with its depth.

In the case of aluminum the present studies reveal that the total variation in Meyer hardness with orientation of the surface indented is less than 10% and that $M_{\{110\}} > M_{\{111\}} > M_{\{100\}}$; they thus confirm the conclusions reached by O'Neill [14] from experiments on less certainly oriented specimens of this metal. They also confirm findings of O'Neill that (i) Meyer's law is obeyed and (ii) M extrapolates to a value M^* that is virtually independent of surface orientation as the impression diameter approaches the indenter diameter. This orientation independence of M^* follows from application of such theories of hardness as those of Daniels and Dunn [4] and Brookes *et al.* [5], which are based on an effective resolved shear stress yield criterion, to the expansion of a hemispherical cavity in a plastic solid. This is because the hemispherical surface of contact between the indenter and the substrate effectively averages over all possible slip plane orientations regardless of the orientation of the surface indented. That M^* is independent of the orientation of the surface in the present experiments thus suggests that the yield behavior of aluminum is little affected by deformation path during spherical indentation. It is similarly interesting that even though this argument ignores all strain-hardening effects it applies equally well to the behavior of two lots of aluminum crystals which appear on the basis of their Meyer indices (2.12 - 2.15 in the

present work and 2.27 - 2.48 in O'Neill's work [14]) to strain harden rather differently. Presumably the greater rate of strain hardening evinced by O'Neill's crystals stems from some precipitation hardening effect associated with their substantially greater impurity content (0.4%).

In comparison with aluminum, nickel exhibits greater strain hardening (Meyer indices 2.35 - 2.38) on all three surfaces, more scatter in M^* and a qualitatively different dependence of Meyer hardness on surface orientation. Since f.c.c. single crystals typically strain harden (in stage II, at least) at rates proportional to their shear moduli [37], the first of these features conceivably derives directly from the greater elastic stiffness of nickel compared with aluminum [38]. Neither of the last two observations, however, is consistent with the models of hardness anisotropy [4, 5] discussed above, and either or both may result from the stronger dislocation-surface interactions arising from this greater stiffness.

Figure 6 reveals that MgO and LiF exhibit qualitatively similar variations of Meyer hardness with surface orientation, as expected from the theories of Daniels and Dunn [4] and Brookes *et al.* [5], but that the magnitude of this anisotropy is greater for MgO. The same figure also reveals that the hardness of MgO decreases with increasing load on all three surfaces studied and has no tendency to converge to any surface orientation-independent value M^* , whereas LiF behaves much more like nickel and aluminum in both these regards. These differences in behavior are all presumed to derive primarily from the much greater incidence of cracking that takes place around impressions in MgO compared with LiF, especially at higher loads. Apparently crack propagation represents a method of producing deformation of MgO beneath an indenter that is sufficiently less energy intensive than dislocation motion that it can — if it develops extensively enough as the load increases — more than offset any effect of strain hardening, thereby allowing the indenter to penetrate deeper and producing a hardness that decreases with load. Moreover, because this cracking in MgO is restricted for the most part to {100} and {110} planes its contribution to the overall hardness probably

varies with surface orientation; this, it is suggested, is why the hardnesses of different MgO surfaces diverge rather than converge as the load increases and cracking contributes an increasingly greater proportion of the total deformation.

This rationalization of the experimental observations ignores the more difficult question of why MgO should fracture more extensively than LiF in the present experiments. This observation cannot be attributed to the difference in specimen preparation, for the chemically polished MgO specimens should have contained fewer surface flaws than their mechanically polished LiF counterparts. In addition, as has already been pointed out, it cannot derive from differences in the relative ease of primary *versus* secondary slip since (i) there is no evidence that secondary slip occurred in either material and (ii) such slip would be expected to occur more easily relative to primary slip in MgO than in LiF [33, 34]. Moreover, since Alden [39, 40] has shown that LiF has a higher latent hardening ratio than MgO it is difficult to reconcile this observation with the usual view that crack nucleation in such crystals takes place at blocked slip bands. Perhaps the answer lies not in the relative ease of dislocation motion in the two crystals but in the relative ease of dislocation nucleation at the tip of a crack. It is unfortunate that the existing theoretical treatments of this process [41, 42] lack the resolution to distinguish between LiF and MgO in this respect. However, the greater polarization occurring in MgO might be expected to raise the ideal shear strength relative to the ideal tensile strength [43] and thus promote enhanced brittleness [44].

5. CONCLUSIONS

A study has been made of the effects of indentation diameter (*i.e.* load) and orientation of the indented surface on the Meyer hardnesses of nickel, aluminum, LiF and MgO. The findings were as follows.

(i) Greater surface displacements were produced by piling-up and sinking-in around indentations in nickel and aluminum than in LiF and MgO.

(ii) These displacements appeared always to derive solely from primary glide, and any

additional deformation that was required to accommodate the shape change in LiF and MgO, which lack five independent primary glide systems, appeared to derive from cracking rather than secondary slip.

(iii) Regardless of the symmetry of the surface indented, all impressions exhibited circular symmetry about the surface normal below the level of the original surface.

(iv) Elastic recovery on unloading was more pronounced in nickel than aluminum and in LiF than MgO, and tended to produce a proportionally greater reduction in indentation diameter than depth. This latter observation is at variance with the reported effect of such recovery on shallower indentations and appears to be a consequence of the proportionally greater contribution made by plastic flow in the formation of deeper craters.

(v) For all four materials Meyer's law was closely obeyed for indentations in all three surfaces, and for nickel, aluminum and LiF the Meyer hardness tended to a value M^* independent of surface orientation as the impression diameter approached the indenter diameter. Nickel exhibited higher Meyer indices (greater work hardening) than aluminum and a different hardness anisotropy. LiF exhibited Meyer indices similar to those of nickel but greater scatter in M^* . In contrast, the Meyer hardness of MgO not only decreased but also exhibited an increasing anisotropy as the indentation diameter decreased. These differences in behavior between MgO and LiF are attributed to a greater ease of dislocation nucleation at the tips of cracks in MgO.

ACKNOWLEDGMENT

This work was supported by the U.S. Army Research Office under Grant DAAG29-78-G-0056.

REFERENCES

- 1 J. H. Westbrook and H. Conrad (eds.), *The Science of Hardness Testing and its Research Applications*, Am. Soc. Metals, Metals Park, Ohio, 1973.
- 2 B. R. Lawn and T. R. Wilshaw, *J. Mater. Sci.*, **10** (1975) 1049.
- 3 M. Garfinkle and R. G. Garlick, *Trans. Metall. Soc. AIME*, **242** (1968) 809.
- 4 F. W. Daniels and C. G. Dunn, *Trans. Am. Soc. Met.*, **41** (1949) 419.
- 5 C. A. Brookes, J. B. O'Neill and B. A. W. Redfern, *Proc. R. Soc. London, Ser. A*, **322** (1971) 73.
- 6 R. W. Armstrong and A. C. Raghuram, in J. H. Westbrook and H. Conrad (eds.), *The Science of Hardness Testing and its Research Applications*, Am. Soc. Metals, Metals Park, Ohio, 1973, p. 174.
- 7 R. W. Calder and R. W. Armstrong, *Mater. Sci. Eng.*, **12** (1973) 59.
- 8 R. W. Armstrong and C. C. Wu, *J. Am. Ceram. Soc.*, **61** (1978) 102.
- 9 B. C. Wonsiewicz and G. Y. Chin, in J. H. Westbrook and H. Conrad (eds.), *The Science of Hardness Testing and its Research Applications*, Am. Soc. Metals, Metals Park, Ohio, 1973, p. 167.
- 10 B. C. Wonsiewicz and G. Y. Chin, *Metall. Trans.*, **1** (1970) 2716.
- 11 G. I. Taylor, *J. Inst. Met.*, **62** (1938) 307.
- 12 D. Tabor, *The Hardness of Metals*, Oxford University Press, Oxford, 1951.
- 13 H. C. H. Carpenter and C. F. Elam, *Proc. R. Soc. London, Ser. A*, **100** (1921) 348.
- 14 H. O'Neill, *J. Inst. Met.*, **30** (1923) 299.
- 15 H. O'Neill, *The Hardness of Metals and its Measurement*, Chapman and Hall, London, 1934.
- 16 L. B. Pfeil, *Iron Steel Inst., Carnegie Scholarship Mem.*, **16** (1927) 153.
- 17 E. R. Petty, *J. Inst. Met.*, **91** (1962-1963) 54.
- 18 L. D. Dyer, *Trans. Am. Soc. Met.*, **58** (1965) 620.
- 19 B. Sestak and S. Libovicky, *Czech. J. Phys.*, **11** (1961) 444.
- 20 J. J. Gilman and W. G. Johnston, in J. C. Fisher, W. G. Johnston, R. Thomson and T. Vreeland (eds.), *Dislocations and Mechanical Properties of Crystals*, Wiley, New York, 1957, p. 116.
- 21 N. Gane and J. M. Cox, *Philos. Mag.*, **22** (1970) 881.
- 22 A. S. Keh, *J. Appl. Phys.*, **31** (1960) 1538.
- 23 M. V. Swain and B. R. Lawn, *Phys. Status Solidi*, **35** (1969) 909.
- 24 R. W. Armstrong and W. H. Robinson, *N. Z. J. Sci.*, **17** (1974) 429.
- 25 A. L. Coulet, F. Minari and L. Capella, *Ser. Metall.*, **4** (1970) 593.
- 26 F. Minari, Y. Maurissen, B. Pichaud and P. Bellandi, *Ser. Metall.*, **4** (1970) 843.
- 27 R. J. Stokes, T. L. Johnston and C. H. Li, *Trans. Metall. Soc. AIME*, **215** (1959) 437.
- 28 B. N. Pramila Bai and N. H. Macmillan, *J. Mater. Sci.*, **14** (1979) 494.
- 29 M. T. Sprackling, *The Plastic Deformation of Simple Ionic Crystals*, Academic Press, London, 1976.
- 30 R. W. Cahn (ed.), *Physical Metallurgy*, North-Holland, London, Amsterdam, 2nd edn., 1970.
- 31 E. Meyer, *Z. Ver. Dtsch. Ing.*, **52** (1908) 645, 740, 835.
- 32 D. G. Rickerby and N. H. Macmillan, in *Proc. 5th Int. Conf. on Erosion by Liquid and Solid Impact*, Cambridge, 1979.
- 33 M. J. Buerger, *Am. Miner.*, **15** (1930) 21.
- 34 H. Mueller, *Am. Miner.*, **16** (1931) 237.

- 35 F. E. Foss and R. C. Brumfield, *Am. Soc. Test. Mater., Proc.*, 22 (1922) 312.
- 36 H. Hertz, *Miscellaneous Papers*, Macmillan, London, 1896.
- 37 R. E. Smallman, *Modern Physical Metallurgy*, Butterworths, London, 1962.
- 38 G. Simmons and H. Wang, *Single Crystal Elastic Constants and Calculated Aggregate Properties: A Handbook*, MIT Press, Cambridge, Massachusetts, 1971.
- 39 T. H. Alden, *Acta. Metall.*, 11 (1963) 1103.
- 40 T. H. Alden, *Trans. Metall. Soc. AIME*, 230 (1964) 649.
- 41 R. W. Armstrong, *Mater. Sci. Eng.*, 1 (1966) 251.
- 42 J. R. Rice and R. Thomson, *Philos. Mag.*, 29 (1974) 73.
- 43 A. Kelly, *Strong Solids*, Oxford University Press, Oxford, 2nd edn., 1973.
- 44 A. Kelly, W. R. Tyson and A. H. Cottrell, *Philos. Mag.*, 15 (1967) 567.

Appendix IV

Proc. 5th Int. Conf. on Erosion by Solid and Liquid Impact

MECHANISMS OF SOLID PARTICLE EROSION IN CRYSTALLINE MATERIALS

D.G. Rickerby and N.H. Macmillan

Materials Research Laboratory
The Pennsylvania State University
University Park, PA 16802, U.S.A.

Erosive mechanisms in ductile (Al and Ni) and semi-brittle (LiF and MgO) materials are being studied at the basic level by impacting monocrystalline specimens of various orientations with single particles. With such specimens effects due to variations in microstructure are eliminated, and it is possible to concentrate on the fundamental erosive processes. In both classes of solid a crater is formed about the centre of impact, but the surrounding damage and the operative mechanisms of material removal differ markedly from one to the other. For the semi-brittle specimens, material is lost as a result of the formation of cleavage cracks around the crater and the intersection of these with the surface and with each other. For the metals, material removal occurs as a result of ductile rupture at the crater rim. This process can lead to measurable mass loss even for a single impact normal to the surface.

INTRODUCTION

Despite the existence of a great deal of empirical data on solid particle erosion, little is known about the basic mechanisms of material removal involved (1, 2). This situation stems from the large number of experimental variables involved, and requires that any systematic investigation of erosion mechanisms keeps this number to a minimum. Thus, the present work was confined to single normal impacts of spherical particles against monocrystalline surfaces. Single impact experiments have previously proved useful for investigating erosive mechanisms (3-5), and spherical particles simulate adequately many of the impacts which occur during erosion by irregular particles (5,6). Furthermore, for normal impact, the motion of a spherical particle can be described analytically, allowing direct calculation of target hardness under dynamic conditions (7,8).

EXPERIMENTAL

Experiments were performed on high and low melting point pairs of ionic (MgO and LiF) and metallic (Ni and Al) monocrystals. The impurities present (see Table 1) were sufficient to affect dislocation mobilities in the ionic crystals (9), but not to affect significantly the flow stresses of the metals (10).

Table 1. Melting points and purities of the crystals

Crystal	Melting Point/°C	Purity	Impurities >50 ppm
MgO	2800	99.94%	Ca, Al, Fe
LiF	845	99.96%	Ca, Fe
Ni	1453	99.97%	Si, Fe
Al	660	99.998%	

{100}, {110} or {111} oriented specimens about 1 cm² in area and about 0.5 cm thick were cut from larger monocrystals. These were first ground on wet SiC papers and then polished on cloth-covered wheels using slurries of Al₂O₃ particles down to 0.05 µm in size. Finally, they were flush-mounted in self-curing resin. A number of MgO specimens also were chemically polished (11) prior to mounting.

The erosive particles were mounted in nylon sabots and fired from a gas gun. Sabot velocities were determined photoelectrically immediately prior to particle-sabot separation at the muzzle (12). Two types of particles were used: steel spheres of diameter 1.59 mm, weight 16.2 mg and VHN ~ 800 kg mm⁻²; and WC-6% Co spheres of diameter 1.58 mm, weight ~ 30 mg and VHN ~ 2000 kg mm⁻². The harder type was required for experiments with MgO in order to minimize the effect of plastic deformation of the particle (7), whereas the steel spheres were sufficiently hard for experiments with the other materials.

The mass losses due to individual impacts were determined gravimetrically. In addition, cross-sectional traces through impact craters were obtained at equidistant (50 µm) intervals by means of a surface profilometer. Crater volumes were determined by measuring the area below the original surface level for each trace and applying the trapezoidal rule. Crater depths and diameters were determined from diametral traces.

THEORETICAL IMPACT MODEL

Consider a rigid sphere of radius r and mass m impinging normally on a plastic-rigid half-space, and assume that the pressure over the area of contact is uniform and has a constant value p (the dynamic hardness) during the impact (7,13). Provided

that all the particle kinetic energy is expended in permanently deforming the target,

$$pV = \frac{1}{2} mv_o^2, \quad (1)$$

where V is the crater volume and v_o is the initial impact velocity. This can be re-written in terms of the crater depth ℓ as

$$p = \frac{mv_o^2}{2\pi\ell^2(r-\ell/3)}, \quad (2)$$

provided that $\ell < r$. Rearranging this expression gives

$$\ell = \left[\frac{mv_o^2}{2\pi p(r-\ell/3)} \right]^{1/2}, \quad (3)$$

from which ℓ may be calculated iteratively by neglecting the $\ell/3$ term in the first instance. Also, the crater diameter d is given by

$$d = 2(2r\ell - \ell^2)^{1/2}. \quad (4)$$

If $\ell > r$, Eq. 2 becomes

$$p = \frac{mv_o^2}{2\pi r^2(\ell-r/3)}, \quad (5)$$

and

$$\ell = \frac{mv_o^2}{2\pi r p} + \frac{r}{3}. \quad (6)$$

A "representative value" of the strain ϵ around a spherical indentation is (7)

$$\epsilon \approx 0.1 \frac{d}{r}; \quad (7)$$

and, for purely plastic behaviour, the impact duration t is given by (7,13)

$$t = \pi/2 \left[\frac{m}{2\pi p r} \right]^{1/2}. \quad (8)$$

It follows that the mean strain rate $\dot{\epsilon}$ during the impact is (8)

$$\dot{\epsilon} \approx 0.15 d \left[\frac{p}{rm} \right]^{1/2} \approx 0.064 \frac{dv_o}{r\ell}. \quad (9)$$

An estimate of the effect of strain hardening may be made by assuming that p varies according to (14)

$$p = kd^{n-2}, \quad (10)$$

where k and n are constants. It can be shown that at the end of an impact for which $\ell < r$ (7),

$$p = \left[\frac{n+2}{4} \right] \frac{1}{2} \frac{mv_o^2}{V}, \quad (11)$$

so that Eq. 2 may still be used, provided it is recognised that the values of p calculated thereby will be lower than the actual end values by a constant factor $(n+2)/4$.

RESULTS

Typical impact craters in chemically polished MgO surfaces are shown in Figs. 1-3. Those in LiF surfaces are essentially similar in appearance. In each case the central crater is surrounded by a complex zone of brittle fracture arising from intersecting {100} and {110} cleavage cracks. The extent of material removal is consequently highly dependent on the crystallographic orientation of the surface (8).

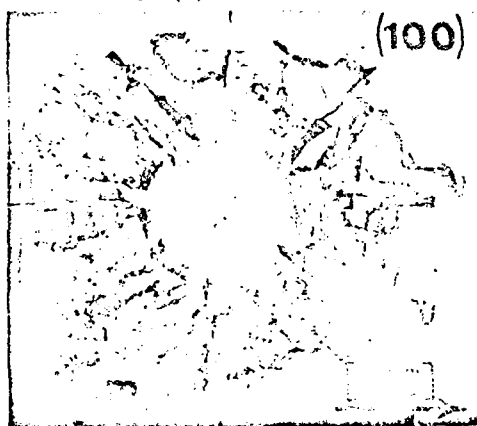


Fig. 1. Crater in a {100} MgO surface due to impact at 204 m s^{-1} .

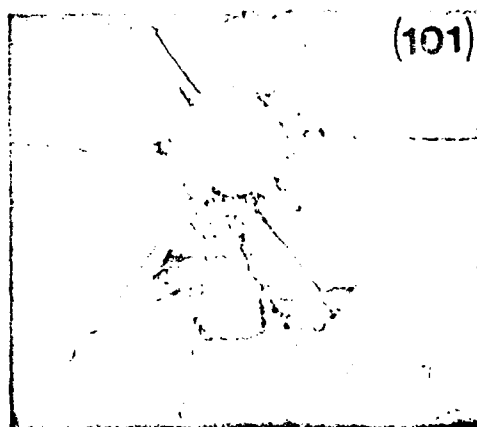


Fig. 2. Crater in a {110} MgO surface due to impact at 118 m s^{-1} .

A diametral profilometer trace through a crater in chemically polished MgO is shown in Fig. 4. The diameter is defined as the distance between the crater walls at the original surface level (broken line), and the depth as the vertical distance from this level to the lowest point in the crater. Trace directions were $\langle 100 \rangle$ on {100} and {110} surfaces and $\langle 211 \rangle$ on {111} surfaces in all cases.

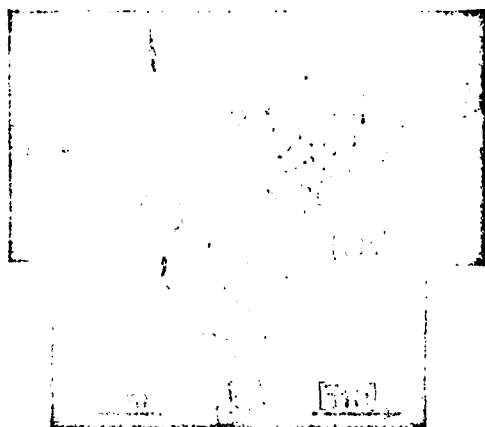


Fig. 3. Crater in a {111} MgO surface due to impact at 168 m s^{-1} .

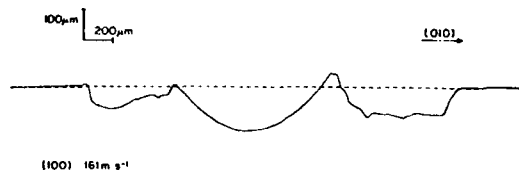


Fig. 4. Diametral trace through an impact crater in a {100} MgO surface.

The variations with impact velocity of crater diameter, depth and volume for chemically polished {100} MgO surfaces are shown in Figs. 5-7. Similar data were obtained for {110} and {111} oriented MgO specimens and for LiF specimens of the same three orientations. Because elastic recovery was negligible in MgO but resulted in a net reduction of crater diameter relative to depth in LiF, the dynamic hardnesses of these materials were calculated from diameters and depths, respectively. The substantial scatter in the data precluded identification of any definitive variation of dynamic hardness with impact velocity.

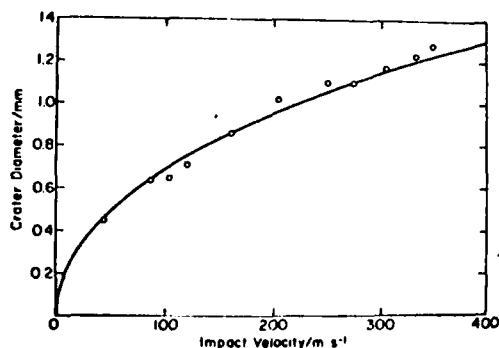


Fig. 5. Variation of crater diameter with impact velocity for {100} MgO surfaces.

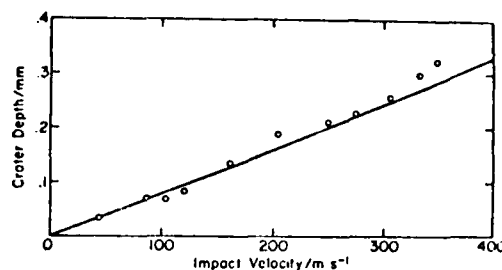


Fig. 6. Variation of crater depth with impact velocity for {100} MgO surfaces.

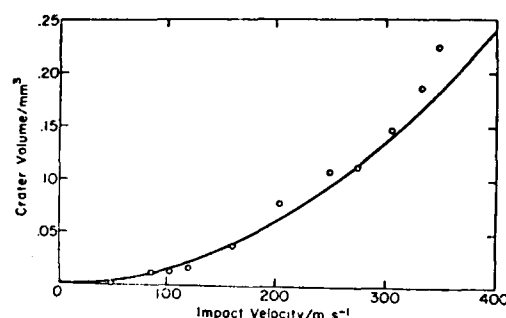


Fig. 7. Variation of crater volume with impact velocity for {100} MgO surfaces.

Functions of the form

$$m_1 = Amv_0^2, \quad (12)$$

where m_1 is the mass loss and A is a constant, were fitted to the experimental mass loss data. A typical example is shown in Fig. 8.

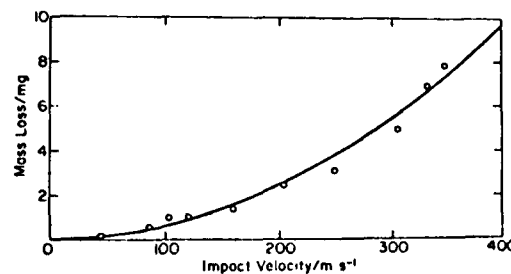


Fig. 8. Variation of mass loss with impact velocity for chemically polished {100} MgO surfaces.

The experimental results for MgO and LiF are summarized in Tables 2 and 3, respectively, which include static Meyer-Vickers hardness M_V^* and Meyer ball hardness M_b (15) values for comparison. These parameters, like the dynamic hardness, are calculated in terms of the projected rather than the actual contact area.

$$^*M_V = VIIN/0.927$$

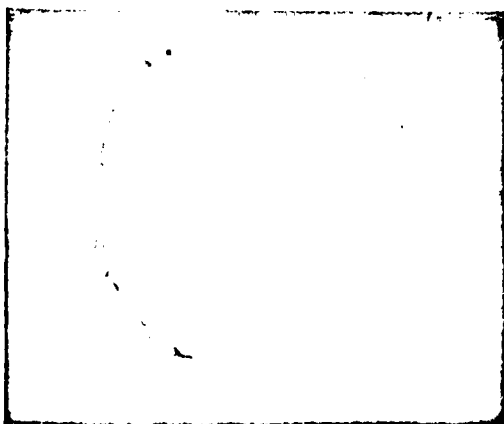
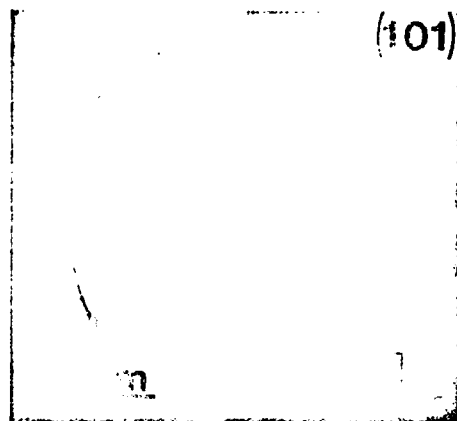
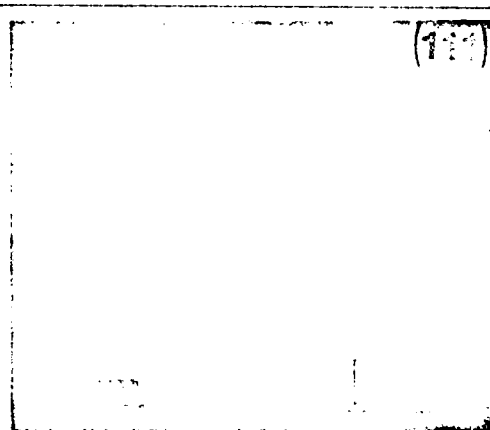
Table 2. Summary of results for MgO

Orien- tation	$p/-2$ kg mm ⁻²	$M_B/-2$ kg mm ⁻²	$M_V/-2$ kg mm ⁻²	A m ⁻² s ²
⁴ {100}	¹ 1030±180	185±23	995±24	2.0×10 ⁻⁶
⁵ {100}	1170±240	213±47	1013±28	3.2×10 ⁻⁶
⁴ {110}	1310±310	236±34	972±29	5.8×10 ⁻⁶
⁵ {110}	1090±240	223±75	1014±30	7.2×10 ⁻⁶
⁴ {111}	1860±470	329±59	999±20	4.0×10 ⁻⁶
¹ ± 1 st. dev. ² 50 kg load ³ 300 g load				
⁴ chemically polished ⁵ mechanically polished				

Table 3. Summary of results for LiF

Orien- tation	$p/-2$ kg mm ⁻²	$M_B/-2$ kg mm ⁻²	$M_V/-2$ kg mm ⁻²	A m ⁻² s ²
{100}	¹ 483±59	97±3	124±1	2.3×10 ⁻⁶
{110}	428±56	105±7	126±2	1.9×10 ⁻⁶
{111}	553±106	106±3	118±3	3.7×10 ⁻⁶
¹ ± 1 st. dev. ² 20 kg load ³ 300 g load				

Figs. 9-11 show impact craters in Ni surfaces. Craters in corresponding Al surfaces are similar in appearance. Substantial pile-up of material is apparent along these directions perpendicular to primary {110}<110> slip traces, whilst the surface between such directions is depressed. At higher velocities there is an increasing tendency for ragged "lips" to form along the raised portions of the crater rim, apparently as a result of extrusion of material between the particle and the strain hardened surface.

Fig. 9. Crater in a {100} Ni surface due to impact at 279 m s⁻¹.Fig. 10. Crater in a {110} Ni surface due to impact at 305 m s⁻¹.Fig. 11. Crater in a {111} Ni surface due to impact at 327 m s⁻¹.

A diametral profilometer trace through a crater in Ni is shown in Fig. 12. The broken lines indicate the original surface level and the outline of the spherical particle, and show that elastic recovery produces a net reduction in crater diameter relative to depth. The same happens in Al, and dynamic hardness was therefore calculated from the depth for both metals.

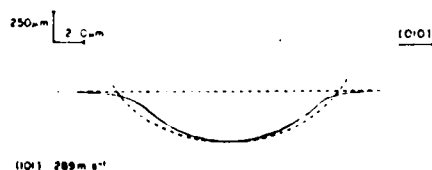


Fig. 12. Diametral trace through an impact crater in a {110} Ni surface.

No variation of the dynamic hardness of Al with impact velocity could be discerned within the experimental scatter; but for Ni there was a definite increase with velocity. Expressions of the form of Eq. 10

were therefore fitted to the hardness data for Ni, assuming that n (i) could and (ii) could not differ from its static value. As seen from Figs. 13 and 14, either assumption ((i) solid lines, (ii) broken lines) provides a reasonable description of the experimental data over the limited range of crater size involved. Moreover, experiments on polycrystalline Al over a wider size range reveal little difference between the dynamic and static values of n (16). Hence, the values of n quoted here are those obtained from other, more precise static spherical indentation studies of the same Ni monocrystals (17).

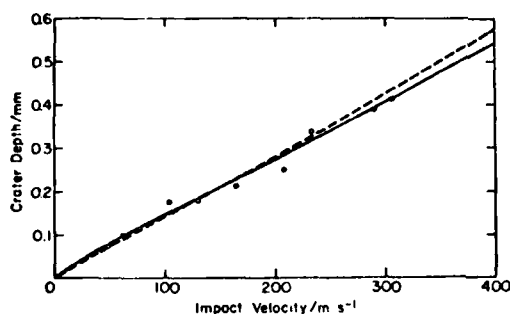


Fig. 13. Variation of crater depth with impact velocity for {110} Ni surfaces.

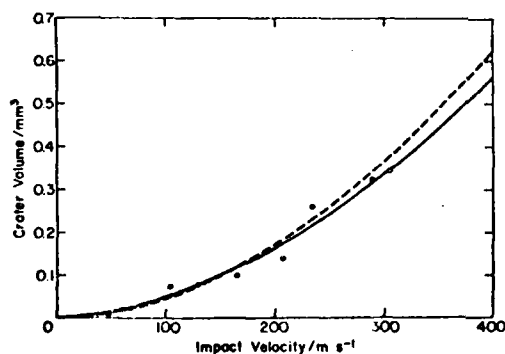


Fig. 14. Variation of crater volume with impact velocity for {110} Ni surfaces.

Mass losses from both metals were small ($\lesssim 10^{-4}$ g), if they occurred at all, and their variability was such that it was impossible to resolve any velocity dependence. Material removal was apparently due to separation of metal from the extruded lips at the crater rim by ductile rupture.

The experimental results for Ni and Al are summarized in Tables 4 and 5, respectively.

Table 4. Summary of results for Ni

Orientation	n	$k/lg \text{ mm}^{-n-2}$		$^1M_V/\text{kg mm}^{-2}$
		dynamic	static	
{100}	2.35	132	81.5	$^{288\pm1}$
{110}	2.38	178	88.2	88 ± 5
{111}	2.36	170	80.7	89 ± 3
$^1500 \text{ g load}$		$^{2\pm 1} \text{ st. dev.}$		

Table 5. Summary of results for Al

Orientation	$p/\text{kg mm}^{-2}$	$^2M_B/\text{kg mm}^{-2}$	$^3M_V/\text{kg mm}^{-2}$
{100}	$^{151\pm7}$	14.6 ± 0.5	18.9 ± 0.5
{110}	73 ± 28	15.9 ± 0.2	18.5 ± 0.4
{111}	63 ± 38	15.5 ± 0.3	16.4 ± 0.5
$^{1\pm 1} \text{ st. dev.}$		$^210 \text{ kg load}$	$^3500 \text{ g load}$

DISCUSSION

Erosive behaviour is highly dependent on particle size (18-20), and even very brittle targets undergo a transition to ductile response, via a semi-brittle regime (21), as the particle size decreases. Moreover, in practical situations the larger particles often can be filtered out, making semi-brittle or ductile erosion the primary cause of concern. Thus, experiments involving larger particles and a semi-brittle target response are of relevance to the engineering use of brittle ceramics.

Surface finish has been shown to significantly affect material removal in single impact experiments with MgO; and it therefore must have a crucial effect on incubation times for multiple impact erosion, even though exerting little influence on the steady-state erosion rate. However, the differences seen in the orientation dependence of mass loss for MgO and LiF are attributed not to variations in surface finish (since chemically and mechanically polished MgO showed the same qualitative orientation dependence), but to differences in flow and fracture behaviour. MgO is more brittle than LiF, and also differs in its relative ease of cleavage on {100} and {110} planes.

Dislocation etch pit studies (8) indicate that the differences between the static and dynamic hardnesses of variously oriented specimens of MgO are compatible with its dislocation velocity-stress relationship (22); and the different hardness anisotropies produced by spherical and pyramidal indenters are evidently due to the change in indenter geometry (8). No evidence of slip on the secondary {100}<110> system was found, even though {110}<110> slip provides only two of the five independent slip systems required for an arbitrary shape change (23). The

additional deformation apparently comes from modes II and III extension of {100} and {110} cleavage cracks.

In both Ni and Al, mass losses from single impacts were extremely small. However, multiple impact studies of metals at normal incidence show that successive impacts eventually roughen the surface and raise the rate of material removal (2,16). The extruded lips formed in higher velocity impacts bear some resemblance to those produced by oblique impacts against other metals (4,5), although more material is removed in this latter case because the lips are larger.

The lack of any distinguishable strain hardening effects in the impact experiments on Al may arise from localized adiabatic heating into the recrystallization range. In contrast, strain hardening was found to occur at comparable rates under both static and dynamic conditions in Ni, which has a higher recrystallization temperature. Interestingly, strain-hardening at the quasi-static rate has also been observed in high purity polycrystalline Al (16) at rather lower impact velocities.

Although it has been proposed that erosion may be related to thermal properties (24,25), the present experiments provide little support for the view that large scale melting occurs. Some softening may occur as a result of adiabatic heating during impacts against such low melting point materials as Al, but the apparent lack of secondary slip in MgO suggests that the temperature never exceeded 600°C over any significant volume in this material (26). The appearance of detached fragments and of the surface damage also supports this view. In the ceramics, sharp edges are formed as a result of cleavage failure, and there is no evidence of the more rounded debris that melting would be expected to produce. Similarly, the appearance of the crater lips formed in the metals suggests that these result from plastic extrusion rather than from splashing of molten material.

It is clear from comparison of the various static and dynamic data that hardness is sensitive to the strain and strain rate at which it is measured. It follows that any attempt to correlate erosion and hardness should be based on a measurement of hardness appropriate to the erosive situation.

Finally, it should be noted that the mass loss per impact will be greater in the multiple than the single impact situation. For ductile materials this happens because impacts occurring in previously strained regions can more easily exhaust the available ductility; and in semi-brittle materials the cause is interaction of the cracks produced by the current impact with those created by prior impacts. In both instances the result is an erosive mass loss exponent greater than two (1), the value which might be anticipated from simple energetic considerations.

ACKNOWLEDGMENTS

This work was supported jointly by the U.S. Army Research Office under Grant No. DAAG29-77-G-0100 and the National Science Foundation under Grant No. DMR-76-02733.

REFERENCES

1. Preece C.M. and Macmillan N.H. 1977, *Ann. Rev. Mat. Sci.* **7**, 95.
2. Finnie I. 1960, *Wear* **3**, 87.
3. Sheldon G.L. and Kanhere A. 1972, *Wear* **21**, 195.
4. Hutchings I.M. and Winter R.E. 1974, *Wear* **27**, 121.
5. Hutchings I.M., Winter R.E. and Field J.E. 1976, *Proc. Roy. Soc. A348*, 379.
6. Bitter J.G.A. 1963, *Wear* **6**, 169.
7. Tabor D. 1951, "The Hardness of Metals" Oxford University Press.
8. Rickerby D.G., Pramila Bai B.N. and Macmillan N.H. 1979, *J. Mat. Sci.*, in press.
9. Sprackling M.T. 1976, "The Plastic Deformation of Simple Ionic Crystals" Academic Press, p. 73.
10. Haasen P. 1970, in "Physical Metallurgy" 2nd Edition (Cahn R.W., ed.) North Holland, Ch. 17.
11. Pramila Bai B.N. and Macmillan N.H. 1979, *J. Mat. Sci.* **14**, 494.
12. Hutchings I.M. and Winter R.E. 1975, *J. Phys. E: Sci. Instrum.* **8**, 84.
13. Andrews J.P. 1930, *Phil. Mag.* **9**, 593.
14. Meyer E. 1908, *Zeits. d. Vereines Deutsch. Ing.* **52**, 645, 740, 835.
15. Shaw M.C. 1966, in "Mechanical Behavior of Materials" (McClintock F.A. and Argon A.S., eds.) Addison-Wesley, p. 445.
16. Rickerby D.G. and Macmillan N.H. 1979, *Wear*, submitted for publication.
17. Rickerby D.G. and Macmillan N.H. 1979, *Mat. Sci. and Eng.*, submitted for publication.
18. Oh H.L., Oh K.P.L., Vaidyanathan S. and Finnie I. 1972, in "The Science of Ceramic Machining and Surface Finishing" NBS Spec. Pub. 348, 119.
19. Sheldon G.L. and Finnie I. 1966, *Trans ASME-J. Eng. Ind.* **88**, 387.
20. Sheldon G.L. 1970, *Trans ASME-J. Basic Eng.* **92**, 619.
21. Lawn B. and Wilshaw R. 1975, *J. Mat. Sci.* **10**, 1049.
22. Singh R.N. and Coble R.L. 1974, *J. Appl. Phys.* **45**, 990.
23. Groves G.W. and Kelly A. 1963, *Phil. Mag.* **8**, 877.
24. Smeltzer C.E., Gulden M.E. and McElmury S.S. 1970, *USAAV Labs. Rep.* 70-36.
25. Ascarelli P. 1971, *U.S. Army Mat. Res. Cent. Tech. Rep.* 71-47.
26. Hulse C.O., Copley S.M. and Pask J.A. 1963, *J. Am. Ceram. Soc.* **46**, 317.

Appendix V

The influence of particle properties on impact damage in LiF

In the course of a broad investigation of the mechanisms of solid particle erosion [1-3], the present authors have used a single-stage gas gun to conduct various impact experiments. In one series of experiments, spherical chrome steel spheres were fired perpendicularly against mechanically polished {100} surfaces of LiF monocrystals at velocities ranging from 50 to 350 m sec⁻¹; and in another series similar size WC-6% Co spheres were fired at similar targets under identical conditions. These experiments revealed several interesting differences in target response arising from the change in particle type. This note both reports these effects and suggests an explanation for their occurrence.

The steel spheres weighed 16.2 mg and had a diameter of 1.5875 mm and a Vickers Hardness Number (VHN) ~800 kg mm⁻²; and the WC spheres weighed 30 ± 1 mg and had a diameter of 1.575 ± 0.025 mm and a VHN ~2000 kg mm⁻² [1]. Examination of spent spheres of both kinds by surface profilometry and microscopy revealed no evidence of departure from sphericity due to plastic deformation during the impact event. In both series of experiments the targets were mechanically polished 10 mm × 10 mm × 5 mm slabs* prepared and mounted as described in [1].

The damage shown in Fig. 1 is typical of that produced by either kind of sphere over a wide range

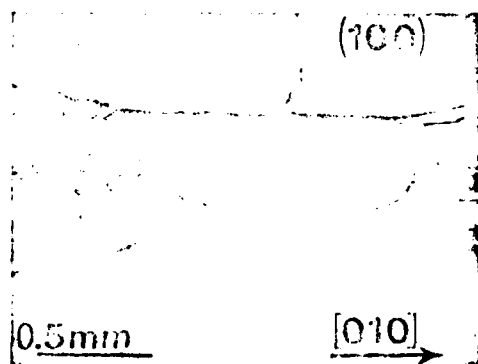


Figure 1 Scanning electron micrograph of the impact damage produced by a steel sphere with a velocity of 204 m sec⁻¹ (70° tilt).

*Obtained from Harshaw Chemical Company, 6801 Cochran Road, Solon, Ohio 44139, USA, and containing as their principal impurities 100 to 200 ppm each of Ca and Fe.

of velocities. It consists of a central crater, apparently formed by a combination of {110}⟨110⟩ glide and modes II and III cleavage crack propagation, and a surrounding region from which material has been lost through intersection of {100} and {110} cleavage cracks with one another and with the free surface. This latter region encroaches further into the central crater as the impact velocity is raised.

To characterize this damage quantitatively, two kinds of measurements were made. First, mass losses were determined gravimetrically; and then profilometer traces were made across each crater in ⟨100⟩ directions at 50 μm intervals. Crater depth *l* (relative to the original surface) and diameter (in the same plane) were determined directly from the deepest (diametral) trace in each case.

In addition, the impact process was modelled by considering a rigid sphere of radius *r* and mass *m* impinging normally on an ideal plastic-rigid half-space and assuming that the pressure over the area of contact is uniform and has a constant value *p* (the dynamic hardness) throughout the impact event [1]. Since this model implies that all of the particle kinetic energy is expended in permanently deforming the target,

$$pV = \frac{1}{2}mv_0^2, \quad (1)$$

where *V* is the crater volume and *v*₀ the impact velocity. Equation 1 can also be written as

$$p = \frac{mv_0^2}{2\pi l^2(r - l/3)}. \quad (2)$$

The mass loss data obtained from the two series of impacts are shown in Fig. 2; and superimposed on each set of data is a parabola of the form

$$m_1 = kmv_0^2, \quad (3)$$

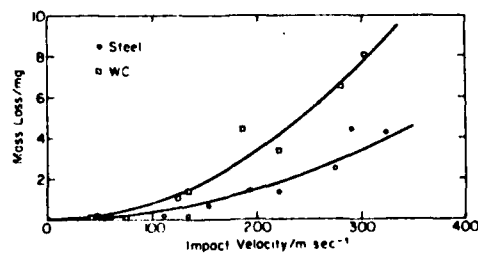


Figure 2 Variation of mass loss with impact velocity.

where m_1 is the mass loss and k the mass loss coefficient. This latter parameter, which is a measure of the "erosive efficiency" of unit mass of impacting particles, rises from 2.3×10^{-6} to $2.8 \times 10^{-6} \text{ m}^{-2} \text{ sec}^2$ when the steel spheres are replaced by those of WC.

Fig. 3 shows the corresponding dynamic hardness values calculated from the measured crater depths by means of Equation 2. A straight line representing the average of the individual values has been drawn through the data obtained from steel spheres, for the scatter in these data precludes identification of any clear velocity dependence of the dynamic hardness; but the curve fitted to the data from the experiments with WC spheres assumes a power function dependence of dynamic hardness on impact velocity. The remarkable feature of these results is that the dynamic hardness is independent of impact velocity and equal to $483 \pm 59 \text{ kg mm}^{-2}$ when steel particles are used, but decreases asymptotically with increasing impact velocity to less than half this value when WC particles are employed. It may be seen from these data that WC spheres produce larger craters and smaller dynamic hardnesses than do steel ones of the same kinetic energy.

It was also discovered from the accompanying surface profilometry measurements that post-impact elastic recovery of the target in general leads to a proportionally greater reduction in crater diameter than depth. The effect of such recovery is, therefore, to reduce the crater dimensions and increase the apparent dynamic hardness; but it is unlikely that the slight differences in the extent of such recovery-induced phenomena produced by

WC as compared to steel spheres can account for the observed differences in dynamic hardness.

The differences in mass loss and dynamic hardness likewise cannot reasonably be attributed to the greater strain and lower strain-rate resulting from the slower deceleration of the more massive WC particles over a longer time and distance. One reason is that the differences in strain ($\approx 1.2\times$) and strain rate ($\sim 2\times$) involved are too small to alter the flow stress sufficiently to account for a factor $2\times$ in the dynamic hardness, and another is that decreasing the strain rate and increasing the strain have opposite effects on the flow and fracture of a semi-brittle solid such as LiF. Specifically, decreasing the strain rate tends to favour flow over fracture, whereas increasing the strain produces more blocked slip bands capable of nucleating cracks.

It therefore seems that the greater mass loss and dynamic hardness values produced by the WC spheres stem from their greater elastic mis-match with the target and their rougher surfaces (which should result in a higher coefficient of friction in the contact region). Since these factors presumably influence the present Boussinesq stress field in much the same manner as they affect the Hertzian stress field [4, 5], they will tend to increase the extent of the annular region around the contact area in which radial tensile stresses act and from which material is lost (Fig. 1). Hence, it is suggested that the greater material loss occurs because the increased size of the region in which tensile stresses act results in propagation of more surface flaws, and that this greater loss leads to a lower dynamic hardness by reducing the lateral elastic constraints on the process of crater formation.

Acknowledgement

Work supported jointly by the US Army Research Office under Grant no. DAAG29-77-G-0100 and the National Science Foundation under Grant no. DMR-76-02733.

References

1. D. G. RICKERBY, B. N. PRAMILA BAI and N. H. MACMILLAN, *J. Mater. Sci.* 14 (1979).
2. *Idem*, Basic Mechanisms of Erosion in Ceramics, in "Proceedings of the Fourth International Meeting on Modern Ceramic Technologies", Saint-Vincent, Italy, May (1979).

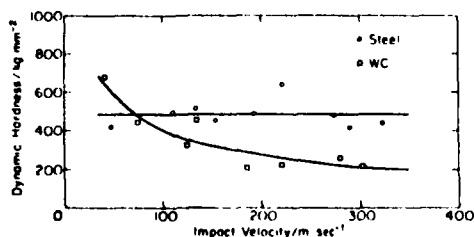


Figure 3 Variation of dynamic hardness with impact velocity.

* \pm one standard deviation.

3. D. G. RICKERBY and N. H. MACMILLAN, Mechanisms of Solid Particle Erosion in Crystalline Materials, in "Proceedings of the Fifth International Conference on Erosion by Solid and Liquid Impact", Cambridge, England, September (1979).
4. K. L. JOHNSON, J. J. O'CONNOR and A. C. WOODWARD, *Proc. Roy. Soc. A* 334 (1973) 95.
5. B. LAWN and R. WILSHAW, *J. Mater. Sci.* 10 (1975) 1049.

Received 4 April
and accepted 11 May 1979

D. G. RICKERBY
B. N. PRAMILA BAI
N. H. MACMILLAN
*Materials Research Laboratory,
The Pennsylvania State University,
University Park,
Pennsylvania 16802,
USA*

The central region of the calcium oxide--gallium oxide system

During attempts to grow single crystal calcium gallate (CaGa_2O_4) from the melt using the Czochralski technique, it became necessary to check the phase diagram in the region of the compound, CaGa_2O_4 since different authors have variously assigned to this mole ratio, no compound [1], two compounds [2], and three compounds [3], nominally all with the formula CaGa_2O_4 . This communication describes investigations on

this system and attempts to rationalize the results obtained and those already published.

Mixtures of calcium carbonate and gallium oxide of the highest commercially available quality, with a total metallic impurity content about 10 ppm, were made in the range 35 to 65 mol% Ga_2O_3 , sixteen mixtures in all. Each sample was subsequently placed in a differential thermal analysis (DTA) unit heated until molten and then cooled. The temperature was then recycled and a DTA trace obtained, the heating and cooling rate being $10^\circ\text{C min}^{-1}$. The samples

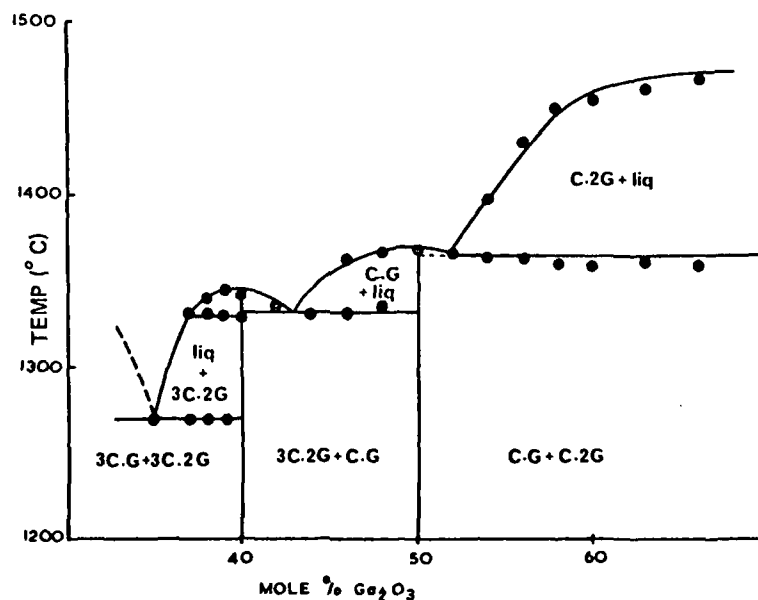


Figure 1 The $\text{CaO-Ga}_2\text{O}_3$ system, C = CaO , G = Ga_2O_3 . Eutectic between 3C.G and 3C.2G at 35 mol% Ga_2O_3 , $1270 \pm 3^\circ\text{C}$. Maximum melting point 35 to 45 mol% $1345 \pm 3^\circ\text{C}$. Eutectic between 3C.2G and C.G at 43 mol% Ga_2O_3 , $1332 \pm 3^\circ\text{C}$. Melting point 50 mol% mixture $1368 \pm 3^\circ\text{C}$.

Appendix VI

BASIC MECHANISMS OF EROSION IN CERAMICS

D. G. RICKERBY, B. N. PRAMILA BAI AND N. H. MACMILLAN

Materials Research Laboratory, The Pennsylvania State University,
University Park, PA 16802 (USA)

ABSTRACT

Erosion by solid particle impact constitutes a serious problem in turbines in electrical power stations, in aero engines, and in any situation where rapidly moving machine parts encounter dust-laden environments. The successful utilization of ceramic materials in components of such systems requires, therefore, an understanding of the fundamental mechanisms of erosion and the material properties which govern them. These mechanisms are being studied, at the most basic level, by impacting single particles against monocrystalline specimens of LiF and MgO. It has been found that erosive mass loss is related to the kinetic energy of the impacting particle and to the crystallographic orientation of the specimen, but does not correlate well with either static or dynamic hardness. The implications of these findings with respect to multiple impact erosion of polycrystalline materials are discussed.

INTRODUCTION

Erosive wear of materials by solid particle impingement is a significant problem in power turbines, aero engines, compressors, and various other instances where particle impact occurs at high velocities (ref. 1). Hence, because it is envisaged that the next generation of power and automotive turbines and coal conversion systems, in particular, will make extensive use of ceramic components, it is essential that the erosive behaviour of such materials should be understood. However, although there exists a great deal of empirical data on erosion, little is known about the basic mechanisms of material removal involved (refs. 1, 2). The work described here is part of a wider program to elucidate these mechanisms for both ceramics and metals, but the present discussion is limited to the former materials.

Systematic study of the basic erosive processes is aided by the reduction of the number of experimental variables to a minimum. Thus, to avoid such complications as grain size effects and variation in particle shape and orientation,

experimental work was limited to single impacts of spherical particles against carefully oriented and polished monocrystalline surfaces. Single impact studies have proved valuable in previous investigations of erosive mechanisms in metals (refs. 3-5); and it has also been pointed out that spherical particles provide a reasonable simulation of many of the impacts occurring during erosion by a stream of irregularly shaped particles (refs. 5, 6). An analytical solution to the equation of motion of an incident spherical particle is only possible if the impact direction is normal to the target surface. Experimental work was therefore confined to normal impacts on surfaces of three different crystallographic orientations.

EXPERIMENTAL

Specimens were prepared by cleaving and cutting MgO and LiF single crystals into approximately 10 mm x 10 mm x 5 mm slabs, with their largest faces oriented parallel to {100}, {110} or {111}. These were successively ground on wet 240, 320, 400 and 600 grit SiC papers, and then mechanically polished on a cloth-covered wheel using aqueous slurries of 1, 0.3 and 0.05 μ m alumina. In order to investigate the effect of surface finish, and to allow dislocation etch pit studies to be performed, some of the MgO specimens were given an additional chemical polish in boiling aqueous H_3PO_4 to which a small amount of concentrated H_2SO_4 or HNO_3 had been added (refs. 7-9). To facilitate handling, the polished specimens were flush-mounted in standard-sized cylinders of a self-curing resin. Subsequent Laue X-ray studies showed that the polished surfaces typically were within 2° of their nominal orientations.

Because impurities are known to affect dislocation mobility in ionic crystals (ref. 10), semi-quantitative spectrochemical analyses were performed on several samples of both LiF and MgO. The results of these tests are summarized in Table 1.

TABLE 1
Spectrochemical analyses of MgO and LiF crystals

Impurity element	Concentration (ppm)	
	MgO	LiF
Ca	100-200	100-200
Al	40-100	40
Mn	50	-
Fe	100-200	100
Si	50	50
Ti	20	-
Mg	-	2-5
Cu	-	5-20

A 16 mm bore nitrogen gas gun, similar in design to that described by Hutchings and Winter (ref. 11), was used to fire erosive particles at the targets. The particles were mounted in nylon sabots, from which they were separated at the end of the barrel by means of an annular steel muzzle block. Sabot velocities were measured at the muzzle with an accuracy $\pm 1\%$ by means of a photoelectric time-of-flight system, and were reproducible to better than $\pm 5\%$ at all firing pressures used.

Two types of particles were used: hardened steel spheres of diameter 1.59 mm and weight 16.2 mg, and WC-6% Co spheres of diameter 1.58 mm and weight 30 ± 1 mg. The Vickers Hardness Numbers (VHN) of these particles were $\sim 800 \text{ kg mm}^{-2}$ and 2000 kg mm^{-2} , respectively. The harder particles were used in the experiments with MgO in order to minimize the effect of plastic deformation of the spheres (ref. 12), but the experiments on LiF were carried out with steel particles exclusively.

Experiments were performed over the velocity range $50 - 350 \text{ m s}^{-1}$, and mass losses were determined by weighing specimens immediately before and after impact. In addition, cross-sectional traces through the craters at equidistant ($50 \mu\text{m}$) intervals were obtained by surface profilometry. A composite topographical map produced by this technique is shown in Fig. 1. Crater volumes were measured by determining the area below the original surface level for each trace and then applying the trapezoidal rule. Crater depths and diameters were determined from the traces corresponding to diametral sections in each case.

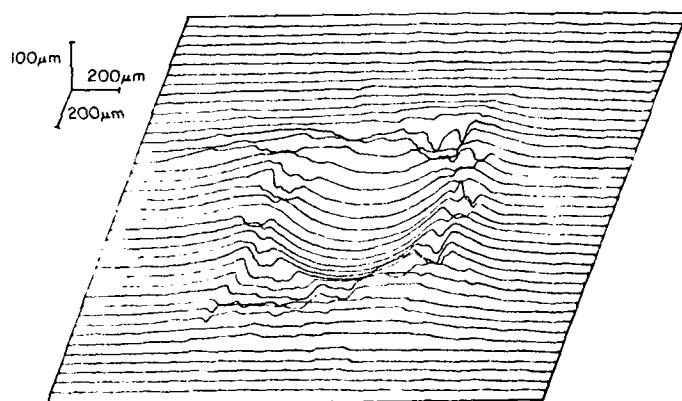


Fig. 1. Profilometer map of an impact crater in MgO .

THEORETICAL IMPACT MODEL

Consider a rigid sphere of radius r and mass m impinging normally on an ideal plastic-rigid half-space. It is assumed that the pressure over the area of contact is uniform and has a constant value p (the dynamic hardness) throughout the entire impact (refs. 12, 13). Instantaneously, the situation is as shown in Fig. 2: the sphere is moving with a velocity v against a resistive force P , the radius of contact is a , and the depth of penetration is y . It follows that $P = \pi a^2 p$, and that the equation of motion of the particle is

$$m\ddot{y} = -\pi a^2 p. \quad (1)$$

It can be shown that the solution of this equation is

$$v^2 = v_0^2 - \frac{2\pi p}{m} (ry^2 - y^3/3), \quad (2)$$

where v_0 is the initial impact velocity. If the particle comes to rest at $y = \ell$, then

$$p = \frac{mv_0^2}{2\pi \ell^2 (r - \ell/3)}, \quad (3)$$

where the relation between ℓ and the crater diameter d is

$$\ell = r - (r^2 - d^2/4)^{1/2}. \quad (4)$$

This model assumes that there is neither deformation of the spherical particle during the impact nor elastic recovery of the deformed surface afterwards, and that strain hardening effects are negligible.

Eqn. 3 can be rewritten

$$pV = \frac{1}{2} mv_0^2, \quad (5)$$

where V is the crater volume. This expression represents a statement of the energy balance implicit in the model - namely, that all the kinetic energy of the particle is expended in plastically deforming the target. Eqn. 3 can also be rearranged to give

$$\ell = \left[\frac{mv_0^2}{2\pi p (r - \ell/3)} \right]^{1/2}. \quad (6)$$

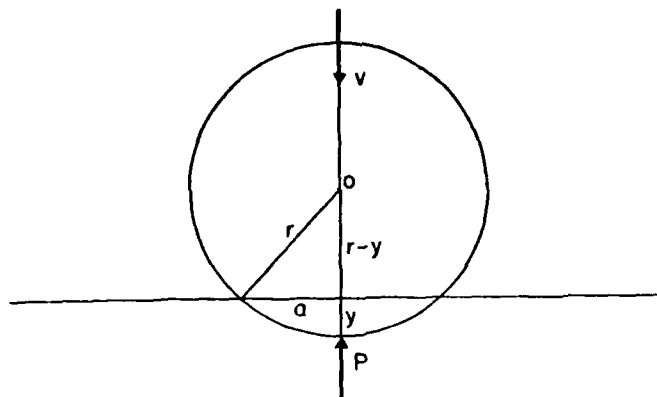


Fig. 2. Schematic diagram of the impact event.

from which ℓ may be calculated by an iterative process starting from

$$\left[\frac{rmv_o^2}{2\pi pr} \right]^{1/2}; \quad (7)$$

and d can then be calculated from ℓ by rearranging Eqn. 4 as

$$d = 2 (2r\ell - \ell^2)^{1/2}. \quad (8)$$

It has been shown (ref. 12) that a "representative value" of the strain ϵ in the complex strain field around a spherical indentation is

$$\epsilon = 0.1 d/r. \quad (9)$$

Also, for purely plastic behaviour, the impact duration t is independent of particle velocity, and is given by (refs. 12, 13)

$$t = \frac{\pi}{2} \left(\frac{m}{2\pi pr} \right)^{1/2}. \quad (10)$$

By combining Eqns. 9 and 10 and then using Eqn. 7 it follows that the mean strain rate $\dot{\epsilon}$ during the impact is

$$\dot{\epsilon} \sim 0.16d \left(\frac{P}{rm} \right)^{1/2} \sim 0.64 \frac{dv_o}{r\ell}. \quad (11)$$

In the present work, typical values of t and $\dot{\epsilon}$ were $\sim 1 \mu\text{m}$ and $\sim 10^5 \text{ s}^{-1}$, respectively.

RESULTS

MgO specimens

Scanning electron micrographs of damage resulting from single impacts of WC spheres against chemically polished MgO surfaces are shown in Figs. 3-5. In each case the central crater is surrounded by a complex zone of brittle fracture arising from intersecting $\{100\}$ and $\{110\}$ cleavage cracks. It is clear that the mode of material removal is highly dependent on crystallographic orientation and can be rationalized in terms of the orientations of the primary and secondary cleavage planes relative to the target surface (ref. 14).

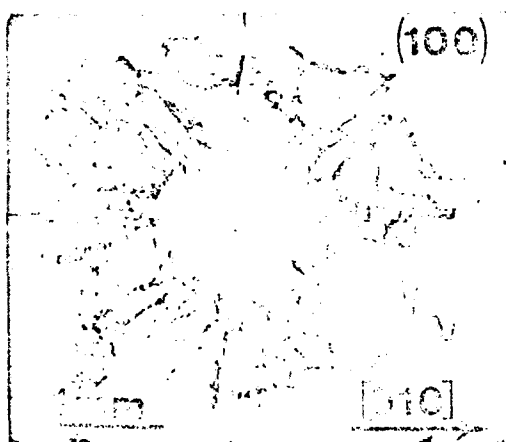


Fig. 3. Crater formed in a $\{100\}$ MgO surface by an impact at 204 m s^{-1} .

A typical profilometer trace through a diametral section of a crater is illustrated in Fig. 6. The diameter is defined as the distance between the crater walls at the level of the original surface (indicated by the broken line), and the depth as the vertical distance from this level to the deepest point in the crater. The trace directions were $\langle 100 \rangle$ on $\{100\}$ and $\{110\}$ surfaces and $\langle 211 \rangle$ on $\{111\}$ surfaces in all cases. At higher impact velocities the surrounding eroded region encroached upon the crater rim, thereby imposing an upper velocity limit on the measurement of crater dimensions.

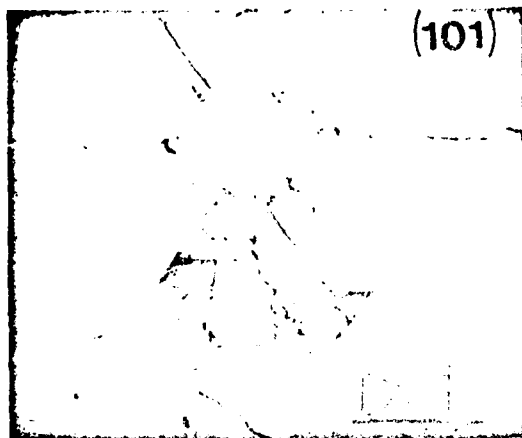


Fig. 4. Crater formed in a {110} MgO surface by an impact at 118 m s^{-1} .



Fig. 5. Crater formed in a {111} MgO surface by an impact at 168 m s^{-1} .

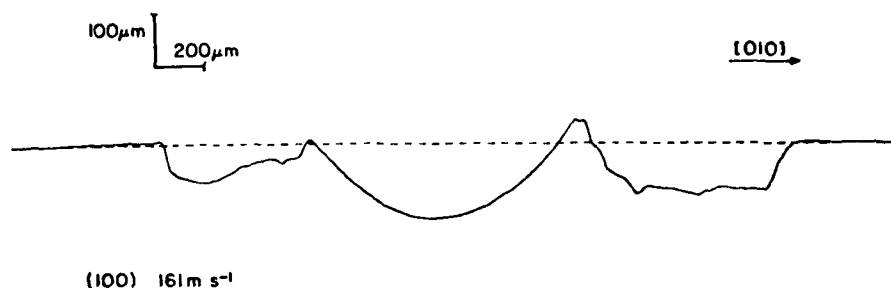


Fig. 6. Diametral trace through an impact crater in a {100} MgO surface.

Figs. 7, 8 and 9 show the variation with impact velocity of the crater diameter, depth and volume, respectively, for chemically polished {100} MgO surfaces. Similar data were obtained for the other two orientations, and for specimens with a mechanical polish only. A value of the dynamic hardness was calculated from each measured crater diameter by means of Eqns. 3 and 4. No definitive variation of the dynamic hardness with velocity was observed, although considerable scatter existed in the data. Thus, a mean value of dynamic hardness was calculated from each set of data; and this was used with Eqns. 5-8 to determine the theoretical crater geometry. The close correspondence between the theoretical lines and the experimental data in Figs. 7-9 indicates that the assumptions made in deriving the model were reasonable.

Regression analyses were performed on all sets of mass loss data in order to fit functions of the form

$$m_1 = kmv_0^2, \quad (12)$$

where m_1 is the mass loss and k is a constant. A typical example is shown in Fig. 10. The reasonably good fits obtained in all cases confirm the hypothesis that, for a single impact, the mass loss is directly proportional to the particle kinetic energy.

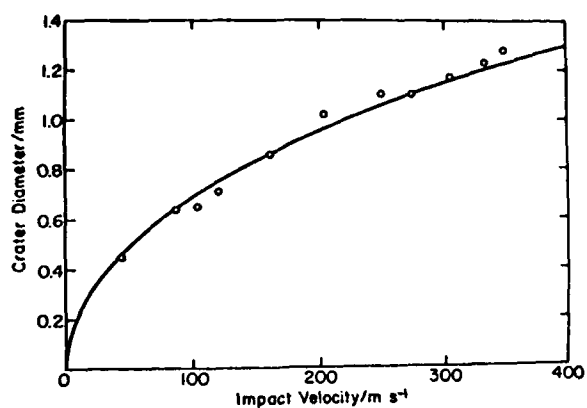


Fig. 7. Variation of crater diameter with impact velocity for {100} MgO surfaces.

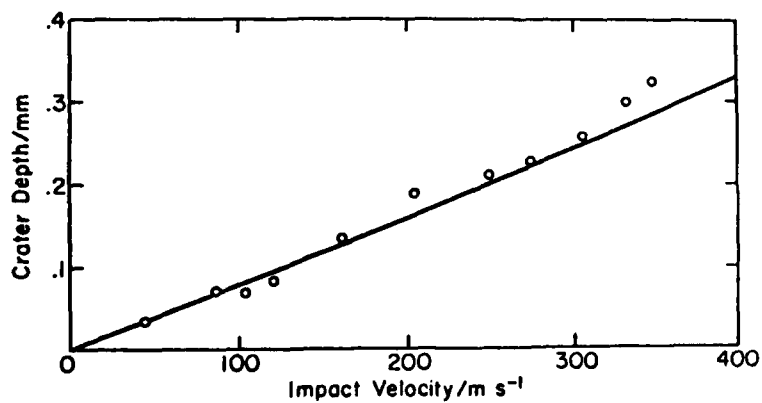


Fig. 8. Variation of crater depth with impact velocity for {100} MgO surfaces.

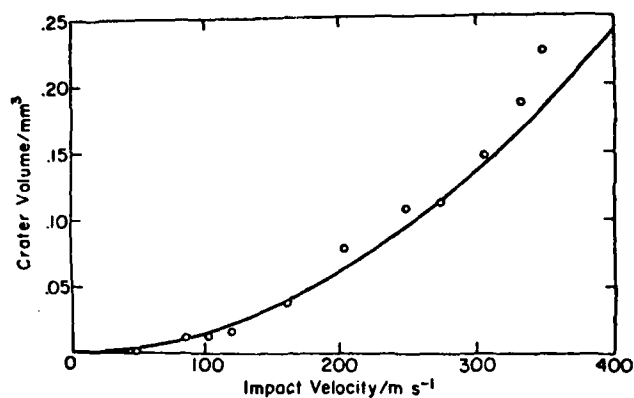


Fig. 9. Variation of crater volume with impact velocity for {100} MgO surfaces.

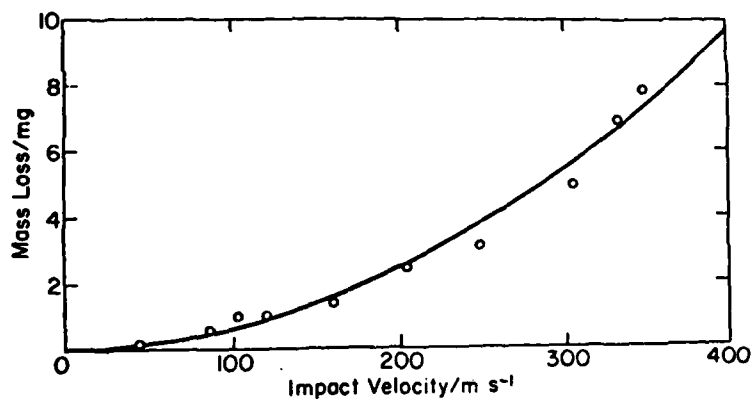


Fig. 10. Variation of mass loss with impact velocity for chemically polished {100} MgO surfaces.

The results of all experiments performed on MgO are summarized in Table 2. Corresponding data for the quasi-static Meyer-Vickers hardness M_V^* and the Meyer ball hardness M_B (ref. 15) are also listed for comparison. M_V was measured at

$$^*M_V = \text{VHN}/0.927.$$

a load of 300 g; and M_B was determined using the WC spheres and a load of 50 kg, which produced indentations comparable in size to those formed by impacts at 100 m s^{-1} . These particular indicators of static hardness were selected because, like the dynamic hardness, they are calculated in terms of the projected rather than the actual area of contact.

TABLE 2
Summary of experimental results for MgO

Orientation	Polish	$p/\text{kg mm}^{-2}$	$M_V/\text{kg mm}^{-2}$	$M_B/\text{kg mm}^{-2}$	$k/\text{m}^{-2}\text{s}^2$
{100}	chemical	$1030 \pm 180^*$	995 ± 24	185 ± 23	2.02×10^{-6}
{100}	mechanical	1170 ± 240	1013 ± 28	213 ± 47	3.17×10^{-6}
{110}	chemical	1310 ± 310	972 ± 29	236 ± 34	5.80×10^{-6}
{110}	mechanical	1090 ± 240	1014 ± 30	223 ± 75	7.18×10^{-6}
{111}	chemical	1860 ± 470	999 ± 20	329 ± 59	3.96×10^{-6}

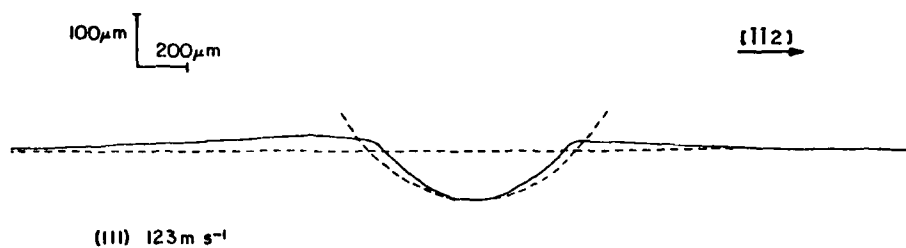
* \pm st. dev.

LiF specimens

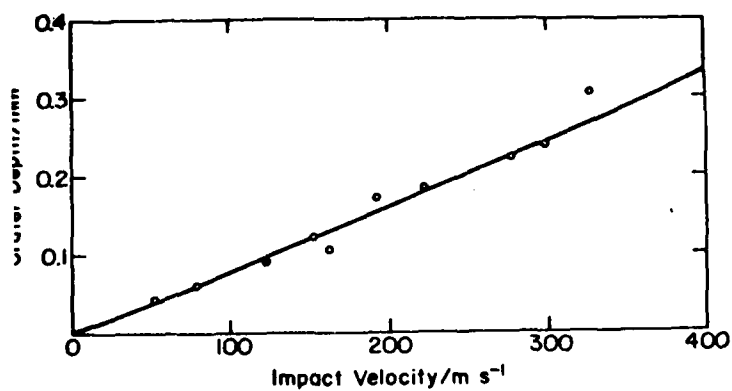
The overall appearance of impact damage in LiF was essentially similar to that in MgO. However, quantitative measurements indicated certain differences. In particular, noticeable elastic recovery occurred in LiF, especially in the deeper craters. This effect was most pronounced for {111} surfaces. Fig. 11 shows a diametral profile through a crater in such a surface superimposed on an outline (broken curve) of the spherical particle. There is a net reduction in the crater diameter relative to the depth, which is the reverse of the effect reported by other workers (refs. 12, 16) in somewhat shallower quasi-static indentations.

Because elastic recovery evidently affected the crater diameter more than the depth in LiF, dynamic hardness calculations were based on the latter dimensions. Experimental data for crater depths and diameters on {111} surfaces are presented in Figs. 12 and 13, respectively. The measured crater diameters tend to be smaller than those predicted theoretically using the mean dynamic hardness. Similar results were obtained for {100} and {110} surfaces, although the discrepancies were less because the effect of elastic recovery was smaller.

Table 3 provides a summary of the relevant dynamic and quasi-static hardness data, and lists the mass loss coefficients for each surface investigated. The load used to determine M_V was again 300 g, but that used in the measurement of M_B was reduced to 20 kg in order to produce indentations of similar geometry to those made in MgO.



g. 11. Diametral trace through an impact crater in a $\{111\}$ LiF surface.



g. 12. Variation of crater depth with impact velocity for $\{111\}$ LiF surfaces.

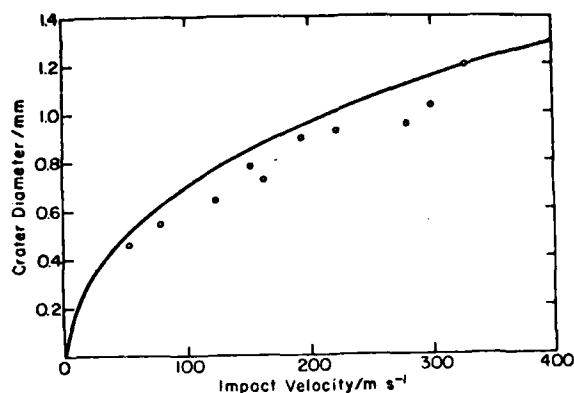


Fig. 13. Variation of crater diameter with impact velocity for {111} LiF surfaces.

TABLE 3

Summary of experimental results for LiF

Orientation	Polish	$p/\text{kg mm}^{-2}$	$M_v/\text{kg mm}^{-2}$	$M_B/\text{kg mm}^{-2}$	$k/\text{m}^{-2}\text{s}^{-2}$
{100}	mechanical	483 ± 59	124 ± 1	97 ± 3	2.30×10^{-6}
{110}	mechanical	428 ± 56	126 ± 2	105 ± 7	1.93×10^{-6}
{111}	mechanical	553 ± 106	118 ± 3	106 ± 3	3.65×10^{-6}

DISCUSSION

Erosive behaviour has generally been characterized as either "brittle" or "ductile" (ref. 17). This nomenclature is somewhat misleading, however, because it is based on the variation of erosion with angle of impingement rather than on the nature of the material removal processes, and even a very brittle substance undergoes a transition from "brittle" to "ductile" erosion behaviour as the particle size is reduced (ref. 18). Moreover, this transition really represents a change from brittle to ductile behaviour via a semi-brittle regime (ref. 19) - i.e., there is an increasing relative contribution of flow versus fracture to the overall deformation as the particle size decreases.

Brittle structural ceramics are primarily exposed to erosion by small particles ($<100 \mu\text{m}$, say), because these are the ones that are most difficult to filter from a gas stream; and therefore most practical erosive situations will involve semi-brittle or even ductile behaviour (refs. 20, 21). Thus, the present experiments involving large erosive particles and semi-brittle target response are of relevance to more brittle ceramics in practical engineering applications.

That there exist significant differences between ductile and semi-brittle erosion is emphasized by the lack of correlation between hardness and mass loss in the present experiments. In contrast, the VHN has been found to be a reasonable indicator of relative ductile erosion behaviour for many, though not all, annealed metals (ref. 1). Some discrepancies may arise from differences in strain and strain rate hardening effects associated with different indenter geometries and loading rates, respectively. It was in order to eliminate the influence of such effects that static and dynamic spherical indentation hardnesses were measured in addition to the Meyer-Vickers hardness. Despite this, no general correlation was found between mass loss and any of these parameters. Thus, although both the crater volume and the mass loss for a single impact are proportional to the particle kinetic energy, the dynamic hardness represents the constant of proportionality in the former case but bears no obvious connection with the latter.

Surface finish has been shown to exert a significant effect on the amount of material removed from a pristine MgO surface by a single impact; and it would therefore be expected to be a crucial factor in determining the incubation period in multiple impact erosion, but to have little effect on the final (steady state) erosion rate. The differences in the orientation dependence of single impact mass loss for MgO and LiF are attributed not to differences in surface finish (since mechanically polished and chemically polished {100} and {110} MgO surfaces showed qualitatively similar orientation dependences), but to differences in the flow and fracture behaviour in the two materials. MgO is more brittle than LiF, and there is also a difference between the two in the relative ease of cleavage on {100} and {110} planes.

The relatively greater anisotropy observed in both the static and dynamic spherical indentation hardnesses as compared to the Meyer-Vickers hardness is apparently due to the change in indenter geometry. The primary slip system is {110}<110> for both crystals. Consequently, a <111> uniaxial stress will produce zero critical resolved shear stress on this system (ref. 22), unlike similar stresses acting parallel to <100> or <110>. Hence, use of a blunt spherical indenter, which in the early stages of contact will exert relatively greater compressive stresses and smaller shear stresses than a "sharper" pyramidal indenter, results in a pronounced hardness maximum on {111} surfaces.

Etching MgO specimens with boiling concentrated HNO_3 (ref. 7) revealed dislocation etch pit arrays similar to those reported for dynamic indentations in NaCl (ref. 23). No evidence of slip on the secondary {001}<110> system was found, even though {110}<110> slip provides only two of the five independent slip systems required to produce an arbitrary shape change (ref. 24). The additional deformation capability appears to be supplied by mode II and III

extension of {100} and {110} cleavage cracks. The differences between the static and dynamic spherical indentation hardnesses (measured at $\dot{\epsilon} \sim 10^{-3} \text{ s}^{-1}$ and $\sim 10^5 \text{ s}^{-1}$, respectively) may be accounted for in terms of the known dislocation velocity-stress relationship for MgO (ref. 25). Extrapolation of these data, using dislocation velocities calculated from the maximum extent of the etch pit arrays, indicates that stresses beneath the indenter would have to be increased by factors comparable to the observed ratio of static to dynamic hardness (ref. 1).

A few relatively long cleavage cracks penetrated into the bulk of the crystals. On {100} surfaces (see fig. 14) these were similar in appearance to the median vent and subsurface lateral cracks formed under a sharp indenter in brittle materials (ref. 19). This phenomenon resulted from the particular orientation of the {100} cleavage planes relative to the surface; and in general such cracks occurred along cleavage planes rather than in directions determined by the stress trajectories beneath the indentation and the singularities in the indenter geometry, which is the case for amorphous materials and sharp indenters. In either event, it is clear that, although such severe cracks little influence material removal in a single impact, they will greatly enhance the rate of removal during subsequent impacts. Consequently, the velocity exponent for multiple impact erosion is substantially greater than two for materials in which the semi-brittle erosive mode is operating (ref. 1).

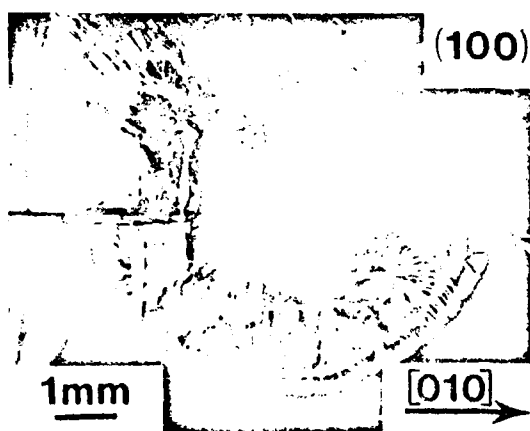


Fig. 14. Subsurface lateral cracking under a 186 m s^{-1} impact crater in a {100} MgO surface.

Finally, it has been proposed that erosion may be related to thermal properties (refs. 26, 27). The melting points of MgO and LiF are rather different ($2800^{\circ}C$ and $845^{\circ}C$, respectively), but no differences in erosion behaviour were observed which could be attributed to this fact. The lack of secondary slip, which would presumably occur if temperatures were above $600^{\circ}C$ (ref. 22) within a significant volume, indicates that adiabatic heating effects are relatively localized. The appearance of detached material and of the surface damage is consistent with cleavage failure, in that sharp edges are seen, whereas melting would be expected to produce more rounded debris. It is therefore concluded that melting of the material contributes negligibly to semi-brittle erosive mechanisms.

ACKNOWLEDGEMENTS

This work was supported jointly by the U.S. Army Research Office under Grant No. DAAG29-77-G-0100 and the National Science Foundation under Grant No. DMR-76-02733.

REFERENCES

- 1 C.M. Preece and N. H. Macmillan, *Ann. Rev. Mater. Sci.*, 7 (1977) 95-121.
- 2 I. Finnie, *Wear*, 3 (1960) 87-103.
- 3 I.M. Hutchings and R.E. Winter, *Wear*, 27 (1974) 121-128.
- 4 I.M. Hutchings and R.E. Winter, *J. Phys. D: Appl. Phys.*, 8 (1975) 8-14.
- 5 I.M. Hutchings, R.E. Winter and J.E. Field, *Proc. Roy. Soc. Lond.*, A348 (1976) 379-392.
- 6 J.G.A. Bitter, *Wear*, 6 (1963) 169-190.
- 7 R.J. Stokes, T.L. Johnston and C.H. Li, *Trans. AIME.*, 215 (1959) 437-444.
- 8 G.W. Groves, Ph.D. Dissertation, University of Cambridge, 1962.
- 9 B.N. Pramila Bai and N.H. Macmillan, *J. Mater. Sci.*, 14 (1979) 494-495.
- 10 M.T. Sprackling, *The Plastic Deformation of Simple Ionic Crystals*, Academic Press, London, 1976, p. 73.
- 11 I.M. Hutchings and R.E. Winter, *J. Phys. E: Sci. Instrum.*, 8 (1975) 84-86.
- 12 D. Tabor, *The Hardness of Metals*, Oxford University Press, London, 1951.
- 13 J.P. Andrews, *Phil. Mag.*, 9 (1930) 593-610.
- 14 D.G. Rickerby, B.N. Pramila Bai and N.H. Macmillan, *J. Mater. Sci.*, (1979) in press.
- 15 F.A. McClintock and A.S. Argon (Eds.), *Mechanical Behaviour of Materials*, Addison-Wesley, Reading, Mass., 1966, p. 445.
- 16 F.E. Foss and R.C. Brumfield, *Proc. ASTM*, 22 (1922) 312-334.
- 17 C.E. Smeltzer, M.E. Gulden and W.A. Compton, *Trans ASME - J. Basic Eng.*, 92 (1970) 639-654.
- 18 H.L. Oh, K.P.L. Oh, S. Vaidyanathan and I. Finnie, in *The Science of Ceramic Machining and Surface Finishing*, Nat. Bur. Stand. Spec. Pub. 348, 1972, pp. 119-132.
- 19 B. Lawn and R. Wilshaw, *J. Mater. Sci.*, 10 (1975) 1049-1081.
- 20 G.L. Sheldon and I. Finnie, *Trans ASME - J. Eng. Ind.*, 88 (1966) 387-392.
- 21 G.L. Sheldon, *Trans ASME - J. Basic Eng.*, 92 (1970) 619-626.
- 22 C.O. Hulse, S.M. Copley and J.A. Pask, *J. Am. Ceram. Soc.*, 46 (1963) 317-323.
- 23 D.R. Pande and T.S. Murty, *J. Phys. D: Appl. Phys.*, 7 (1974) 403-406.
- 24 G.W. Groves and A. Kelly, *Phil. Mag.*, 8 (1963) 877-887.
- 25 R.N. Singh and R.L. Coble, *J. Appl. Phys.*, 45 (1974) 990-995.
- 26 C.E. Smeltzer, M.E. Gulden, S.S. McElmury and W.A. Compton, *USAAV Labs. Rep.* 70-36, 1970.
- 27 P. Ascarelli, *U.S. Army Mat. Mech. Res. Cent. Tech. Rep.* 71-47, 1971.

Appendix VII

THE EROSION OF ALUMINUM BY SOLID PARTICLE IMPINGEMENT AT NORMAL INCIDENCE

D. G. RICKERBY and N. H. MACMILLAN

Materials Research Laboratory, The Pennsylvania State University, University Park, Pa. 16802 (U.S.A.)

(Received June 18, 1979)

Summary

A rotating arm apparatus was used to study the erosion of polycrystalline aluminum by 1.58 mm diameter WC-6% Co spheres impinging at normal incidence. Dynamic hardness values were obtained from measurements of the impact craters and compared with corresponding quasi-static values. In addition, material removal was monitored gravimetrically, and quantitative information was obtained on threshold and incubation phenomena and steady state erosion behavior. The variation of the velocity dependence of erosion with the number of particle impacts was derived from these data. Supporting scanning electron microscope studies suggest that the mechanism of material removal responsible for ductile erosion at near normal incidence is somewhat different from that which operates at shallower angles. The similarities and differences between these mechanisms are discussed, and it is suggested that together they account for the characteristic variation of ductile erosion with angle of impingement.

1. Introduction

The erosive wear of materials by repeated solid particle impingement is as yet incompletely understood. The literature contains an ever increasing amount of empirical data on the subject but relatively little conclusive information about mechanisms [1]. However, single impact studies on metals have suggested several possible mechanisms for the removal of material from ductile targets [2-5]. Furthermore, it has been shown that spherical particles can provide a reasonable simulation of the majority of impacts occurring during erosion by typical equiaxed, but irregularly shaped, particles [5, 6]. It is nevertheless apparent that single impact experiments alone cannot provide a complete understanding of erosion in ductile materials. In particular, a single impact at normal incidence on a pristine target surface produces negligible material removal, at least at lower velocities, whereas

substantial loss occurs as a result of multiple impacts under otherwise similar conditions.

It has been discovered empirically that erosion, which is defined as the mass of material removed per unit mass of impinging particles, can generally be described by a power function of the impact velocity [1], with the velocity exponent lying between 2.0 and 3.4 for metals, depending on the particular experimental conditions involved [7 - 11]. A value of exactly 2 might be anticipated from simple energetic considerations, and Finnie [7, 12] and others [13 - 15] have proposed theories of ductile erosion which predict just such a result. It has also been suggested that the larger exponents often found in practice are due to some size effect arising from an increase in the effective flow stress of the target as the stressed volume decreases [8].

Numerous attempts have been made to correlate erosion with various mechanical and/or physical properties of the target material [1], and the Vickers hardness number (VHN) has been shown to give a reasonable indication of the relative erosion resistance of many, but not all, annealed metals [8]. However, like any indentation hardness parameter, VHN is both strain and strain rate dependent [16], and this may account for some of the discrepancies. It is therefore of interest to measure the hardness under conditions which more closely approach those obtaining during erosion. This is most easily done by using spherical particles, for this allows impact at normal incidence to be modelled analytically and the dynamic hardness to be calculated directly.

2. Experimental

A schematic diagram of the erosion apparatus is shown in Fig. 1. The specimen is mounted near one end of a counter-balanced rotor arm inside a steel tank which can be evacuated to about 1 Torr by means of a rotary vacuum pump. The arm itself is a 6061-T6 aluminum alloy tube of length 0.25 m, wall thickness 2.1 mm, and outside diameter 19 mm, and is balanced for high speed operation by mounting a dummy specimen at the opposite end to the real one. A 1 hp electric motor rotates the arm at a speed controlled by a rheostat and continuously monitored by a photoelectric tachometer. Figure 2 shows the shaft speeds attained at different applied voltages for tank pressures of 1 atm and about 1 Torr. The distance from the centre of the shaft to the centre of each specimen is 0.115 m, and thus the nominal specimen velocity is $0.72 f$, where f is the frequency of rotation. A stream of erosive particles falls vertically into the path of the specimen from a gravity feed system consisting of a 2 m long, 12.5 mm \times 2.5 mm rectangular cross-section chute supplied from a sealed hopper. This design ensures that the falling particles form a more or less planar array parallel to the face of the oncoming specimen. In the present work, the particles used were 1.58 mm diameter WC-6% Co spheres having a mass of about 30 mg and a VHN of about 2000 kgf mm⁻². These are sufficiently massive that their motion is rel-

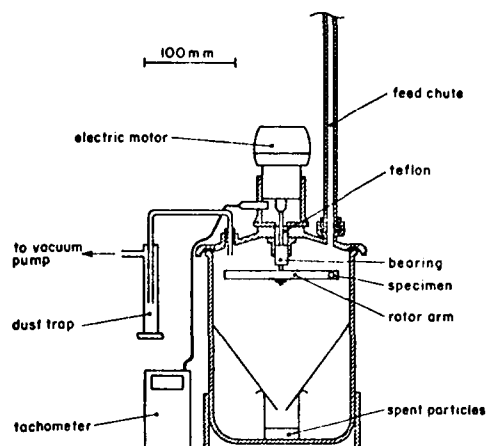


Fig. 1. Schematic diagram of the rotating arm erosion apparatus.

atively little affected by aerodynamic influences at low specimen velocities. For convenience, therefore, the apparatus was only evacuated when working at specimen velocities greater than 80 m s^{-1} .

This sort of rotating arm apparatus offers substantial advantages over the types of equipment in which the erosive particles are transported towards a stationary target by high velocity gas streams [9]. For example, impact velocities can be more easily and precisely defined, and uncertainties about the effect of eddying of the gas flow around the target on particle trajectories are eliminated. More important from the present point of view, however, is the capability for introducing small numbers of particles in a controlled manner.

In order to interpret the experimental data, it is necessary to know the ratio of the number of impacts N_i to the number of particles N_p admitted to the apparatus. Suppose, therefore, that the particles are falling vertically with a uniform velocity u and that the cross-sectional radii of the arm and the specimen are A and R , respectively. Then, if the width of the particle stream is $2R$, the requisite ratio is given by

$$\frac{N_i}{N_p} = \frac{\pi f R}{2u} \quad f \leq \frac{u}{2(A + R)} \quad (1)$$

or

$$\frac{N_i}{N_p} = \frac{fR(\pi - \theta + \frac{1}{2} \sin 2\theta)}{2u} \quad f \geq \frac{u}{2(A + R)} \quad (2)$$

where

$$\theta = \cos^{-1} \left\{ \frac{(u/f) - 2A}{2R} \right\}$$

The experimentally determined values of N_i/N_p are plotted in Fig. 3, and superimposed on these data are (i) a broken line indicating the variation predicted by the above equations from the photographically measured mean vertical particle velocity of about 3 m s^{-1} and (ii) a solid line representing the theoretical variation multiplied by an experimentally determined factor of 0.84 to allow for the finite size of the particles and the fact that some fall outside the idealized parallel-sided stream.

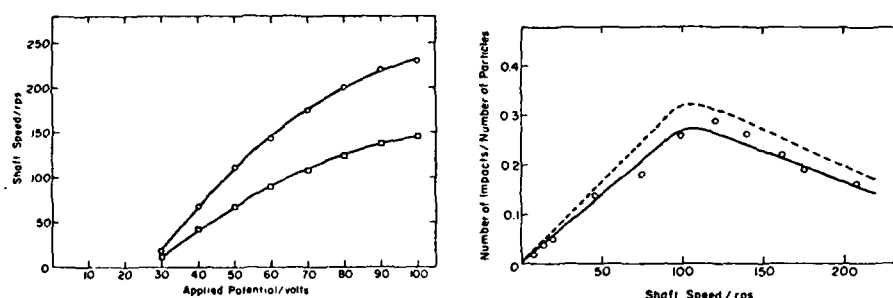


Fig. 2. Dependence of shaft speed on the voltage applied to the motor: ○, 1 Torr; □, 1 atm.

Fig. 3. Ratio of number of impacts to number of particles entering the apparatus *vs.* shaft speed.

The specimens were 15 mm long, 12.5 mm diameter cylinders prepared from a cast ingot of 99.9% pure aluminum having an average grain size of about 4 - 5 mm and a VHN of $24 \pm 1 \text{ kgf mm}^{-2}$. Their surfaces were rough ground on wet SiC paper and then polished on cloth-covered wheels using a series of aqueous slurries of successively finer Al_2O_3 particles down to $0.05 \mu\text{m}$ in size. Finally, each specimen (which weighed about 5 g) was weighed on a precision balance to $\pm 10 \mu\text{g}$.

Each specimen was eroded incrementally at some selected impact velocity for long enough to establish steady state behavior and was removed from the apparatus for weighing and examination in the scanning electron microscope after each increment. On replacement in the apparatus, the specimens were rotated through approximately 90° in an attempt to cancel out as far as possible any effects arising from the small horizontal velocity and vertical particle concentration gradients existing across their faces. Only very few impacts were produced in the first increment at each velocity, so that surface profilometer studies could be carried out on the individual impact craters before they began to overlap. These studies provided series of traces at $50 \mu\text{m}$ intervals from which the crater dimensions were determined.

3. Theoretical

Suppose that a rigid spherical particle of radius r and mass m impinges at normal incidence on an ideal plastic-rigid half-space, and assume that the

pressure over the area of contact is uniform and has a constant value p (the dynamic hardness) throughout the entire impact [16, 17]. Then, by solving the equation of motion of the particle [18], it can be shown that

$$p = \frac{mv_0^2}{2\pi l^2(r - l/3)} \quad (3)$$

where v_0 is the initial impact velocity and l is the depth of penetration when the particle comes to rest. It is implicit in this model that there is neither deformation of the particle nor elastic recovery of the crater. Thus, all the kinetic energy of the particle is expended in permanently deforming the target, and eqn. (3) can also be written in the form

$$pV = \frac{1}{2} mv_0^2 \quad (4)$$

where V is the crater volume. Rearranging eqn. (3) gives

$$l = \left\{ \frac{mv_0^2}{2\pi p(r - l/3)} \right\}^{1/2} \quad (5)$$

from which l can be calculated iteratively by initially neglecting the $l/3$ term on the right-hand side. It also follows that the crater diameter d is related to l by

$$d = 2(2rl - l^2)^{1/2} \quad (6)$$

An order of magnitude estimate of the plastic strain rate $\dot{\epsilon}$ during the impact event can be made by combining expressions for the representative strain in the complex strain field around the indentation [16] and the impact duration [16, 17]. This gives [18]

$$\dot{\epsilon} \approx 0.064 \left(\frac{dv_0}{rl} \right) \quad (7)$$

from which the dynamic strain rates in the present work were estimated to be about 10^5 s^{-1} .

As it stands, the preceding analysis takes no account of the effect of strain hardening. However, for static indentations in materials which strain harden, it has been found empirically that Meyer's law [19] is widely obeyed. This law states that

$$p = kd^{n-2} \quad (8)$$

where n and k are constants. If it is assumed that a relation of similar form applies under dynamic conditions, it can be shown [16] that

$$p \approx \left(\frac{n+2}{4} \right) \frac{\frac{1}{2} mv_0^2}{v} \quad (9)$$

at the end of the impact. Since n typically lies between 2 and 2.5, the difference between the values of p obtained from eqns. (4) and (9) is about 10% at most. It follows that the previous analysis can still be used when strain hardening occurs, provided that it is recognized that the value of p calculated

thereby underestimates the actual end values of the dynamic hardness by a factor $(n + 2)/4$.

4. Results

A typical diametral profilometer trace through an isolated impact crater is shown in Fig. 4. Measurements of crater depths relative to the original surface level (broken line) were made directly from such traces, and the corresponding crater volumes were determined by first measuring the areas below this same level for the complete set of parallel traces through each crater and then applying the trapezoidal rule. The results are shown in Figs. 5 and 6, respectively.

Dynamic hardness values were calculated from the measured crater depths, rather than from the diameters as is usual in static experiments, for two reasons. Firstly, it was more difficult to define the diameter unequivocally than the depth because of the displacement of the surface immediately outside the crater (see Fig. 4); and secondly, previous measurements of both dynamic [20] and static [21] indentations indicate that elastic recovery tends to reduce the diameter relative to the depth at large penetrations. This effect is the reverse of that reported for proportionally shallower static

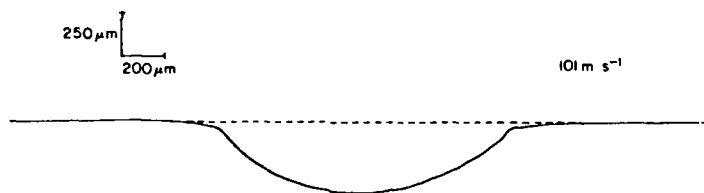


Fig. 4. Diametral trace through an impact crater.

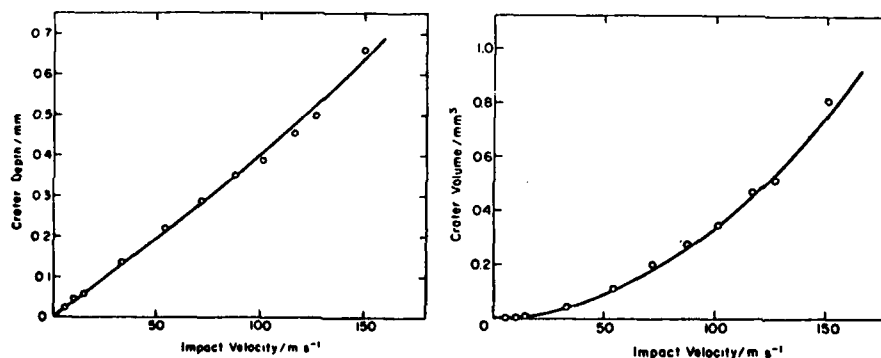


Fig. 5. Variation of crater depth with impact velocity.

Fig. 6. Variation of crater volume with impact velocity.

indentations made by somewhat larger spheres [16] and has been discussed elsewhere [21]. The dynamic hardness values obtained in this fashion are plotted in Fig. 7 as a function of crater diameter as calculated from crater depth by means of eqn. (6), together with the corresponding quasi-static Meyer hardness data [16, 19]. These latter measurements were made at a strain rate of about 10^{-3} s^{-1} , and the indentation diameters were measured directly by means of an optical microscope fitted with a micrometer eyepiece. These data reveal the Meyer index n to be 2.21 and 2.24 under static and dynamic conditions, respectively, indicating that the strain-hardening properties of aluminum are little influenced by increasing the strain rate by eight orders of magnitude.

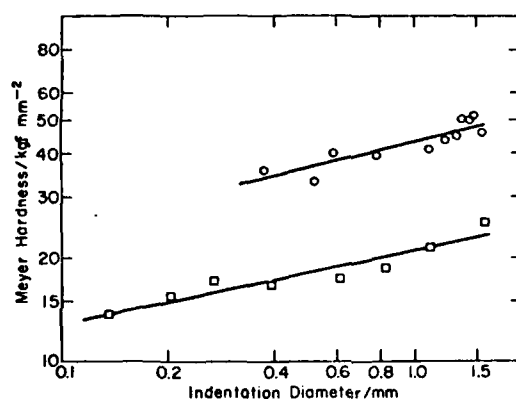


Fig. 7. Variation of static and dynamic hardness with size of impression: \circ , dynamic; \square , static.

The inception and evolution of the process of erosion are illustrated by the six scanning electron micrographs comprising Fig. 8. At first (Fig. 8(a)), impacts are scattered and essentially independent of one another; but as more impacts occur (Fig. 8(b)), craters begin to overlap, producing a distinctive "ridging" in regions where material has been highly strained as a result of more than one impact. As the number of craters continues to increase (Fig. 8(c)), such regions are further strained by additional impacts until metal begins to extrude in the form of thin platelets (Fig. 8(d)), the occasional ductile failure of which causes the first material removal. Further impacts increase the number of these platelets (Fig. 8(e)), thereby increasing the extent of material removal until a steady state condition is attained (Fig. 8(f)). Thereafter there is no further change in the overall appearance of the surface, and the erosion remains constant. It should be noted that the particular surface illustrated was subjected to relatively low velocity impacts, and that the various deformation regimes become less clearly defined at higher impact velocities. Under such conditions even a single pair of overlapping craters may produce material removal.

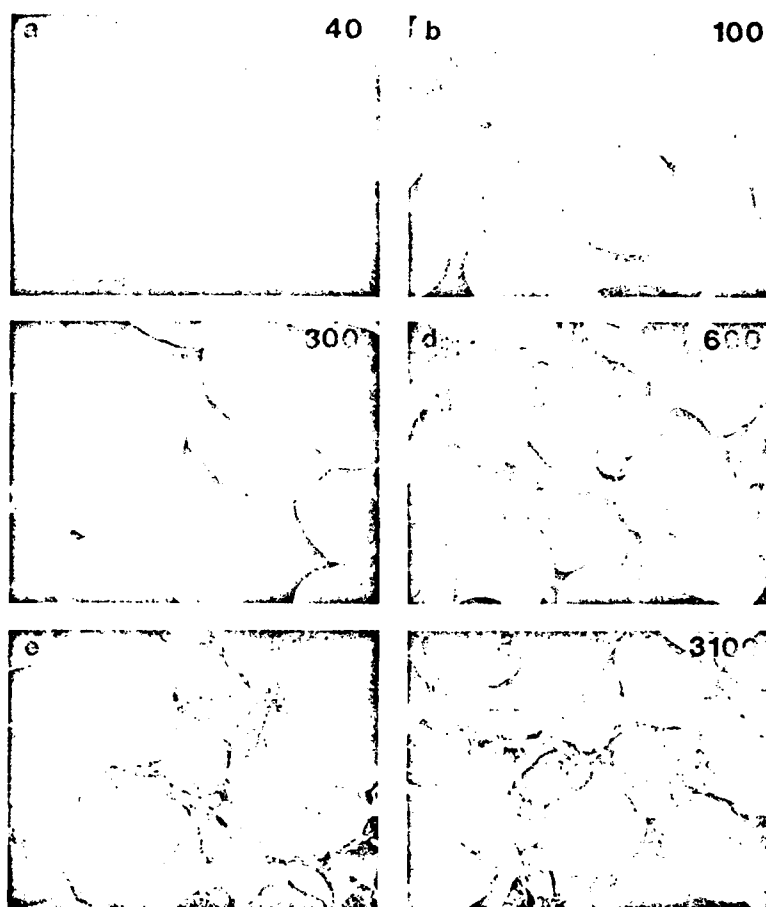


Fig. 8. Evolution of erosive damage due to repeated impacts at 54 m s^{-1} . The numbers indicate the cumulative number of impacts on the specimen.

The appearances of surfaces characteristic of the linear erosion regime for different impact velocities are illustrated in Fig. 9. As the velocity increases, not only does crater size increase but also the extent of the regions over which deformation leads to extrusion of platelets of metal. Whereas at lower impact velocities platelets are small and scattered, and occur in relatively few of the regions of crater overlap, at higher velocities the regions between craters consist of multiple platelets of much greater size.

The data obtained from the mass loss measurements are presented in Fig. 10. Each set of data is characterized by (i) a threshold number of impacts below which material removal is negligible, (ii) a succeeding incubation region over which erosion increases with increasing numbers of impacts, and finally (iii) a linear erosion regime. Curves were fitted to the data in the incubation region by assuming power function relations of the form where

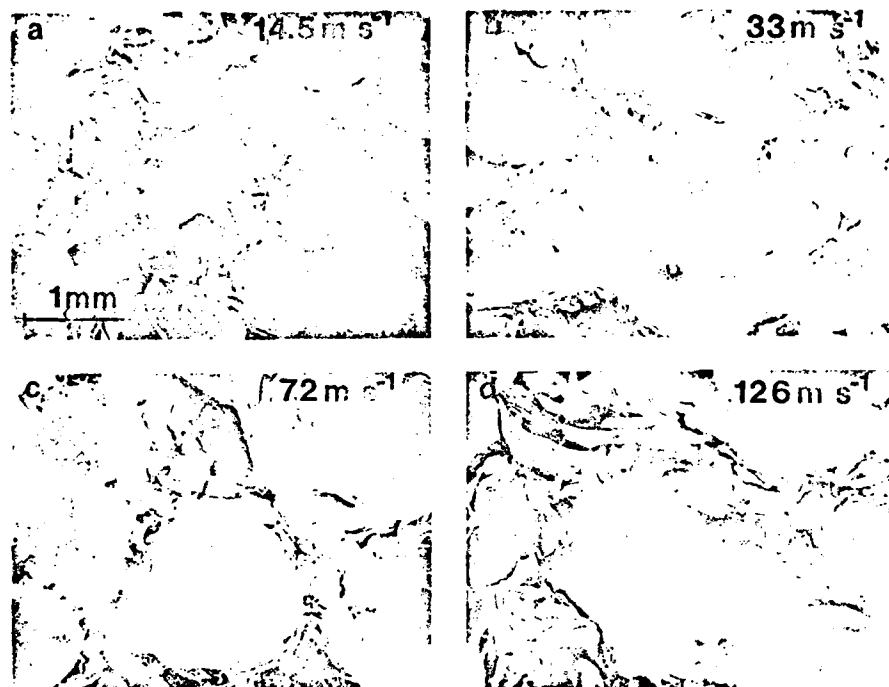


Fig. 9. Appearance of target surfaces in the linear erosion regime for various impact velocities.

$$m_e = b(N_i - N_0)^\beta \quad (10)$$

m_e is the mass of material eroded, $N_0(v_0)$ is the threshold number of impacts, and b and β are constants for a given erosive environment. The variation of the threshold number of impacts with impact velocity is shown in Fig. 11, from which it can be determined empirically that N_0 is proportional to $v_0^{-5.8}$.

The dimensionless erosion E may be defined formally by the expression

$$E = \frac{1}{m} \frac{dm_e}{dN_i} \quad (11)$$

Hence, during incubation

$$E = \frac{b\beta}{m} (N_i - N_0)^{\beta-1} \quad (12)$$

but once steady state conditions prevail, the erosion is given by the slope of the linear region of the mass loss curve divided by the average particle mass. Under these conditions, the variation of erosion with impact velocity can be represented by an expression of the form [1]

$$E = av_0^\alpha \quad (13)$$

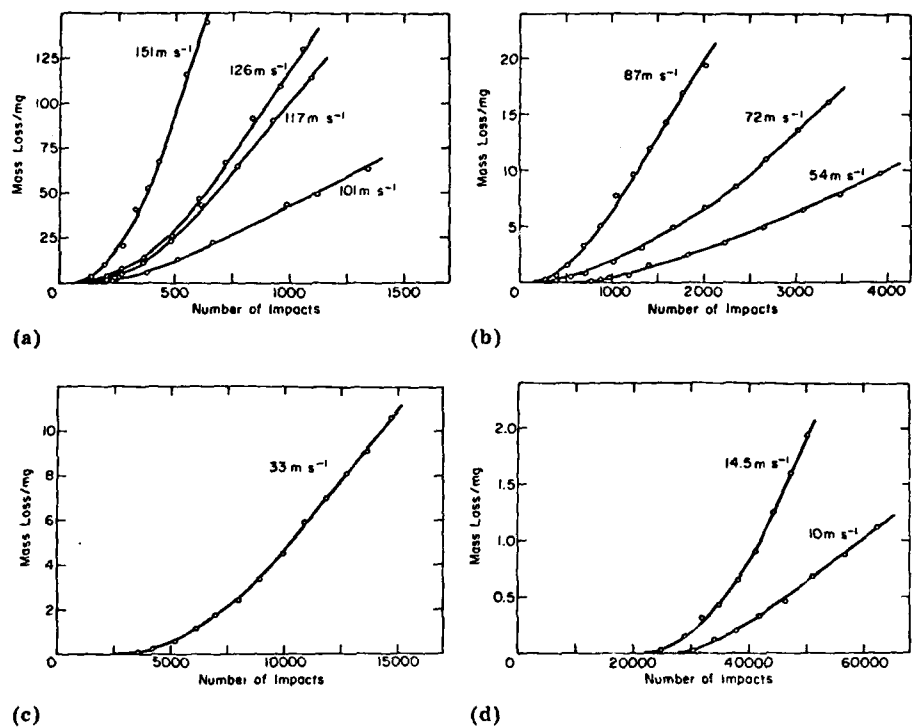


Fig. 10. Experimental mass loss curves.

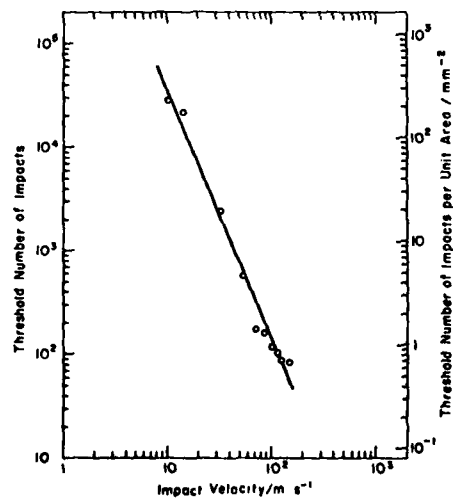


Fig. 11. Variation of threshold number of impacts with impact velocity.

where a and α are constants. More generally, however, a and α are dependent on the post-threshold number of impacts $N_i - N_0$, and the value of the velocity exponent α appropriate to a particular value of $N_i - N_0$ must be obtained by first using eqn. (11) to evaluate E at that value for each impact velocity in turn and then fitting a power function of v_0 to the resultant values of E . The example shown in Fig. 12 represents the situation after a sufficiently large number of impacts that the erosion is linear at all impact velocities investigated and gives the velocity exponent as 3.3. Finally, Fig. 13

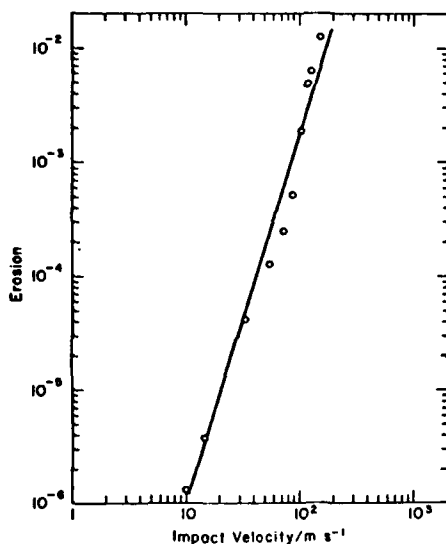


Fig. 12. Variation of erosion in the linear regime with impact velocity.

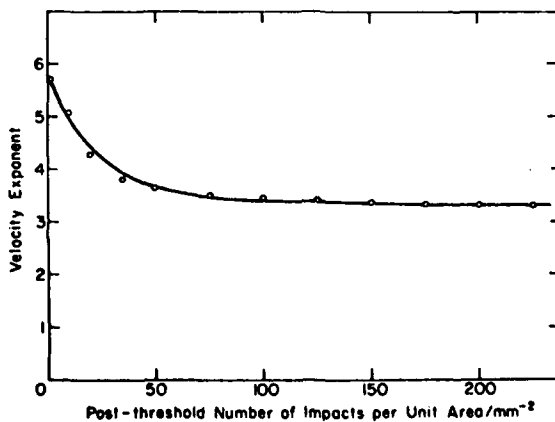


Fig. 13. Variation of velocity exponent with number of impacts.

shows the variation of the velocity exponent with the post-threshold number of impacts, as determined by performing similar calculations for a range of values of $N_i - N_0$. It is apparent that the exponent decreases with increasing numbers of impacts and approaches asymptotically the value of 3.3 obtained when the erosion is linear at all impact velocities.

5. Discussion

The experimental evidence indicates that the ductile erosion mechanism operative when spherical particles impact in a direction normal to the surface is rather different from that which operates for oblique impingement. For single, independent impacts there was no evidence at any velocity of the sort of lip formation at the crater rim seen in oblique incidence experiments [3 - 5]. Rather, the mechanism of material removal at normal incidence appears to be the detachment of thin platelets of metal that are formed only when impact craters overlap. In contrast to the lips formed by oblique impacts, which generally are quite bulky and project above the surface level, these platelets tend to be thinner and in many cases to lie almost parallel to the surface.

These morphological differences may be interpreted in terms of the different dynamics of crater formation in the two cases. In oblique impact there is substantial lateral displacement of material by a ploughing mode of deformation [4, 5], which leads to the formation of a raised rim ahead of the particle. In contrast, the deformation occurring during normal impact is more evenly distributed around the crater, unless existing deformation from previous impacts presents a locally inclined and hardened surface to the incoming particle. If sufficiently pronounced, such a perturbation can result in the extrusion of the hardened surface material between the particle and the softer substrate, but extensive ploughing-type deformation is precluded because the impact direction is still normal to the overall average surface.

Lip formation due to oblique impact is more pronounced in strain-hardened specimens than in annealed specimens [3], apparently because the deformation due to crater formation becomes localized more quickly in strain-hardened metals [16]; and platelet formation presumably is similarly dependent on the degree of strain hardening, with the result that the threshold number of normal impacts required to initiate erosion is related to both the probability of craters overlapping and the amount of strain hardening arising from each impact. Since both of these factors increase with crater size, there is a marked increase in the threshold number of impacts as the impact velocity decreases. Furthermore, after the initiation of erosion, an ever-decreasing amount of additional strain hardening takes place as subsequent impacts harden and reduce the extent of those areas not yet fully hardened. This process, which gradually increases the extent of platelet formation and causes the erosion to approach asymptotically its steady state value, manifests itself experimentally in the incubation period observed in Fig. 10.

The velocity exponent observed in the linear erosion regime in the present work is substantially higher than the value of 2.26 reported by Finnie *et al.* [8] for the erosion of 99% pure aluminum by SiC grit about 0.25 mm in size at an impingement angle of 20° . However, velocity exponents of 2.8 and 2.34 have been recorded in single-impact experiments in which 2.3 mm diameter steel spheres impinged at a similar angle against strain-hardened and annealed aluminum alloy surfaces, respectively [2], so it is evident that this parameter is greatly influenced by experimental conditions. It should also be noted that the type of size effects which previously have been invoked [8] to explain velocity exponents greater than 2 cannot explain the present results because strain hardening leads to an increase rather than a decrease in the flow stress as the crater size increases. In addition, it is clear that the velocity exponent decreases with increasing number of impacts because more impacts are required to strain harden the surface fully at lower velocities and develop the erosion through its threshold and incubation regimes to its steady state condition.

The well-known dependence of erosion on the angle of impingement [7, 8] appears to be explicable in terms of the relative contributions of the lip and platelet mechanisms to total material removal at different angles. Experimentally it is found that the variation of mass loss with impingement angle is of similar form in both single and multiple impact experiments at relatively shallow angles [4, 5], but that the amount of material removed by single, independent impacts is too small to account for the mass losses produced by multiple impacts at steeper angles. Evidently, lip detachment during individual impact events is the dominant mechanism in both the single impact and multiple impact situations at shallower angles, and the formation and detachment of platelets as a result of interaction between successive impacts accounts for the additional mass loss observed in the multi-impact situation at normal and near-normal incidence. In this view, erosion at intermediate angles is presumably due to a combination of three mechanisms — primary lip formation and detachment during a single impact, secondary removal of pre-existing lips by subsequent impacts, and detachment of platelets formed as a result of crater overlap.

In general, indentation hardness is influenced by both the strain and the strain rate at which it is measured [16]. It is therefore of interest to discover here that while there is little difference in the rate of strain hardening of aluminum under static and dynamic conditions, there is an approximately twofold increase in the hardness when the strain rate is increased from about 10^{-3} to about 10^5 s^{-1} . Moreover, since the ratio of dynamic to static flow stress varies considerably for different materials [22, 23], it follows that a more critical test of any correlation between hardness and erosion would involve a hardness parameter determined under conditions which approximate those occurring in the typical erosive impact.

Finally, it has been suggested that erosion may somehow be related either individually or collectively to such thermal properties as the melting point [24], the coefficient of linear thermal expansion [25], or the specific

AD-A088 571

PENNSYLVANIA STATE UNIV UNIVERSITY PARK MATERIALS RE--ETC F/6 7/4
MECHANISMS OF EROSION.(U)
AUG 80 N H MACMILLAN

DAA629-79-C-0104

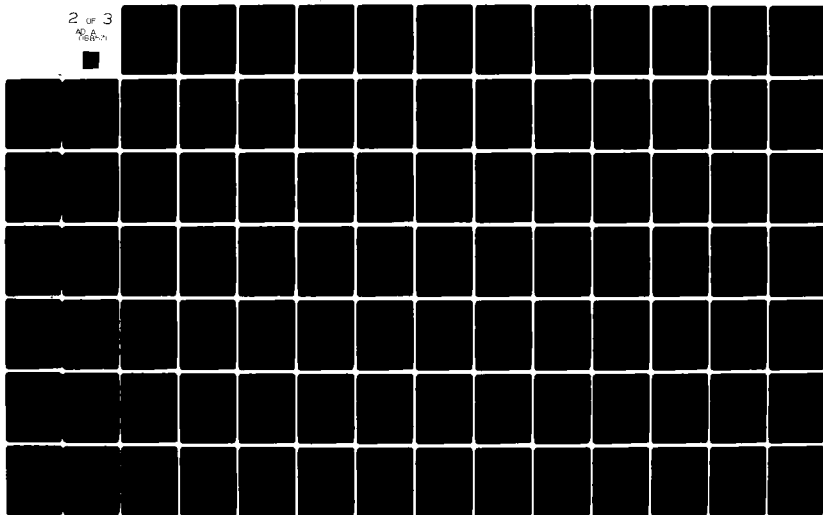
UNCLASSIFIED

ARO-14084.13-MS

NL

2 OF 3

AD-A
168-7



heat [26]. It is therefore worthy of note that the present experiments provide no evidence that large-scale melting occurs. Specifically, the appearance of both the eroded surface and the detached fragments of metal is consistent with plastic deformation rather than splashing of molten material. However, a certain amount of thermal softening may occur as a result of adiabatic heating in a material having a melting point as low as that of aluminum. It is therefore concluded that although adiabatic effects could play a significant role in ductile erosion [27], the contribution due to actual melting is negligible, at least at subsonic impact velocities.

Acknowledgment

This work was supported by the U.S. Army Research Office under Grant No. DAAG29-78-G-0056.

References

- 1 C. M. Preece and N. H. Macmillan, *Annu. Rev. Mater. Sci.*, 7 (1975) 95.
- 2 G. L. Sheldon and A. Kanhere, *Wear*, 21 (1972) 195.
- 3 I. M. Hutchings and R. E. Winter, *Wear*, 27 (1974) 121.
- 4 I. M. Hutchings and R. E. Winter, *J. Phys. D*, 8 (1975) 8.
- 5 I. M. Hutchings, R. E. Winter and J. E. Field, *Proc. R. Soc. London, Ser. A*, 348 (1976) 379.
- 6 J. G. A. Bitter, *Wear*, 6 (1963) 169.
- 7 I. Finnie, *Wear*, 3 (1960) 87.
- 8 I. Finnie, J. Wolak and Y. Kabil, *J. Mater.*, 2 (1967) 682.
- 9 J. E. Goodwin, W. Sage and G. P. Tilly, *Proc. Inst. Mech. Eng., London*, 184 (1969) 287.
- 10 G. P. Tilly and W. Sage, *Wear*, 16 (1970) 447.
- 11 I. Kleis, *Wear*, 13 (1969) 199.
- 12 I. Finnie, *Proc. 3rd U.S. Natl. Congr. of Applied Mechanics*, ASME, New York, 1958, p. 527.
- 13 J. G. A. Bitter, *Wear*, 6 (1963) 5.
- 14 C. E. Smeltzer, M. E. Gulden and W. A. Compton, *J. Basic Eng.*, 92 (1970) 639.
- 15 G. P. Tilly, *Wear*, 23 (1973) 87.
- 16 D. Tabor, *The Hardness of Metals*, Oxford Univ. Press: Clarendon Press, Oxford, 1951.
- 17 J. P. Andrews, *Philos. Mag.*, 9 (1930) 593.
- 18 D. G. Rickerby, B. N. Pramila Bai and N. H. Macmillan, *J. Mater. Sci.*, 14 (1979) 1807.
- 19 E. Meyer, *VDI Z.*, 52 (1908) 645, 740, 835.
- 20 D. G. Rickerby and N. H. Macmillan, *Proc. 5th Int. Conf. on Erosion by Liquid and Solid Impact*, Cambridge, 1979, p. 29 - 1.
- 21 D. G. Rickerby and N. H. Macmillan, *Mater. Sci. Eng.*, 40 (1979) 251.
- 22 A. C. Whiffin, *Proc. R. Soc. London, Ser. A*, 194 (1948) 300.
- 23 R. M. Davies, *Proc. R. Soc. London, Ser. A*, 197 (1949) 416.
- 24 C. E. Smeltzer, M. E. Gulden, S. S. McElmury and W. A. Compton, *Rep. 70-36*, USAAV Lab., 1970.
- 25 P. Ascarelli, *Tech. Rep. 71-47*, U.S. Army Materials and Mechanics Research Center, 1971.
- 26 I. M. Hutchings, *Wear*, 35 (1975) 371.
- 27 R. E. Winter and I. M. Hutchings, *Wear*, 34 (1975) 141.

Appendix VIII

On the Oblique Impact of a Rigid Sphere Against a Rigid-Plastic Solid

D. G. Rickerby and N. H. Macmillan
Materials Research Laboratory
The Pennsylvania State University
University Park, PA 16802, USA

Previous workers have sought to explain the variation in crater volume observed when hardened steel spheres impact at different angles against mild steel plates by numerically modelling a rigid sphere striking an ideal rigid-plastic half-space. The present note shows that the discrepancy between experiment and their theoretical prediction from this model can be significantly reduced by incorporating a more accurate calculation of the area of contact into the analysis.

INTRODUCTION

In the course of their studies of solid particle erosion, Hutchings et al.¹ endeavored to predict the variation of crater volume with impact angle for a rigid sphere impinging obliquely against an ideal rigid-plastic half-space. They used an iterative numerical procedure to solve the equation of motion of the sphere and compute the volume it sweeps out during the impact event; and they compared the predictions of their model with the results of experiments in which they fired 9.5 mm diameter hardened steel spheres at mild steel targets. Their data are shown in Figure 1, and reveal a significant discrepancy between theory and experiment. This note points out that this discrepancy largely disappears when a better description of the area of contact between the sphere and the target^{2,3} is incorporated into the impact model.

IMPACT ANALYSIS

Figure 2(a) shows a sphere of radius r and mass m which has penetrated a target to a depth l at a time t long enough after first contact that it no longer completely fills the crater formed thus far. The initial point of detachment O' serves as the origin of a Cartesian coordinate system so oriented that the target surface and the velocity vector of the sphere lie in the planes $O'zx$ and $O'xy$, respectively. $BEDF$ is the diametral section of the sphere perpendicular to the current velocity vector; and A_1 is the area of the segment $BFCE$ of this circle lying below the original target surface. A_2 denotes the area of the circular segment $AECF$, which lies in the plane $O'zx$ and has a radius a . The other parameters needed to define the problem are identified in Figure 2(b), which represents the section through Figure 2(a) in the plane $O'xy$. Note that the angle of incidence α is taken to be negative when the penetration of

the sphere into the target is increasing. This is consistent with the usual convention that angles measured anti-clockwise from the x-axis are regarded as negative, and avoids the need to use different sets of equations to describe the motion into and out of the target.

In their analysis of the situation represented by Figures 2(a) and (b), Hutchings et al. ignored gravitational effects and assumed that the principal retarding force P exerted on the sphere by the target derives from a normal indentation pressure, or dynamic hardness, p_d that is uniformly distributed over the contact area and is independent of both the velocity and the depth of penetration of the sphere. Then, to simplify computation, they further assumed that this force acts along RO and is proportional to the area of the circle with AB as diameter. Additionally, they assumed that a small frictional force μP , where the coefficient of friction $\mu \approx 0.05$,^{1,4} acts tangentially through O . In reality, however, the system of forces acting on the sphere can be represented by a force through O (which can be resolved into components parallel and perpendicular to RO) plus a couple. In effect, therefore, Hutchings et al. approximated the couple and the component of force acting perpendicular to RO by an effective frictional force determined by a fixed value of μ . This force represents the sum of the forces required to shear junctions between asperities on the surfaces in contact and to deform the underlying solid.⁵ A similar treatment of the forces acting on the sphere is adopted in the present work, the only difference being that the area of contact is calculated more accurately.

As long as the sphere remains in contact with the entire surface of the crater, calculation of the area of contact is straightforward. Thus, if hardness is defined as load divided by the projected area of contact, the motion prior to detachment at O' can be described by

$$m\ddot{x} = -\mu P \quad (1)$$

and

$$m\ddot{y} = P, \quad (2)$$

where $P = \pi a^2 p_d$.

After detachment, the calculation of the area of contact becomes more complex. Nevertheless, because the crater dimensions obtained from the model are sensitive to error in this area, it is desirable to perform this calculation more accurately than did Hutchings et al. With the present definition of hardness this can be done relatively easily, for projection of the actual contact area onto the plane defined by AB and O'z gives exactly the same projected area as does projection of A_1 and A_2 onto the same plane. It follows that the equations* governing the translational motion of the center of the sphere after detachment are

$$m\ddot{x} = -P \sin (\alpha + \beta) - \mu P \cos (\alpha + \beta) \quad (3)$$

$$\text{and} \quad m\ddot{y} = P \cos (\alpha + \beta) - \mu P \sin (\alpha + \beta), \quad (4)$$

where

$$P = p_d [A_1 \sin (\gamma - \alpha) + A_2 \cos \gamma],$$

$$\gamma = \sin^{-1} \{ [\ell - r (1 - \cos \alpha)] / 2r \sin \beta \}$$

$$\text{and } \beta = \sin^{-1} (AB/2r) = \sin^{-1} \{ [(a - r \sin \alpha)^2 + (\ell - r (1 - \cos \alpha))^2]^{1/2} / 2r \}.$$

Furthermore, once it is recognized that the geometry of the impact crater is completely determined by the motion and the variation in area of the segment BFCE after detachment at O', it is also easy to calculate the crater volume. The method adopted was to separate the motion of the segment during any time interval t to $t + \delta t$ into rotational and translational parts. Then, it can be shown that the volume δV_t swept out by the segment BFCE (which is perpendicular to the current translational velocity vector) as a result of the translational component of motion is given by

$$\delta V_t = (A_1 + \frac{1}{2} \frac{dA_1}{dt} \delta t) (v + \frac{1}{2} \frac{dv}{dt} \delta t) \delta t. \quad (5)$$

*Provided that the sign convention adopted for α is observed, there is no inconsistency between Fig. 2(b) and equations (3) and (4).

Also, since the rotation of BFCE is about an axis through O parallel to $O'z$, it follows from the formula for the volume of a sphere containing a cylindrical hole that the volume δV_r resulting from this rotational displacement is given by

$$\delta V_r = \frac{2}{3} \left| \frac{d\alpha}{dt} \delta t \right| \left[r^2 - \frac{1}{4} \left(\frac{r - l}{\cos \alpha} + \frac{r - l - \frac{dl}{dt} \delta t}{\cos(\alpha + \frac{d\alpha}{dt} \delta t)} \right)^2 \right]^{3/2} . \quad (6)$$

Hence, the total volume V of the impact crater can be found from

$$V = \int_{t=0}^{t=\tau} dV_t + \int_{t=0}^{t=\tau} dV_r , \quad (7)$$

where τ is the duration of the impact event.

CALCULATIONS AND CONCLUSIONS

To compare the predictions of the present model with the data from Hutchings et al. presented in Figure 1, a straightforward iterative numerical procedure was used to solve the equations of motion and compute V from equations (5) to (7). Values of 3546 mg, 4.75 mm and 0.05 were assigned to m , r and μ , respectively, and the initial value of v was set to 270 m s^{-1} . Calculations were performed for initial values of α ranging from -10° to -80° , using a time increment δt of $0.2 \text{ } \mu\text{s}$ between iterations; and p_d was varied until the "best fit" to the experimental data in Figure 1 was obtained. Since τ decreased from $\sim 30 \text{ } \mu\text{s}$ to $\sim 20 \text{ } \mu\text{s}$ as α changed from -10° to -80° , each integrand in equation (7) was evaluated in at least 100 steps. This proved sufficient to determine V to within $\sim 0.1\%$.

The results, which are presented in Figure 1, show that if p_d is taken to be 3.0 GPa the present method of calculation provides much better agreement with

experiment than that used by Hutchings et al. Subsidiary calculations showed that two-fold variations in the value of μ have but a marginal effect on the crater volume. This implies that the total force acting on the sphere during the impact event, cannot act very far from the line RO, and hence that the approximation used to model forces other than that acting along RO does not substantially affect the calculations. Physically, the reason appears to be that the couple arising from the frictional force acting on each element of the area of contact tends to cancel out that due to the normal force acting on each such element. It is thus suggested that the discrepancy between theory and experiment observed by Hutchings et al. derives primarily from their method of calculating the contact area rather than from their assumptions about the forces acting on the particle or from the very simple constitutive relation used in their model. Such discrepancy as still remains presumably derives from pile-up of displaced material ahead of the moving sphere, the effect of which is not taken into account in either case.

ACKNOWLEDGEMENT

Work supported by the U.S. Army Research Office under Contract No. DAAG29-79-C-0104.

REFERENCES

1. I. M. Hutchings, R. E. Winter and J. E. Field, Proc. Roy. Soc. Lond. A348, 379 (1976).
2. G. Birkhoff, G. D. Birkhoff, W. E. Bleick, E. H. Handler, F. D. Murnaghan and T. L. Smith, Ricochet off Water, AMP Memo. 42.4M (1944).
3. W. Johnson and S. R. Reid, J. Mech. Eng. Sci. 17, 71 (1975).
4. F. P. Bowden and P. A. Persson, Proc. Roy. Soc. Lond. A260, 433 (1961).
5. F. P. Bowden and D. Tabor, The Friction and Lubrication of Solids, Part 1, p. 91, Oxford University Press, London (1954).

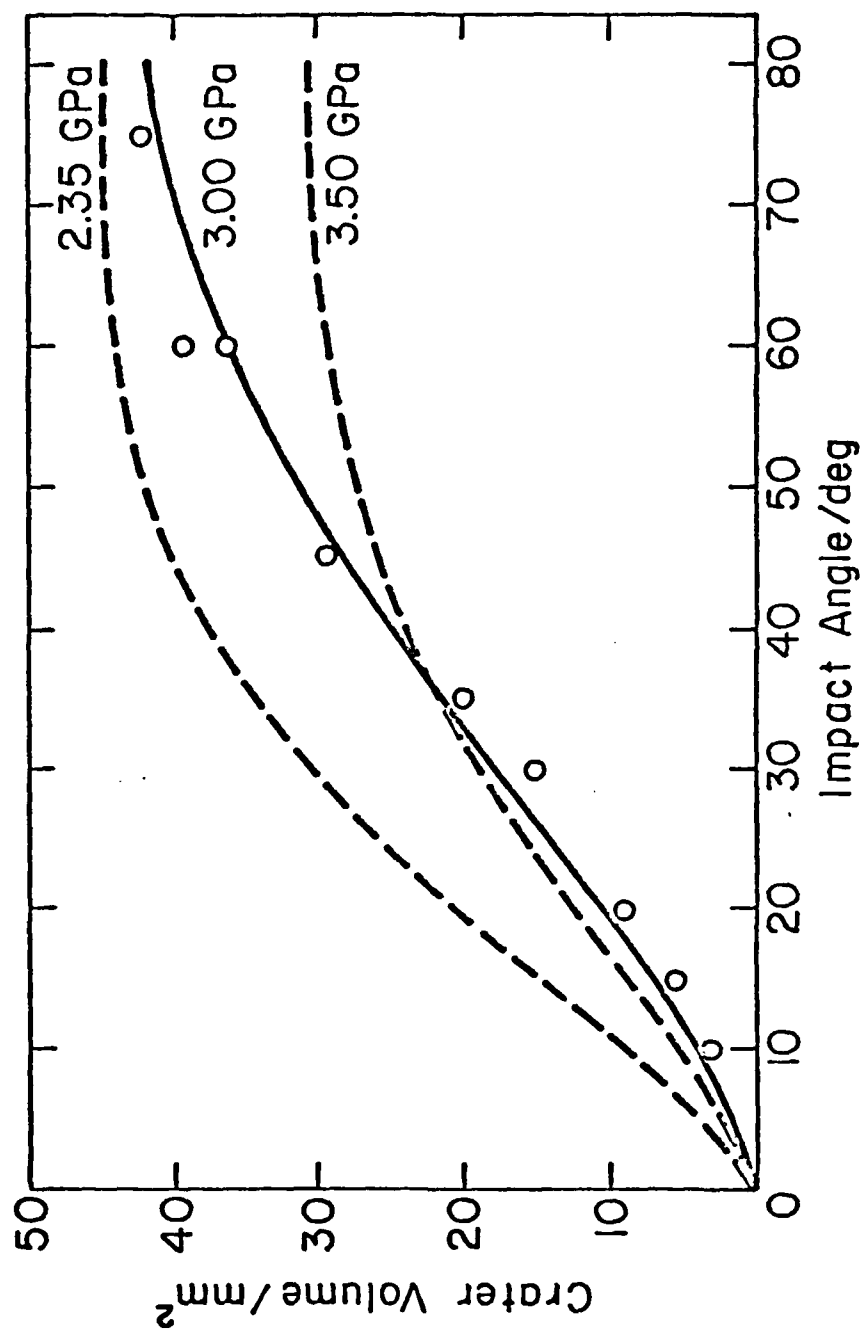


Figure 1 The dependence of crater volume on impact angle for a 9.5 mm diameter steel sphere impinging on mild steel at 270 m s^{-1} . The open circles and the dotted lines are the experimental data and theoretical predictions, respectively, of Hutchings et al.; the solid line is the present theoretical prediction.

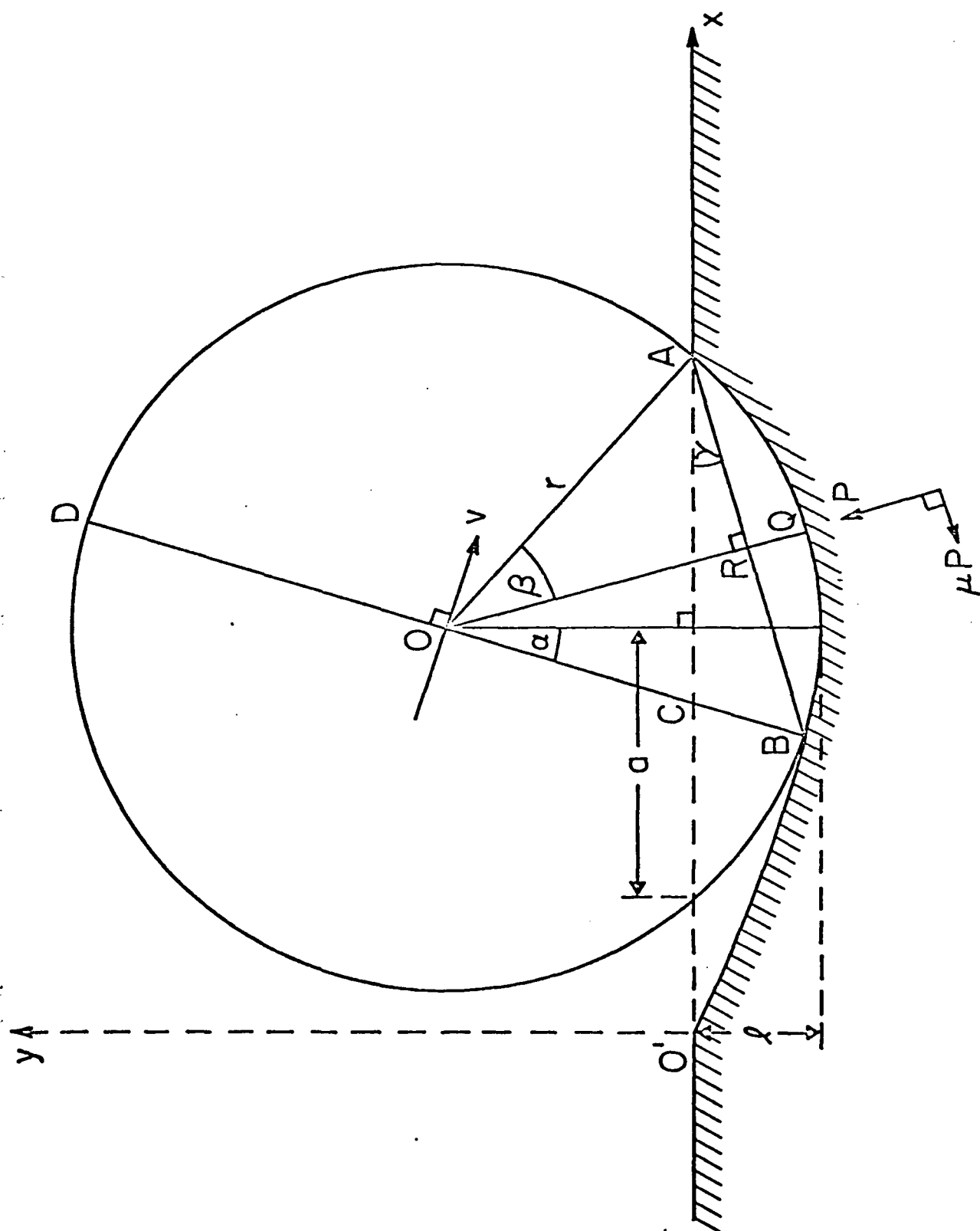


Figure 2(b) Section through the sphere and the target showing the forces

Appendix IX

The Effect of Approach Direction on Damage in MgO
Due to Spherical Particle Impact

D. G. Rickerby and N. H. Macmillan
Materials Research Laboratory
The Pennsylvania State University
University Park, PA 16802, USA

The damage produced by spherical particle impact against {100} surfaces of MgO has been investigated over a range of impact angles for a fixed particle velocity and over a range of particle velocities for a fixed impact angle. The mass of material removed by each impact was determined gravimetrically, and the crater and surrounding damage were studied by means of surface profilometry and scanning electron microscopy. A numerical computer model of the crater formation process was developed, and was shown to predict crater geometries which agree closely with those observed experimentally. This same model also provided estimates of the dynamic hardness, the contact time and the energy transmitted to the surface during the impact. The dynamic hardness was $\sim 25\%$ less than that measured in previous normal impact studies [1] on MgO of similar static hardness. The contact time and energy calculations give some insight into the reasons why the energy balance model, which successfully describes the velocity dependence of mass loss under normal impact conditions, breaks down for oblique impact.

1. INTRODUCTION

The present authors have previously reported [1] the results of single impact experiments in which spherical particles impinged at normal incidence against monocrystalline MgO surfaces of various crystallographic orientations. Both the volume of the crater produced and the mass of material removed from the surrounding region were found to be orientation dependent and proportional to the kinetic energy of the particle. In many situations of practical interest, however, erosion derives from solid particle impact at oblique as well as normal incidence, and it is therefore necessary to consider the effect of impact angle on erosive damage. Hence, the experiments described in the present paper extend the previous work by varying both the impact angle of the particle and the crystallographic direction of the component of the velocity vector parallel to the specimen surface.

Multiple impact experiments on ceramics and glasses [2-5] indicate that erosion increases as the impact angle increases from zero (grazing incidence), but generally passes through a maximum somewhat before the normal is reached. This maximum cannot be rationalized in terms of a simple energy balance model of the erosive process such as that proposed by Bitter [2]. It is therefore of interest to assess the influence on erosion of such additional factors as the contact time and frictional forces, which are not considered in this model. To this end a computer was used to calculate the particle trajectory during impact by an iterative numerical method.

2. EXPERIMENTAL

Monocrystalline MgO specimens with {100} oriented target faces approximately 10 mm x 10 mm in size were cleaved from a large single crystal, chemically polished [6], and mounted in resin as in the previous work [1]. Table I shows the results of an emission spectroscopic analysis of the crystal, and suggests that both the total cation impurity content and the content of Fe plus Al lie within the range of variation found in the crystals used in the earlier work.

TABLE I Semi-quantitative spectrochemical analysis of the MgO crystal

<u>Element</u>	<u>Concentration (ppm)</u>
Ca	100
Al	20
Mn	30
Fe	200
Si	100

Not detected: Cr, Ti, V, Ni, Be, Cu, Ag, Na, Co, Zr, Cd, Zn, Sn, Bi, Ge, In, Ga, Pb, Sr, Ba.

The particles used in the present experiments were WC - 6%Co spheres similar to those used previously. They were of nominal diameter 1.575 ± 0.025 mm, weighed 30 ± 1 mg, and had a Vickers hardness number (VHN) ~ 2000 kg mm⁻². These particles were fired at the specimens by means of a nitrogen powered gas gun, and the particle velocities were determined to within $\pm 1\%$ by means of a photoelectric time-of-flight device. The specimens were mounted on a goniometer stage which allowed the impact angle to be varied independently of the angle of rotation of

the target surface about its normal.

In one series of experiments a study was made of the damage produced at an impact velocity of $200 \pm 5 \text{ m s}^{-1}$ as the impact angle increased from 10° to 90° . Two sets of data were obtained, one with the particle velocity component parallel to the target surface directed along $\langle 100 \rangle$ and the other with it parallel to $\langle 110 \rangle$. In another series of experiments the impact velocity was varied from 50 m s^{-1} to 320 m s^{-1} while the impact angle remained fixed at 30° to the surface. In this series the parallel component of the particle velocity was always directed along $\langle 100 \rangle$.

In some cases an indirect measurement of the velocity of the rebounding particle was made by arranging for it to impinge normally against the surface of an aluminum block. By measuring the depth of the crater thus produced it was possible to calculate the rebound velocity of the particle from the results of previous studies of crater formation in the same aluminum [7]. However, this technique was limited to those relatively small impact angles for which the aluminum block did not interfere with the flight of the particle between the gun muzzle and the MgO target.

The impact damage was characterized firstly by measuring gravimetrically the mass of material removed, and thereafter by examining the damaged region using scanning electron microscopy and surface profilometry. These last studies provided a series of parallel, equidistant cross-sectional profiles along the long axis of each crater. The crater volume could thus be determined by measuring the areas between the crater boundary and the original surface level for this series of profiles, and then applying the trapezoidal rule. In addition, crater depth relative to the same level was measured from that profile corresponding to the deepest cross-section through the crater.

Static indentation tests were also performed on the same chemically polished {100} MgO surfaces. The Meyer hardness M [8] was determined using a WC - 6% Co sphere of the type used in the impact experiments with an applied load of 50 kg, and the Meyer-Vickers hardness M_v^* was determined using a standard Vickers diamond pyramid indenter with an applied load of 300 g. The measurements of indentation diameters or diagonals, as appropriate, were made along $\langle 100 \rangle$ directions in each case. Both of these hardness parameters are defined as the applied load divided by the projected area of contact, as is the dynamic hardness used in the impact model. The measured mean values of M and M_v and their standard deviations were $190 \pm 20 \text{ kg mm}^{-2}$ and $950 \pm 20 \text{ kg mm}^{-2}$, respectively.

* $M_v = \text{VHN} / 0.927$

3. THEORETICAL

Being mathematically tractable, the normal impact problem has received a reasonable amount of attention [8,9]. Consequently, only the pertinent results are given here. It is supposed that a rigid spherical particle of radius r and mass m impinges normally on a plastic-rigid half-space, and that the indentation pressure (dynamic hardness) p_d remains constant throughout the impact. If all the kinetic energy of the particle is assumed to be dissipated in plastic deformation of the target, then

$$p_d V = \frac{1}{2} m v_0^2, \quad (1)$$

where V is the crater volume and v_0 is the initial velocity of the particle. The contact time t_c is independent of the impact velocity, and is given by

$$t_c = \frac{\pi}{2} \left(\frac{m}{2\pi p_d r} \right)^{\frac{1}{2}}. \quad (2)$$

The oblique impact problem is more complicated because the equation of motion of the particle cannot be solved analytically. Hence, a computer program, details of which are discussed elsewhere [10], has been developed to provide a numerical solution by an iterative method. The approach used is similar to that adopted by Hutchings, Winter and Field [11], but incorporates a more accurate description of the area of contact [12,13].

Figure 1 illustrates the situation at some time long enough after the beginning of the impact that the sphere is no longer in contact with the entire surface of the crater. At this instant the particle velocity, which was initially v_0 at an angle α_0 to the x -axis, has reached a value v at an angle α , and the arc of contact in the x - y plane subtends an angle 2β at the center of the sphere. It should be noted that, by convention, α is negative when

the y-component of particle velocity is directed into the surface. The principal retarding force P is taken to act along RO , and is assumed to derive from a constant, uniform indentation pressure acting over the projection of the area of contact onto the plane perpendicular to RO . In addition, a frictional force μP is taken to act tangentially through Q . As long as the sphere remains in contact with the entire surface of the crater, the motion can be described by

$$m\ddot{x} = -\mu P \quad (3)$$

and $m\ddot{y} = P. \quad (4)$

However, once the sphere detaches from the surface at O' , the equations governing its translational motion become

$$m\ddot{x} = -P \sin (\alpha + \beta) - \mu P \cos (\alpha + \beta) \quad (5)$$

and $m\ddot{y} = P \cos (\alpha + \beta) - \mu P \sin (\alpha + \beta). \quad (6)$

Each of these two pairs of equations can be solved numerically over that part of the motion to which it is applicable by means of an iterative procedure in which time is incremented in equal steps of appropriate duration. This procedure yields the complete particle trajectory, together with values of crater depth and volume, rebound velocity and rebound angle of the particle, and contact time.

4. RESULTS

Figure 2 shows the damage produced by 200 m s^{-1} impacts in which the velocity component of the particle parallel to the target surface was directed along $\langle 100 \rangle$. Although its appearance varies strikingly with impact angle, the damage consists in general of a crater formed mainly by plastic deformation, together with a peripheral region in which fracture occurs predominantly on $\{100\}$ and $\{110\}$ planes. As the impact angle is decreased, this latter region tends to concentrate increasingly around the exit side of the crater. Similar observations apply to the damage shown in Fig. 3, which was produced at the same impact velocity and angles, but with the parallel component of the particle velocity directed along $\langle 110 \rangle$. The effect of this change in approach direction on the appearance of the damage is most apparent at the smaller impact angles.

The series of micrographs shown in Fig. 4 illustrates the effect of varying the particle velocity while keeping the impact angle constant at 30° . At lower velocities the damage outside the crater is concentrated along the $\langle 110 \rangle$ directions on the exit side. As the velocity is increased, these regions grow in size and are supplemented by smaller amounts of similar damage on the entrance side. Finally, at velocities above $\sim 200 \text{ m s}^{-1}$, the damaged regions begin to coalesce and to encroach back into the crater itself, resulting in significantly enhanced material removal.

Further details of the damage produced by impacts at an angle of 10° are shown in Fig. 5. ** With the parallel component of particle velocity along $\langle 100 \rangle$, the slip lines around the crater all lie perpendicular to this direction, indicating that the deformation is produced by slip on tautozonal $\{110\}$ planes inclined

** The white debris on the surface was identified by energy dispersive x-ray analysis as WC.

at 45° to it. However, when this velocity component lies along $\langle 110 \rangle$, two intersecting sets of slip lines are seen on each side of the crater. From the orientation of these lines, it can be deduced that the active $\{110\}$ planes in this instance are inclined at 60° to the parallel velocity component and lie in two different zones. Figure 5 also reveals that inside the craters are networks of cracks lying predominantly perpendicular to the direction of the parallel velocity component. This cracking becomes less extensive as the impact angle increases towards 90° and, at any given impact angle, is usually more pronounced for a $\langle 110 \rangle$ orientation of the parallel velocity component than for a $\langle 100 \rangle$ orientation.

Near normal incidence any intersecting slip lines are generally confined, as in Fig. 6a, to narrow regions along $\langle 110 \rangle$ directions; and detailed examination of the eroded areas around the crater reveals complex patterns of cleavage steps on the fracture surfaces, such as those seen in Fig. 6b.

Nowhere in any of these micrographs is there any evidence of target melting during impact; and scanning electron microscopic studies of spent erosive particles revealed only insignificant amounts of MgO on their surfaces.

The crater profiles shown in Figs. 7, 8 and 9 are cross-sections along the long axes of the craters of Figs. 2, 3 and 4, respectively. Comparison of Figs. 7 and 8 reveals that crater shape does not differ greatly when the direction of the parallel component of particle velocity changes from $\langle 100 \rangle$ to $\langle 110 \rangle$. The broken lines superimposed on the profiles represent the crater shapes predicted theoretically—i.e., the envelopes of the successive positions of the circular boundary of the particle as generated by the computer program. Such discrepancies as exist presumably arise from experimental errors in the impact velocity and impact angle, and from the effect of elastic recovery of the target (which was not included in the theoretical model). The particles were hard enough that they did not undergo any appreciable plastic deformation during the impact, thereby eliminating this potential source of error.

The variation of crater volume with impact angle at an impact velocity of 200 m s^{-1} is shown in Fig. 10, and the variation with velocity at an angle of 30° is shown in Fig. 11. The lines fitted to the experimental data correspond to the predictions of the computer model when p_d is taken as 780 kg mm^{-2} . This overall mean value of p_d , which has a standard deviation of 70 kg mm^{-2} , was obtained by making a first estimate from the volumes of the two normal impact craters, and then successively correcting this value until the discrepancies between the calculated and experimental crater volumes were minimized. The individual mean values of p_d for the three sets of volume data presented in Figs. 10 and 11 showed no significant deviation from the overall mean. The overall value was therefore used in all final computations in this paper. A value of 0.1 was adopted for μ as being a reasonable estimate for a WC sphere sliding at high speeds on MgO [14,15] in any crystallographic direction [16]. Varying μ between 0.05 and 0.2 affected the computed particle trajectories only marginally, so errors in μ within this range would not greatly alter the predictions of the model.

Measurements of crater depths were taken from the deepest profiles along each crater, and are shown in Figs. 12 and 13. The computer generated lines are a reasonable fit to the experimental data, confirming that no large discrepancies exist between the experimental and theoretical crater geometries. It is therefore concluded that neglecting plastic and frictional anisotropy and elastic recovery does not lead to any gross errors in the numerical calculations.

Mass loss as a function of impact angle at an impact velocity of 200 m s^{-1} is shown in Fig. 14. The general trend is similar for both orientations of the parallel component of particle velocity: the material removal increases monotonically with impact angle until a maximum is reached at $\sim 80^\circ$, and then a slight decrease occurs as the angle approaches 90° . Similar maximum values occur in both cases, but the peak is somewhat sharper when the parallel component lies along $\langle 110 \rangle$

rather than $\langle 100 \rangle$. The two data points at 90° represent impacts performed under nominally identical conditions, and therefore give an indication of the variability of the experimental data. The variation of the mass loss with impact velocity at an impact angle of 30° is shown in Fig. 15. If a power function relationship between mass loss and impact velocity is assumed, the best fit to these data is obtained with a velocity exponent of 3.3. However, an exponential function of the velocity fits the complete data somewhat better, while a power function with a velocity exponent of 2.2 provides a reasonable fit to those data obtained at velocities below 220 m s^{-1} .

Computer predictions of particle rebound velocities are shown in Figs. 16 and 17, together with the limited number of experimental data obtainable. These show that agreement between theory and experiment is good for impacts at relatively small angles to the surface. Although no data are available for angles nearer the normal, it is likely that agreement would be less satisfactory in such cases because the rebound velocity would be more strongly affected by the elastic recovery of the target.

The energy transferred from the particle to the target during a single impact can easily be estimated from the computer model described in the previous section, since the total energy lost by the impinging particle is $\frac{1}{2}m(v_0^2 - v_R^2)$, where v_R is the particle rebound velocity. In this model particle rotation is neglected, and it is assumed that an amount pV of the energy transmitted to the target is used in plastic work, while the remainder is dissipated in overcoming frictional resistance. Both $\frac{1}{2}m(v_0^2 - v_R^2)$ and pV are plotted in Figs. 18 and 19 as functions of impact angle and velocity, respectively; and also shown is the parameter $\frac{1}{2}mv_0^2 \sin^2 \alpha_0$, which corresponds to the transfer of energy to the target implied by Bitter's theory of erosion [2]. The parameters shown in Fig. 18 vary in a similar manner with impact angle, and the fraction of the total energy transferred which is dissipated as frictional work decreases markedly as the impact angle

increases. Bitter's theory assumes that the energy transferred to the target during an impact is proportional to v_0^2 , irrespective of the impact angle, while the computer model indicates that the parameters $\frac{1}{2}m(v_0^2 - v_R^2)$ and pV vary as $v_0^{2.20}$ and $v_0^{2.25}$, respectively, for an impact angle of 30° . The experimentally observed variation of mass loss with velocity at this angle is therefore consistent with the energy balance derived from the computer model, at least for impact velocities $\lesssim 200 \text{ ms}^{-1}$.

Finally, the computed values of the contact time t_c and the detachment time t_d at which the particle begins to separate from the surface of the crater are shown as functions of impact angle and impact velocity in Figs. 20 and 21, respectively. The contact time decreases slowly with increasing impact angle up to $\sim 60^\circ$, but then falls off rapidly as this angle approaches 90° . In contrast, it increases slowly with increasing impact velocity at an impact angle of 30° .

5. DISCUSSION

The dynamic hardness data obtained from the present experiments not only have an overall mean value $\sim 25\%$ lower than that measured previously on a $\{100\}$ surface [1], but also exhibit a twofold reduction in their coefficient of variation. In addition, the amount of material removed by a single normal impact at 200 m s^{-1} was about 40% less than in the previous experiments. These differences appear to be too large to attribute merely to random scatter, but are difficult to explain unambiguously on the basis of the data presently available.

The reduction in the coefficient of variation probably reflects the fact that all of the specimens used in the present work came from the same large monocrystal, and thus were of more consistent purity than the specimens used in the earlier work. It is also possible that the lower dynamic hardness and the reduction in the amount of material removed by fragmentation stem from a reduction in yield stress and/or work hardening and a concomitant increase in ductility, all of which derive from a lower total trivalent (Fe^{3+} plus Al^{3+}) cation impurity content [17-20] in the present specimens. However, the spectrochemical analyses performed on the different specimens lack both the capacity to distinguish between Fe^{2+} and Fe^{3+} ions and the sensitivity necessary to confirm this hypothesis. Furthermore, the corresponding reductions in the quasi-static Meyer and Meyer-Vickers hardnesses that should accompany any such reduction in impurity content were not observed, for the former did not change significantly and the latter decreased only $\sim 5\%$. This may indicate that quasi-static and dynamic hardness measurements are not strictly comparable, because they measure the stresses necessary to maintain very different numbers of dislocations in motion at very different average velocities; and there is evidence [21-23] that the stress required to maintain a given dislocation velocity varies more rapidly with Fe^{3+} content than does the yield stress [20].

In addition, it is important to recognize certain limitations of the methods used in both this work and the previous study to derive the dynamic hardness from the impact crater geometry. In both cases the separate contributions of such effects as work-hardening, plastic anisotropy, material pile-up ahead and to the sides of the impacting particle, stress-wave propagation and fracture are ignored; and the net result of all these effects is interpreted in terms of a single parameter—the dynamic hardness. Consequently, changes in this parameter can only be directly related to changes in dislocation glide behavior to the extent that this latter phenomenon dominates the process of crater formation. Unfortunately, the relative importance of dislocation glide in the present experiments is not clear.

It should also be realized that any change in the impact conditions has the effect of differently weighting the averaging process implicit in the derivation of the dynamic hardness. Thus, it is conceivable that an apparent difference in dynamic hardness could arise even in the absence of any change in dislocation glide behavior, merely because the present value was obtained from a series of impacts made over a different range of velocities and angles from those in the previous experiments. This cannot be the full explanation, however, for the concomitant reduction in mass loss at normal incidence cannot be rationalized in the same fashion. It is therefore suggested that the observed differences arise at least in part from an increased sensitivity of hardness to impurity content at higher strain rates. If confirmed, this hypothesis might have important implications with respect to the erosion resistance of ceramic materials.

As far as can be ascertained from the present experiments, neither hardness anisotropy nor frictional anisotropy appear to exert a significant influence on crater shape. This was to be expected in the case of frictional anisotropy, which is low for blunt sliders [16]. However, it is rather more surprising that effects due to hardness anisotropy are not more evident when craters are formed

along different crystallographic directions in the target surface, because the Knoop indentation hardness of a $\{100\}$ MgO surface doubles as the long axis of the indenter rotates from $\langle 100 \rangle$ to $\langle 110 \rangle$ [24]. The differences between the slip line patterns produced around low angle impact craters along $\langle 100 \rangle$ and $\langle 110 \rangle$ are due to slip occurring predominantly on two tautozonal slip planes in the former case and on four planes in two different zones in the latter. Apparently, the combined effects of the different resolved shear stresses acting on the active slip planes in the two cases, the different dislocation-dislocation interactions occurring [25], and the different fracture processes initiated by these interactions [26] do not produce changes in crater geometry significantly greater than those arising from experimental error.

The simple assumption that the mass loss is proportional to the energy transmitted to the target during the impact is only partially successful in accounting for the observed variation of mass loss with impact angle. In particular, the maximum mass loss occurs at an angle of $\sim 80^\circ$ rather than at normal incidence as predicted theoretically. This appears to be associated with the predicted rapid increase in contact time that accompanies reduction of the impact angle from 90° to 70° , for such an increase would be expected to promote the formation of longer cracks in the damaged region around the crater and thus to increase the amount of material removed from the surface. At smaller impact angles the contact time varies more slowly, and hence the experimental data conform more closely to the behavior expected from an energy balance model. This result also suggests that any increase in stress wave interaction arising from a longer contact time has only a minor effect on material removal. Differences in the amount of material removed in impacts for which the parallel component of particle velocity lies along $\langle 100 \rangle$ rather than $\langle 110 \rangle$ presumably reflect the different orientations of the non-radially symmetric stress field generated around

the moving particle with respect to the dominant {100} and {110} cleavage planes. It is also interesting that the general form of the angular dependence of the mass loss arising from a single impact is similar to that found in multiple impact experiments [2-5].

For impacts at 30° to the surface, the energy balance model embodied in the computer program successfully accounts for the experimentally observed variation of mass loss with impact velocity, at least up to velocities $\sim 200 \text{ ms}^{-1}$. At higher velocities, however, material removal tends to be increasingly greater than expected on the basis of this model. Thus, the velocity exponent obtained by fitting a power law curve to experimental mass loss data increases as the measurements are extended to higher impact velocities. The variation of the contact time with impact velocity does not appear to be sufficiently pronounced to account fully for this effect. Rather, it appears that the increased mass loss is associated with the removal of material from within the crater itself at velocities well below those at which this occurs for normal impact. This suggests that frictional traction is responsible for dragging material out of the crater. Such a mechanism would be expected to operate primarily at smaller impact angles, where the proportion of the available energy used in frictional work is greater.

It is thus apparent that even a theory based on the more precise energy balance derived from the computer program cannot explain fully all features of the erosion of materials which respond in a semi-brittle manner to particle impact. The replacement of the analytical approximations used previously by a more precise numerical calculation of the energy transferred to the target during the impact has resulted in some improvement in the correlation between theory and experiment. Those discrepancies which still remain appear to be qualitatively explicable in terms of the differences in contact times and frictional effects arising from variations in impact angle and particle velocity.

ACKNOWLEDGEMENT

Work supported by the U.S. Army Research Office under Contract No.
DA 29-79-C-0104.

REFERENCES

1. D. G. RICKERBY, B. N. PRAMILA BAI and N. H. MACMILLAN, *J. Mater. Sci.* 14 (1979) 1807.
2. J. G. A. BITTER, *Wear* 6 (1963) 5.
3. G. L. SHELDON, *Trans ASME - J. Basic Eng.* 92 (1970) 619.
4. C. E. SMELTZER, M. E. GULDEN and W. A. COMPTON, *Trans ASME - J. Basic Eng.* 92 (1970) 639.
5. H. L. OH, K. P. L. OH, S. VAIDYANATHAN and I. FINNIE, "The Science of Ceramic Machining and Surface Finishing," edited by S. J. Schneider and R. W. Rice (NBS Special Publication 348, 1972) p.119.
6. B. N. PRAMILA BAI and N. H. MACMILLAN, *J. Mater. Sci.* 14 (1979) 494.
7. D. G. RICKERBY and N. H. MACMILLAN, *Wear* (1979) in the press.
8. D. TABOR, "The Hardness of Metals" (Oxford University Press, London, 1951).
9. J. P. ANDREWS, *Phil. Mag.* 9 (1930) 593.
10. D. G. RICKERBY and N. H. MACMILLAN, *Int. J. Mech. Sci.* (1979) in the press.
11. I. M. HUTCHINGS, R. E. WINTER and J. E. FIELD, *Proc. Roy. Soc. Lond.* A348 (1976) 379.
12. G. BIRKHOFF, G. D. BIRKHOFF, W. E. BLEICK, E. H. HANDLER, F. D. MURNAGHAN and T. L. SMITH, "Ricochet off Water," AMP Memo. 42.4M (1944).
13. W. JOHNSON and S. R. REID, *J. Mech. Eng. Sci.* 17 (1975) 71.
14. F. P. BOWDEN and P. A. PERSSON, *Proc. Roy. Soc. Lond.* A260 (1961) 433.
15. D. R. MILLER, *Proc. Roy. Soc. Lond.* A269 (1962) 368.
16. F. P. BOWDEN and C. A. BROOKES, *Proc. Roy. Soc. Lond.* A295 (1966) 244.
17. G. W. GROVES and M. E. FINE, *J. Appl. Phys.* 35 (1964) 3587.
18. M. SRINIVASAN and T. G. STOEBE, *J. Appl. Phys.* 41 (1970) 3726.
19. R. W. DAVIDGE, *J. Mater. Sci.* 2 (1967) 339.
20. C. N. AHLQUIST, *J. Appl. Phys.* 46 (1975) 14.
21. R. N. SINGH and R. L. COBLE, *J. Appl. Phys.* 45 (1974) 981.

22. R. N. SINGH and R. L. COBLE, J. Appl. Phys. 45 (1974) 990.
23. R. N. SINGH and R. L. COBLE, J. Appl. Phys. 45 (1974) 5129.
24. C. A. BROOKES, J. B. O'NEILL and B. A. W. REDFERN, Proc. Roy. Soc. Lond. A322 (1971) 73.
25. B. H. KEAR, A. TAYLOR and P. L. PRATT, Phil. Mag. 5 (1959) 665.
26. Y. T. CHOU and R. W. WHITMORE, J. Appl. Phys. 32 (1961) 1920.

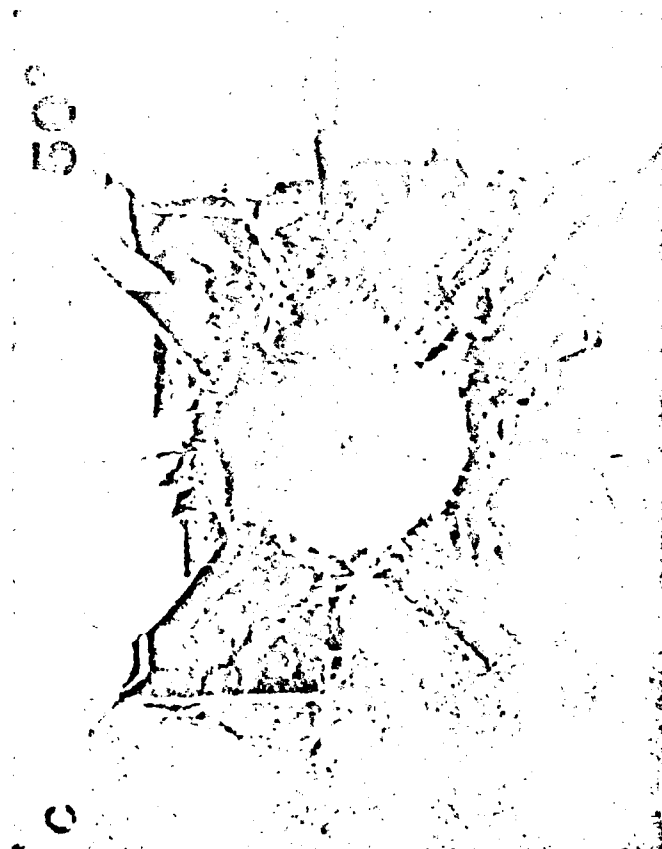
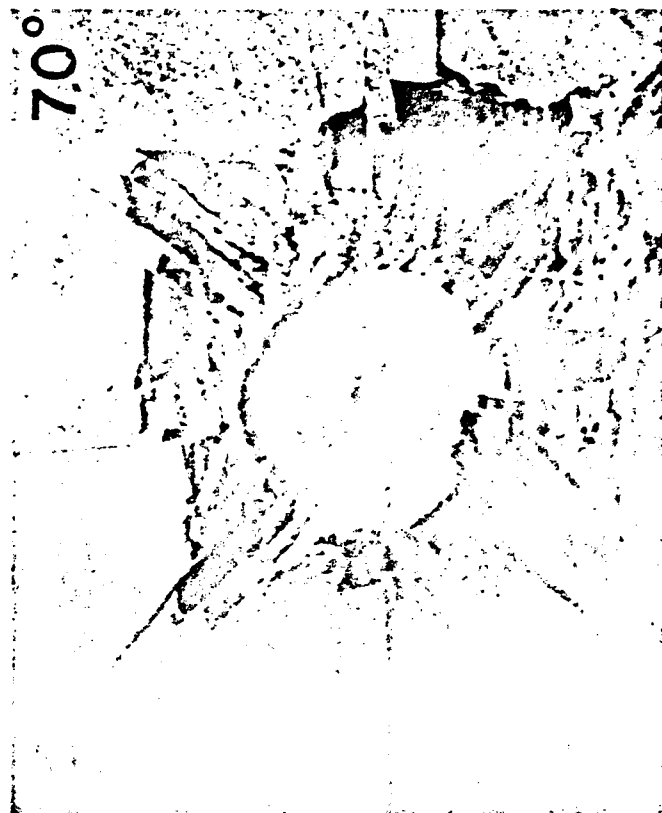
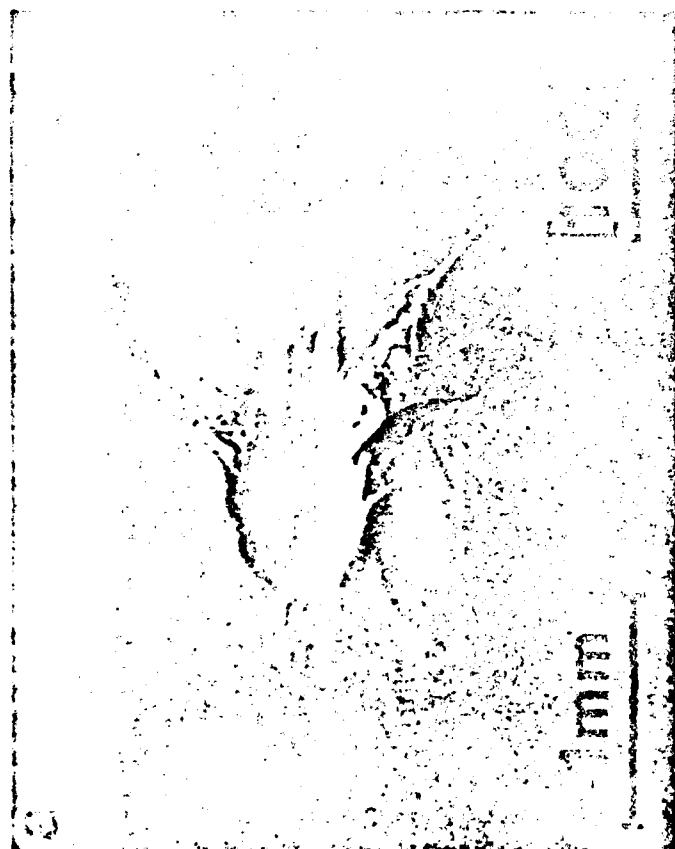
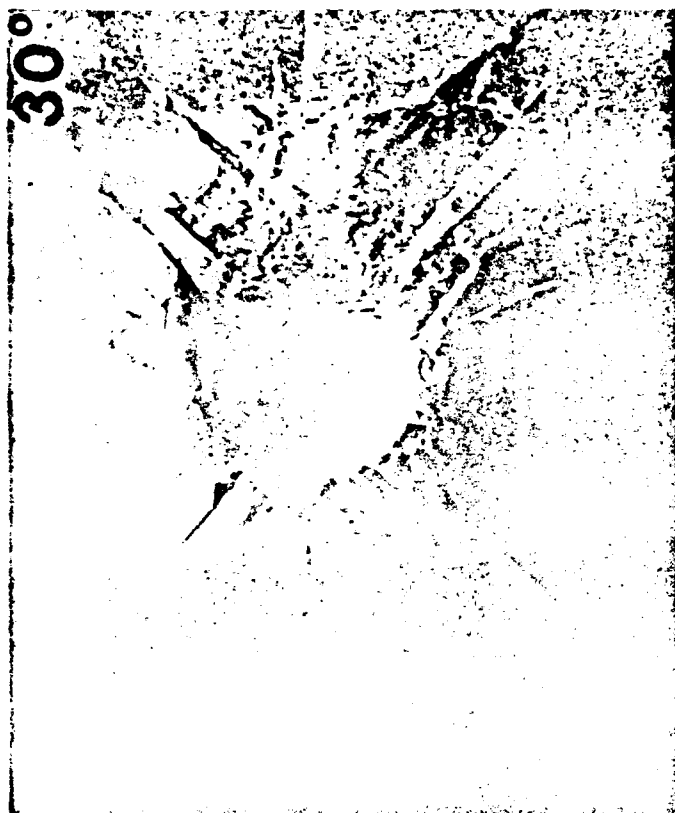


Figure 2 Scanning electron micrographs of craters formed along $\langle 100 \rangle$ by 200 m s^{-1} impacts at various angles.

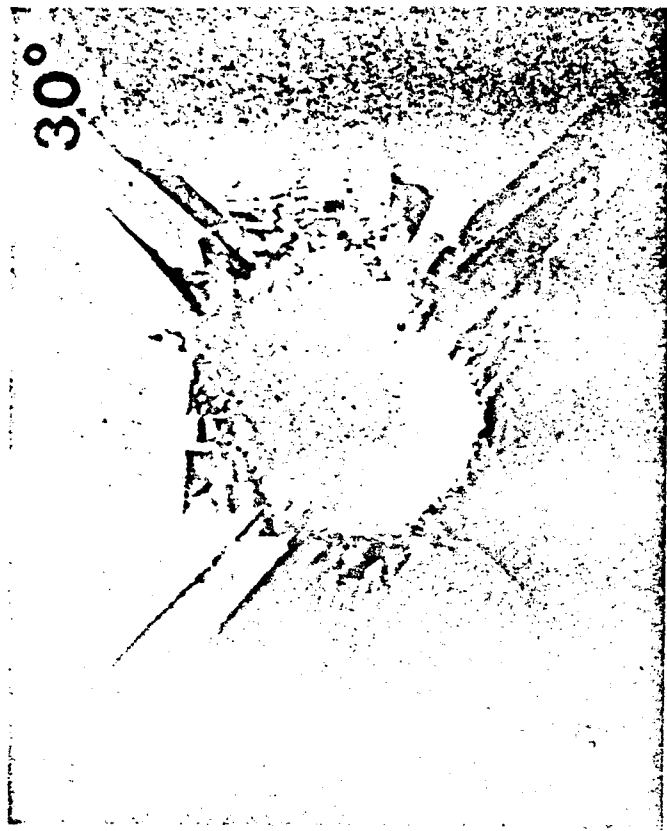
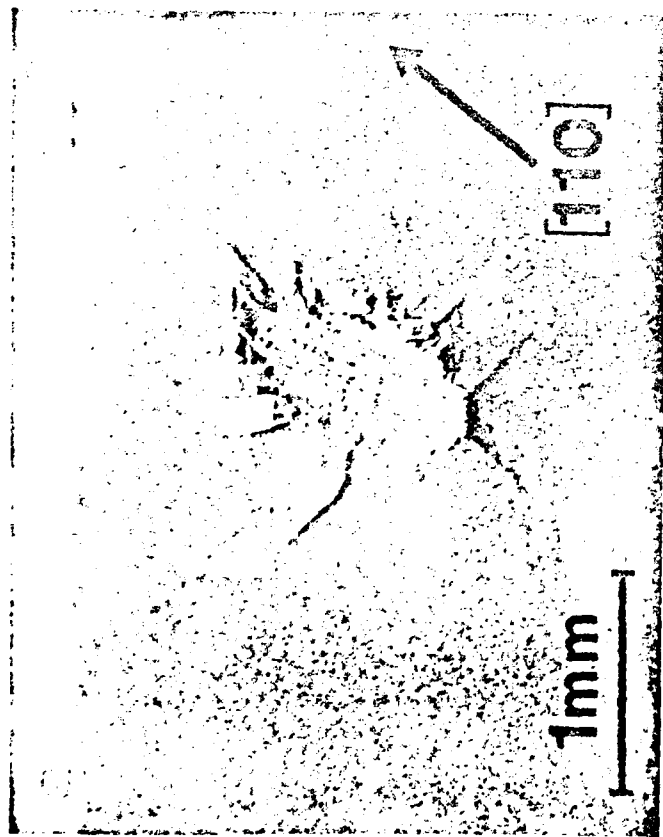


Figure 3 Scanning electron micrographs of craters formed along $[110]$ by 200 m s^{-1} impacts at various angles.

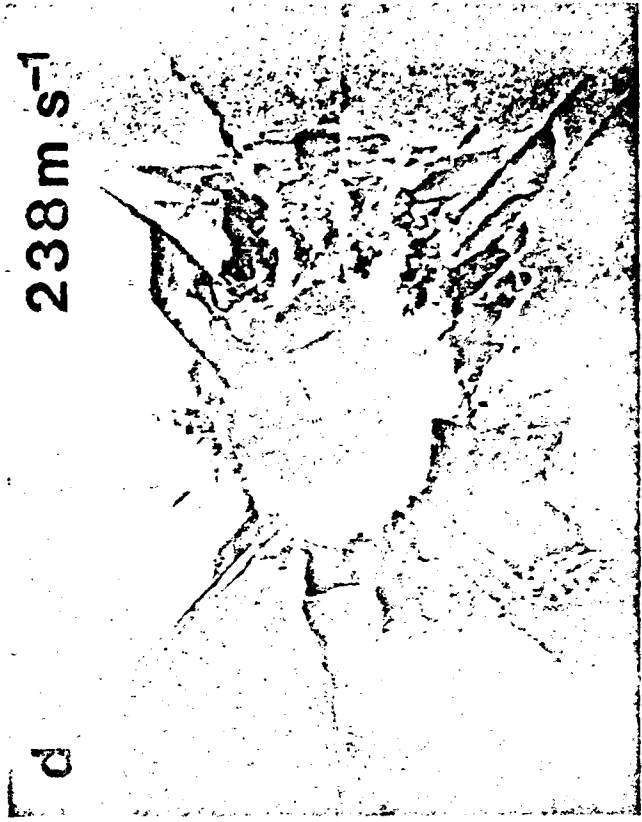
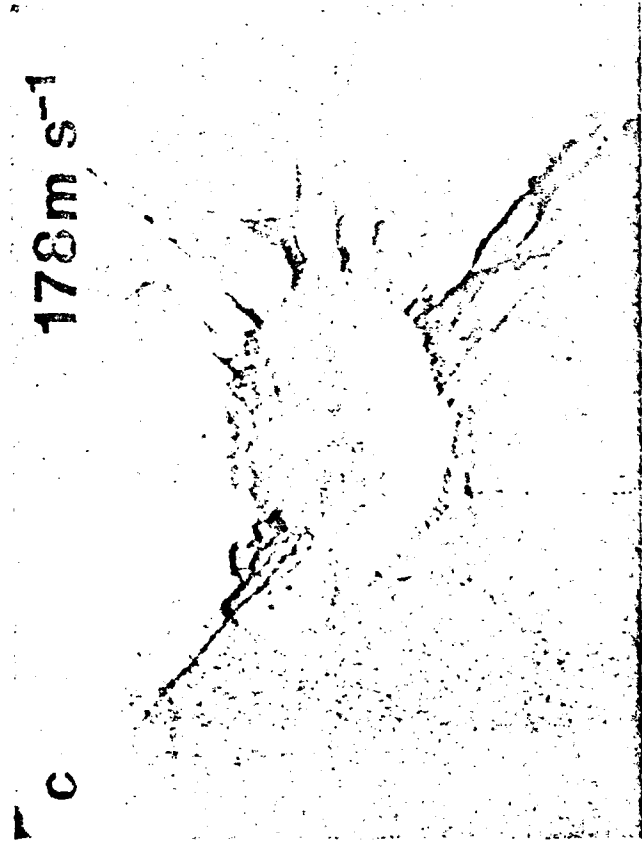
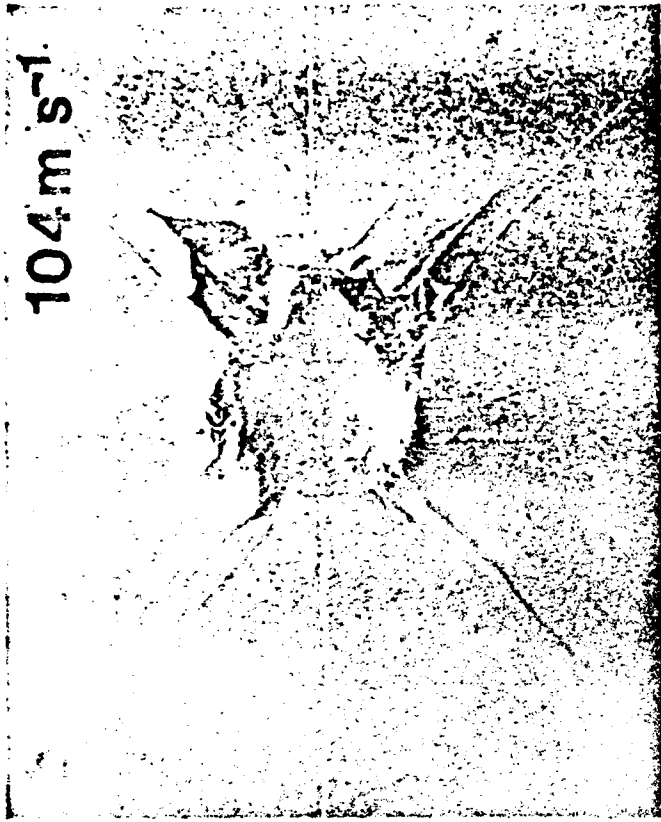
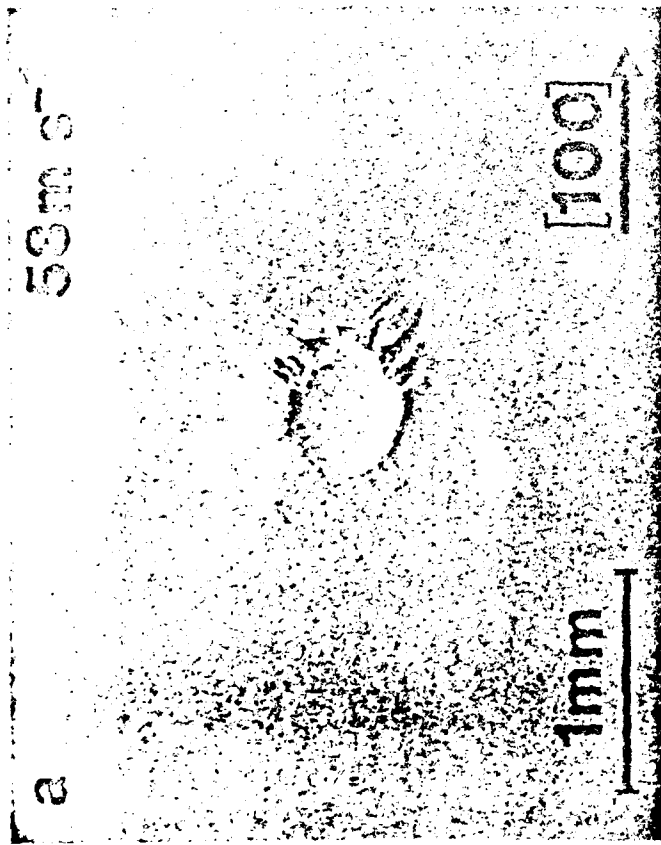


Figure 4 Scanning electron micrographs of craters formed along $\langle 100 \rangle$ by different velocity impacts at 30° to the surface.

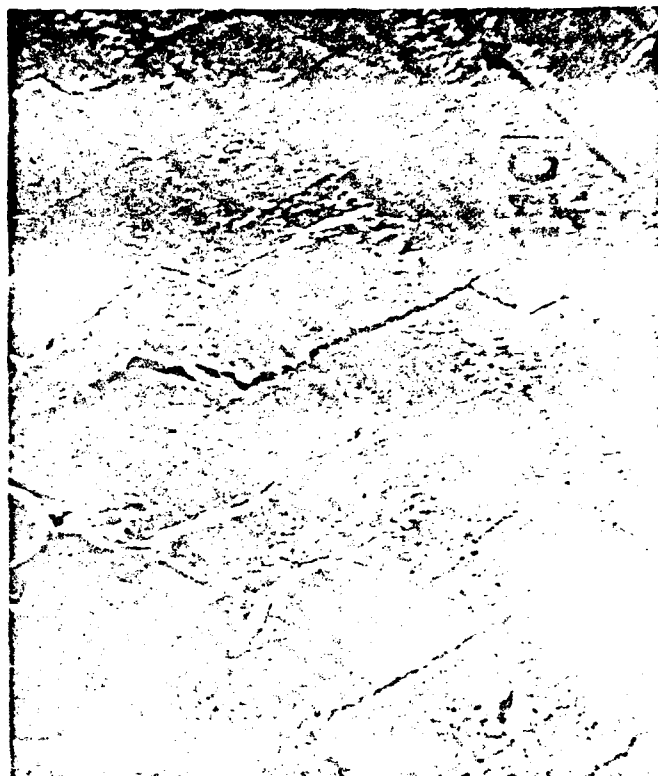
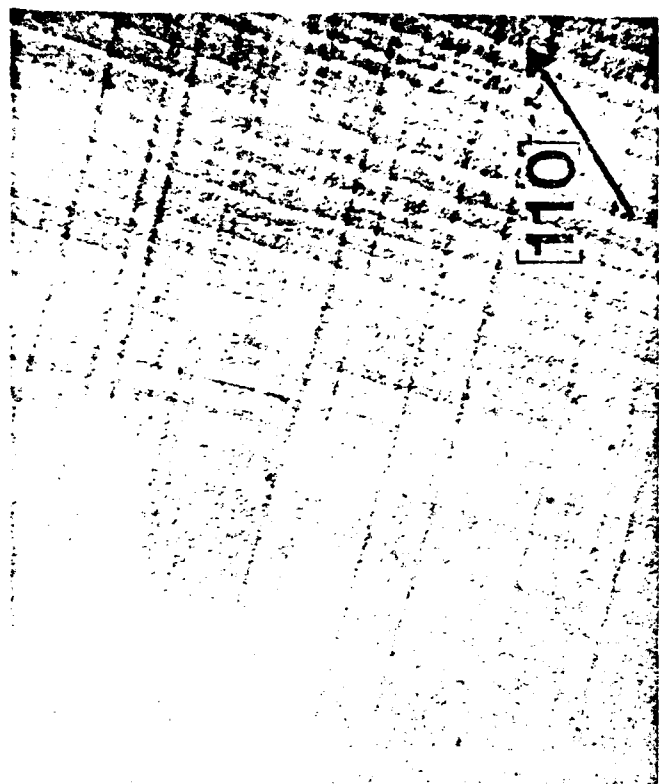


Figure 5 Detailed views of (a and b) slip outside the crater and (c and d) fracture inside produced by 10° impacts at 200 m s^{-1} . The arrows indicate the direction of the component of particle velocity parallel to the

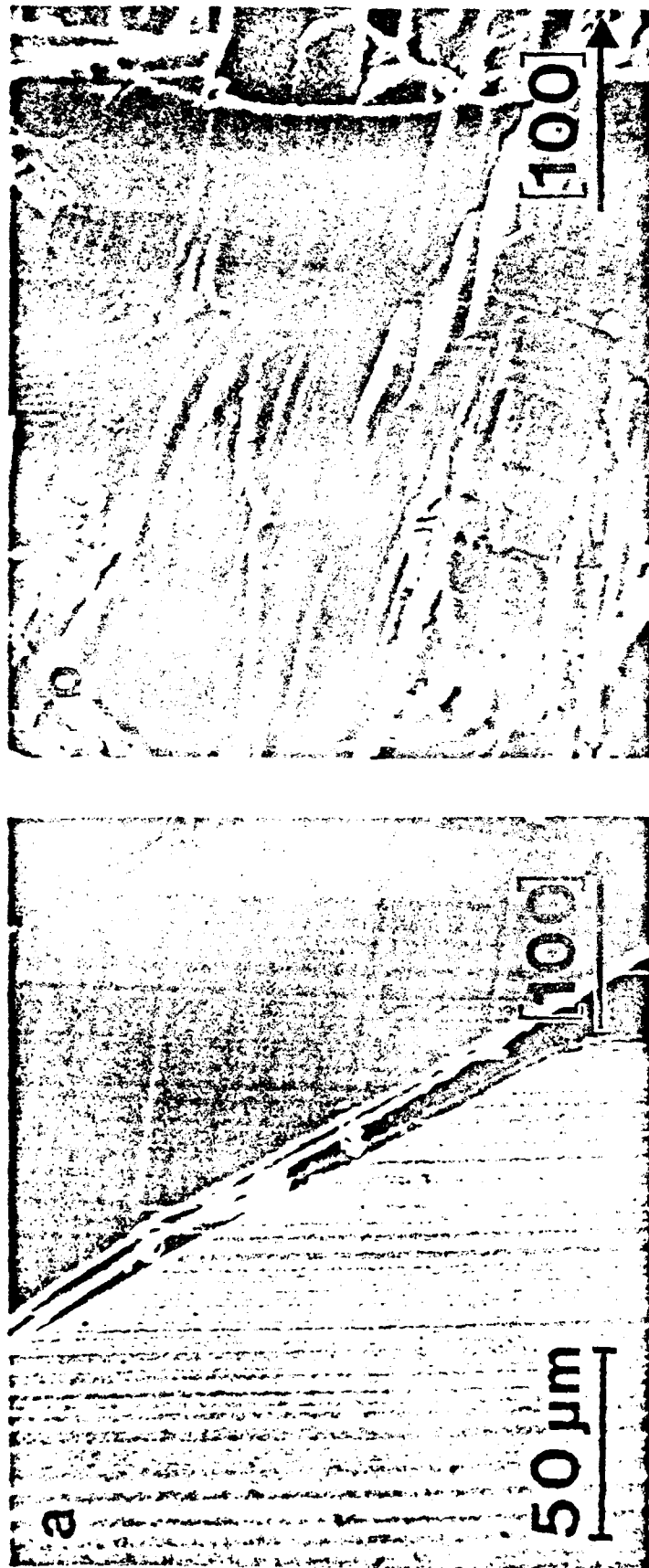
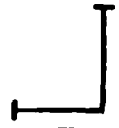



Figure 6 Details of (a) slip outside and (b) fracture in the eroded region around a crater made along $\langle 100 \rangle$ by a 200 m s^{-1} impact at 70° to the surface.

0.1 mm  0.2 mm

$v_0 = 200 \text{ m s}^{-1}$

$[100]$ 

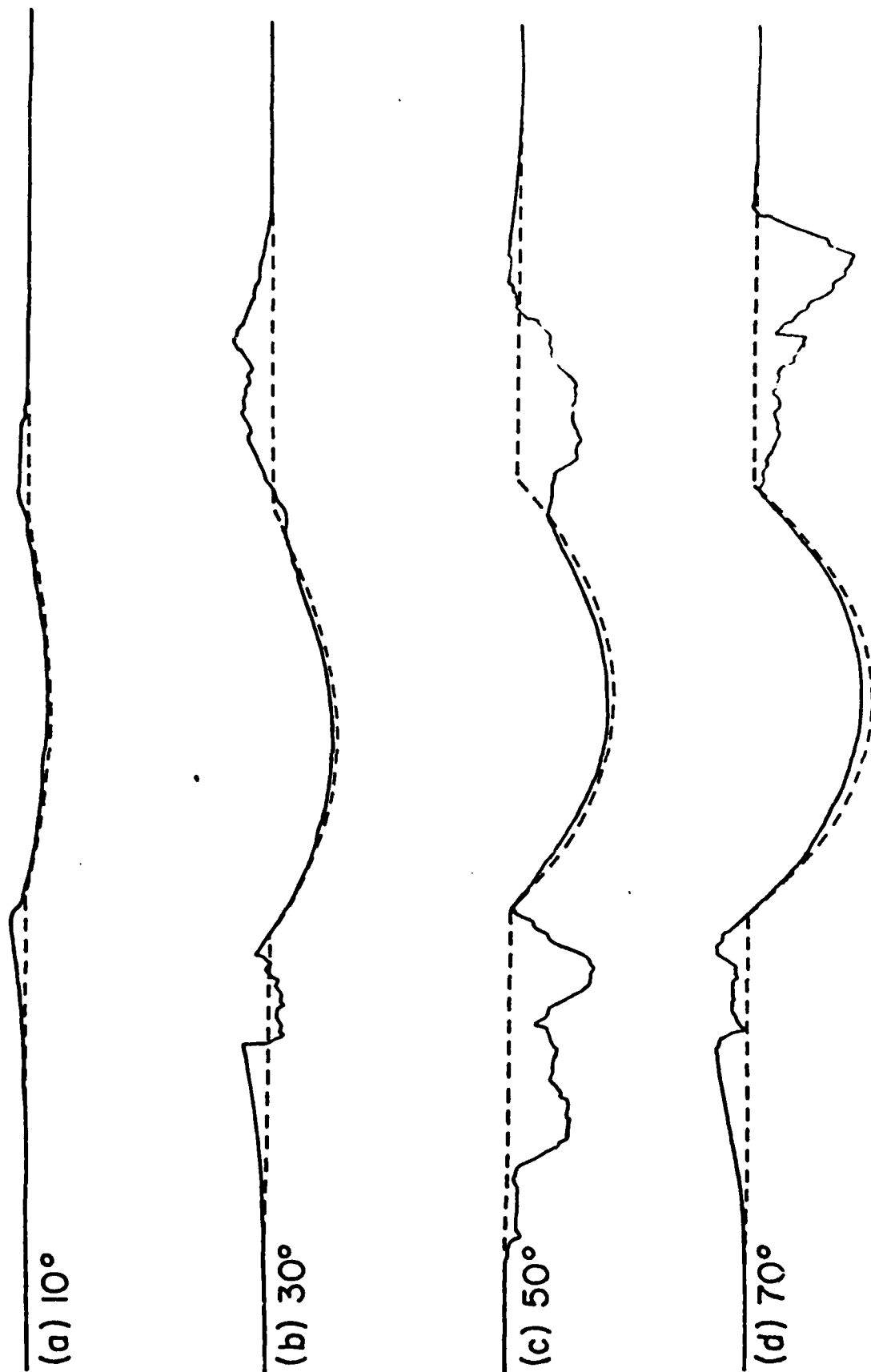


Figure 7 Profilometer traces along the axes of the craters shown in Figure 2.

0.1 mm
0.2 mm

$v_0 = 200 \text{ m s}^{-1}$

$[110]$

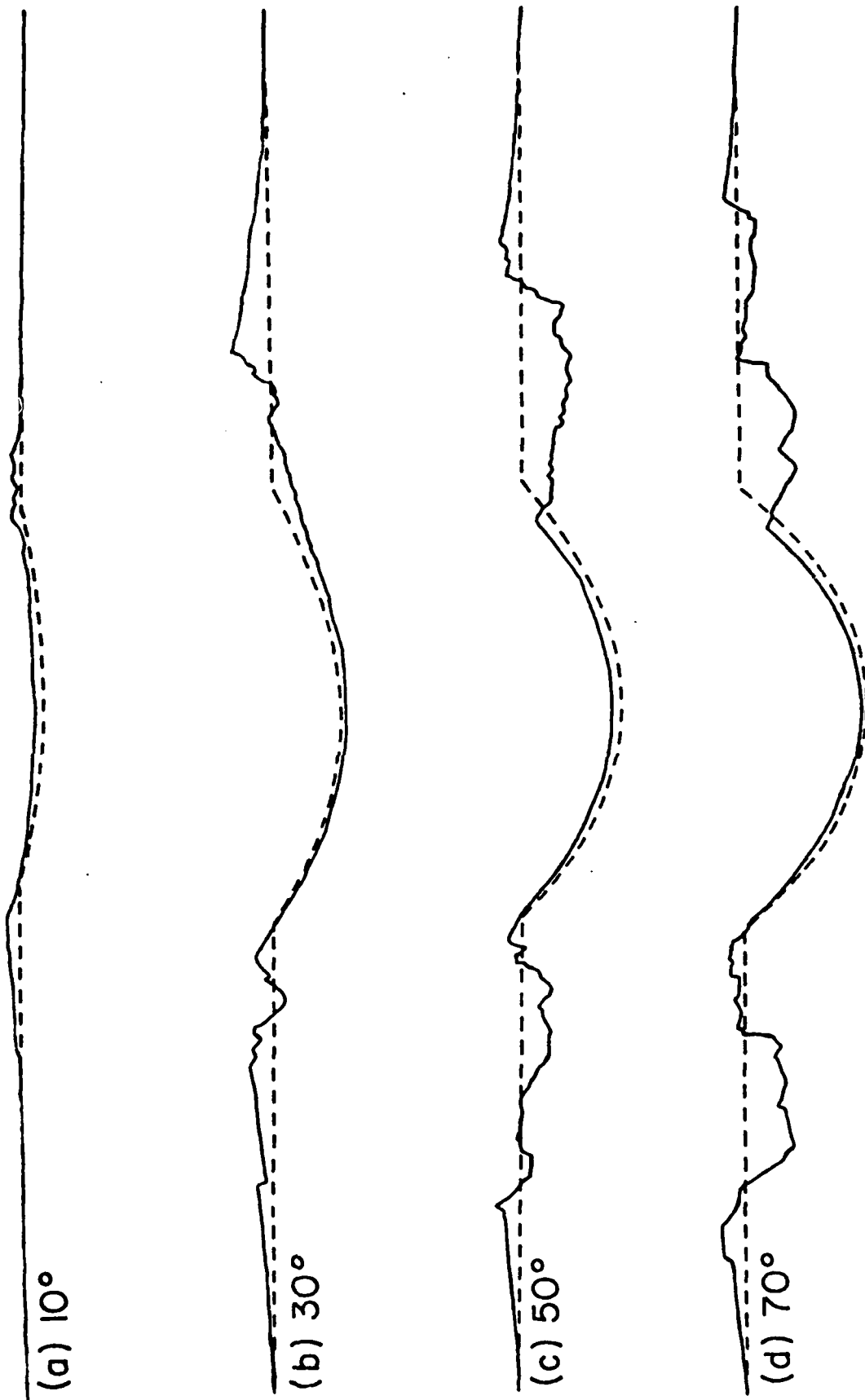



Figure 8 Profilometer traces along the axes of the craters shown in Figure 3.

0.1 mm  0.2 mm

$\alpha_0 = 30^\circ$

$[100]$ 

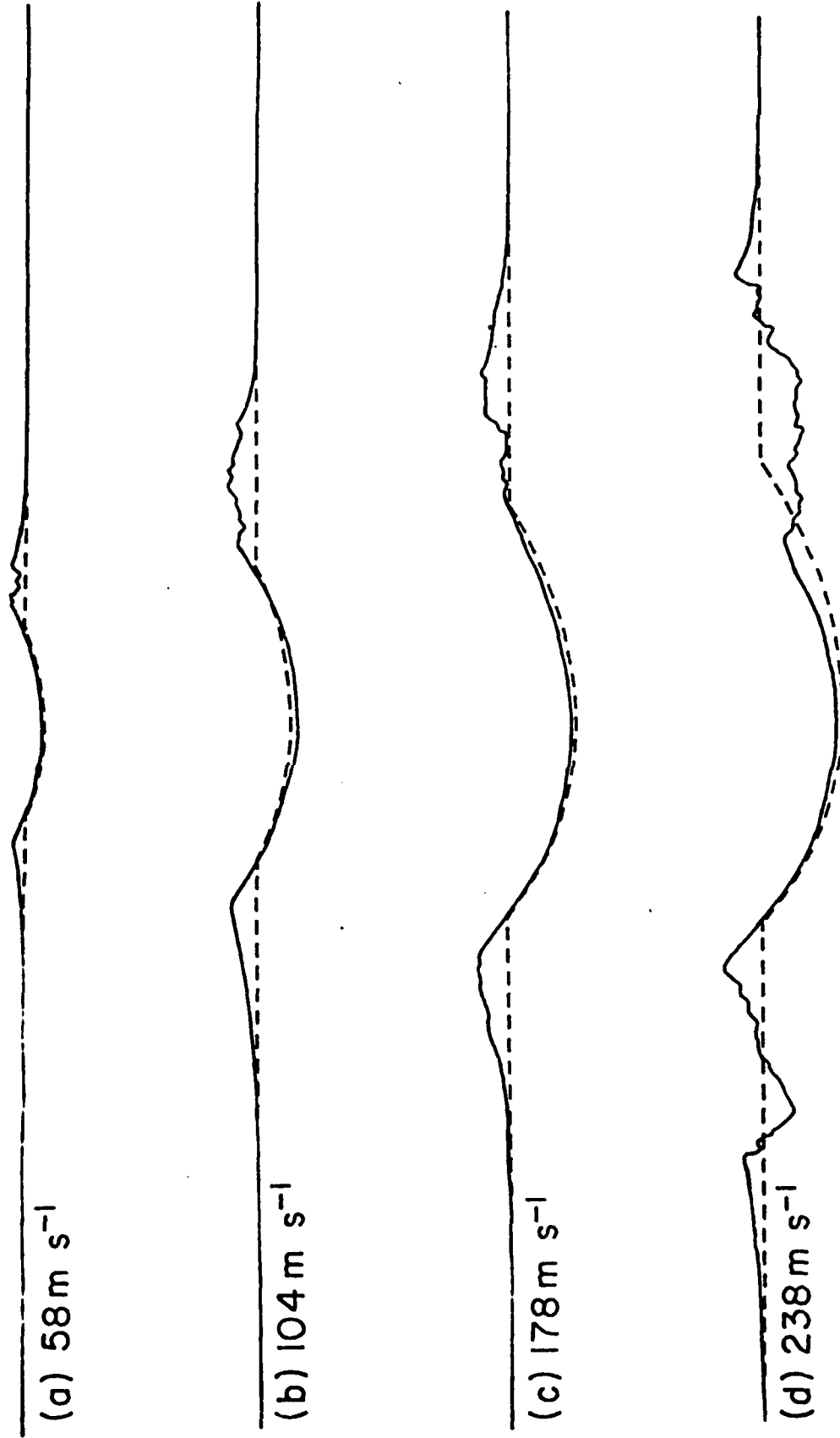


Figure 9 Profilometer traces along the axes of the craters shown in Figure 4.

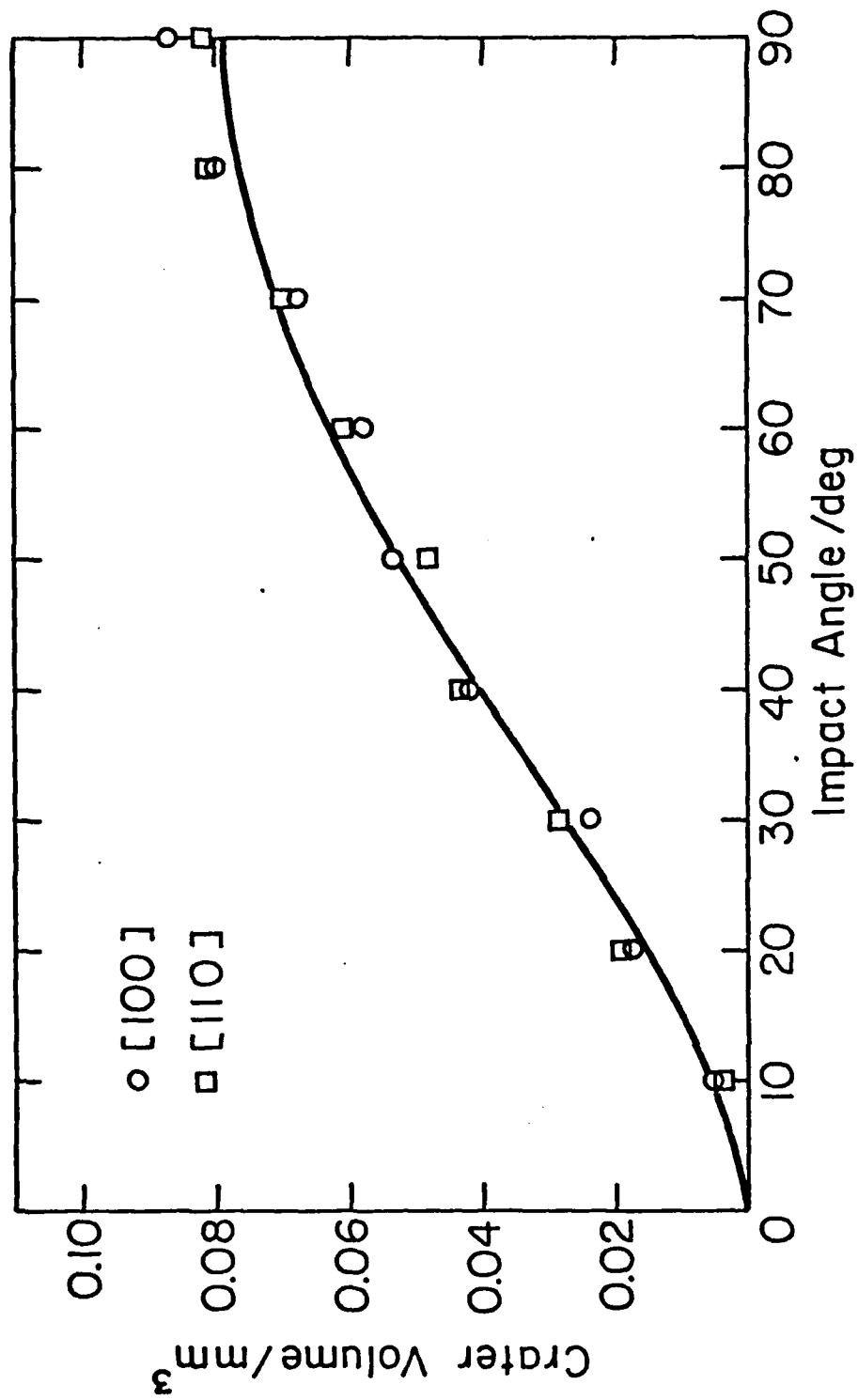


Figure 10 Variation of crater volume with impact angle at an impact velocity of 200 ms^{-1} .

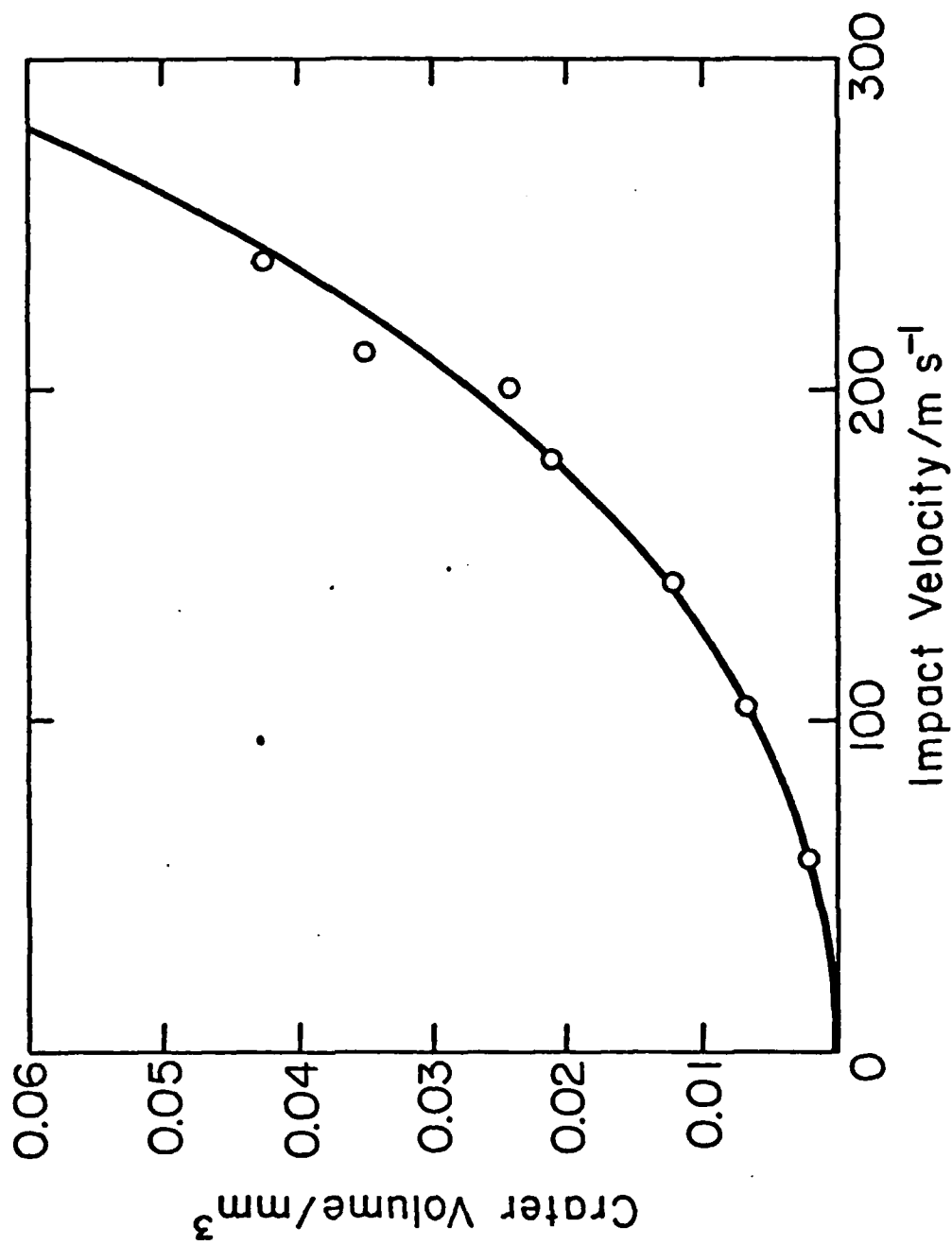


Figure 11 Variation of crater volume with impact velocity at an impact angle of 30°.

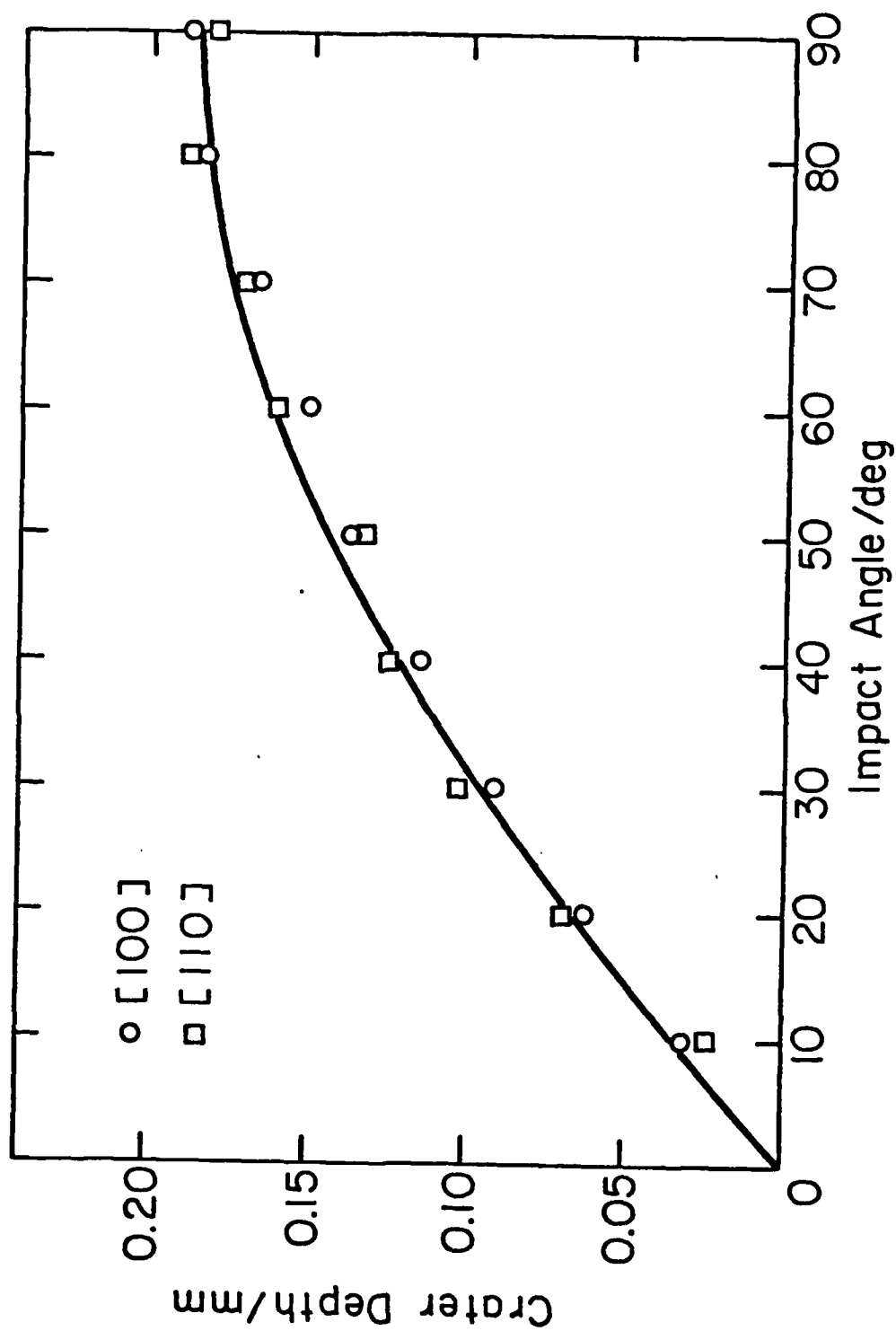


Figure 12 Variation of crater depth with impact angle at an impact velocity of 200 m s^{-1} .

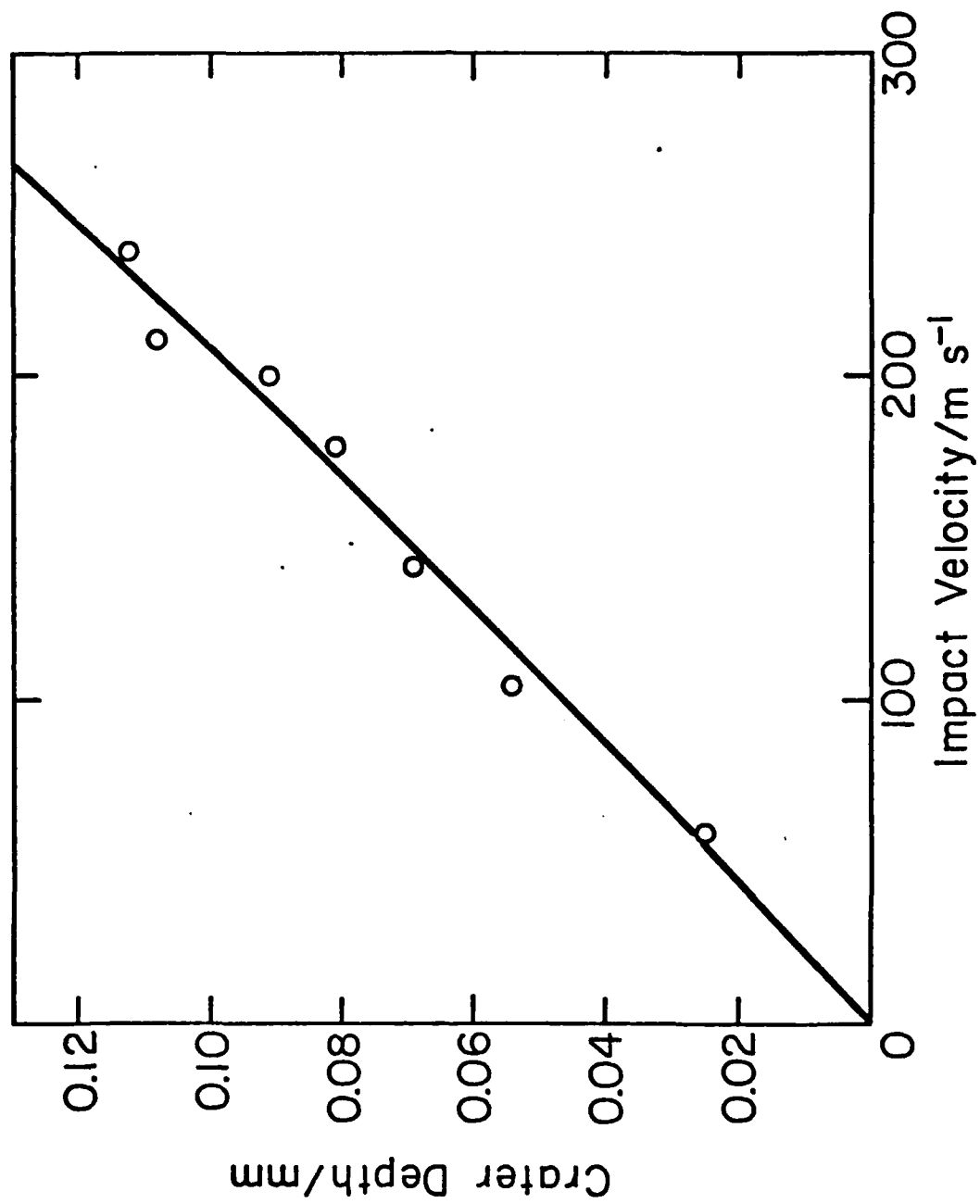


Figure13 Variation of crater depth with impact velocity at an impact angle of 30°.

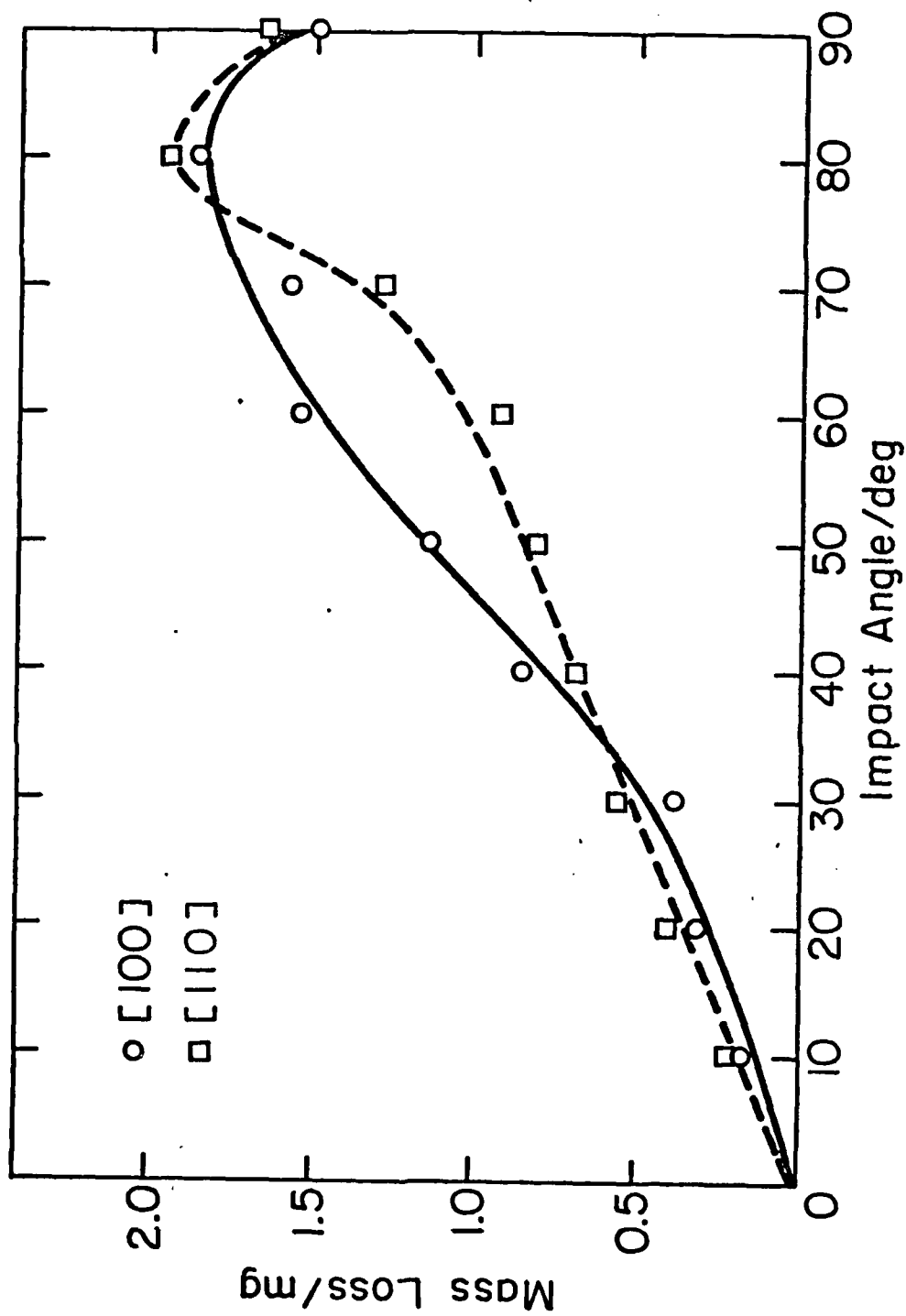


Figure 14 Mass loss as a function of impact angle at an impact velocity of 200 m s^{-1} .

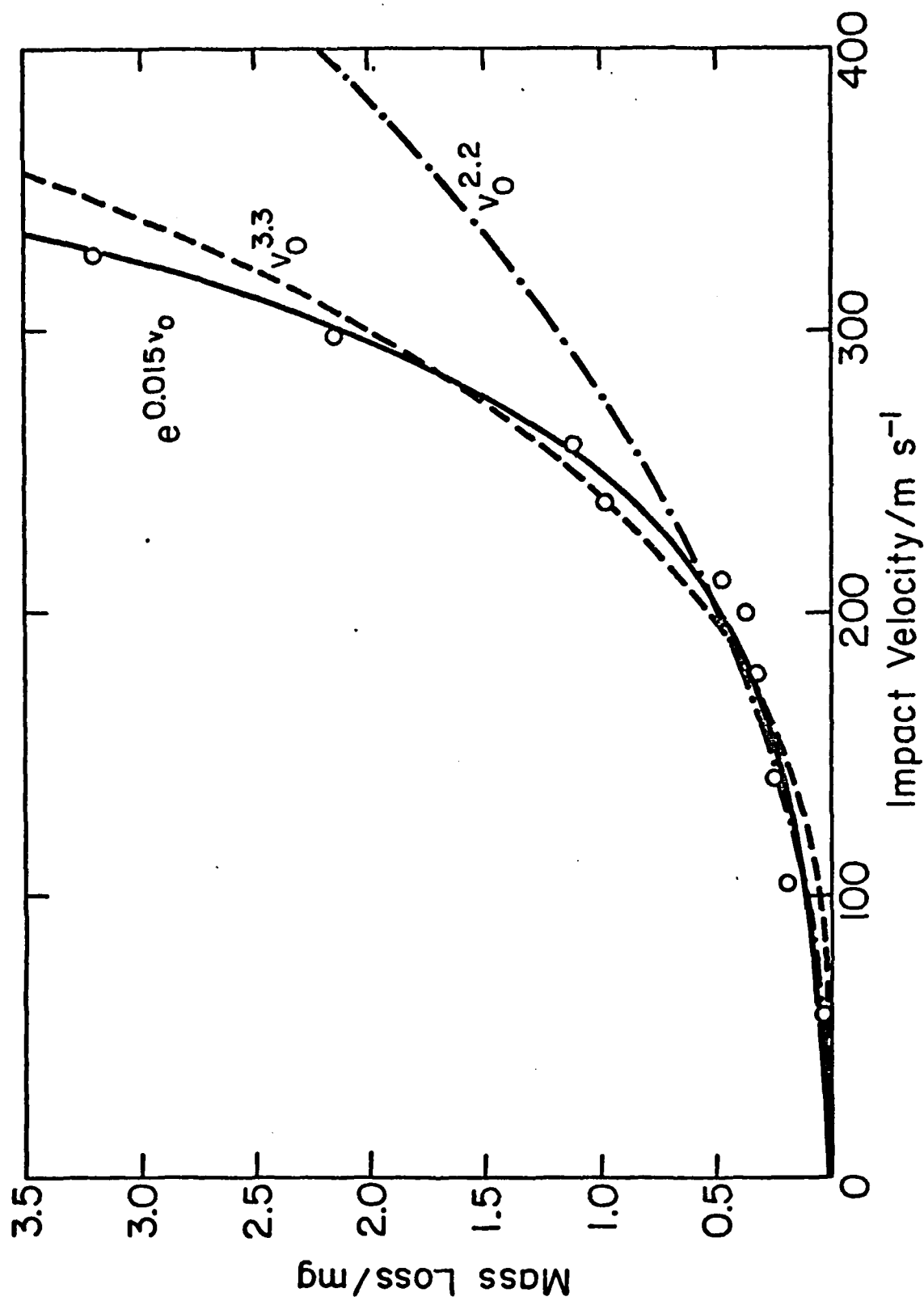


Figure 15 Mass loss as a function of impact velocity at an impact angle of 30°.

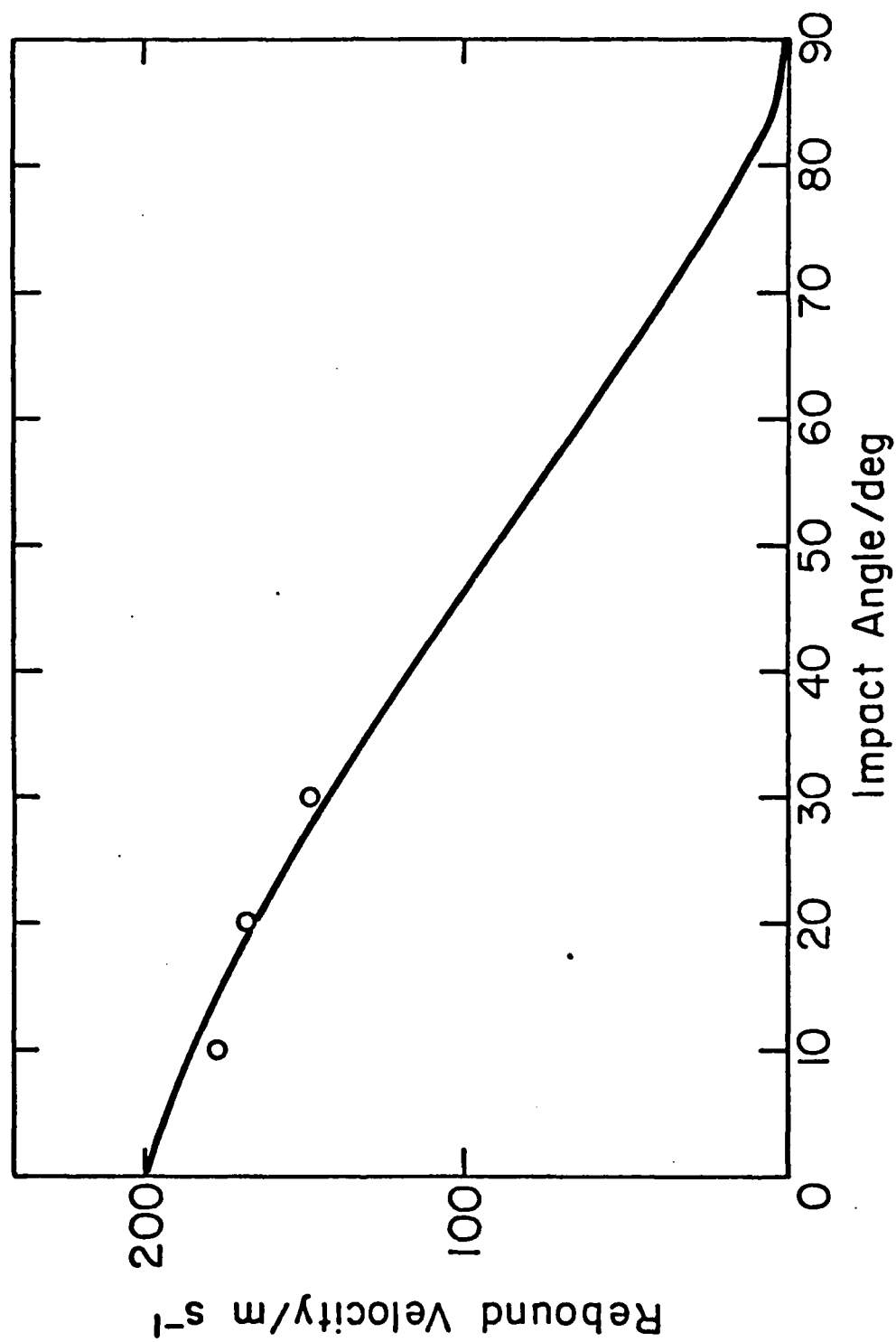


Figure 16 Rebound velocity as a function of impact angle at an impact velocity of 200 m s^{-1} .

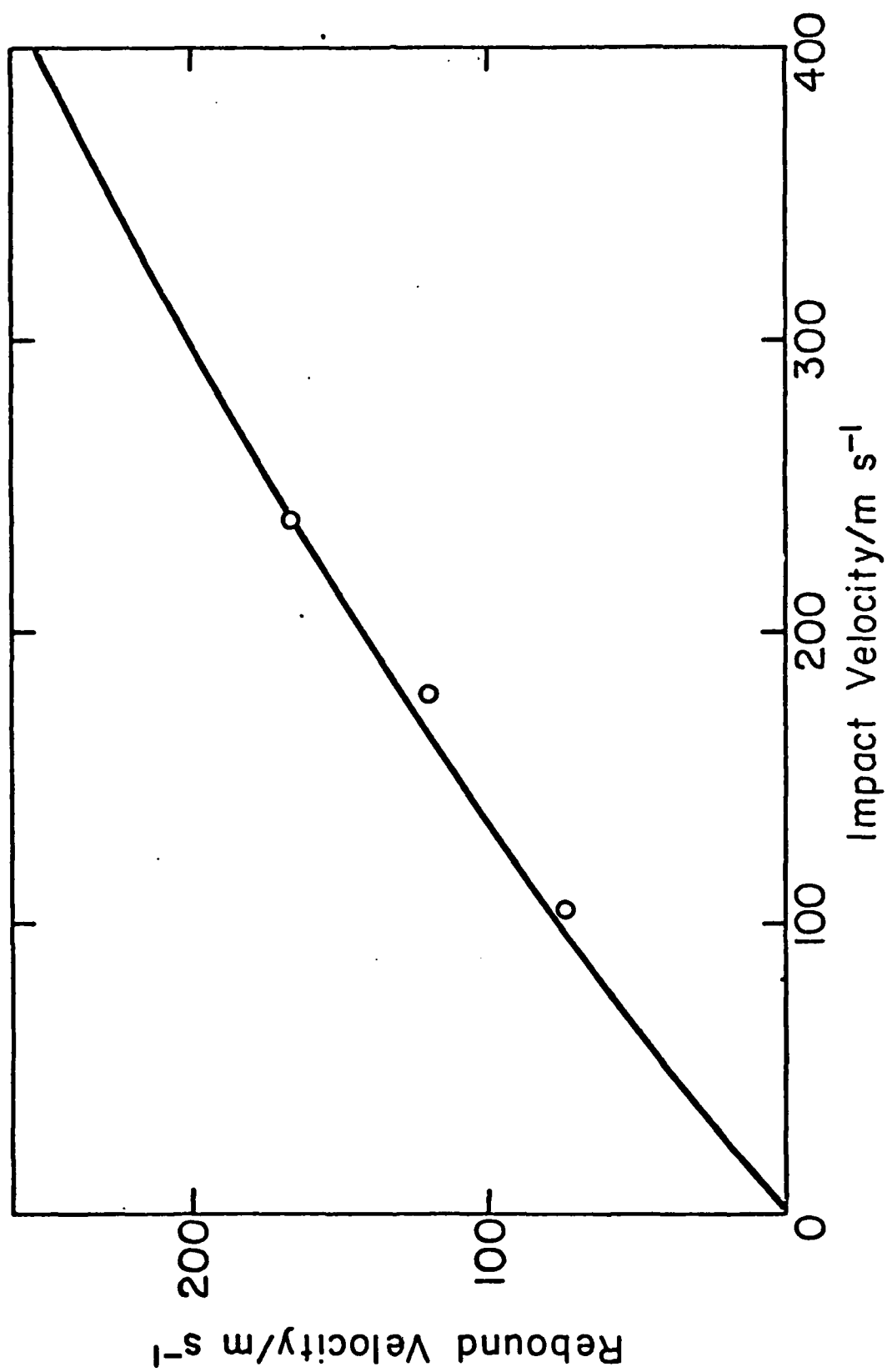


Figure 17 Rebound velocity as a function of impact velocity at an impact angle of 30°.

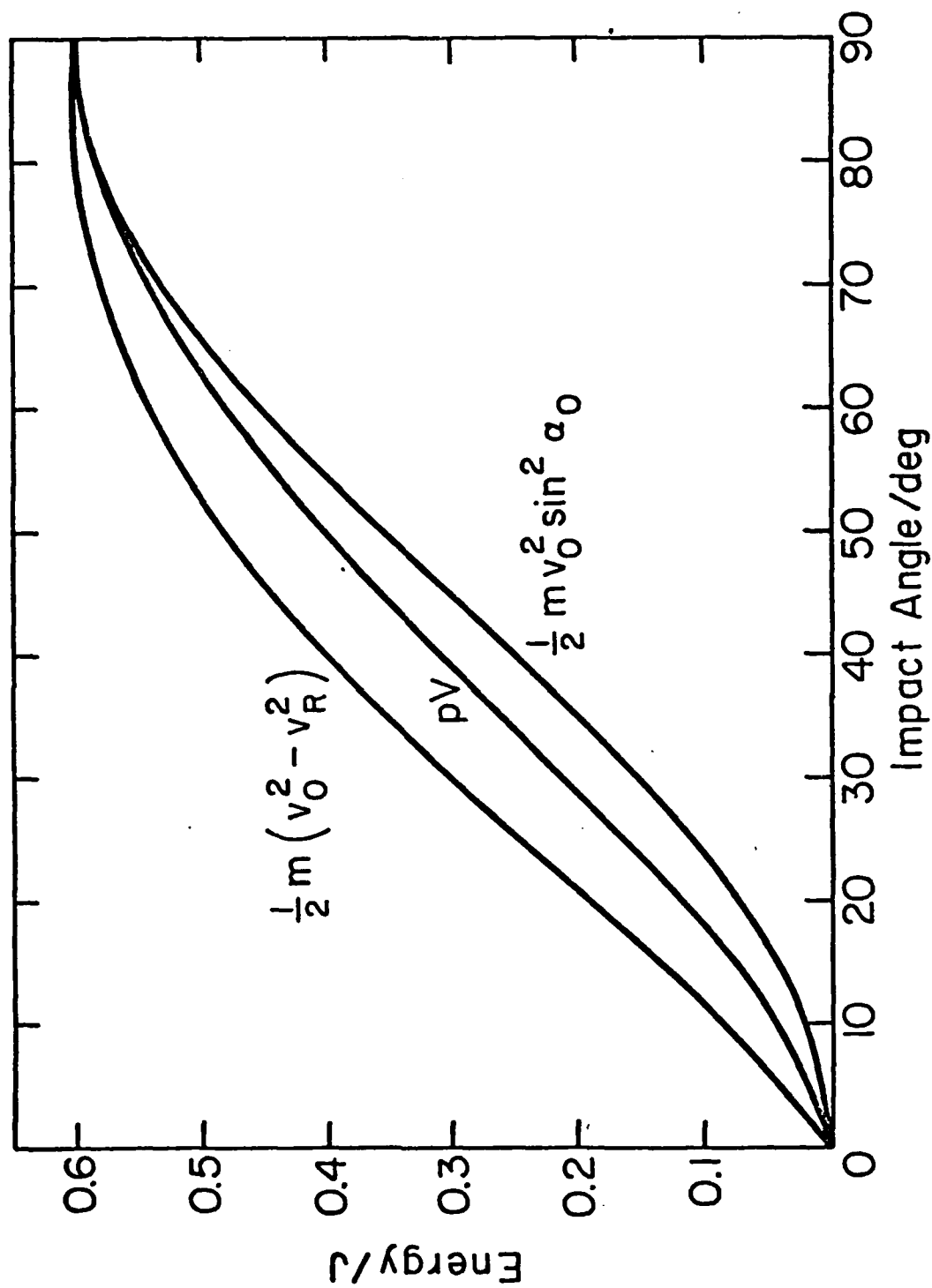


Figure 18 Comparison of different predictions of energy transfer as functions of impact angle at an impact velocity of 200 m s^{-1} .

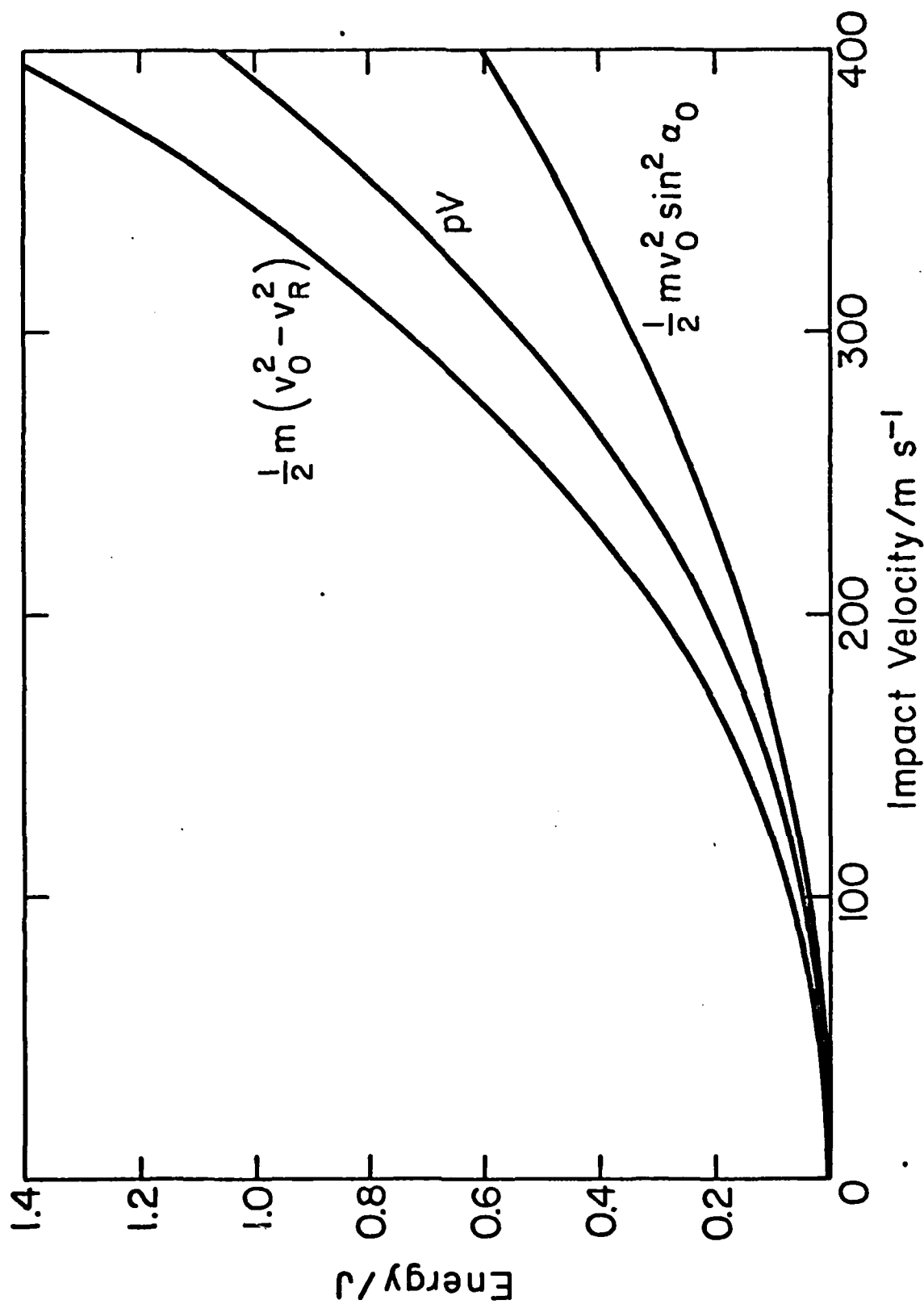


Figure 19 Comparison of different predictions of energy transfer as functions of impact velocity at an impact angle of 30°.

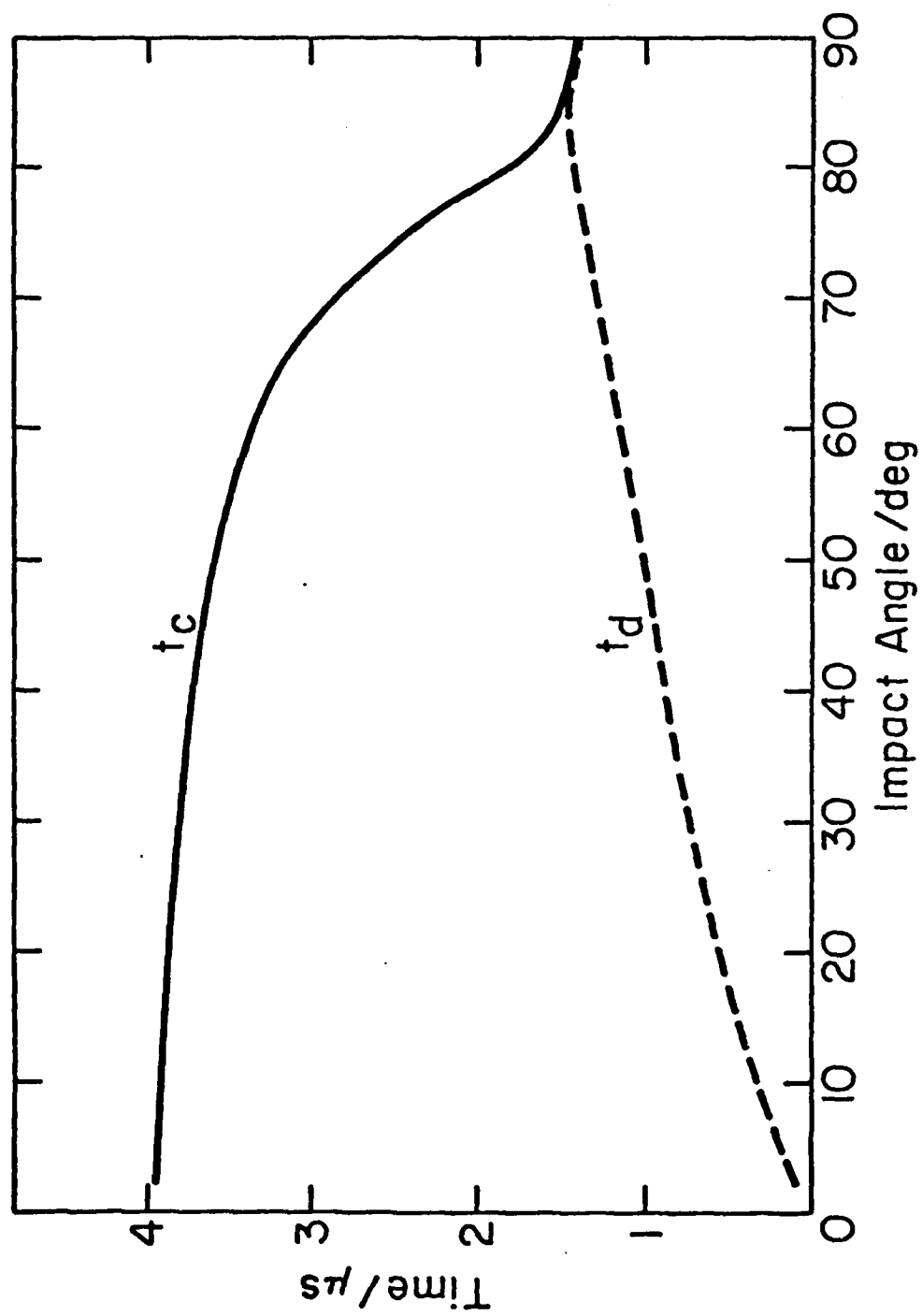


Figure 20 Contact and detachment times as functions of impact angle at an impact velocity of 200 m s^{-1} .

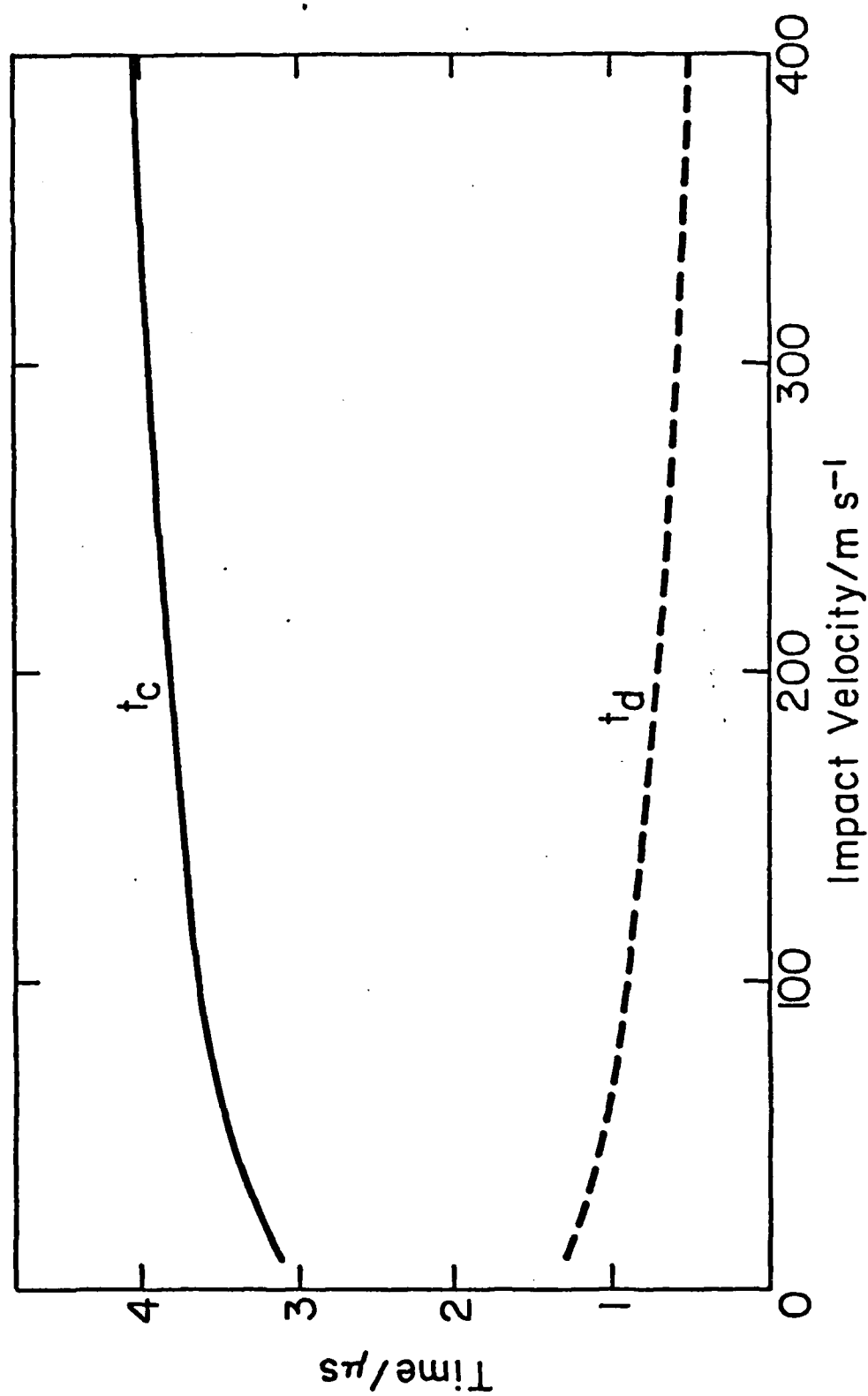


Figure 21 Contact and detachment times as functions of impact velocity at an impact angle of 30°.

Appendix X

The Erosion of MgO by Solid Particle Impingement at Normal Incidence

D. G. Rickerby and N. H. Macmillan
Materials Research Laboratory
The Pennsylvania State University
University Park, PA 16802

SUMMARY

A study has been made of the erosion of almost fully dense, fine-grained MgO by WC-6% Co spheres impinging at normal incidence with velocities between 10 and 90 m s⁻¹. The diameters of the spheres ranged from ~0.35 to 1.58 mm. Scanning electron microscopy revealed the damage to consist of a central crater surrounded by the sort of array of (transgranular) radial and/or median and lateral cracks characteristic of an elastic-plastic impact. However, although the crater had a thin lining of plastically deformed material, it appeared to have been formed primarily by localized transgranular and intergranular fracture processes, suggesting that any mode of irreversible deformation in the contact region will suffice to produce the changeover from Hertzian cracking to radial, median and lateral cracking. The accompanying gravimetric studies showed that mass loss--which occurred primarily by intersection of lateral cracks with radial and/or median cracks--increased threefold during the short incubation period in which the as-received surface evolved into its steady-state eroded condition. During this period the exponent relating erosion to impact velocity decreased monotonically to a value less than that predicted by any of the current theories of erosion in the elastic or elastic-plastic impact regimes. Nor are these theories any more successful at explaining either the observed particle size dependence of the erosion of polycrystalline MgO or the differences in the way in which the static and dynamic hardnesses of monocrystalline and polycrystalline MgO vary with strain rate.

INTRODUCTION

Until recently, understanding of the erosion of ceramics by solid particle impingement (reviewed in Refs. 1 and 2) was based largely on the work of Finnie and co-workers[3-7]. Starting from the assumption that ceramics behave in an ideally brittle manner, these authors combined Hertz's analysis[8] of the stresses arising from static elastic contact between a sphere and a half-space with Weibull's probabilistic treatment[9] of the fracture behavior of a brittle material. The resultant model is only semi-quantitative, but it does provide a satisfactory rationalization of the many different empirical relationships between erosion and particle size or particle velocity that have been reported. It also provides an explanation of the tendency of brittle materials to erode in a manner more characteristic of ductile materials when the erosive particles are small enough[10,11]. An essentially similar model has recently been proposed by Sargent et al.[12].

During the last decade, however, it has become widely recognized that many ceramics exhibit some plasticity in response to "sharp" contact loading, and that this plasticity exerts a significant effect on the nature and extent of the cracking that takes place in and around the region of contact. In particular, plastic flow beneath a hard indenter or impacting particle tends to suppress the formation of Hertzian cone cracks and promote instead or in addition the creation of characteristic arrays of lateral (wing) and/or median (normal or star) and/or radial (Palmquist) and/or conical[†] cracks (vents)* about the plastic zone. The formation of such arrays during static indentation has been studied in materials

[†] These cone cracks are distinguished from the Hertzian cone cracks formed in a purely elastic contact because their different inclination to the specimen surface suggests that plastic deformation was involved in their formation.

* The nomenclature used to describe these cracks is far from settled.

as diverse as hardened steel[13], WC-Co cermets[14-17], polymethylmethacrylate[18-20], solid high explosives[21], Ge[22,23], Si[23,24], SiC[23, 25-27], Al_2O_3 [23,26,28-30], LiF[31], NaCl[23,30], ZnS[30], ZnSe[30], quartz[24], a spinel[30], Si_3N_4 [30], various rocks[32,33], fused SiO_2 [24] and a wide variety of silicate glasses[24,30,34-44]. In addition, numerous attempts have been made to understand the deformation processes involved in the nucleation of these cracks[23,38,42,45,46], the (fracture) mechanics of their propagation[17,19,20, 35,47-57], and their role in material removal processes[58-64] and strength degradation[65-78]. Useful reviews are given by Lawn et al.[34,79,80] Essentially similar arrays of cracks have also been produced in silicate glasses[81-95], various minerals[91], LiF[96-101], NaCl[97], MgO[96,98,100-104], ZnS[95,104,105], MgF_2 [104,106], Si_3N_4 [104,106], Al_2O_3 [106], $MgAl_2O_4$ [104], ZrO_2 [95, 107] and WC-Co cermets[104] by the impact (usually at normal incidence) of solid particles at velocities in the range $\sim 10^2$ - 10^3 m s⁻¹. Moreover, just as in the case of static indentation, there have been a variety of attempts[29,95,104, 105,108,109] to use fracture mechanics to explain the propagation of these cracks and their role in material removal processes, and also to predict the strength degradation resulting from their propagation[110-117]. In addition, a few studies[118-120] have been made of the flow processes occurring immediately below the impacting particle.

Two conclusions relevant to the erosion of ceramics by solid particle impact have emerged from this plethora of single contact studies. One is that the primary determinants of such erosion under fixed erosive conditions (i.e., when the size, density, shape, material, velocity and direction of approach of the impacting particle are held constant) are (a) the dynamic hardness and (b) the dynamic fracture toughness of the target. Essentially, the former determines the target resistance to the plastic flow processes necessary to nucleate cracks in and around the region of contact and the latter the extent of propagation

of whatever cracks are nucleated. The other conclusion is that the removal of material from pristine surfaces results primarily from the nucleation and growth of lateral cracks rather than the deeper-penetrating median and/or cone cracks. On heavily eroded surfaces, however, material removal must be a more complex process that is also influenced by interactions between cracks formed at adjacent impact sites. This is one reason why it is difficult to predict the rates at which ceramic materials will erode from the results of single impact studies. And when irregular erosive particles are employed, a second reason is that mass loss per impact can vary one thousand-fold from one impact to another, depending on particle shape and orientation at impact[121].

Consequently, the few attempts[30,104,108,109,122] that have been made to predict erosion rates from single particle elastic-plastic impact damage mechanics have mostly been dimensional analyses designed to rationalize the (intuitively obvious) experimental observation that, in the elastic-plastic contact regime, erosion decreases with increasing target hardness and fracture toughness. It should also be recognized that the hardness and fracture toughness values used to test the predictions of these analyses were for the most part obtained from room temperature tests performed on macroscopic specimens under static or near-static conditions. The individual impact events that cause erosion, however, typically involve deformation processes that are driven by transient applied loads and occur in microseconds over distances more likely to be measured in microns than millimeters; and it is not clear by how much hardness and fracture toughness are affected by the high strain rates, the adiabatic heating and the large compressive stresses characteristic of such events. Nor is it clear in ceramics of complex microstructure just how hardness and fracture toughness will vary from one randomly selected impact site to another.

At its present level of sophistication, therefore, mathematical modelling of the erosion of ceramics by solid particle impact has little or nothing to

say about such topics as the inception and evolution of mass loss from pristine surfaces, the variation of mass loss with impact angle, the relation between mass loss and microstructure, and the conditions under which melting could occur in the contact region. Nor are the currently available experimental data entirely unequivocal about these questions. For example, the existence of "incubation" phenomena in the early stages of the erosion of pristine surfaces has been observed in SiC[123], but not in MgF₂[121]. (Incubation effects occur also in borosilicate glass under elastic impact conditions[124], and a theory has been proposed to explain them[125,126]). Likewise, increasing the erosive particle size from smaller than to larger than some characteristic microstructural dimension has been reported to change the appearance of the eroded surface of SiC without altering the slope of the plot of erosion versus particle size[123], but to produce quite different variations of mass loss with impact angle in different refractory concretes[127]. Significant, but as yet unexplained, effects of microstructure are also apparent in the different dependencies of mass loss on particle size and impact velocity observed in hot-pressed and reaction-bonded Si₃N₄, glass-bonded Al₂O₃ and hot-pressed MgF₂[106]. And indirect evidence for the occurrence of melting during impact continues to accumulate from studies on alumina and mullite refractories[128], Al₂O₃ and silicate glasses[129], and metallic glasses[130].

In the absence of the necessary dynamic hardness and dynamic fracture toughness data, mathematical modelling of impact also fails to predict whether erosion should increase or decrease with increase in temperature--though it does suggest that this question should be resolved by a trade-off between the opposing effects of a weak dependence of mass loss on dynamic hardness, which is expected to decrease markedly with increasing temperature, and a stronger dependence on dynamic fracture toughness, which latter probably increases but slowly with increasing temperature[122]. It is therefore not surprising to find that raising

the temperature from 25 to 1000°C increases the erosion of hot-pressed Al_2O_3 and Si_3N_4 [131], sintered Al_2O_3 [131] and calcium aluminate-bonded Al_2O_3 [132] at shallow impact angles (where plastic flow plays its most important role in the material removal process [131]), but has no significant effect at normal incidence.

The present work attempts to answer some of the questions raised in the preceding paragraphs by studying erosion in the elastic-plastic impact regime under the simplest possible conditions--normal impact of identical, rigid, spherical particles against a fine-grained, almost fully dense, single-phase ceramic at room temperature. Under such conditions the individual impact event is sufficiently reproducible that it is possible to resolve the incubation phenomena associated with the early stages of erosion. Also, the equation of motion of the impacting particle can be solved analytically to obtain the dynamic hardness from the dimensions of the impact crater. An additional simplification was the use throughout the work of erosive particles large enough to ensure that the impact crater was always very much larger than the grain size.

EXPERIMENTAL METHODS AND MATERIALS

The erosion experiments were carried out using a rotating arm apparatus that has been described in a previous paper [133]. Essentially, this apparatus consists of a steel tank which can be evacuated to ~1 torr and houses a counter-balanced, tubular, Al alloy arm that is rotated through a free-falling screen of erosive particles by an externally-mounted, variable-speed electric motor. The specimens consisted of 6 mm thick, 16.5 mm diameter discs of MgO , the edges of which were protected by an annular Al alloy cover containing a central aperture 12.5 mm in diameter. Each disc was cemented to the end of a 12.5 mm diameter, 9 mm long cylinder of Al alloy, which in turn fitted into a recess in the end of the rotor arm.

Because this specimen configuration differed slightly from that used previously[133], it was necessary to recalibrate the apparatus to determine the ratio of the number of impacts N_i against the MgO specimen to the number of particles N_p introduced. Since impacts could not occur at the periphery of the exposed area due to the ~ 2 mm high raised rim of the cover, the effective specimen radius was taken to be $(R-r)$, where R is the radius of the aperture and r the radius of the particles. Then, if A and f are the radius of the cross-section and the frequency of rotation of the arm, respectively, and u and $2R$ are the vertical velocity and the width of the stream of falling particles, respectively, it can be shown that

$$\frac{N_i}{N_p} = \frac{\pi f (R-r)^2}{2Ru} \quad (1)$$

if $f \leq u/2(A-R)$, and that

$$\frac{N_i}{N_p} = \frac{f (R-r)^2 (\pi - \theta + \frac{1}{2} \sin 2\theta)}{2Ru} \quad (2)$$

if $f \geq u/2(A-R)$, where $\theta = \cos^{-1} \left[\frac{(u/f) - 2(A-R)}{2(R-r)} \right]$.

Figure 1 shows the values of N_i/N_p determined experimentally using 1.58 mm diameter WC-6% Co spheres falling with a (photographically determined) average velocity of $\sim 3 \text{ m s}^{-1}$. The line drawn through these data points represents the theoretical prediction of equations (1) and (2) multiplied by an empirical correction factor of 0.82 to allow for those particles which fell outside the idealized parallel-sided stream.

The MgO specimens used in this study were all cut from the same 6 mm thick sheet of hot-pressed polycrystalline material*. This had a translucent appearance, a grain size of $\sim 10 \mu\text{m}$, a density of $\sim 99.5\%$ of that of an MgO monocrystal, and the impurity content listed in Table 1. All measurements were made on the as-received surface.

* Kindly supplied by Dr. T. Vasilos of Avco Corp., Waltham, Mass.

Table 1 Results of an Emission Spectrographic Analysis
of the Impurity Content of the Target Material.

Element	Concentration (ppm)
Si	500
Al	100
Fe	300
Mn	10
Ca	200
Ag	5
Cu	2

Not detected: B, Cr, Ni, Ti, Be, Na, Mo, Zr, Co, Zn, Sn, Ge, In, Bi, Ga, Pb,
Sb, Y, Yb, Ba, Sr, La

Each specimen was eroded incrementally at some fixed impact velocity in the range 10 to 90 m s⁻¹, and was weighed with a precision of ± 10 μ g after each such increment. Also, since the specimens were all eroded at normal incidence, they could be rotated through 90° about the impact direction each time they were replaced in the apparatus in an attempt to cancel out the effects of the slight horizontal velocity and vertical particle concentration gradients existing across the surface being eroded. The erosive particles were all WC-6% Co spheres having a density of 1.5×10^4 kg m⁻³ and a Vickers hardness number of ~ 2000 kg mm⁻². Those used in the majority of the experiments had a diameter of 1.58 ± 0.03 mm and weighed 30 ± 1 mg. However, in order to investigate the effect of particle size, a few experiments were also performed with spheres having diameters of 1.14 ± 0.02 mm and 0.35 ± 0.10 mm, and weighing 11.5 ± 0.5 mg and 0.10 to 0.60 mg, respectively. None of these spheres deformed plastically upon impact with the target, and only in rare cases did they fracture. Nor did they exhibit any tendency to embed themselves in the target surface.

THEORETICAL CONSIDERATIONS

Provided that the elastic contribution to the total deformation is small, the impingement at normal incidence of a hard (non-yielding) sphere against a plastically deformable target that exhibits little work hardening may conveniently be described by assuming that the pressure over the area of contact is uniform and has a constant value p (the dynamic hardness)[134,135]. Solving the resultant equation of motion yields[102]

$$pV = \frac{1}{2} mv_0^2, \quad (3)$$

where V is the crater volume, m the mass of the sphere and v_0 the impact velocity. A value of p can thus be found by measuring the crater diameter d and calculating its volume as that of a spherical cap having the same radius r as the sphere.

An approximate allowance for the effect of work hardening can be incorporated into the model if it is assumed that Meyer's Law[136-8] applies under dynamic as well as static conditions--i.e., that

$$p = k d^{n-2}, \quad (4)$$

where k and n (the Meyer index) are constants. Solution of the corresponding equation of motion yields

$$p \approx \left(\frac{n+2}{4} \right) \frac{mv_0^2}{2V} \quad (5)$$

at the end of the impact[134]. This expression is similar in form to equation (3), which therefore can be applied even when work hardening occurs provided that it is remembered that the value of the terminal dynamic hardness obtained thereby is underestimated by a factor $(n+2)/4$.

RESULTS

Figure 2 shows the damage produced by single, normal impacts of the 1.58 mm diameter spheres against as-received target surfaces. The crater produced at the lowest impact velocity (20 m s^{-1} , Figure 2(a)) has a relatively smooth interior and, although it is surrounded by a few short radial or median cracks, exhibits little evidence of material removal, except perhaps from its rim. As the impact velocity increases, however, material first spalls away from the interior surface of the crater in small quantities, Figure 2(b), and then flakes off in larger quantities from the region surrounding the crater as a result of the intersection of radial or median cracks with (subsurface) lateral cracks, Figures 2(c) and (d).

Due to this loss of material from the periphery of the crater at higher impact velocities, accurate dynamic hardness values could only be obtained for velocities $\leq 25 \text{ m s}^{-1}$. These data are shown in Figure 3, together with static Meyer hardness* values obtained by pressing one of the 1.58 mm diameter WC-6% Co spheres into the as-received surface at loads ranging from ~ 50 to 600 N. The very similar Meyer indices in the two cases (static, 2.57; dynamic, 2.59) suggest that the work hardening behavior of the target is little affected by strain rate.

Typical areas of the surfaces of specimens that have been eroded until the average amount of material removed per impact reached a constant value are shown in Figure 4. In comparison with the single impact damage, the change in appearance with impact velocity is less striking. In every case the eroded surface has an uneven topography made up of remnants of semi-obliterated impact craters, fracture surfaces created by lateral cracking, and radial and/or median fractures. The

* The Meyer hardness is defined as the load divided by the area obtained by projecting the actual area of contact onto the original, undeformed surface.

scale of each of these features increases with increasing impact velocity, but the major mechanism of material removal appears in all cases to be the detachment from the exposed target surface of more-or-less petal-shaped flakes formed by intersection of lateral cracks with radial and/or median cracks.

Details of individual impact sites on heavily eroded surfaces are shown in Figure 5. In Figure 5(a) a magnified view of the crater seen at lower center in Figure 4(a) reveals that about half of the original, spherical cap-shaped impression remains standing proud of the fracture surfaces exposed by the lateral cracks nucleated beneath it. And the still higher magnification micrograph presented in Figure 5(b) shows that the smooth interior of this crater consists of a thin layer of extremely heavily plastically deformed grains of MgO. The interesting features are that (i) this layer is only one or two grain diameters thick and (ii) the underlying material exposed at its edge exhibits both transgranular and intergranular fractures, but little evidence of gross plastic deformation. Figures 5(c) and (d) are high magnification micrographs of regions respectively situated outside and inside a partly obliterated impact crater on a surface that had been heavily eroded at a velocity of 70 m s^{-1} . The former, which shows a fracture surface formed by lateral fracture and subsequently intersected by a radial or median crack, reveals that both cracks follow intergranular fracture paths; and the latter shows both another intergranular radial or median crack and the mixture of intergranular and transgranular failure that occurs immediately below the impacting particle. In this case much of the thin overlayer of heavily plastically deformed material that originally lined the crater has been removed by subsequent impacts, and the debris that remains is typically $\sim 1 \text{ }\mu\text{m}$ in size.

The mass loss data obtained with the 1.58 mm diameter spheres are shown in Figures 6, 7 and 8. At every velocity studied, there was an initial incubation period during which the average mass of material removed per impact increased

asymptotically with the number of impacts to some (velocity dependent) steady-state value. Particularly at the higher impact velocities, Figure 8, this incubation period was of very limited extent and would not have been visible had irregularly-shaped erosive particles been employed. Power functions of the form

$$m_e = bN_i^\beta, \quad (6)$$

where m_e represents the mass loss due to erosion and b and β are constants for given erosive conditions, were fitted to the data in the incubation period at each impact velocity; and the (dimensionless) erosion E , which is defined by

$$E = \frac{1}{m} \frac{dm_e}{dN_i}, \quad (7)$$

was then calculated from the expression

$$E = \frac{b\beta}{m} N_i^{\beta-1}. \quad (8)$$

Figure 9 compares the dependence of steady-state (linear) erosion on impact velocity v_o with the corresponding dependence of mass loss obtained from single, normal impacts of the same size spheres against as-received target surfaces. The curve fitted to the multiple impact data is of the form

$$E = av_o^\alpha, \quad (9)$$

where a is a constant and the velocity exponent $\alpha = 2.1$. However, the single impact data were found to be better represented by an equation of the form

$$E = a_1 (v_o^2 - v_\tau^2), \quad (10)$$

where a_1 is another constant and v_τ is the threshold velocity (25 m s^{-1} in the present case) for detectable mass loss. Note that during steady-state erosion (i) the mass loss per impact at impact velocities greater than v_τ is roughly three times that produced by a similar impact against the as-received surface and (ii) material is removed at velocities less than v_τ , so that the effective threshold velocity tends towards zero as more and more impacts occur. In

consequence, equation (9) could also be applied to erosion during the incubation period whenever sufficient impacts occurred to produce measurable mass loss from all specimens. The variation with number of impacts of the velocity exponent α calculated in this fashion is shown in Figure 10.

The change in the appearance of the steady-state eroded surface with decrease in erosive particle size at an impact velocity of 50 m s^{-1} may be seen by comparing Figures 4(c) and 11. Essentially, the difference is one of scale rather than nature: all three sizes of particle produce the same characteristic combination of partly obliterated craters, lateral fracture surfaces and radial and/or median fractures. The corresponding mass loss data are shown in Figure 12, where they are plotted against the mass rather than the number of particles impacting the target. And Figure 13 reveals that in the steady state represented by the linear portions of the curves presented in Figure 12 the erosion of MgO by WC-6% Co spheres depends on particle diameter to the power 0.57.

DISCUSSION

Single impacts of hard, millimeter-size WC-6% Co spheres against almost fully dense, fine-grained, polycrystalline MgO at normal incidence produce permanent craters surrounded by the sort of array of radial, median and lateral cracks characteristic of impacts in which a significant amount of plastic deformation occurs beneath the indenter. The interior of the crater is smooth and exhibits evidence of very extensive plastic deformation. However, this plastic deformation extends only to a depth of one or two grain diameters (~ 10 to $20 \text{ }\mu\text{m}$), and crater formation is accommodated primarily by the elastic strain "trapped" in and around the region of contact as a result of the cracking that occurs during the impact event. Immediately beneath the crater many short cracks are formed. Some are intergranular and others transgranular, but none

appear to extend for more than a few grain diameters. They are presumed to develop because they represent the easiest way for the individual grains of the target material, which has only two independent primary glide systems[139] and a very high critical resolved shear stress for secondary glide at or near room temperature[140], to accommodate the strain imposed by the impacting particle. In contrast, the (radial, median and lateral) cracks formed beyond the crater rim in response to the impact loading are few in number but extend over distances of a crater diameter or more. These latter cracks are all intergranular.

The important conclusion to be drawn from these observations is that it is not necessary to have extensive plastic flow (i.e., dislocation glide) per se in the contact region to produce radial and/or median and/or lateral cracking: microcracking--and, presumably, any other irreversible mode of deformation capable of releasing strain energy--will do just as well.

Mass losses large enough to be detected in the present experiments (i.e., $\geq 10 \mu\text{g}$) occurred at all impact velocities after a sufficient number of impacts, but only at velocities $\geq 25 \text{ m s}^{-1}$ for single impacts against as-received surfaces. Invariably, the dominant mechanism of material removal was detachment from the target surface of more-or-less petal-shaped flakes formed by intersection of lateral cracks with radial and/or median cracks. Interaction between cracks formed at adjacent impact sites and repeated stressing of existing cracks by subsequent impacts both appeared to play an important role in this flaking process, because the average mass loss per impact during steady-state erosion at any impact velocity $\geq 25 \text{ m s}^{-1}$ was about three times that produced by a similar velocity impact against the as-received target surface. The same processes also appear to be responsible for the absence of any threshold velocity for the occurrence of mass loss under multiple impact conditions. A secondary source of mass loss was spalling away of the heavily plastically deformed material lining the impact craters, some of which material could occasionally be found adhering

to the spent erosive spheres. Such spalling accounted for only a small fraction of the total mass loss, but is noted here because it does not appear to have been observed in other studies of the erosion of ceramics. No evidence was seen melting in the impact zone.

An important result of the present studies is that they show quite unambiguously that the erosion of ceramics exhibits an incubation phase when the starting surface is not too heavily damaged. This result is implied by the three-fold increase in average mass loss per impact observed to accompany the changeover from single impact to steady-state erosion conditions, and is demonstrated explicitly by the shape of the mass loss curves presented in Figures 6, 7, 8 and 12. These latter curves also make clear why there is controversy in the literature on this point[121,123]: the incubation period is so short that it would be virtually impossible to document by means of an experiment employing irregular erosive particles which can give rise to thousand-fold variations in the mass loss they produce per impact. Indeed, comparison of the present mass loss curves with those obtained for polycrystalline Al under identical erosive conditions[133], shows that the incubation period for the metal is $\sim 100 \times$ that for the ceramic. The reason is two-fold. First, because extensive cracking occurs around the impact craters in MgO, the area of the target affected by each impact is much greater than in the case of Al. And second, the flaking process primarily responsible for material removal from MgO can be operated by individual impacts, whereas the process of platelet formation responsible for mass loss during the erosion of Al at normal incidence requires many overlapping impacts to cause it to occur. One noteworthy consequence of this difference in mechanism is that, even under steady-state erosion conditions, material removal from MgO must occur from non-work hardened surfaces.

Because the impact crater did not remain intact for impacts at velocities $\gtrsim 25 \text{ m s}^{-1}$, only two dynamic hardness values were obtained from the present

study, Figure 3. These values are consistent with a Meyer index of 2.59, and suggest that the target work hardens rapidly beneath the impacting particle. In contrast, previous studies[98,100-103] of the normal impact of the same 1.58 mm diameter spheres against variously polished {100}, {110} and {111} surfaces of MgO single crystals from two different sources showed the dynamic hardness to be independent of crater diameter in every case, implying a complete lack of work hardening and a Meyer index of exactly two. Likewise, there is a marked difference in the response of the same materials to static indentation by the same spheres: the polycrystalline material exhibits a Meyer index of 2.57, indicative of rapid work hardening, and {100}, {110} and {111} oriented single crystals exhibit Meyer indices ranging from 1.59 to 1.73[141], implying that they work soften. Correspondingly, the ratio of the dynamic to the static hardness, which has a value of $\sqrt{2}$ and is independent of crater diameter in the case of the polycrystalline material, rises with increasing crater diameter from 3 or 4 to 5 or 6 for single crystal surfaces of different orientation.

Strictly speaking of course, the use in the preceding paragraph of the term work hardening, with its implication of dislocation-dislocation interactions leading to a steady increase in yield stress as more and more strain accumulates, is something of a misnomer, as is the use of the term work softening. The reason is that in none of the experiments discussed is either the static (Meyer) hardness or the dynamic hardness a true measure of the stress to produce dislocation motion. Rather, each parameter is used as a convenient indicator of the total force required to operate all of the inter-related flow and fracture processes occurring in and around the region of contact. However, while it seems reasonably certain that most of the fracture occurring around impact craters and indentations in MgO is initiated by dislocation interactions, it is not clear how the stress required to produce these interactions (i.e., the hardness) depends on such (microstructure-sensitive) parameters as slip line

length, slip line spacing, dislocation density, etc. Nor is it clear by how much the increase in fracture toughness associated with the changeover in the mode of crack extension from {100} and/or {110} cleavage in a single crystal to intergranular propagation in the present polycrystalline material affects the elastic constraints in the region of contact under either static or dynamic conditions. At the present time, therefore, no detailed explanation of these data is possible. It is interesting to note, however, that such seemingly similar materials as MgO, LiF and NaCl all differ appreciably in the way in which their hardness varies with strain rate[97-103,141], as do Ni and Al[100,133, 141,142]. Evidently it will be no easy task to unravel the relationship of dynamic hardness and dynamic fracture toughness to microstructure.

Finally, it is noted that none of the theories of erosion in either the elastic or the elastic-plastic impact regime provides an adequate explanation of the observed dependence of erosion on either impact velocity (Figure 10) or particle size (Figure 13). In particular, since none of these theories has sufficient resolution to distinguish between the incubation and steady-state erosion regimes, each predicts a constant velocity exponent in the range 2.4 to 3.2[122]. Yet the present study shows that the velocity exponent decreases monotonically from ~ 3.5 to ~ 2.1 in the course of the incubation period. The same behavior has also been observed in polycrystalline Al, although the incubation period is much longer and the range of variation of the velocity exponent rather larger[133]. In the case of the particle size exponent, the discrepancy between theory and experiment is more glaring: theory predicts an exponent of 3.7 to 4.2[122], but the present experiments yield a value of 0.57.

ACKNOWLEDGEMENT

This work was supported by the U. S. Army Research Office under Grant No. DAAG29-79-C-0104.

REFERENCES

- 1 C.M. Preece and N.H. Macmillan, *Ann. Rev. Mater. Sci.*, 7 (1975) 95.
- 2 G.P. Tilly, *Wear*, Academic Press (1979), *Treatise on Materials Science and Technology*, Vol. 13, p. 287.
- 3 I. Finnie, *Wear*, 3 (1960) 87.
- 4 I. Finnie and H. Oh, *Proc. 1st Cong. of Int. Soc. Rock Mechanics*, Laboratório Nacional de Engenharia Civil, Lisbon, Portugal (1966) Vol. 2, p. 99.
- 5 H.L. Oh, K.P.L. Oh, S. Vaidyanathan and I. Finnie, *National Bureau of Standards Special Publ. No. 348*, National Bureau of Standards, Gaithersburg, Maryland (1972) 119.
- 6 G.L. Sheldon and I. Finnie, *J. Eng. Ind.*, 88 (1966) 393.
- 7 G.L. Sheldon, *J. Basic Eng.*, 92 (1970) 619.
- 8 H. Hertz, *J. Reine Angew. Math.*, 92 (1881) 156.
- 9 W. Weibull, *Ing. Vetenskaps Akad. Handlingar*, Stockholm, No. 151 (1939) 1.
- 10 G.L. Sheldon and I. Finnie, *J. Eng. Ind.*, 88 (1966) 387.
- 11 H. Uetz and J. Föhl, *Wear*, 20 (1972) 299.
- 12 G.A. Sargent, P.K. Mehrotra and H. Conrad, *Proc. 5th Int. Conf. on Erosion by Solid and Liquid Impact*, Cavendish Laboratory, Cambridge, England (1979) Paper No. 28.
- 13 C.J. Studman and J.E. Field, *J. Phys. D*, 9 (1976) 857.
- 14 S. Palmquist, *Jernkontorets Ann.*, 141 (1957) 300.
- 15 S. Palmquist, *Arch. Eisenhüttenwesen*, 33 (1962) 29.
- 16 I.M. Ogilvy, C.M. Perrott and J.W. Suiter, *Wear*, 43 (1977) 239.
- 17 H.E. Exner, *Trans. AIME*, 245 (1969) 677.
- 18 K.E. Puttick, *J. Phys. E*, 6 (1973) 116.
- 19 K.E. Puttick, L.S.A. Smith and L.E. Miller, *J. Phys. D*, 10 (1977) 617.
- 20 K.E. Puttick, *J. Phys. D*, 11 (1978) 595.
- 21 J.T. Hagan and M.M. Chaudhri, *J. Mater. Sci.*, 12 (1977) 1055.
- 22 R.K. Banerjee and P. Feltham, *J. Mater. Sci.*, 9 (1974) 1478.
- 23 J. Lankford and D.L. Davidson, *J. Mater. Sci.*, 14 (1979) 1662.
- 24 M.V. Swain, Ph.D. Thesis, Univ. of New South Wales, Australia (1973).
- 25 J. Lankford and D.L. Davidson, *J. Mater. Sci.*, 14 (1979) 1669.
- 26 B.J. Hockey and B.R. Lawn, *J. Mater. Sci.*, 10 (1975) 1275.
- 27 M.G.S. Naylor and T.F. Page, *Proc. 5th Int. Conf. on Erosion by Solid and Liquid Impact*, Cavendish Laboratory, Cambridge, England (1979) Paper No. 32.
- 28 J. Lankford, *Fracture Mechanics of Ceramics*, Plenum Press, New York (1978) Vol. 3, p. 245.
- 29 J. Lankford, *Scripta Met.*, 11 (1977) 349.
- 30 A.G. Evans and T.R. Wilshaw, *Acta Met.*, 24 (1976) 939.
- 31 M.V. Swain and B.R. Lawn, *phys. stat. sol.*, 35 (1969) 909.
- 32 J. Paone and S. Tandanand, *Trans. ASME*, 235 (1966) 113.
- 33 M.V. Swain and B.R. Lawn, *Indentation Fracture in Brittle Rocks and Glasses*, Tech. Rep. MML-TR-76-12C, Martin-Marietta Labs., Baltimore, Maryland (1976).
- 34 B.R. Lawn and T.R. Wilshaw, *J. Mater. Sci.*, 10 (1975) 1049.
- 35 B.R. Lawn and M.V. Swain, *J. Mater. Sci.*, 10 (1975) 113.
- 36 M.V. Swain and J.T. Hagan, *J. Phys. D*, 9 (1976) 2201.
- 37 K. Phillips, *J. Mater. Sci.*, 11 (1976) 2354.
- 38 J.T. Hagan and M.V. Swain, *J. Phys. D*, 11 (1978) 2091.
- 39 K.W. Peter, *J. Non-Cryst. Sol.*, 5 (1970) 103.
- 40 K. Peter, *Glastech. Ber.*, 37 (1964) 333.
- 41 E. Dick, *Glastech. Ber.*, 43 (1970) 16.
- 42 M.V. Swain, *J. Am. Ceram. Soc.*, 62 (1979) 318.

- 43 J.T. Hagan, J. Mater. Sci., 14 (1979) 462.
44 A. Arora, D.B. Marshall and B.R. Lawn, J. Non-Cryst. Sol., 31 (1979) 415.
45 B.R. Lawn and A.G. Evans, J. Mater. Sci., 12 (1977) 2195.
46 J.T. Hagan, J. Mater. Sci., 14 (1979) 2975.
47 R.K. Viswanadham and J.D. VENABLES, Met. Trans., 8A (1977) 187.
48 C.M. Perrott, Wear, 45 (1977) 293.
49 C.M. Perrott, Wear, 47 (1978) 81.
50 B.R. Lawn, T. Jensen and A. Arora, J. Mater. Sci., 11 (1976) 573.
51 B.R. Lawn, M.V. Swain and K. Phillips, J. Mater. Sci., 10 (1975) 1236.
52 A.G. Evans and E.A. Charles, J. Am. Ceram. Soc., 59 (1976) 371.
53 M.G. Mendiratta and J.J. Petrovic, J. Mater. Sci., 11 (1976) 973.
54 B.R. Lawn and D.B. Marshall, J. Am. Ceram. Soc., 62 (1979) 347.
55 B.R. Lawn and E.R. Fuller, J. Mater. Sci., 10 (1975) 2016.
56 D.B. Marshall and B.R. Lawn, J. Mater. Sci., 14 (1979) 2001.
57 M.V. Swain, J. Mater. Sci., 11 (1976) 2345.
58 M.V. Swain, Wear, 35 (1975) 185.
59 B.R. Lawn, Wear, 33 (1975) 369.
60 M.V. Swain, Proc. Roy. Soc. Lond., A366 (1979) 575.
61 K.E. Puttick, M.A. Shahid and M.M. Hosseini, J. Phys. D, 12 (1979) 195.
62 K. Peter and E. Dick, Glaztech. Ber., 40 (1967) 470.
63 M.V. Swain, Fracture Mechanics of Ceramics, Plenum Press, New York (1978) Vol. 3, p. 257.
64 J.D.B. Veldkamp, N. Hattu and V.A.C. Snijders, Fracture Mechanics of Ceramics, Plenum Press, New York (1978) Vol. 3, p. 273.
65 R.M. Gruver and H.P. Kirchner, J. Am. Ceram. Soc., 56 (1973) 21.
66 B.R. Lawn, S.M. Wiederhorn and H.H. Johnson, J. Am. Ceram. Soc., 58 (1975) 428.
67 B.R. Lawn, E.R. Fuller and S.M. Wiederhorn, J. Am. Ceram. Soc., 59 (1976) 193.
68 J.J. Petrovic, R.A. Dirks, L.A. Jacobson and M.G. Mendiratta, J. Am. Ceram. Soc., 59 (1976) 177.
69 B.R. Lawn and D.B. Marshall, Phys. and Chem. Glasses, 18 (1977) 7.
70 M.V. Swain, J.T. Hagan and J.E. Field, J. Mater. Sci., 12 (1977) 1914.
71 J.T. Hagan, M.V. Swain and J.E. Field, Phys. and Chem. Glasses, 18 (1975) 101.
72 D.B. Marshall and B.R. Lawn, J. Am. Ceram. Soc., 60 (1977) 86.
73 D.B. Marshall and B.R. Lawn, J. Am. Ceram. Soc., 61 (1978) 21.
74 D.B. Marshall, B.R. Lawn, H.P. Kirchner and R.M. Gruver, J. Am. Ceram. Soc., 61 (1978) 271.
75 B.R. Lawn and D.B. Marshall, J. Am. Ceram. Soc., 62 (1979) 106.
76 P. Chantikul, B.R. Lawn and D.B. Marshall, J. Am. Ceram. Soc., 62 (1979) 340.
77 P. Chantikul, D.B. Marshall, B.R. Lawn and M.G. Drexhage, J. Am. Ceram. Soc., 62 (1979) 551.
78 D.B. Marshall, B.R. Lawn and P. Chantikul, J. Mater. Sci., 14 (1979) 2225.
79 B.R. Lawn and D.B. Marshall, Fracture Mechanics of Ceramics, Plenum Press, New York (1978) Vol. 3, p. 205.
80 B.R. Lawn and T.R. Wilshaw, Fracture of Brittle Solids, Cambridge University Press, England (1975).
81 J.P.A. Tillet, Proc. Phys. Soc., B69 (1956) 47.
82 Y.M. Tsai and H. Kolsky, J. Mech. Phys. Sol., 15 (1967) 263.
83 G.P. Cherepanov and V.B. Sokolinsky, Eng. Fract. Mech., 4 (1972) 205.
84 C.G. Knight, M.V. Swain and M.M. Chaudhri, J. Mater. Sci., 12 (1977) 1573.
85 M.M. Chaudhri and S.M. Walley, Phil. Mag., 37A (1978) 153.

- 86 M.M. Chaudhri and P.A. Brophy, *J. Mater. Sci.*, 15 (1980) 345.
- 87 H.P. Kirchner and R.M. Gruver, *Mater. Sci. and Eng.*, 28 (1977) 153.
- 88 H.P. Kirchner and R.M. Gruver, *Mater. Sci. and Eng.*, 33 (1978) 101.
- 89 M.M. Chaudhri, C.G. Knight and M.V. Swain, *Proc. 12th Int. Cong. on High Speed Photography*, Soc. Photo-Optical Instrumentation Engineers, Washington, D.C. (1977) 371.
- 90 J.F. Vedder and J.-C. Mandeville, *J. Geophys. Res.*, 79 (1974) 3247.
- 91 J.F. Vedder, *Earth Planet. Sci. Lett.*, 11 (1971) 291.
- 92 L.A. Glenn, *J. Mech. Phys. Sol.*, 24 (1976) 93.
- 93 M.M. Chaudhri and S.M. Walley, *Fracture Mechanics of Ceramics*, Plenum Press, New York (1978) Vol. 3, p. 349.
- 94 H.P. Kirchner and R.M. Gruver, *Fracture Mechanics of Ceramics*, Plenum Press, New York (1978) Vol. 3, p. 365.
- 95 D.M. Richard and H.P. Kirchner, *Proc. 5th Int. Conf. on Erosion by Solid and Liquid Impact*, Cavendish Laboratory, Cambridge, England (1979) Paper No. 27.
- 96 S.V. Hooker and W.F. Adler, *Fracture Mechanics of Ceramics*, Plenum Press, New York (1978) Vol. 3, p. 333.
- 97 M.M. Chaudhri and A. Stephens, *Proc. 13th Int. Conf. on High Speed Photography and Photonics*, Japan. Soc. Precision Eng., Tokyo, Japan (1979) 726.
- 98 B.N. Pramila Bai, M.S. Thesis, The Pennsylvania State University, University Park, Pennsylvania (1978).
- 99 D.G. Rickerby, B.N. Pramila Bai and N.H. Macmillan, *J. Mater. Sci.*, 14 (1979) 3006.
- 100 D.G. Rickerby and N.H. Macmillan, *Proc. 5th Int. Conf. on Erosion by Solid and Liquid Impact*, Cavendish Laboratory, Cambridge, England (1979) Paper No. 29.
- 101 D.G. Rickerby, B.N. Pramila Bai and N.H. Macmillan, *Energy and Ceramics*, Elsevier, Lausanne, Switzerland (1980) 752.
- 102 D.G. Rickerby, B.N. Pramila Bai and N.H. Macmillan, *J. Mater. Sci.*, 14 (1979) 1807.
- 103 D.G. Rickerby and N.H. Macmillan, *The Effect of Approach Direction on Damage in MgO Due to Spherical Particle Impact*, *J. Mater. Sci.*, in press.
- 104 A.G. Evans, M.E. Gulden and M. Rosenblatt, *Proc. Roy. Soc. Lond.*, A361 (1978) 343.
- 105 A.G. Evans and T.R. Wilshaw, *J. Mater. Sci.*, 12 (1977) 97.
- 106 M.E. Gulden, ASTM Special Tech. Publ. No. 664, ASTM, Philadelphia (1979) 101.
- 107 H.P. Kirchner, R.M. Gruver, D.M. Richard and R.C. Garvie, *Mater. Sci. and Eng.*, 40 (1979) 49.
- 108 A.G. Evans, *Fracture Mechanics of Ceramics*, Plenum Press, New York (1978) Vol. 3, p. 303.
- 109 A.G. Evans, *Erosion*, Academic Press, New York (1979) *Treatise on Materials Science and Technology*, Vol. 16, p. 1.
- 110 A.G. Evans, *J. Am. Ceram. Soc.*, 56 (1973) 405.
- 111 S.M. Wiederhorn and B.R. Lawn, *J. Am. Ceram. Soc.*, 60 (1977) 451.
- 112 H.P. Kirchner and R.M. Gruver, *Mater. Sci. and Eng.*, 28 (1977) 249.
- 113 H.P. Kirchner, *J. Am. Ceram. Soc.*, 61 (1978) 161.
- 114 H.P. Kirchner and R.M. Gruver, *Mater. Sci. and Eng.*, 34 (1978) 25.
- 115 S.M. Wiederhorn and B.R. Lawn, *J. Am. Ceram. Soc.*, 62 (1979) 66.
- 116 B.R. Lawn, D.B. Marshall and S.M. Wiederhorn, *J. Am. Ceram. Soc.*, 62 (1979) 71.
- 117 S.M. Wiederhorn, B.R. Lawn and B.J. Hockey, *J. Am. Ceram. Soc.*, 62 (1979) 639.

- 118 B.J. Hockey and S.M. Wiederhorn, Proc. 5th Int. Conf. on Erosion by Solid and Liquid Impact, Cavendish Laboratory, Cambridge, England (1979) Paper No. 26.
- 119 J. Narayan and J. Washburn, Wear, 23 (1973) 128.
- 120 J. Narayan, Wear, 25 (1973) 99.
- 121 M.E. Gulden, J. Am. Ceram. Soc., 63 (1980) 121.
- 122 A.W. Ruff and S.M. Wiederhorn, Erosion, Academic Press, New York (1979) Treatise on Materials Science and Technology, Vol. 16, p. 69.
- 123 J.L. Routbort, R.O. Scattergood and A.P.L. Turner, Wear, 59 (1980) 363.
- 124 W.F. Adler, J. Non-Cryst. Sol., 19 (1975) 335.
- 125 W.F. Adler, Wear, 37 (1976) 345.
- 126 W.F. Adler, Wear, 37 (1976) 353.
- 127 M.S. Crowley, Ceram. Bull., 48 (1969) 707.
- 128 C.S. Yust and R.S. Crouse, Wear, 51 (1978) 193.
- 129 B.J. Hockey, Private Communication (1980).
- 130 A.S. Argon, Private Communication (1980).
- 131 B.J. Hockey, S.M. Wiederhorn and H. Johnson, Fracture Mechanics of Ceramics, Plenum Press, New York (1978) Vol. 3, p. 379.
- 132 S.M. Wiederhorn and D.E. Roberts, Ceram. Bull., 55 (1976) 185.
- 133 D.G. Rickerby and N.H. Macmillan, Wear, 60 (1980) 369.
- 134 D. Tabor, The Hardness of Metals, Clarendon Press, Oxford (1951) p. 47.
- 135 J.P. Andrews, Phil. Mag., 9 (1930) 593.
- 136 E. Meyer, Zeits. d. Vereines Deutsch. Ing., 52 (1908) 645.
- 137 E. Meyer, Zeits. d. Vereines Deutsch. Ing., 52 (1908) 740.
- 138 E. Meyer, Zeits. d. Vereines Deutsch. Ing., 52 (1908) 835.
- 139 G.W. Groves and A. Kelly, Phil. Mag., 8 (1963) 877.
- 140 C.O. Hulse, S.M. Copley and J.A. Pask, J. Am. Ceram. Soc., 46 (1963) 317.
- 141 D.C. Rickerby and N.H. Macmillan, Mater. Sci. and Eng., 40 (1979) 251.
- 142 N.C. Sink, M.S. Thesis, The Pennsylvania State University, University Park, Pennsylvania (1978).

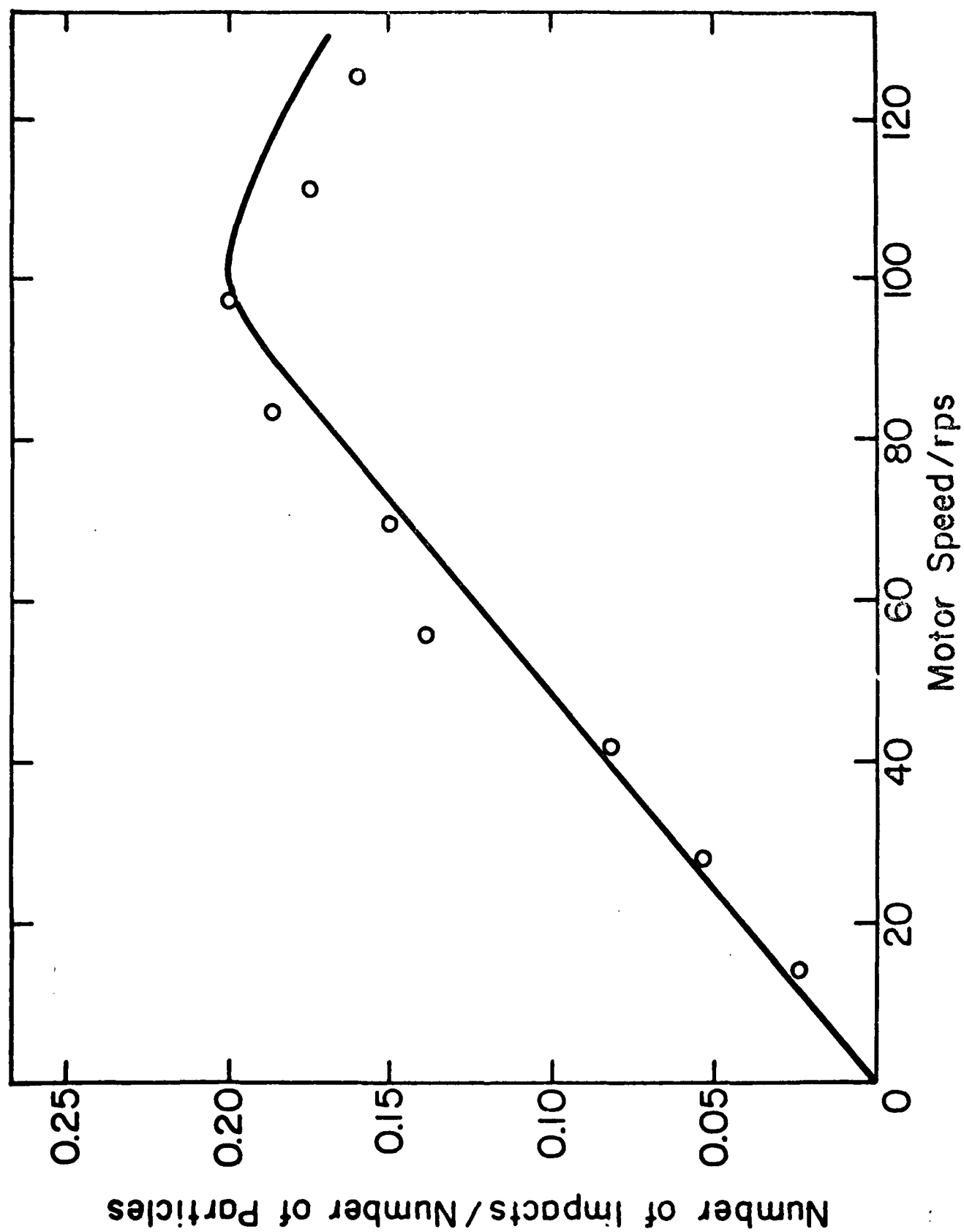


Figure 1 Ratio of number of impacts to number of spheres entering the apparatus versus motor speed.

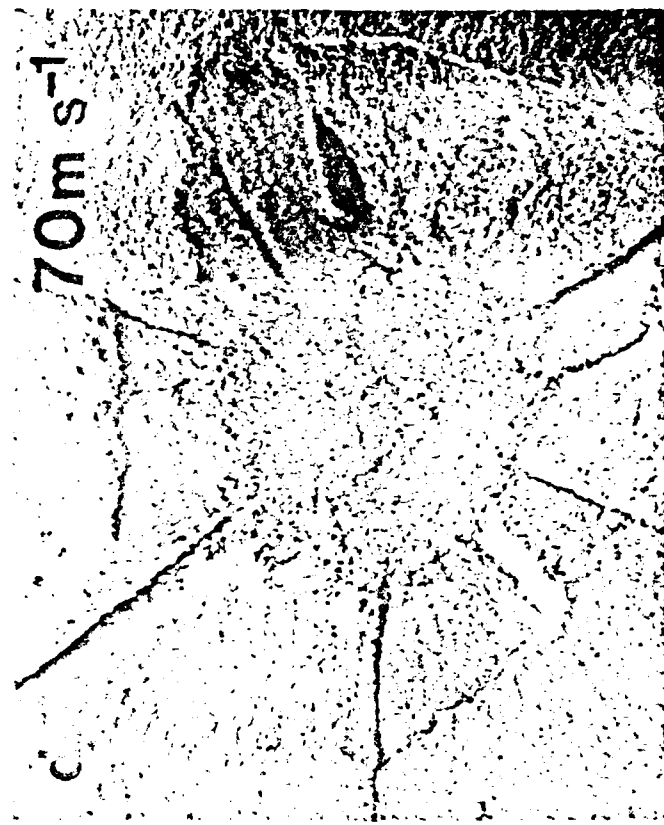
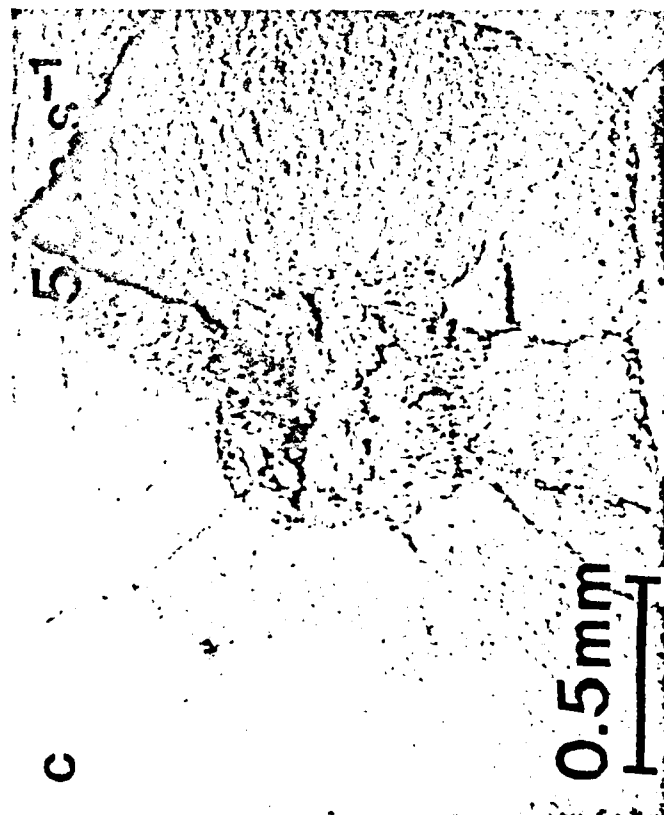
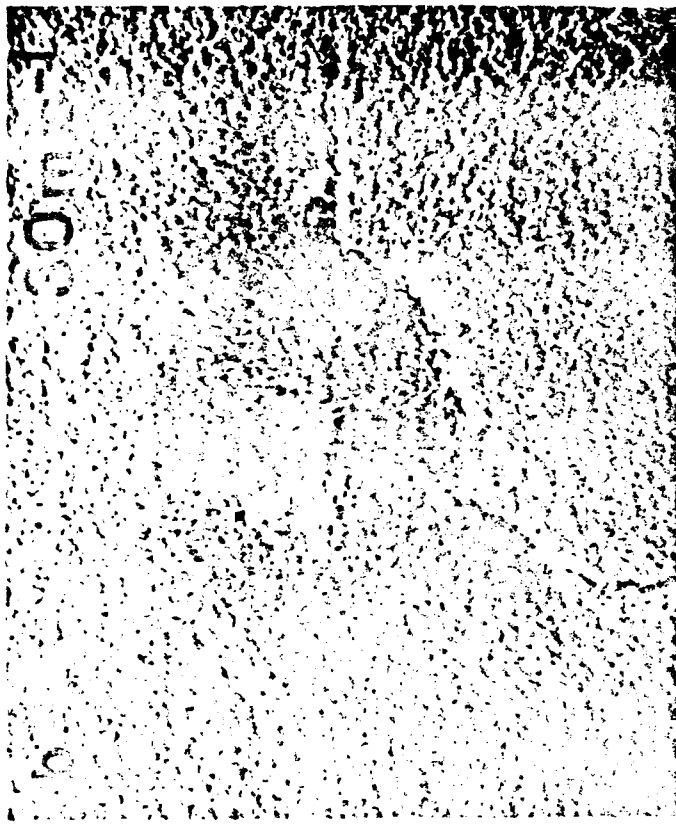
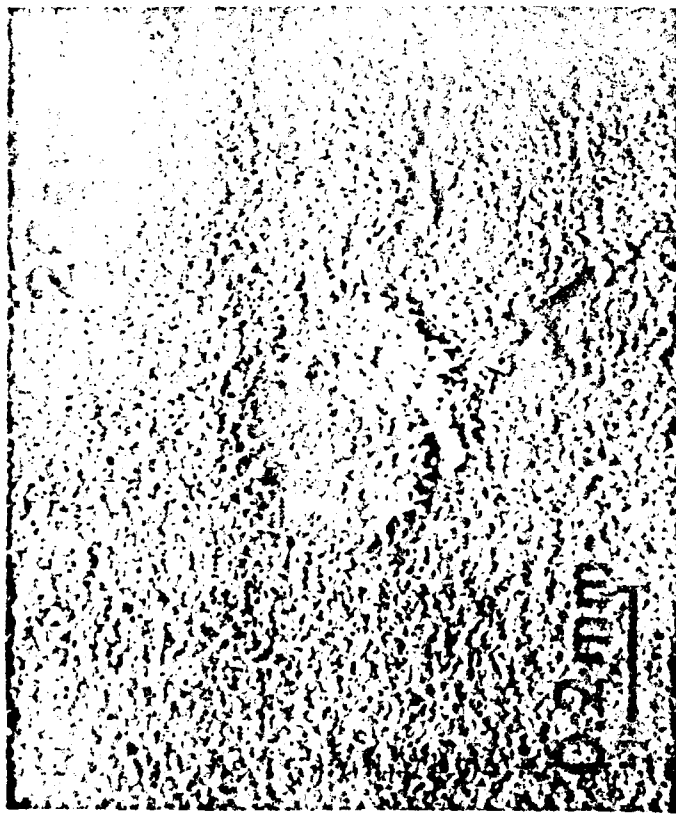


Figure 2 Damage due to single impacts of 1.58 mm diameter spheres at different velocities.

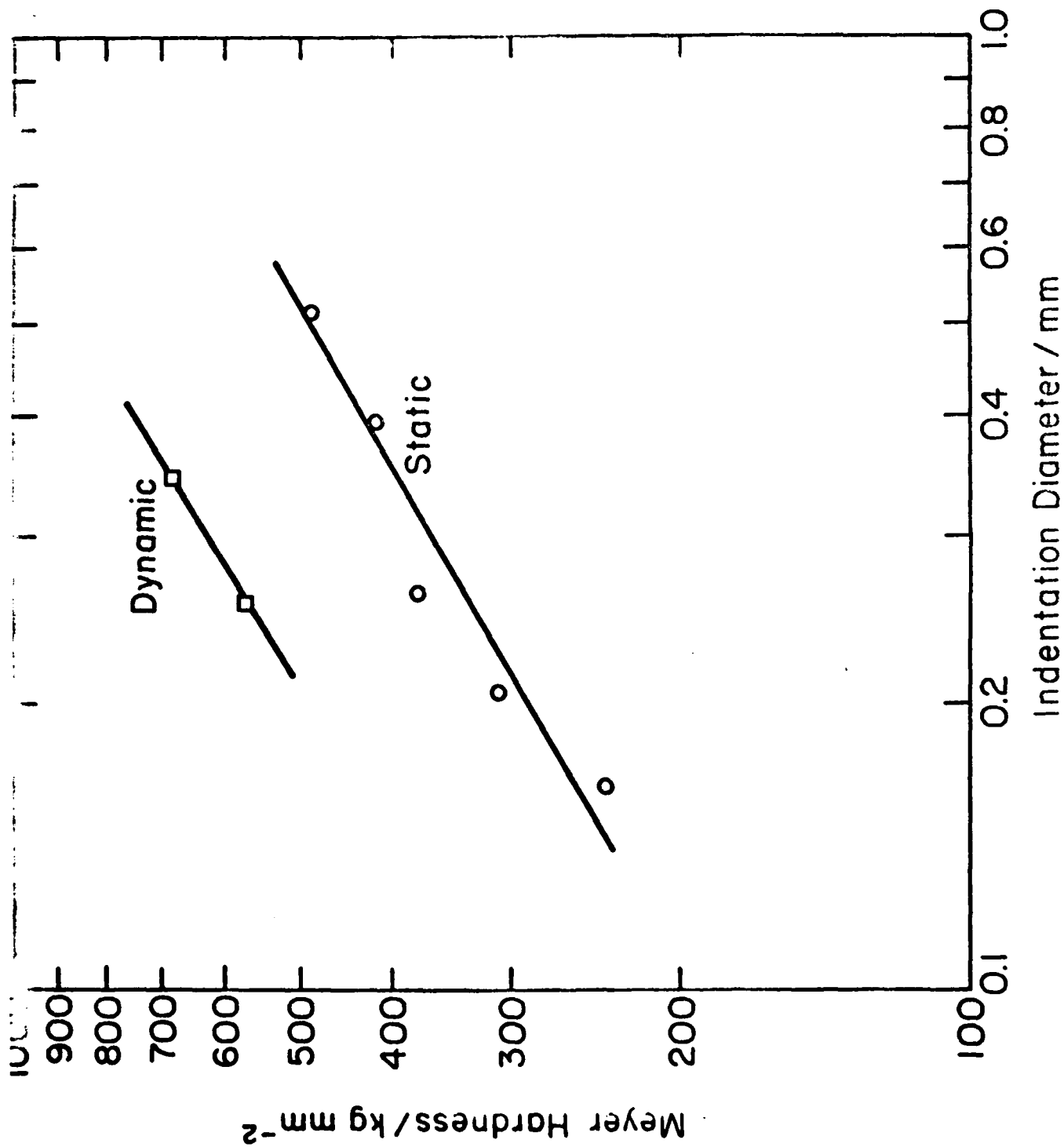


Figure 3 Variation of static (Meyer) and dynamic hardness with diameter of the crater produced by a 1.58 mm diameter sphere.



Figure 4 Steady-state erosion damage produced by 1.58 mm diameter spheres impacting at different velocities.

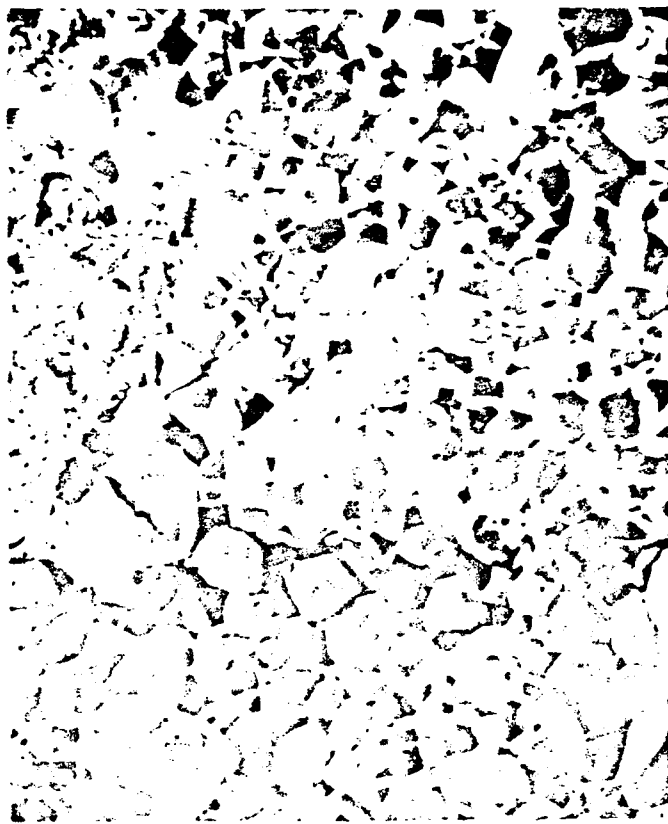
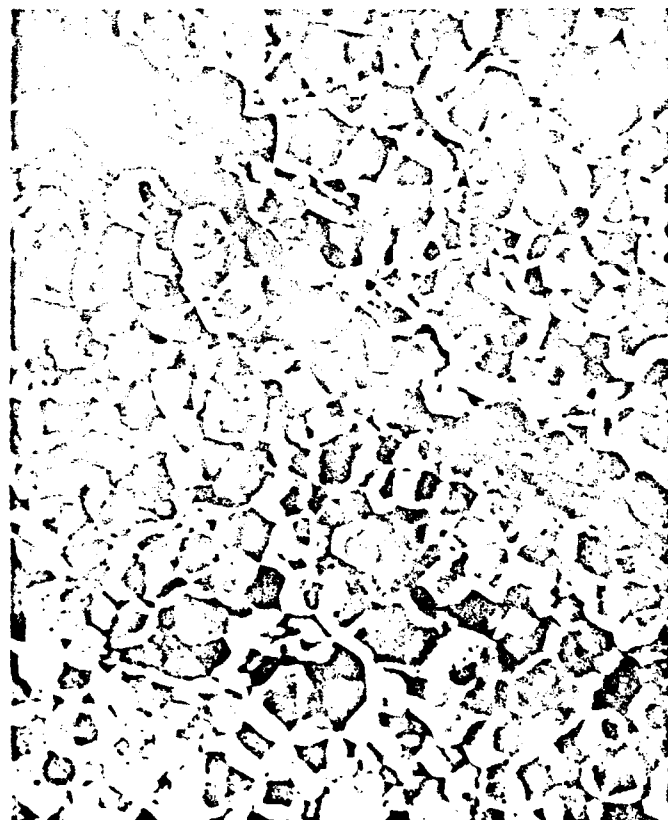


Figure 5 Details of the steady-state erosion damage produced by 1.58 mm diameter spheres impacting at 20 m s^{-1} (a and b) and 70 m s^{-1} (c and d).

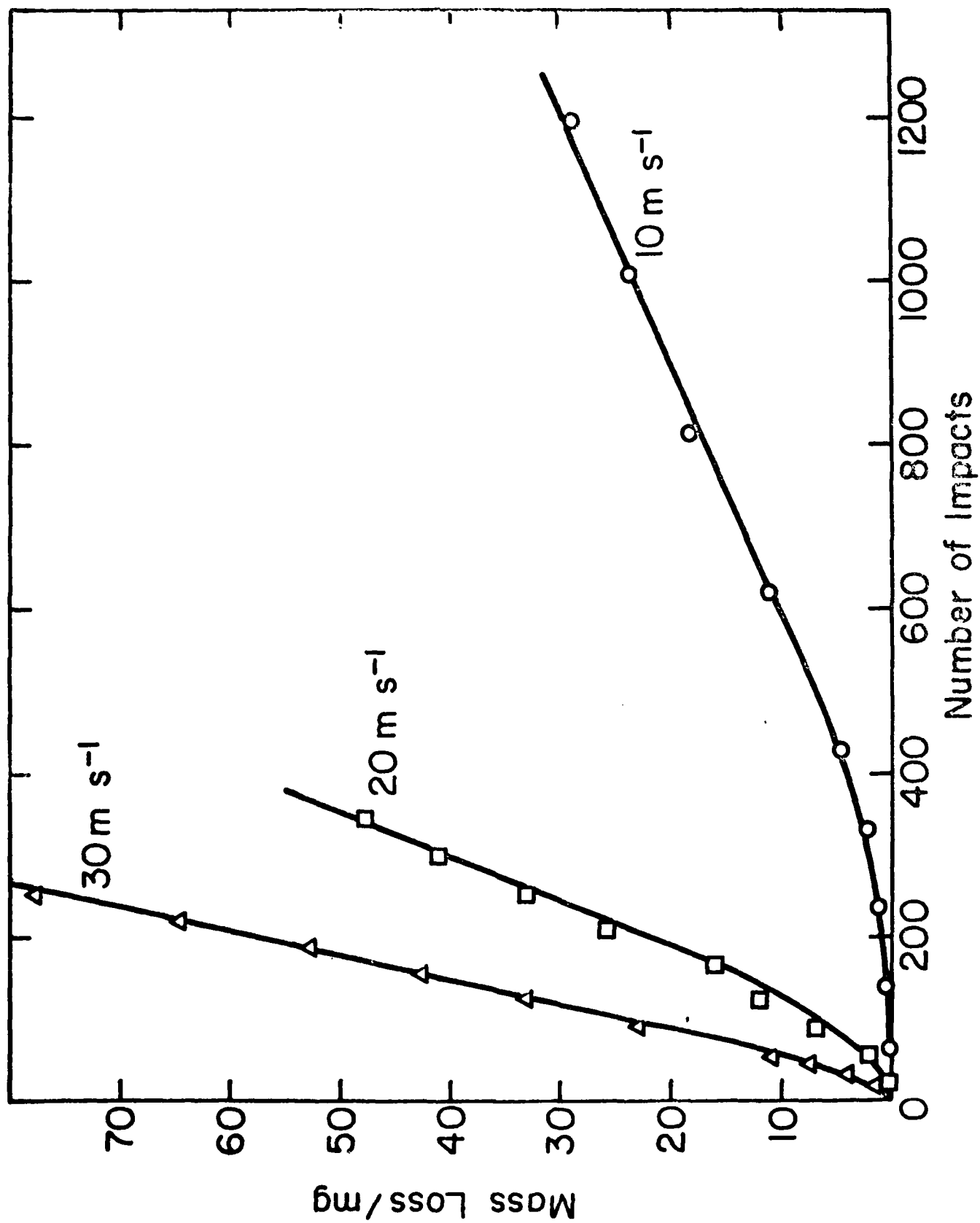


Figure 6 Experimental mass loss curves for 1.58 mm diameter spheres.

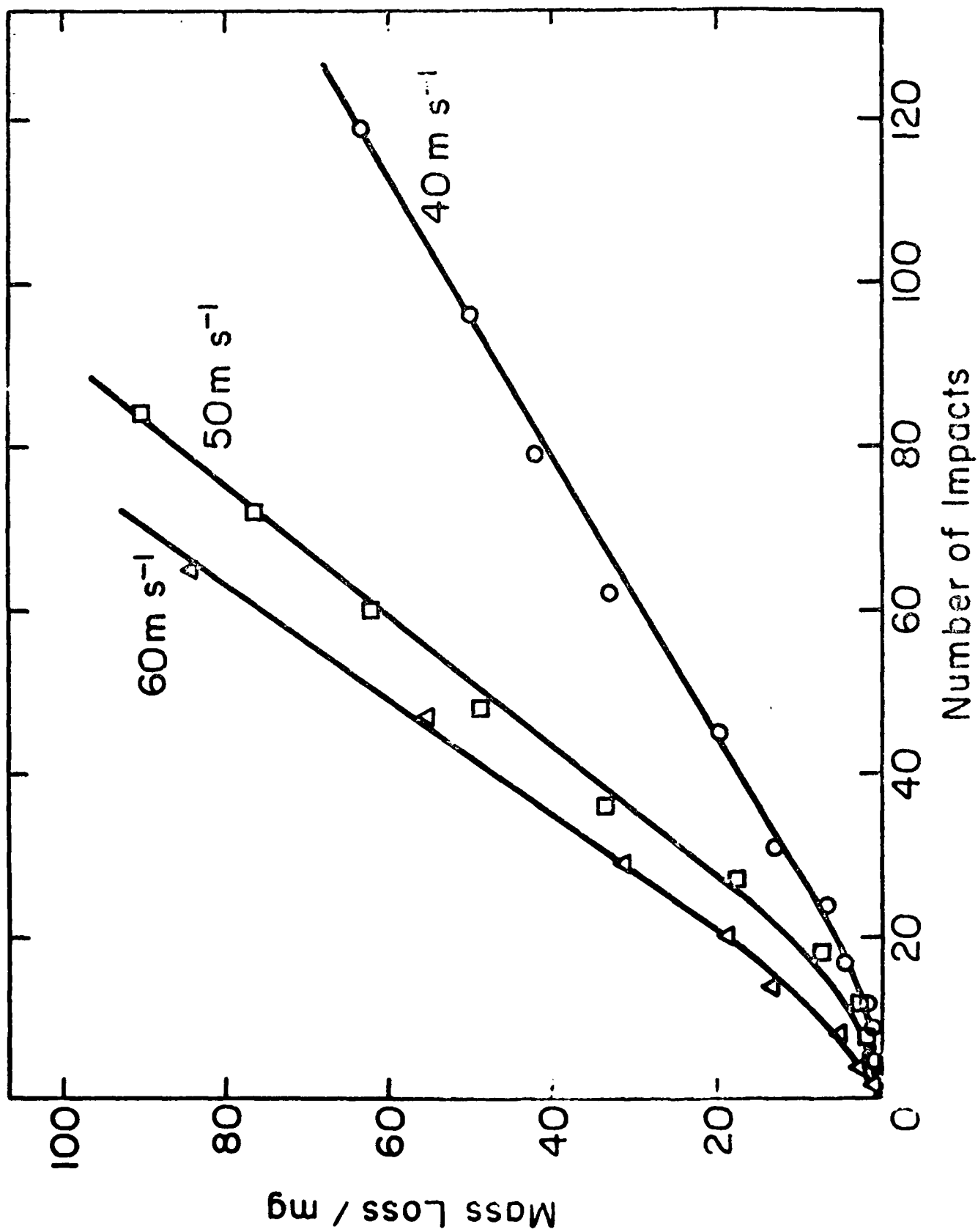


Figure 7 Experimental mass loss curves for 1.58 mm diameter spheres.

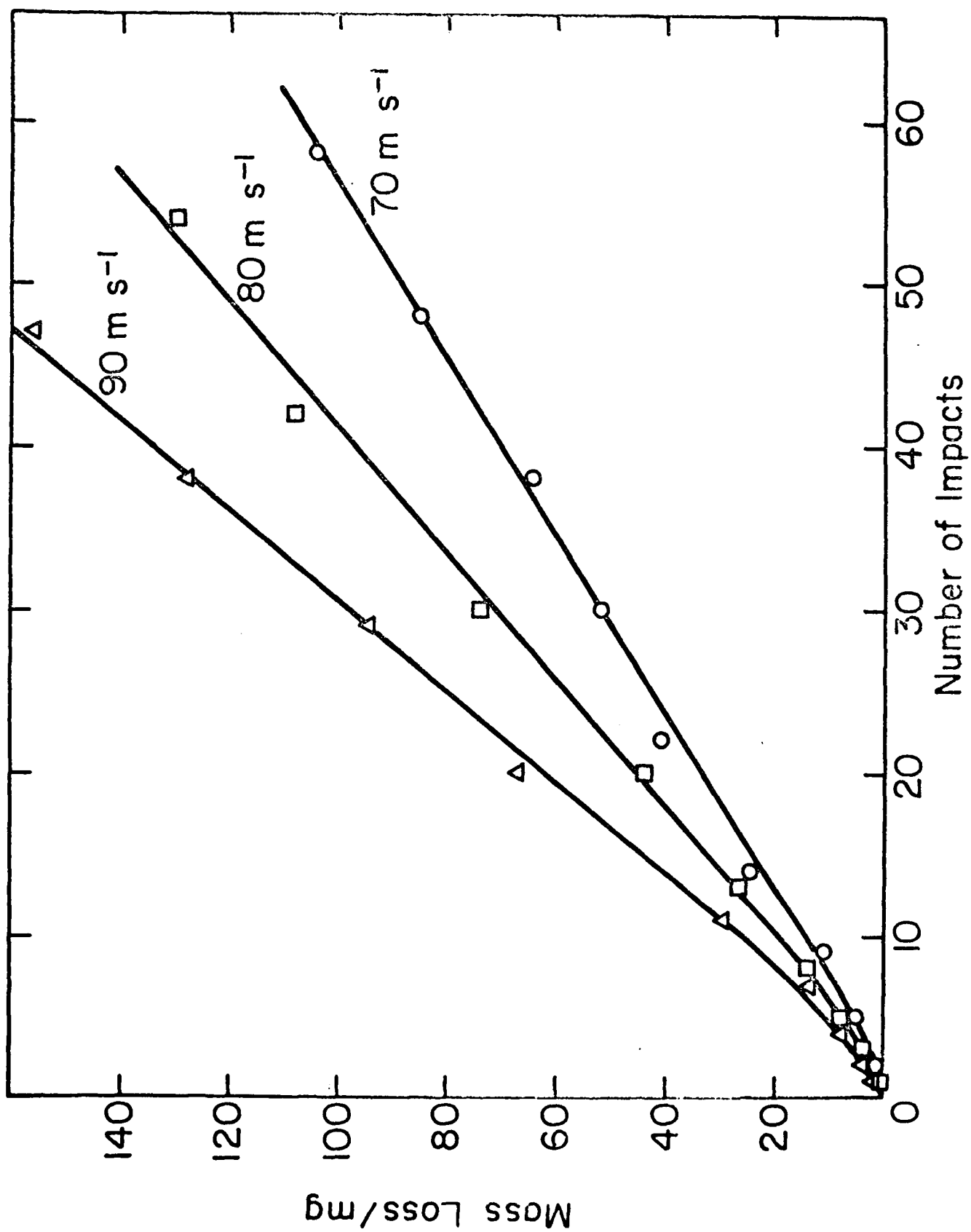


Figure 8 Experimental mass loss curves for 1.58 mm diameter spheres.

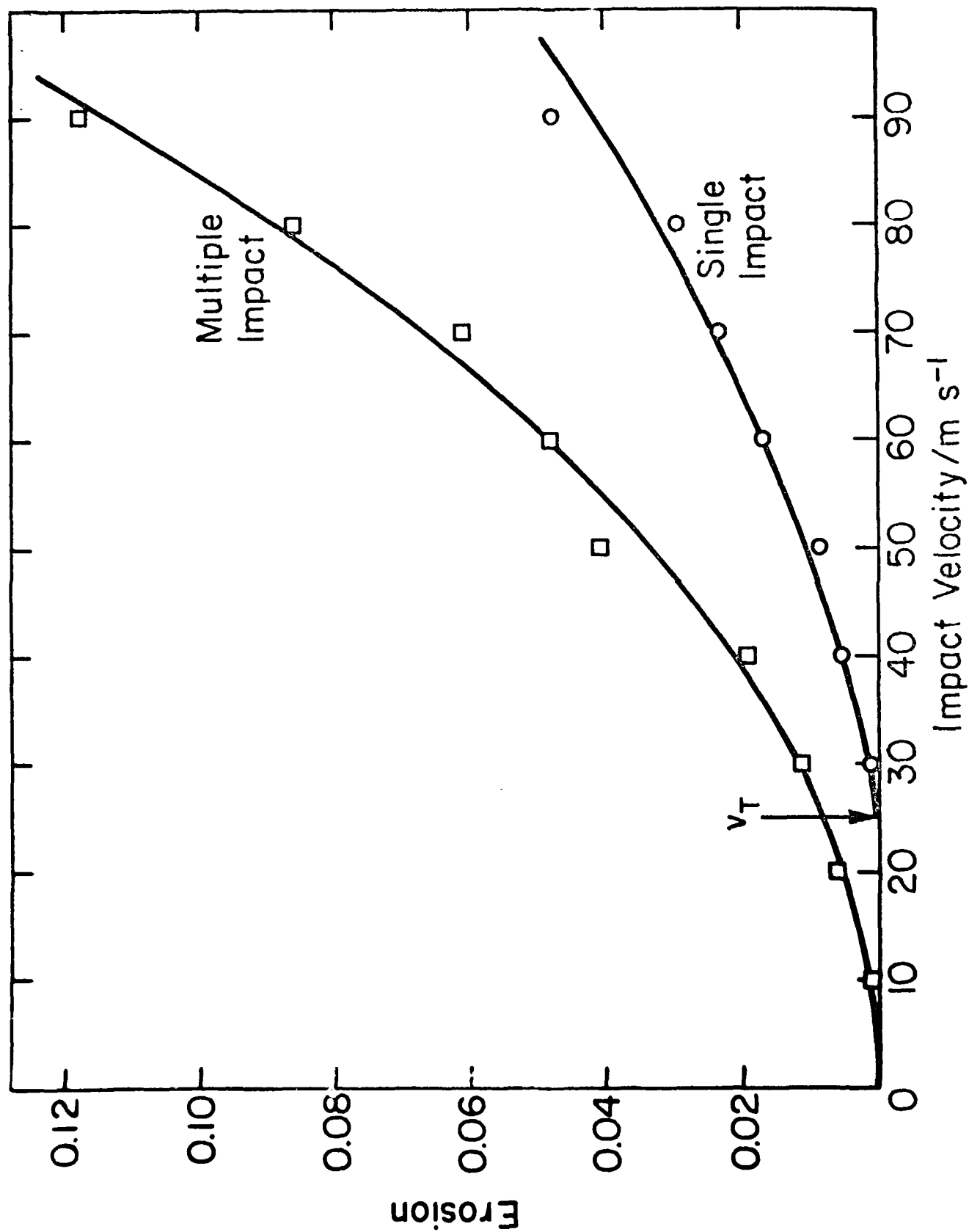


Figure 9 Erosion by 1.58 mm diameter spheres as a function of impact velocity under single and multiple impact conditions.

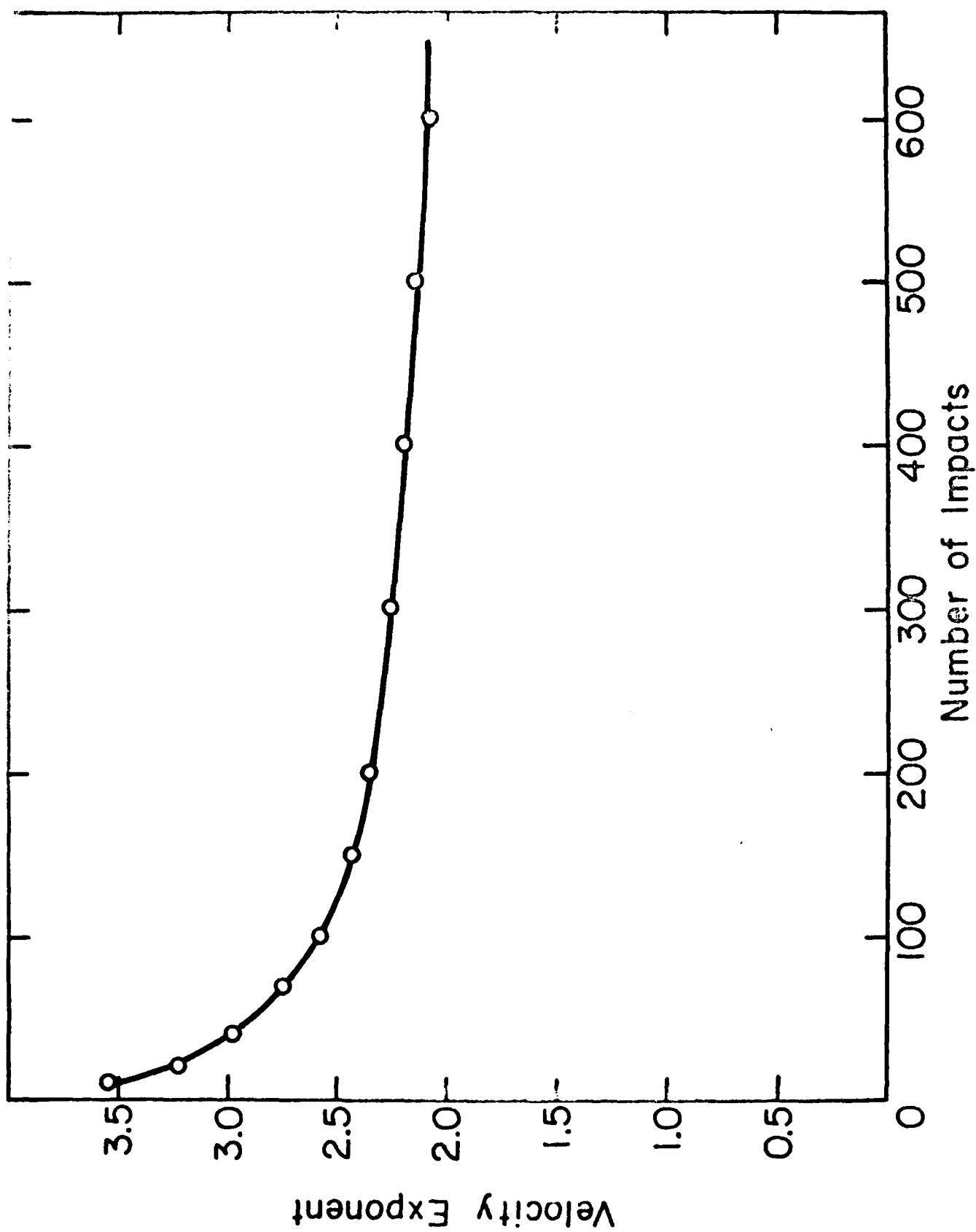


Figure 10 Variation of exponent relating erosion by 1.58 mm diameter spheres to impact velocity as a function of number of impacts.

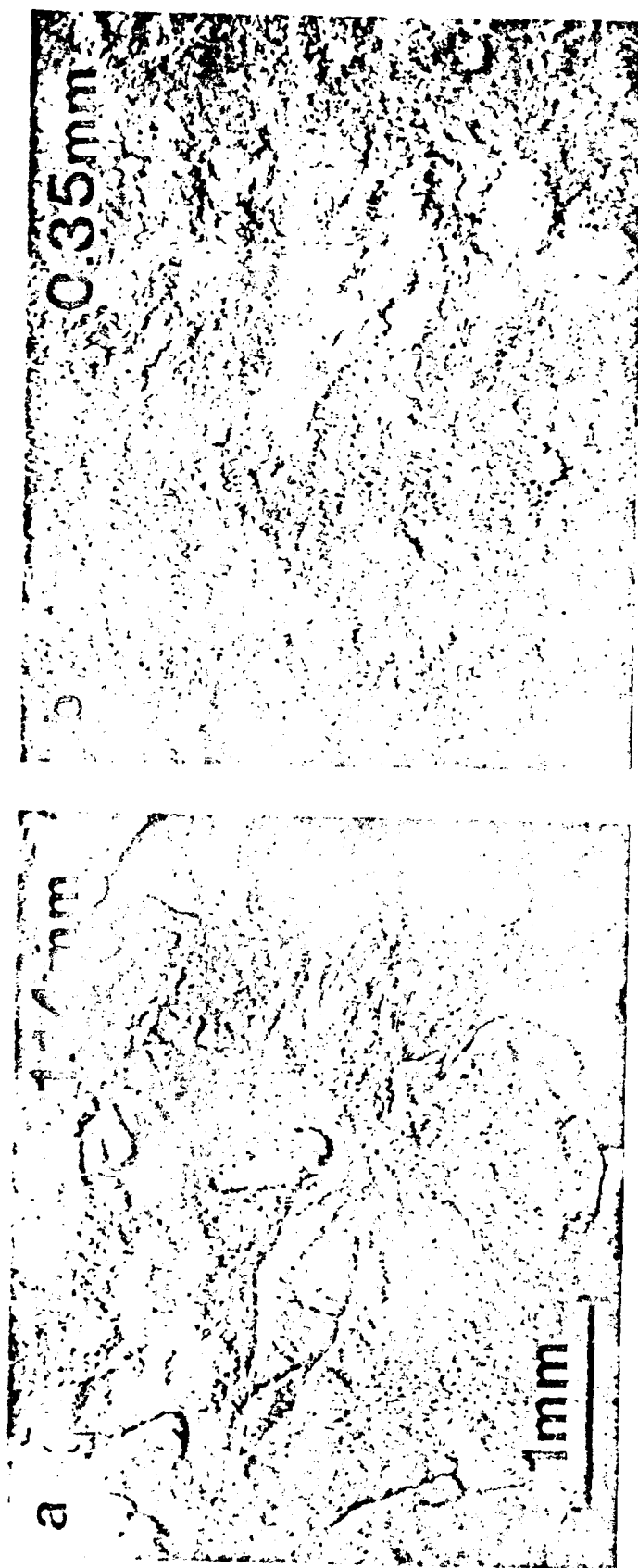


Figure 11 Steady-state erosion damage produced by different diameter spheres impacting at 50 m s^{-1} .

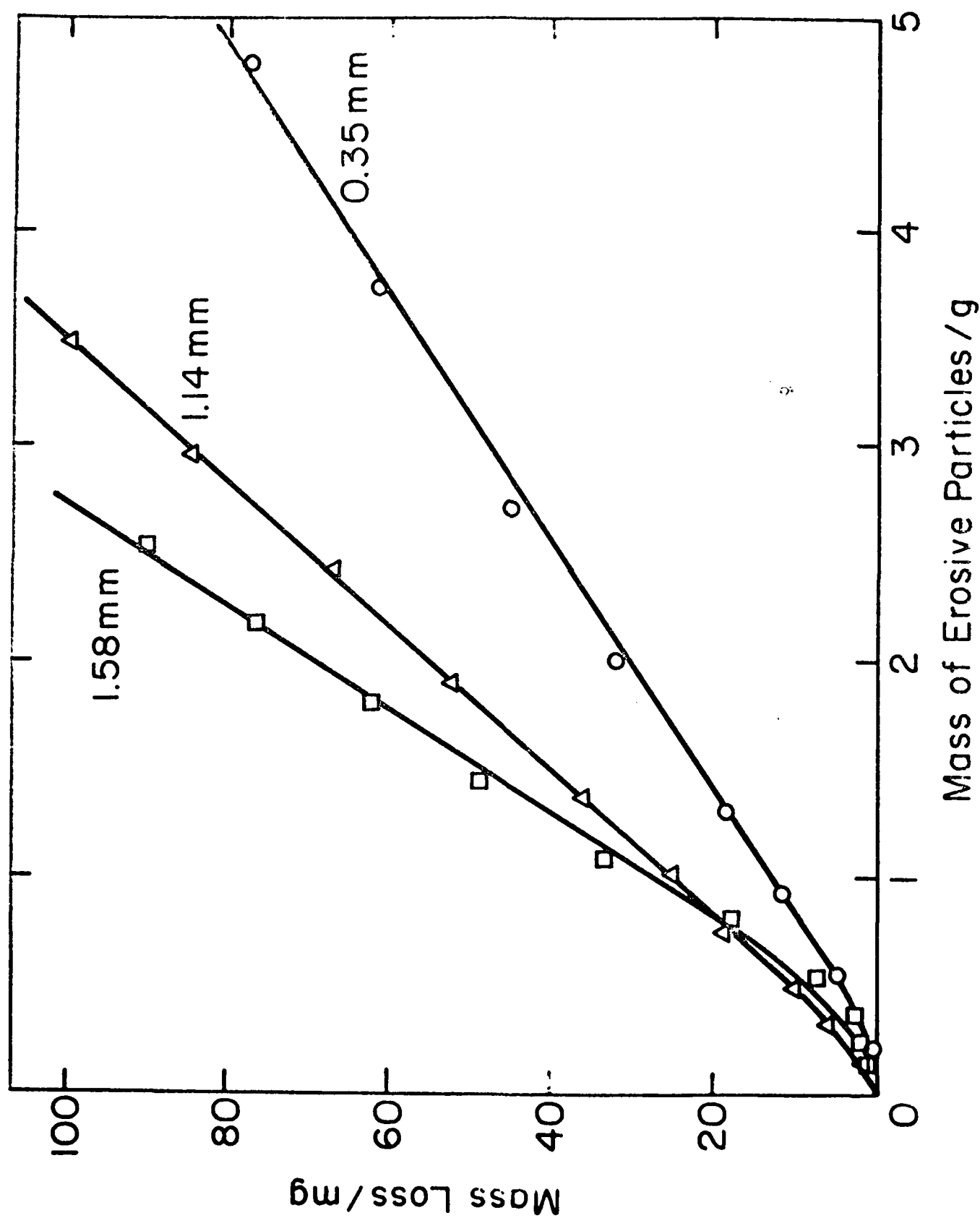


Figure 12 Experimental mass loss curves for different diameter spheres impacting at 50 m s^{-1} .

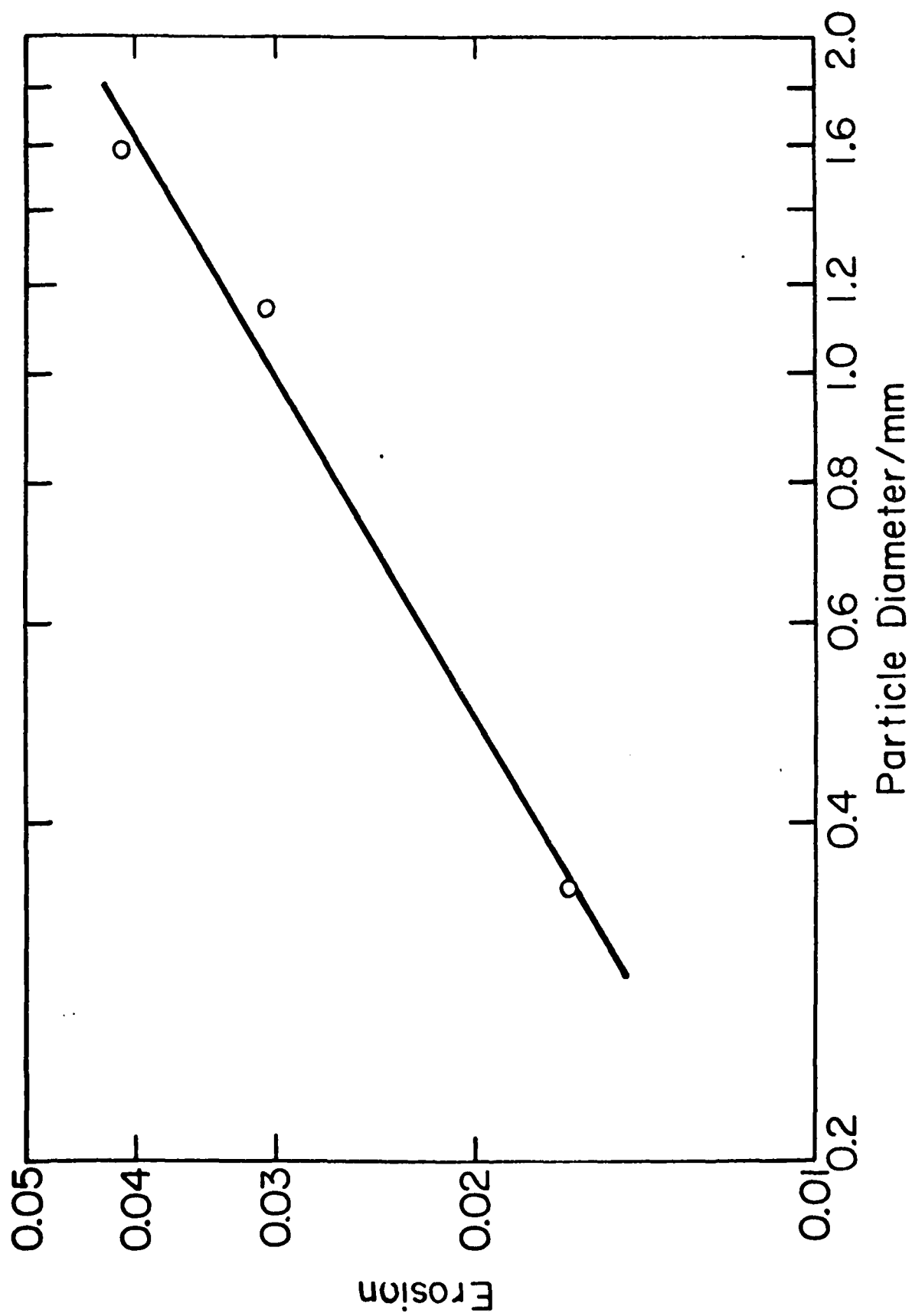


Figure 13 Variation of erosion in the steady-state regime with sphere diameter at an impact velocity of 50 m s^{-1} .

Appendix XI

The Erosion of Aluminum by Solid Particle Impingement at Oblique Incidence

D. G. Rickerby and N. H. Macmillan
Materials Research Laboratory
The Pennsylvania State University
University Park, PA 16802

SUMMARY

Scanning electron microscopy, surface profilometry and weight loss measurements have been used to characterize the erosion of coarse-grained aluminum by 1.58 mm diameter WC-6% Co spheres impinging at different angles with velocities ranging from 10 m s^{-1} to 130 m s^{-1} . In addition, data obtained from these experiments have been used to test a recently developed computer model of the process of crater formation by oblique impact. The dynamic hardness data required as input to this model came from previous studies of the normal impact of the same spheres against the same target material. The results show that the computer model successfully predicts the variation of crater depth and volume with impact angle and velocity, but is less successful at predicting crater length at the shallow impact angles and high impact velocities that produce the greatest pile-up of displaced material at the exit end of the crater. It is also suggested on the basis of the scanning electron microscopy studies that the same mechanism of material removal operates at all angles of impact, and that this involves the detachment from the target of thin platelets formed by extrusion of piled-up material between subsequently arriving particles and the underlying substrate. In this view, the role of ploughing deformation (or of cutting deformation when angular erosive particles are involved) is two-fold: first, it creates the piled-up material for subsequent particles to extrude; and second, in so doing, it so reconfigures the target surface that a disproportionately large number of impact events take place against elements of surface area oriented more nearly

perpendicular to the particle velocity vector than the original target surface. Finally, it is also shown that the exponent relating erosion to velocity is greater for impacts at an angle of 30° than for normal impacts, that this exponent decreases with the post-threshold number of impacts per unit area at both these impact angles, and that this number varies with impact angle and velocity in the opposite manner to steady-state erosion.

INTRODUCTION

In a recent study[1], the present authors used a rotating arm apparatus to study the room temperature erosion of polycrystalline aluminum by 1.58 mm diameter WC-6% Co spheres impacting at normal incidence with velocities ranging from $\sim 10 \text{ m s}^{-1}$ to $\sim 150 \text{ m s}^{-1}$. The results showed that these spheres neither deformed plastically nor fragmented upon impact. Nor, at the particular impact velocities used, did they exhibit any tendency to embed themselves in the target surface. It was also found that the mechanism of material removal responsible for erosion by a stream of such spheres at near-normal incidence is somewhat different from that observed to operate when they impact singly at shallower angles[2-5]. Specifically, normal impacts appeared to cause mass loss only when they occurred in sufficient numbers to first form and then detach thin platelets of metal from regions of crater overlap. These platelets were thinner in proportion to their lateral dimensions than the rather bulky shear lip typically formed along the rim of the exit end of the crater by the ploughing type of deformation associated with a single oblique impact[2-5], and they tended to lie parallel to the target surface rather than to project above it. The obvious inference[1] is that the two mechanisms together account for the characteristic variation of the erosion of a ductile material with impact angle[6-8].

Because the spherical shape of the erosive particles employed allowed the impact event to be modelled analytically, the same study also provided values of

the dynamic hardness of aluminum appropriate to the (high strain and strain rate) conditions pertaining during erosive impacts at different velocities. The availability of these data make it possible to extend to aluminum the numerical model of the oblique impact of a rigid sphere against a rigid-plastic target that has recently been developed by the present authors and successfully applied by them to mild steel[9] and monocrystalline MgO[10].

Accordingly, the twin aims of this work were to: (i) investigate the mechanism(s) of material removal responsible for the erosion of polycrystalline aluminum by obliquely incident streams of rigid spherical particles travelling with different velocities; and (ii) attempt to provide a quantitative explanation of the observed variation of the corresponding single impact crater size and shape with impact angle and velocity.

EXPERIMENTAL METHODS AND MATERIALS

With the single exception that a different rotor arm having appropriately oriented mounting recesses at its ends for the real and dummy specimens was required for each impact angle investigated, the experimental methods, the target material and the erosive particles used in this work were all exactly the same as in the previous study[1]. This modification did, however, necessitate making for each combination of impact angle and velocity a separate determination of the ratio of the number of impacts against the specimen N_i to the number of particles admitted to the apparatus N_p . The results for the particular combinations of interest in the present study--impacts over the whole range of angle at 50 m s^{-1} (69.4 rps) and over velocities ranging from $\sim 10 \text{ m s}^{-1}$ (13.9 rps) to $\sim 130 \text{ m s}^{-1}$ (180 rps) at an angle of 30° --are shown in Figures 1 and 2, respectively. The curve fitted to both sets of data is

$$\frac{N_i}{N_p} = K \frac{f R \sin \alpha_o}{2u}, \quad (1)$$

where f is the frequency of rotation of the rotor arm*, R the radius of the target face of the specimen (6.25 mm), α_0 the nominal impact angle, u the vertical velocity of the (free-falling) particles as they cross the path of the specimen, and K a correction factor to allow for the finite size of the particles, the fact that different portions of the target surface and the rotor arm pass through the screen of particles at slightly different times, and the fact that some particles fall outside the idealized parallel-sided stream. u was determined photographically to be $\sim 3 \text{ m s}^{-1}$, and K is 0.746 in Figure 1 and 0.770 in Figure 2. It should be noted that because u is non-zero the actual impact angle and velocity differ from their nominal values by $\tan^{-1} (u/0.72 f)$ and $[(u + 0.52 f^2)^{\frac{1}{2}} - u]$, respectively.

THEORY

Because the relevant equation of motion cannot be solved analytically, it is necessary to resort to numerical methods to calculate the trajectory followed by a rigid sphere of radius r and mass m after it impacts with velocity v_0 at an angle α_0 against the surface of an ideal rigid-plastic half-space characterized by a dynamic hardness (indentation pressure) p . The present authors have developed a computer program to provide such a solution by an iterative method [9,10]. Their program uses an approach similar to that adopted by Hutchings et al.[4], but incorporates a more accurate description of the area of contact[11,12].

Figure 3 illustrates the situation at some time long enough after first contact that the sphere no longer completely fills the crater it is in the process of creating. At this instant the particle velocity v is directed at an angle α to the target surface, and the arc of contact in the x - y plane subtends an angle 2β at the center of the sphere. α is chosen to be negative when the penetration of the sphere into the target is increasing, since this (i) is

* The actual specimen velocity is $0.72 f$.

consistent with the usual convention that angles measured anti-clockwise from the x-axis are regarded as negative and (ii) avoids the need to use different sets of equations to describe the motion into and out of the target. Gravitational effects are ignored, and the principal retarding force P --which derives from the indentation pressure p acting (uniformly) over the projection of the area of contact onto the plane perpendicular to RO --is assumed to act along RO . In addition, a frictional force μP is assumed to act tangentially through Q .

As long as the sphere remains in contact with the entire surface of the crater, its motion is defined by

$$m\ddot{x} = -\mu P \quad (2)$$

$$\text{and} \quad m\ddot{y} = P. \quad (3)$$

Once the sphere detaches from the target surface at O' , however, the equations governing its translational motion become

$$m\ddot{x} = -P \sin(\alpha + \beta) - \mu P \cos(\alpha + \beta) \quad (4)$$

$$\text{and} \quad m\ddot{y} = P \cos(\alpha + \beta) - \mu P \sin(\alpha + \beta). \quad (5)$$

Each of these pairs of equations can be solved numerically over the part of the motion to which it is applicable by means of an iterative procedure in which time evolves in incremental steps of the appropriate duration. This procedure yields the complete particle trajectory, together with values of crater length, width, depth and volume, particle rebound angle and velocity, time from first contact to detachment at O' and total contact time.

In the cases of mild steel[9] and MgO[10], the assumption that p remained constant throughout the impact event led to good agreement between theory and experiment. However, the normal impact studies performed previously on the polycrystalline aluminum of interest here show[1] that this material work hardens quite rapidly. Specifically, if p is expressed in kgf mm^{-2} and the final diameter ℓ of the impact crater in mm, it was found empirically that

$$p = 41 \ell^{0.24}. \quad (6)$$

Accordingly, in all of the computer modelling reported herein, p (and hence P) was recalculated at each iteration from equation 6. For this purpose ℓ was taken as the radius of the circle of contact prior to detachment at O' and as the length $O'A$ (Figure 3) thereafter.

RESULTS

Figures 4 and 5 show the damage produced on mechanically polished surfaces of 99.9% pure cast aluminum by 1.58 mm diameter WC-6% Co spheres impacting at various angles with a velocity of 50 m s^{-1} and with various velocities at an angle of 30° , respectively. In each micrograph the component of the particle velocity tangential to the target surface runs horizontally across the field of view from left to right.* The grain size of the target was 4-5 μm , so most of the craters can be assumed to be contained within a single grain of random orientation. The most obvious features of note are (i) the characteristic pile-up of displaced material and development of a shear lip at the exit end of the craters formed at the higher impact velocities and lower impact angles and (ii) the random distortions of the crater shape resulting from the random orientation of the grain or grains impacted. In a few cases--notably Figures 5(b) and (d)--the slip lines resulting from the pile-up of material about the crater rim are clearly visible. None of these craters were made at a high enough velocity to produce any detectable mass loss.

After the micrographs shown in Figures 4 and 5 were obtained, a surface profilometer was used to make a parallel series of traces across each crater in the direction of the tangential component of the particle velocity. For each crater these traces were spaced 50 μm apart, and the deepest one of the series (the major diametral trace) was presumed to define the length and the depth of

* The same convention is also adopted in Figures 6, 7, 24 and 25.

that crater relative to the original target surface. The solid lines in Figures 6 and 7 show the major diametral traces corresponding to the craters seen in Figures 4 and 5, respectively, at a vertical to horizontal magnification of 1.5x; and the length and depth data taken from these and similar traces of craters formed at different impact velocities and/or angles are plotted in Figures 8 to 11. In addition, the trapezoidal rule was used to determine the volume of each crater (relative to the same surface) from planimetric measurements of the areas defined by the (complete) set of traces obtained from it. The results of these determinations are plotted in Figures 12 and 13.

The dotted lines superimposed on the measured traces in Figures 6 and 7 and both the dotted and the solid lines drawn through the data points in Figures 8 to 13 were obtained from the computer model of the impact event. In these six figures the deviations of the actual impact angles and velocities from their nominal values were taken into account when computing the dotted lines, but not when computing the solid lines. These deviations were also ignored in computing the dotted traces in Figures 6 and 7.

In all of this modelling, a constant value of 0.1 was used for the coefficient of friction, although there is evidence (from experiments in which rapidly spinning (steel) balls were either brought into continuous contact with [13] or dropped onto [14] flat plate specimens of different metals) that this parameter decreases with increase in both the velocity and the depth of penetration of the sphere. The justification for this simplification is that the calculations performed previously for mild steel [9] and MgO [10] targets show the crater dimensions obtained from the model to be relatively insensitive to two-fold variations in the coefficient of friction.

The values of the crater dimensions and other impact characteristics obtained from the computer model are also sensitive to the time increment between successive iterations of the basic algorithm used in their evaluation. This is

particularly true of the crater volume under conditions of near-normal incidence. The reason is that this quantity differs from all others calculated in that it derives not from the total number of iterations occurring during impact, but only from those that take place after the sphere detaches from the target surface at 0' (Figure 3)--an event that occurs later and later in the collision as the angle of impact approaches 90°. As a result, it proved necessary to reduce the time increment from 0.1 to 0.02 μ s at impact angles greater than 85° in order to maintain an accuracy of better than 1% in all computations.

Several features of Figures 6 to 13 should be noted. In particular, the experimental profilometer traces (Figures 6 and 7) show the increasing importance of pile-up of displaced material about the exit end of the crater at shallower impact angles and higher impact velocities; and comparison of these traces with the traces obtained from the computer model shows how this breaks down in such situations due to its failure to take account of where the material displaced by the sphere moves to. The same failure of the model is also apparent in its systematic overestimation of crater length at shallow angles of impact (Figure 8) and high impact velocities (Figure 9). Despite these difficulties, however, the model is very successful in predicting both crater depth and crater volume as functions of impact angle and velocity (Figures 10 to 13), particularly when the differences between the actual and nominal values of these variables are taken into account. The measured traces also provide a quantitative indication of the amount of surface relief produced by individual impacts: typically, the angle between the surface normals at the entrance and exit ends of a major diametral trace ranges from 2 or 2.5 times the impact angle for shallow impacts to 1 or 1.5 times this angle at near normal incidence.

The mass loss data obtained by varying the impact angle while holding the impact velocity constant at 50 m s⁻¹ are shown in Figures 14 and 15; and Figures 16 to 18 present further such data obtained by varying the impact velocity at a

AD-A068 571

PENNSYLVANIA STATE UNIV UNIVERSITY PARK MATERIALS RE--ETC F/G 7/4
MECHANISMS OF EROSION.(U)
AUG 80 N H MACMILLAN

DAA629-79-C-0104

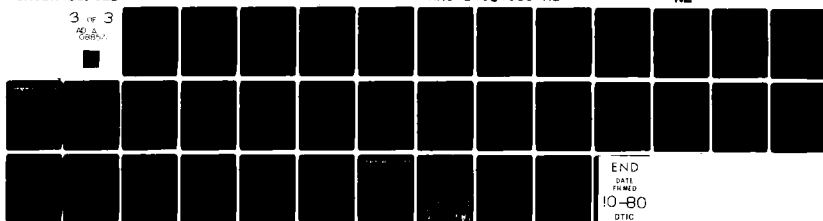
UNCLASSIFIED

ARO-14084.13-MS

NL

3 of 3

40-10-80



END
DATE
FILMED
10-80
DTIC

constant impact angle of 30° . Each curve is characterized by a threshold number of impacts below which the mass loss was not measurable (i.e., $\lesssim 10 \mu\text{g}$), a succeeding incubation period during which the mass loss increases with increasing number of impacts, and a steady-state (linear) erosion regime in which the mass loss per impact remains constant. The curves fitted to the data in the incubation period are power functions of the form

$$m_e = b (N_i - N_o)^\beta, \quad (7)$$

where m_e is the mass of material eroded away, N_o is the threshold number of impacts, and b and β are constants for a given erosive environment. And in the steady-state erosion regime straight lines are fitted to the data.

It follows that the dimensionless erosion E , which may be defined by

$$E = \frac{1}{m} \frac{dm_e}{dN_i}, \quad (8)$$

is given by

$$E = \frac{b\beta}{m} (N_i - N_o)^{\beta-1} \quad (9)$$

during the incubation period and by the ratio of the slope of the mass loss curve to the mass of one erosive sphere during steady-state erosion. Under these latter conditions, the variation of erosion with impact velocity can be represented by an expression of the form

$$E = a v_o^\gamma, \quad (10)$$

where a and γ are constants. In the incubation regime, however, a and γ are dependent on the post-threshold number of impacts $N_i - N_o$, and the value of the velocity exponent γ appropriate to any particular value of $N_i - N_o$ has to be obtained by a two-step process. This involves first using equation 8 to evaluate E at the chosen value of $N_i - N_o$ for several different values of v_o and then using equation 10 to find the value of γ most nearly consistent with the resultant pairs of values of E and v_o .

The results obtained by analyzing the mass loss data from Figures 14 to 18 according to this scheme are presented in Figures 19 to 23. Figure 19 shows that, when the impact velocity is held constant at 50 m s^{-1} , the steady-state erosion varies with impact angle in very much the same manner as for other ductile metals[6-8]--i.e., it rises rapidly from zero at glancing contact to a maximum at an angle of 20 to 30° , and then falls off with further increase in angle. Usually this decrease is monotonic, but the present data--like another recently published set of data for aluminum[15]--exhibit a slight increase in erosion as the impact angle approaches 90° . The corresponding variation of the threshold number of impacts for detectable mass loss is shown in Figure 20, and it is not surprising to see that this number varies with impact angle roughly as the inverse of the steady-state erosion. Figures 21 and 22 show the way in which the same two parameters vary with impact velocity at an impact angle of 30° . The solid lines fitted to these data imply velocity exponents of 2.98 and -2.67, respectively, which may be compared with the values of 3.3 and -2.5* obtained at normal impact (dashed lines)[1]. In analogous fashion, Figure 23 provides a comparison of the way in which the velocity dependence of erosion (i.e., γ in equation 10) varies during the incubation period at impact angles of 30° (data points and solid line) and 90° (dashed line)[1].

Finally, Figures 24 and 25 show the target surface topographies resulting from steady-state erosion at the same impact angles and velocities as used to obtain the single impact craters presented in Figures 4 and 5, respectively. Note that in none of these micrographs is there any evidence either of target melting or of erosive particles or fragments thereof becoming embedded in the target. Nor is there any evidence of formation of the sort of "ribbon-like" debris characteristic of micromachining; and only in a few places is there any

* Not -5.8 as erroneously reported in reference 1.

suggestion that bulky shear lips were formed by ploughing deformation of the target. Rather, just as at normal incidence[1], the dominant feature of each micrograph is a large number of thin platelets lying more-or-less parallel to the original target surface. For completeness, it is also noted that examination of the spent spheres showed no evidence of either plastic deformation or fragmentation.

DISCUSSION

The absence of any detectable mass loss associated with the formation of any of the single impact craters shown in Figures 4 and 5 is consistent with previous observations[2,16] that obliquely impacting spherical particles cause detachment of shear lips from the surface of polycrystalline 1100 aluminum only at impact velocities $> 200 \text{ m s}^{-1}$. Likewise, shear lip formation at the rims of the craters produced by normal impacts of similar particles against {100}, {110} and {111} oriented aluminum single crystals begins only at velocities of this order[17]. Such observations confirm graphically a result that has long been known from studies of abrasion[18]--namely, that "ploughing" deformation is a very inefficient method of removing material from the surface of a workpiece (target). The corollary to this statement is the inference that shear lip detachment is unlikely to play a major role in the erosion of ductile materials by spherical particles at the impact velocities involved in the present work.

The preceding statement notwithstanding, single impact studies can contribute to understanding the mechanisms of material removal responsible for such erosion. In the present case, for example, the major diametral traces of single impact craters shown in Figures 6 and 7 serve to delineate the substantial surface relief that can develop during erosion. Seen from the perspective of subsequent erosive particles, the effect of this relief is to foreshorten the entrance sides of the pre-existing craters, where the local surface has been made more

nearly parallel to the impact velocity vector, and to emphasize the exit sides, where piled-up material presents a local surface more nearly normal to this vector. In consequence, erosion at a given, supposedly constant angle of impact actually involves impacts distributed over a wide range of angles in such a manner that more occur at the higher angles than at the shallower angles. Furthermore, because of the shape of the exit end of a crater, these higher angle impacts take place not against a massive half-space, but against hillocks that are much smaller than the impacting particles and are little constrained as to how they deform. It is therefore suggested that (i) platelet formation and detachment is the dominant mechanism of material removal under oblique as well as near-normal impact conditions, and (ii) this process occurs under oblique impact conditions by the extrusion of the hillocks formed at the exit ends of craters between subsequently arriving erosive particles and the underlying (and already work hardened) target material.* Shear lip detachment also occurs from time to time of course--as, for example, from the righthand (exit) end of the most prominent crater in Figure 25(d)--but from the evidence of Figures 24 and 25 it has to be concluded that this is a far less important mechanism of material removal than platelet formation and detachment over the whole range of erosive conditions examined in this work. The formation of similar platelets by the impact of spherical steel shot against 1100 aluminum at an angle of 60° has also been reported[20].

Single impact studies are also useful in the study of erosion because they provide measurements of crater dimensions that can be used to test mathematical models of the mechanical behavior of solids at high strain rates. In this respect, the present studies show that a simple constitutive relationship,

* Under normal impact conditions "ridges" analogous to these hillocks develop in the regions of crater overlap[1,19].

derived empirically from normal impact studies and incorporating a power law representation of work hardening[1], can successfully predict the variation with both impact angle and velocity of several of the characteristic dimensions of the craters formed by obliquely impacting spheres. Specifically, the model very accurately predicts both the profile of the entrance side of the crater (Figures 6 and 7) and the crater depth (Figures 10 and 11). It is less successful in predicting the crater length, particularly at shallower impact angles and higher impact velocities (Figures 8 and 9), because it fails to take into account the pile-up of displaced material at the exit end of the crater; but in spite of this it provides a remarkably accurate estimate of crater volume (Figures 12 and 13).

Comparison of the plots of crater volume (Figures 12 and 13) and mass loss (Figures 14 and 18) show that the fraction of the displaced material that is actually removed from the target by a single impact during steady-state erosion increases sharply with increasing impact velocity and decreasing impact angle. At an impact angle of 30° , for example, the fraction increases from < 0.01 at 10 m s^{-1} to > 0.20 at 130 m s^{-1} ; and at a velocity of 50 m s^{-1} , the corresponding increase is from ~ 0.01 at normal incidence to ~ 0.18 at an impact angle of 10° . Likewise, when mild steel is eroded by the impact of hardened steel spheres at an angle of 30° , the corresponding fraction is 0.08 at an impact velocity of 50 m s^{-1} and 0.25 when this velocity increases to 400 m s^{-1} [3-5]. Since increases in impact velocity and decreases in impact angle also lead to increased pile-up of material at the exit ends of impact craters, these observations support the contention that mass loss occurs primarily by the extrusion of this piled-up material into platelets during subsequent impacts. In addition, they suggest that attempts should be made in future work to seek some sort of quantitative relationship between (say) the amount of material piled-up above the level of the original surface and the mass loss per impact or the size and shape of the

debris produced. Establishment of such a relationship would provide the link between crater volume and mass loss necessary to give the theory a quantitative predictive capability.

Except in the case of "type II cutting" by angular particles having small negative rake angles, for which the entire contents of the crater are removed [4,5,21,22], such a link between crater volume and mass loss is missing from all theories of ductile erosion. Consequently, critical comparisons of competing theories with experiment can only be made in qualitative rather than quantitative terms--a limitation that greatly reduces their value. The problem is graphically illustrated by comparing the present data on the variation of steady-state erosion with impact angle (Figure 19) with those obtained from similar studies by other authors[23-25]. Although these studies used a variety of sizes of spherical and angular particles made of several different materials, and consequently involved different amounts of "type I cutting" and ploughing[4,5,21,22], they all found a qualitatively similar dependence of steady-state erosion on impact angle. Where the results differ is in the value of the angle at which the maximum erosion occurs, the ratio of the erosion at any given angle to the maximum erosion and so-on. Intuitively, it seems reasonable to assume that these quantitative differences derive from the different crater geometries and amounts of pile-up of displaced material produced by the different erosive particles involved. But proof of this assumption will require a considerable amount of accurate, quantitative experimental work to establish whatever relationships exist between particle geometry, crater geometry, pile-up and mass loss.

Much the same sort of difficulty arises in trying to understand in detail the velocity dependence displayed by the present erosion data. For example, Figures 21 and 23, respectively, show that the exponent relating erosion to impact velocity is lower at an impact angle of 30° than at normal incidence both

under steady-state conditions and during the incubation period; and the same trend has previously been observed under steady-state conditions for copper[26], 1100 aluminum[27] and 6061-T0 aluminum alloy[28], although the values of the exponents involved are somewhat different. Thus, switching from eroding aluminum with non-fragmenting WC-6% Co spheres, which exhibited no tendency to embed themselves as they ploughed across the target surface, to eroding copper with angular Al_2O_3 particles, many of which fragmented as they cut the target surface and left pieces of themselves embedded in it, did not alter the basic trend in the data, but merely the numbers involved. However, the only theoretical explanation of the observed trend extant is based on a cutting model of erosion which assumes that the entire contents of the crater are detached from the target at each impact[15,27].

In conclusion, it is noted that Figures 20 and 23 show the threshold number of impacts for detectable mass loss to vary with impact angle and velocity more-or-less inversely as the steady-state erosion, as might intuitively be expected. Again, however, it is only the trend in the data, and not the numerical values involved, that can easily be rationalized, and it remains unclear why the steady-state erosion is more sensitive to velocity at normal incidence than at an impact angle of 30° while the reverse is true for the threshold number of impacts.

ACKNOWLEDGEMENT

Work supported by the U.S. Army Research Office under Grant. No. DAAG29-79-C-0104.

REFERENCES

- 1 D. G. Rickerby and N. H. Macmillan, *Wear*, 60 (1980) 369.
- 2 I. M. Hutchings and R. E. Winter, *Wear*, 27 (1974) 121.
- 3 I. M. Hutchings and R. E. Winter, *J. Phys. D*, 8 (1975) 8.
- 4 I. M. Hutchings, R. E. Winter and J. E. Field, *Proc. R. Soc. London, Ser. A*, 348 (1976) 379.
- 5 I. M. Hutchings, *Erosion: Prevention and Useful Application*, Special Tech. Publ. No. 664, ASTM, Philadelphia, Pennsylvania (1978) 59.
- 6 C. M. Preece and N. H. Macmillan, *Annu. Rev. Mater. Sci.*, 7 (1975) 95.
- 7 A. W. Ruff and S. M. Wiederhorn, *Erosion (Treatise on Materials Science and Technology, Vol. 16)* Academic Press, New York (1979) p. 69.
- 8 G. P. Tilly, *Wear (Treatise on Materials Science and Technology, Vol. 13)* Academic Press, New York (1979), p. 287.
- 9 D. G. Rickerby and N. H. Macmillan, *On the Oblique Impact of a Rigid Sphere Against a Rigid-Plastic Solid*, *Int. J. Mech. Sci.*, in press.
- 10 D. G. Rickerby and N. H. Macmillan, *The Effect of Approach Direction on Damage in MgO Due to Spherical Particle Impact*, *J. Mater. Sci.*, in press.
- 11 G. Birkhoff, G. D. Birkhoff, W. E. Bleick, E. H. Handler, F. D. Murnaghan and T. L. Smith, *Ricochet off Water*, AMP Memo. 42.4M (1944).
- 12 W. Johnson and S. R. Reid, *J. Mech. Eng. Sci.*, 17 (1975) 71.
- 13 F. P. Bowden and E. H. Freitag, *Proc. R. Soc. London, Ser. A*, 248 (1958) 350.
- 14 F. P. Bowden and P. A. Persson, *Proc. R. Soc. London, Ser. A*, 260 (1961) 433.
- 15 I. Finnie, A. Levy and D. H. McFadden, *Erosion: Prevention and Useful Application*, Special Tech. Publ. No. 664, ASTM, Philadelphia, Pennsylvania (1978) 36.
- 16 P. G. Shewmon, *Erosion by Liquid and Solid Impact*, Cavendish Laboratory, Cambridge, England (1971) Paper No. 37.
- 17 N. C. Sink, M.S. Thesis, The Pennsylvania State University, University Park, Pennsylvania (1978).
- 18 L. E. Samuels, *Sci. Am.*, 239 (1978) 132.
- 19 T. Christman and P. G. Shewmon, *Wear*, 52 (1979) 57.

- 20 A. V. Levy, Erosion by Liquid and Solid Impact, Cavendish Laboratory, Cambridge, England (1979) Paper No. 39.
- 21 R. E. Winter and I. M. Hutchings, Wear, 29 (1974) 181.
- 22 I. M. Hutchings, Int. J. Mech. Sci., 19 (1977) 45.
- 23 J. G. A. Bitter, Wear, 6 (1963) 169.
- 24 J. H. Neilson and A. Gilchrist, Wear, 11 (1968) 111.
- 25 G. L. Sheldon and I. Finnie, J. Eng. Ind. (Trans. ASME B) 88 (1966) 387.
- 26 L. K. Ives and A. W. Ruff, Erosion: Prevention and Useful Application, Special Tech. Publ. No. 664, ASTM, Philadelphia, Pennsylvania (1978) 5.
- 27 I. Finnie and D. H. McFadden, Wear, 48 (1978) 181.
- 28 G. L. Sheldon and A. Kanhere, Wear, 21 (1972) 195.

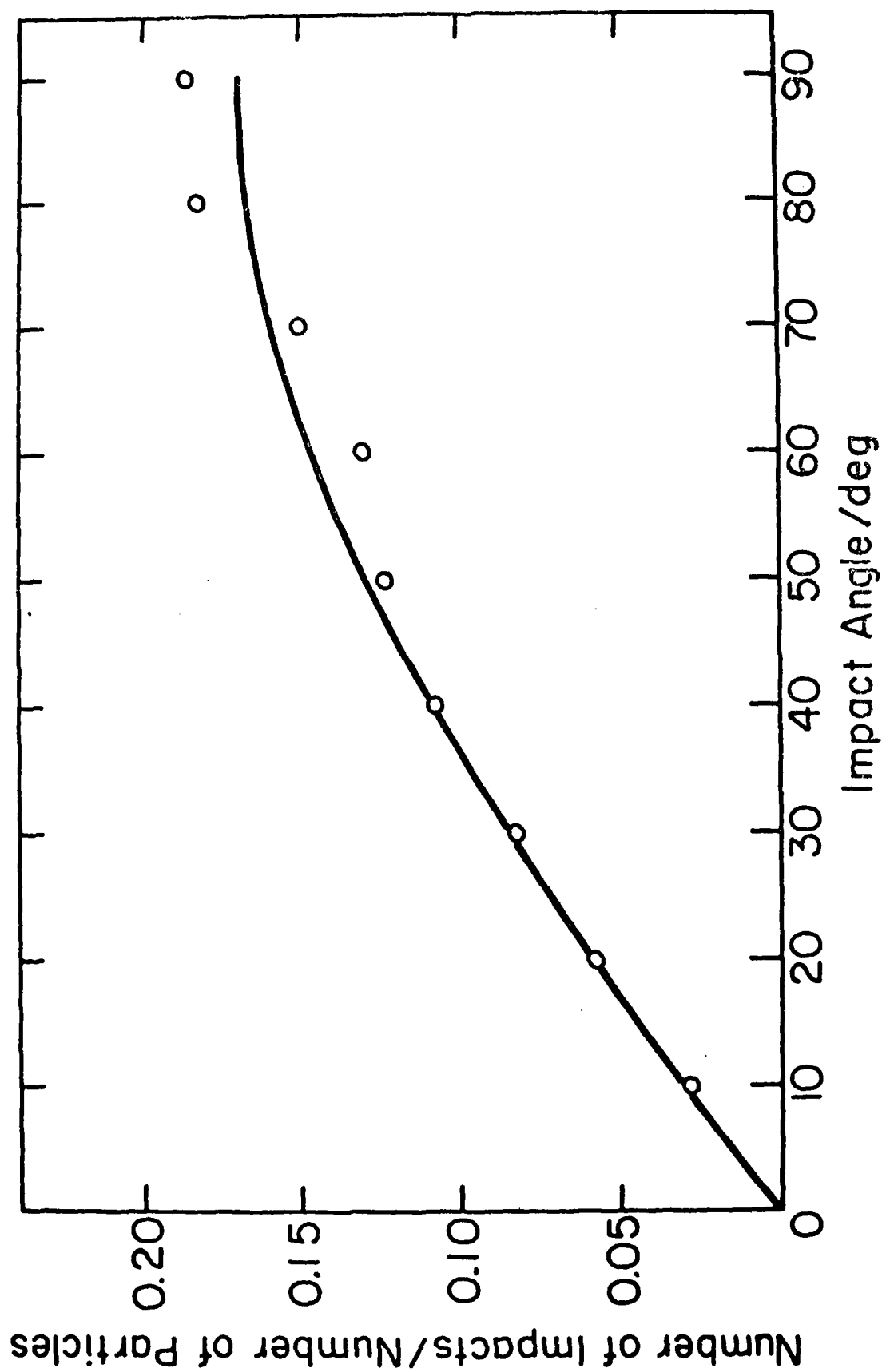


Figure 1 Ratio of number of impacts to number of particles entering the apparatus versus nominal impact velocity of 50 m s^{-1} .

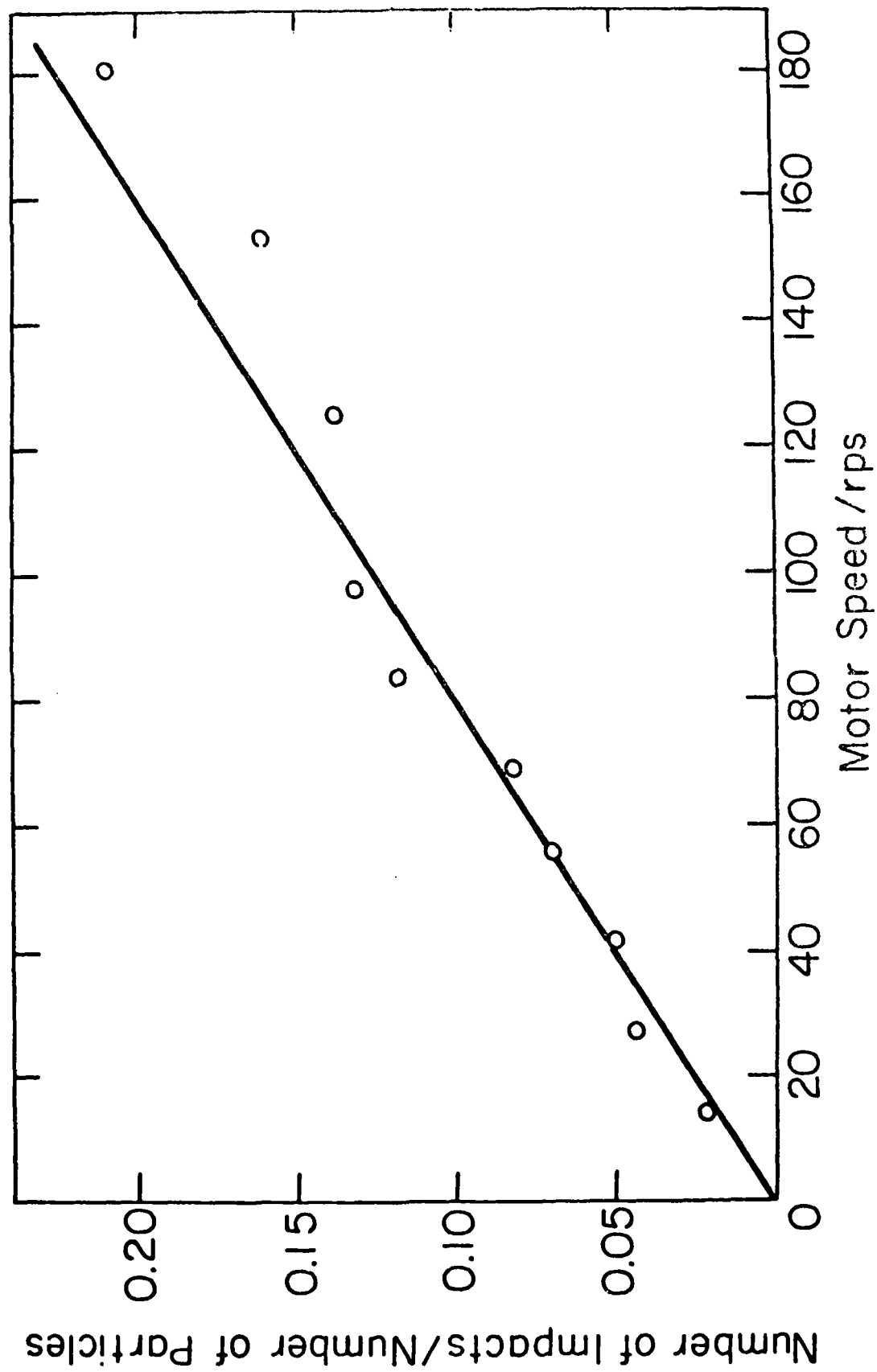


Figure 2 Ratio of number of impacts to number of particles entering the apparatus versus motor speed ($1/f$) at a nominal impact angle of 30° .

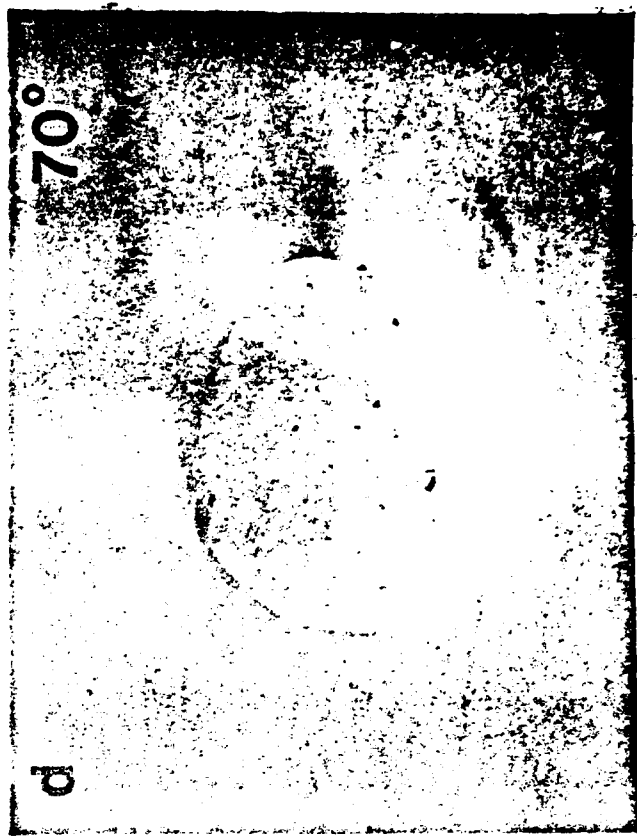
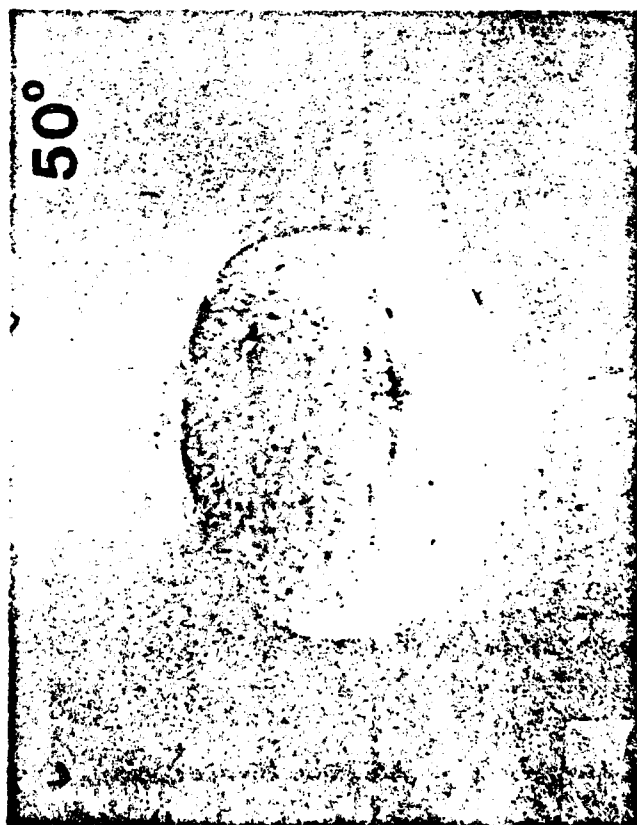
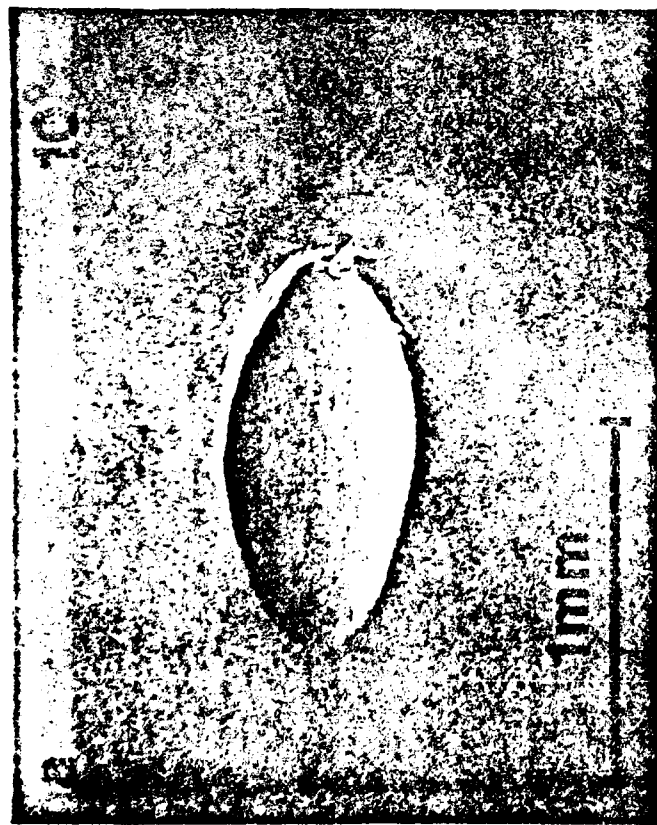


Figure 4 Damage produced by single particles impacting with a nominal velocity of 50 m s^{-1} at various nominal angles.

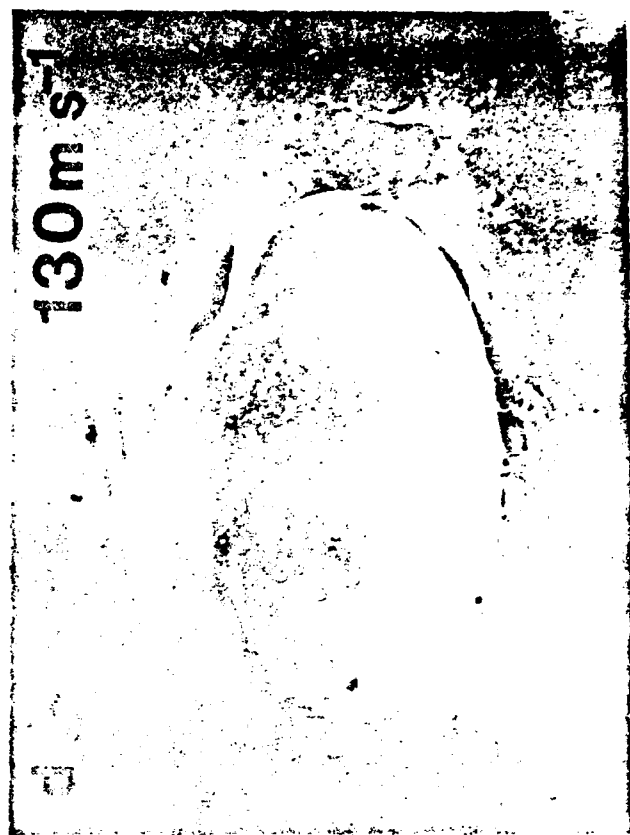
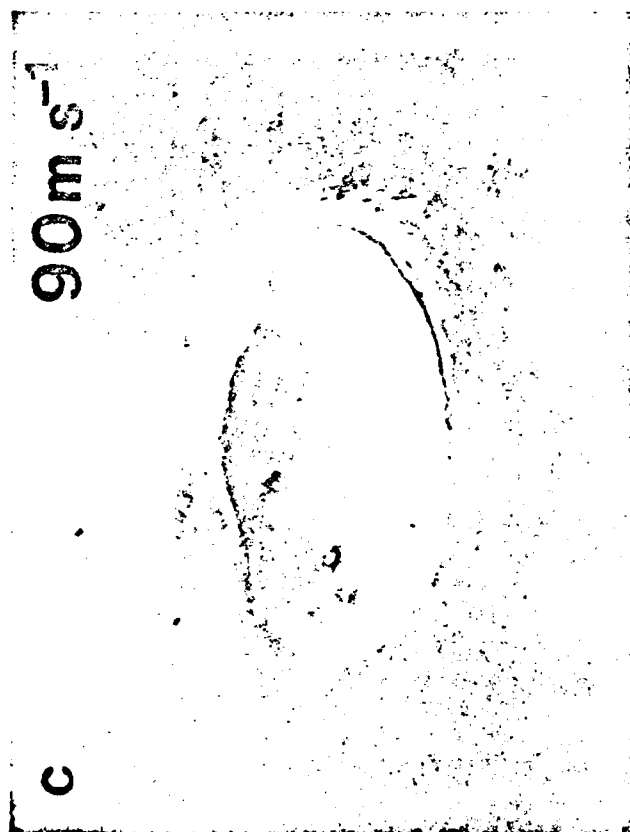
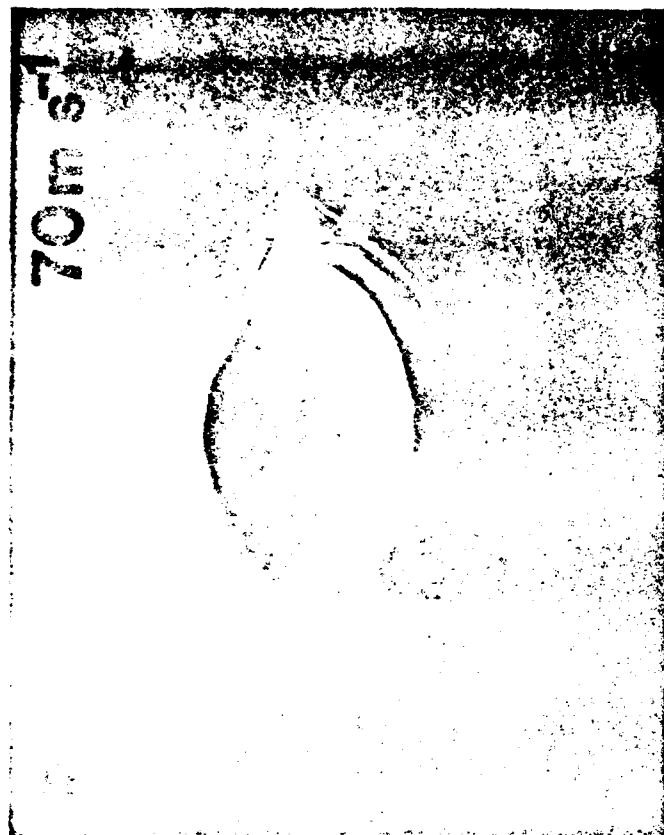
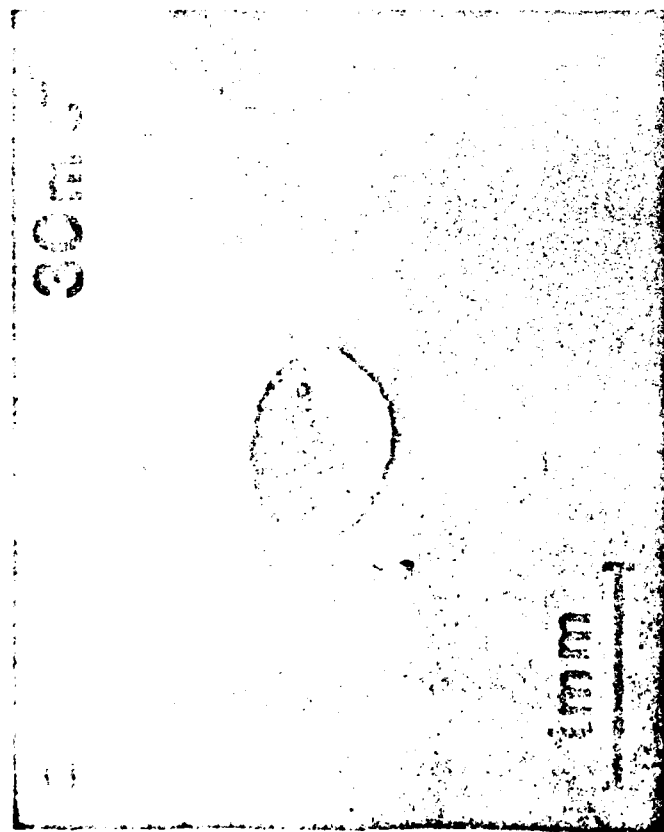


Figure 5 Damage produced by single particles impacting at a nominal angle of 30° with various nominal velocities.

0.1 mm
0.2 mm

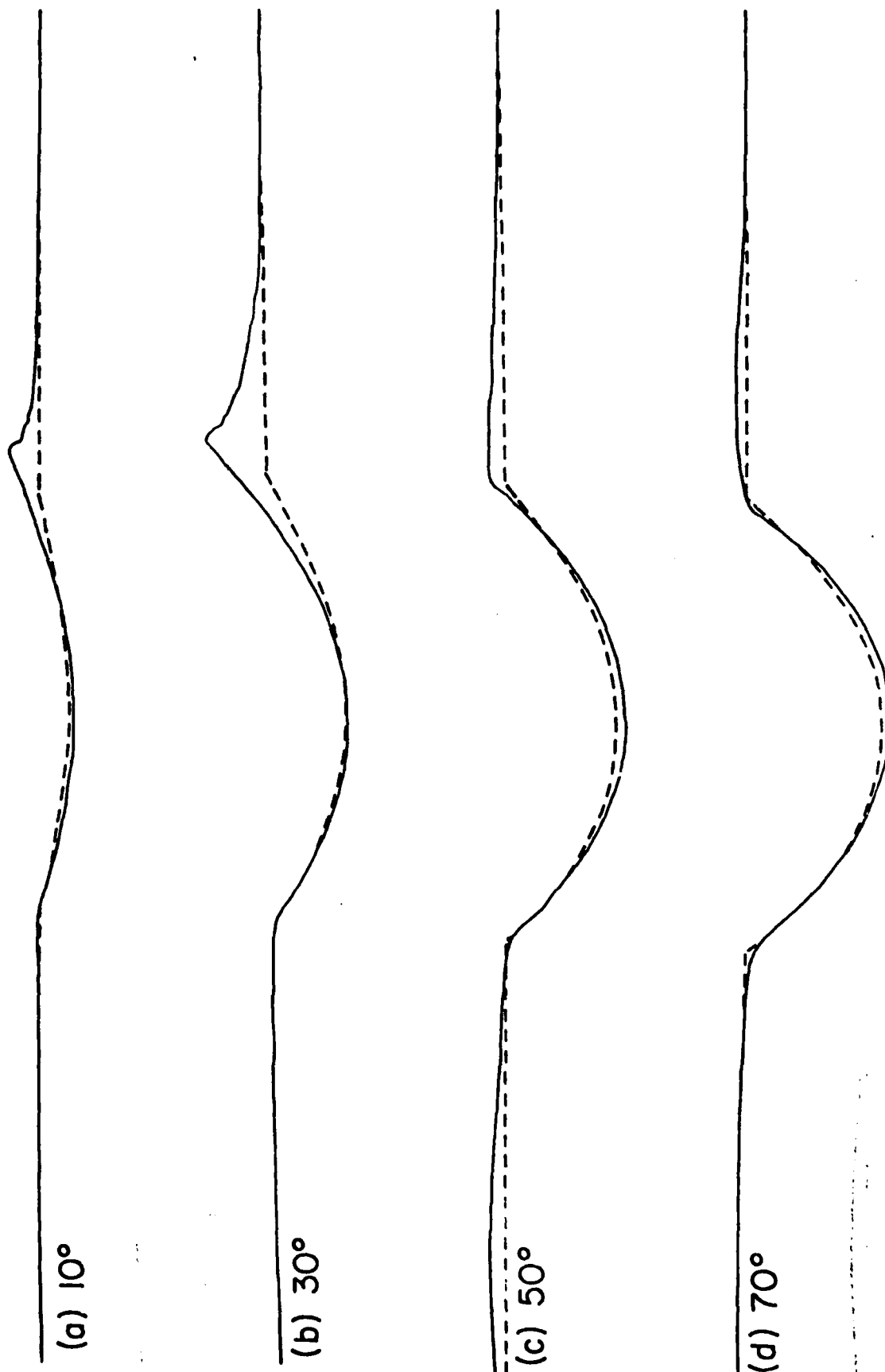



Figure 6 Measured (solid line) and calculated (dotted line) major diametral traces of craters produced by single particles impacting with a nominal velocity of 50 m s^{-1} at various nominal angles.

0.1 mm  0.2 mm

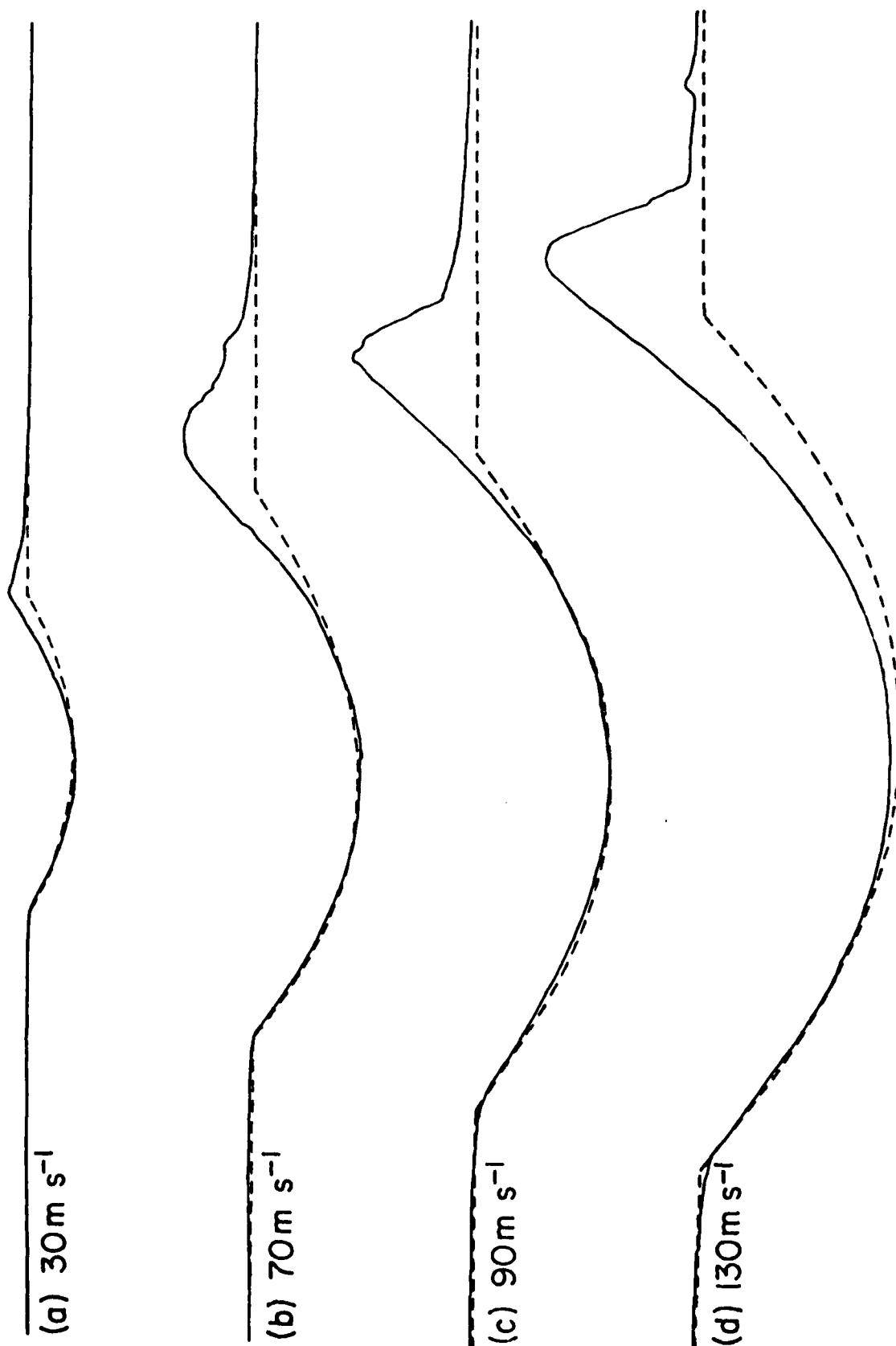


Figure 7 Measured (solid line) and calculated (dotted line) major diametral traces of craters produced by single particles impacting at a nominal angle of 30° with various nominal velocities.

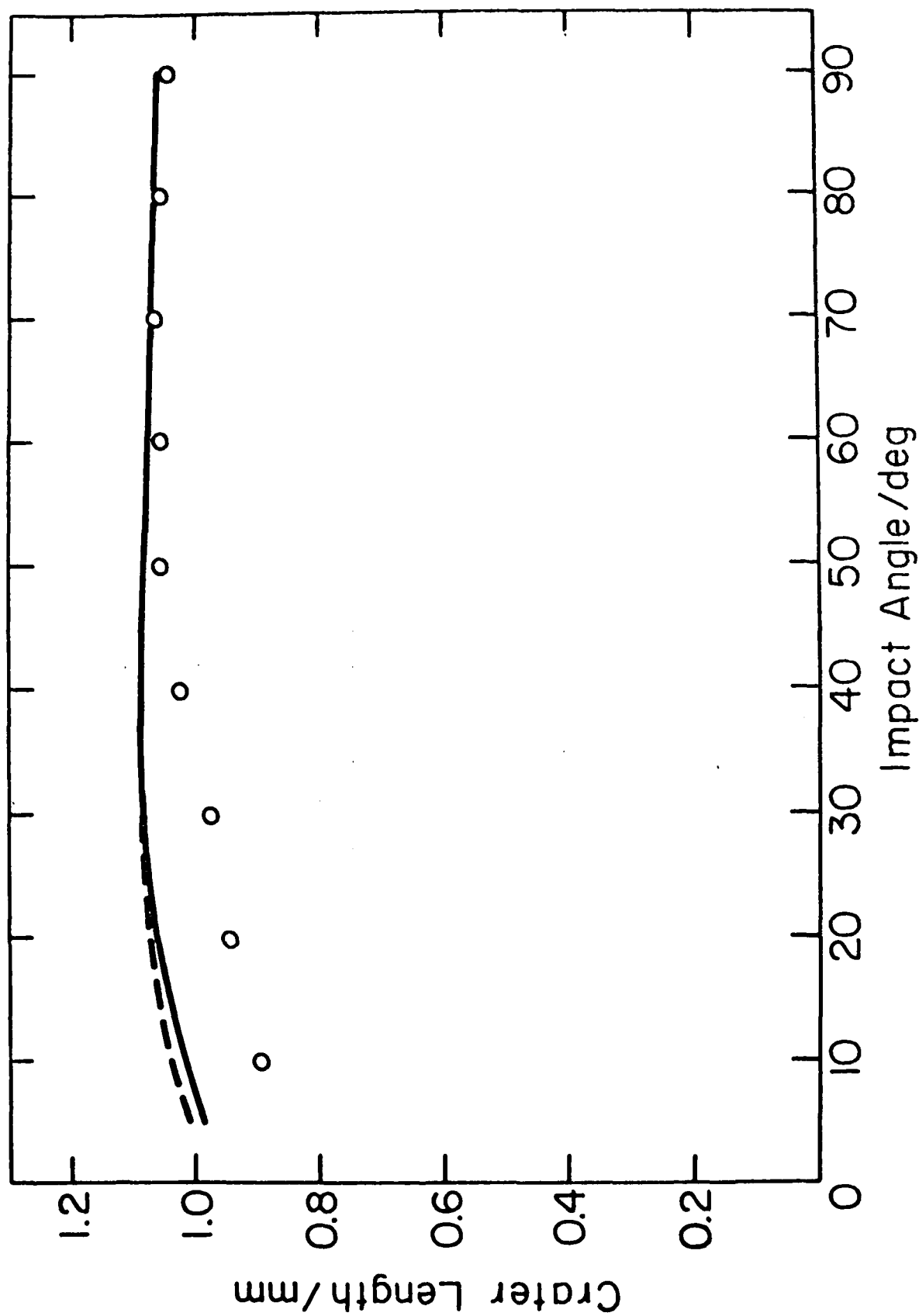


Figure 8 Crater length versus nominal impact angle at a nominal impact velocity of 50 m s^{-1} .
Data points measured, lines calculated.

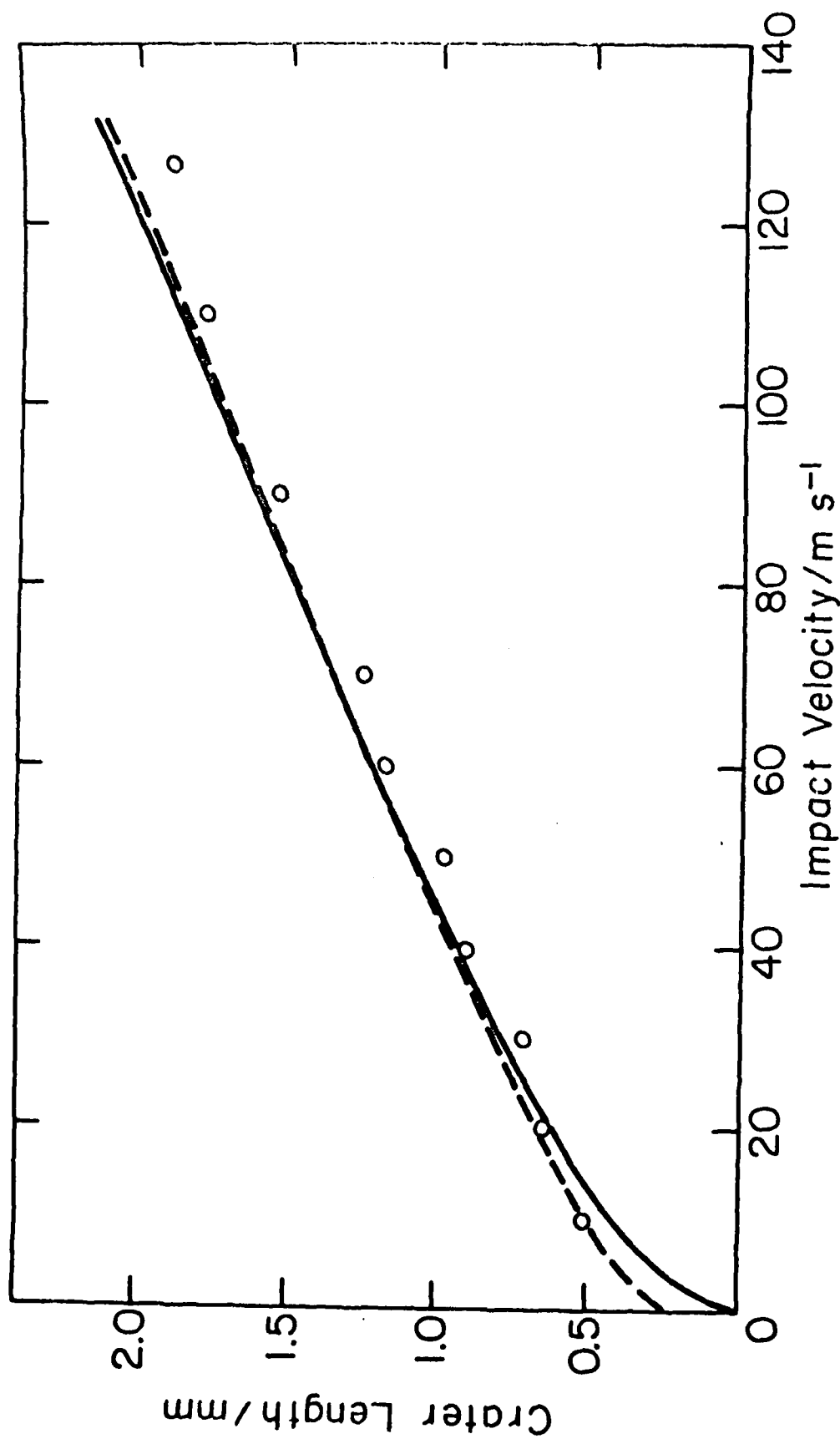


Figure 9 Crater length versus nominal impact velocity at a nominal impact angle of 30°. Data points measured, lines calculated.

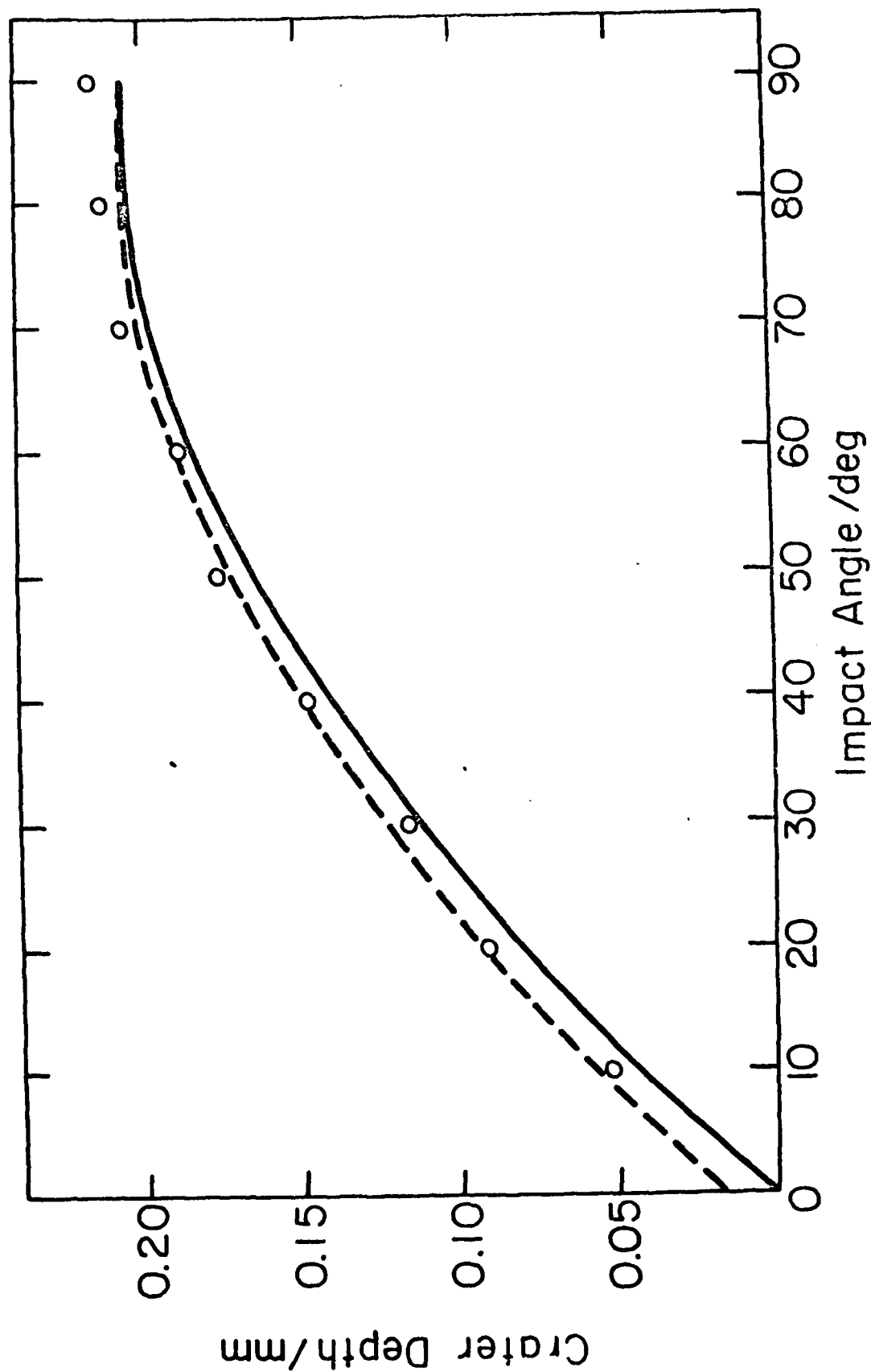


Figure 10 Crater depth versus nominal impact angle at a nominal impact velocity of 50 m s^{-1} .
Data points measured, lines calculated.

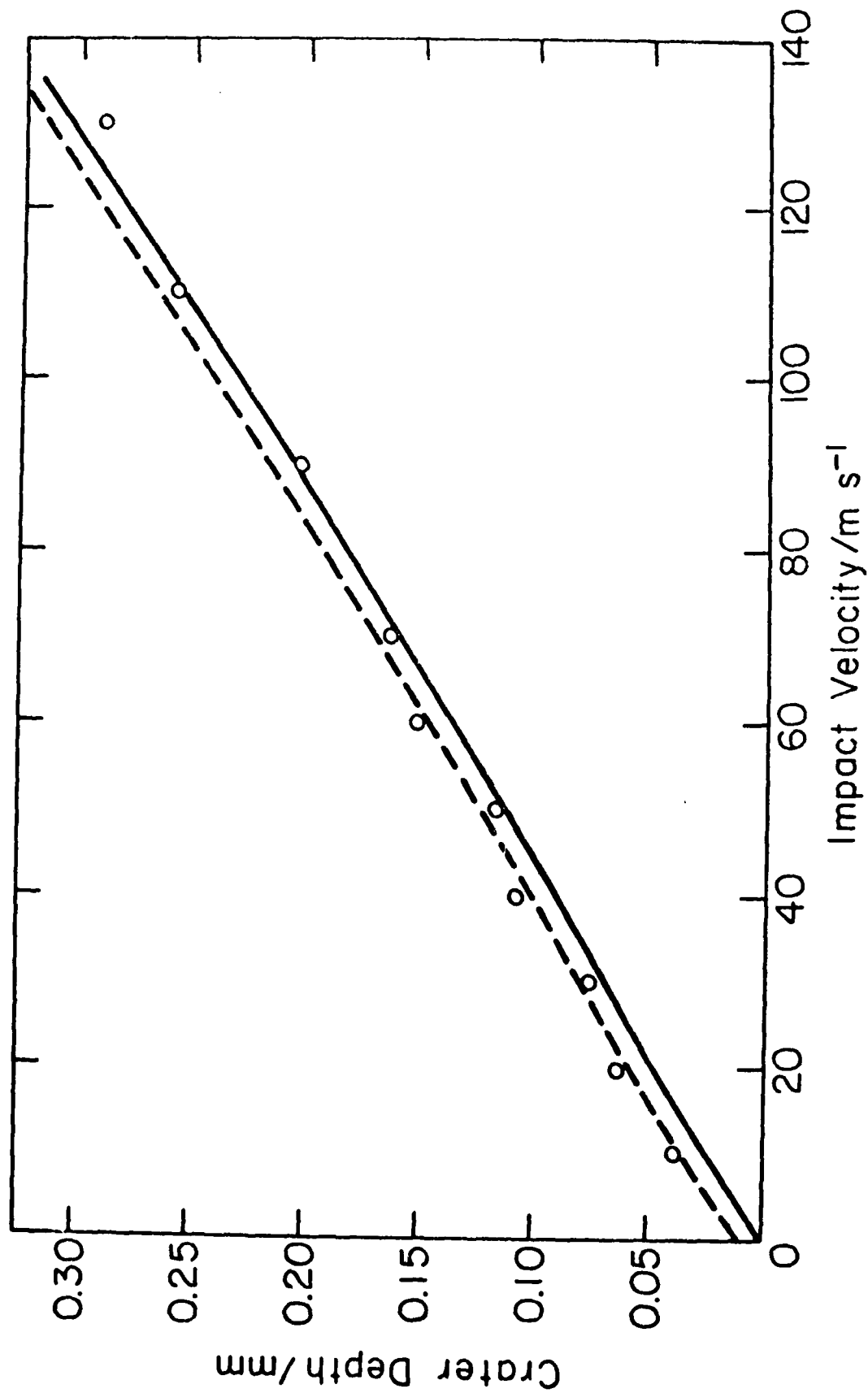


Figure 11 Crater length versus nominal impact velocity at a nominal impact angle of 30°. Data points measured, lines calculated.

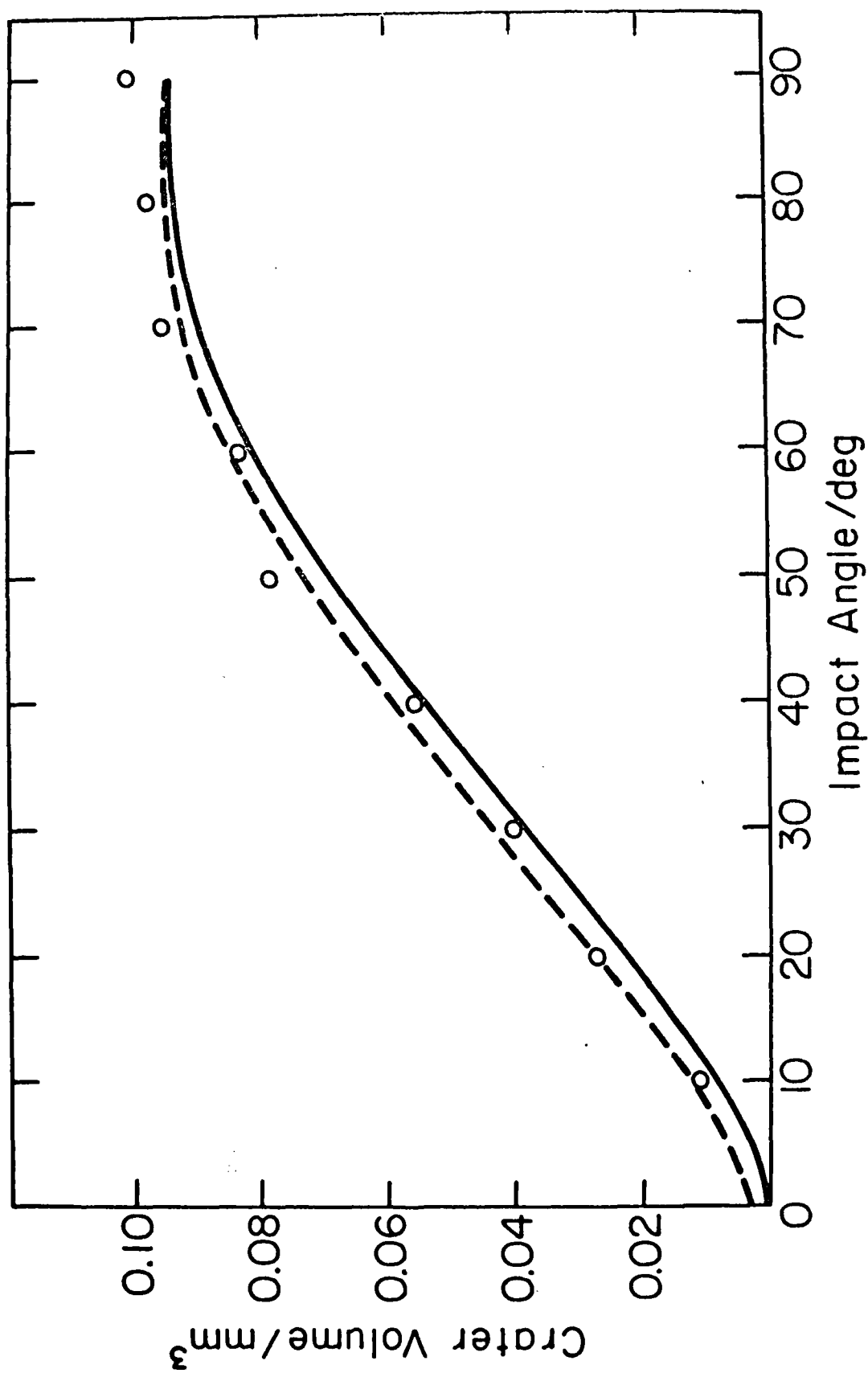


Figure 12 Crater volume versus nominal impact angle at a nominal impact velocity of 50 m s⁻¹.
Data points measured, lines calculated.

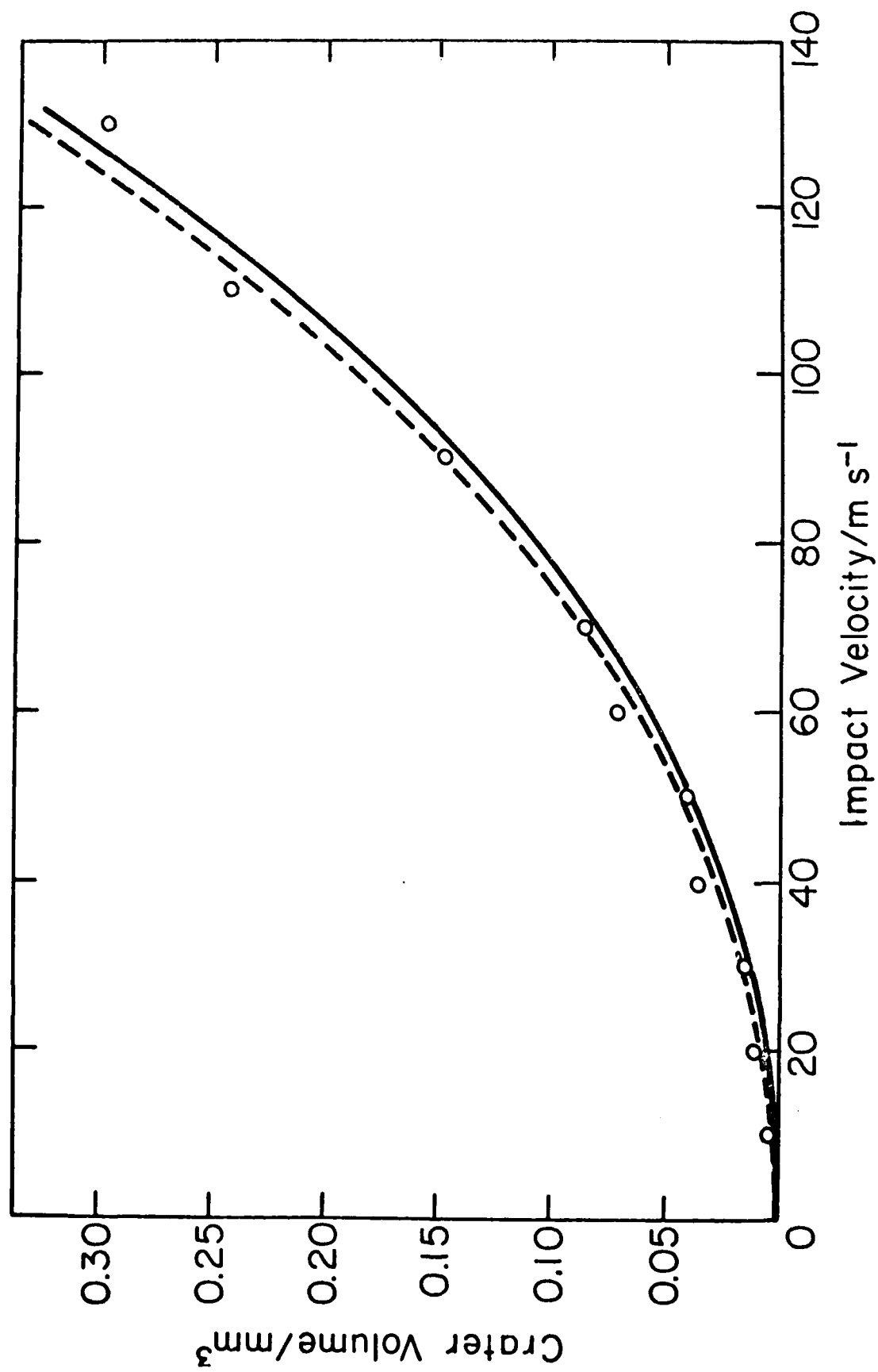


Figure 13 Crater volume versus nominal impact velocity at a nominal impact angle of 30°. Data points measured, lines calculated.

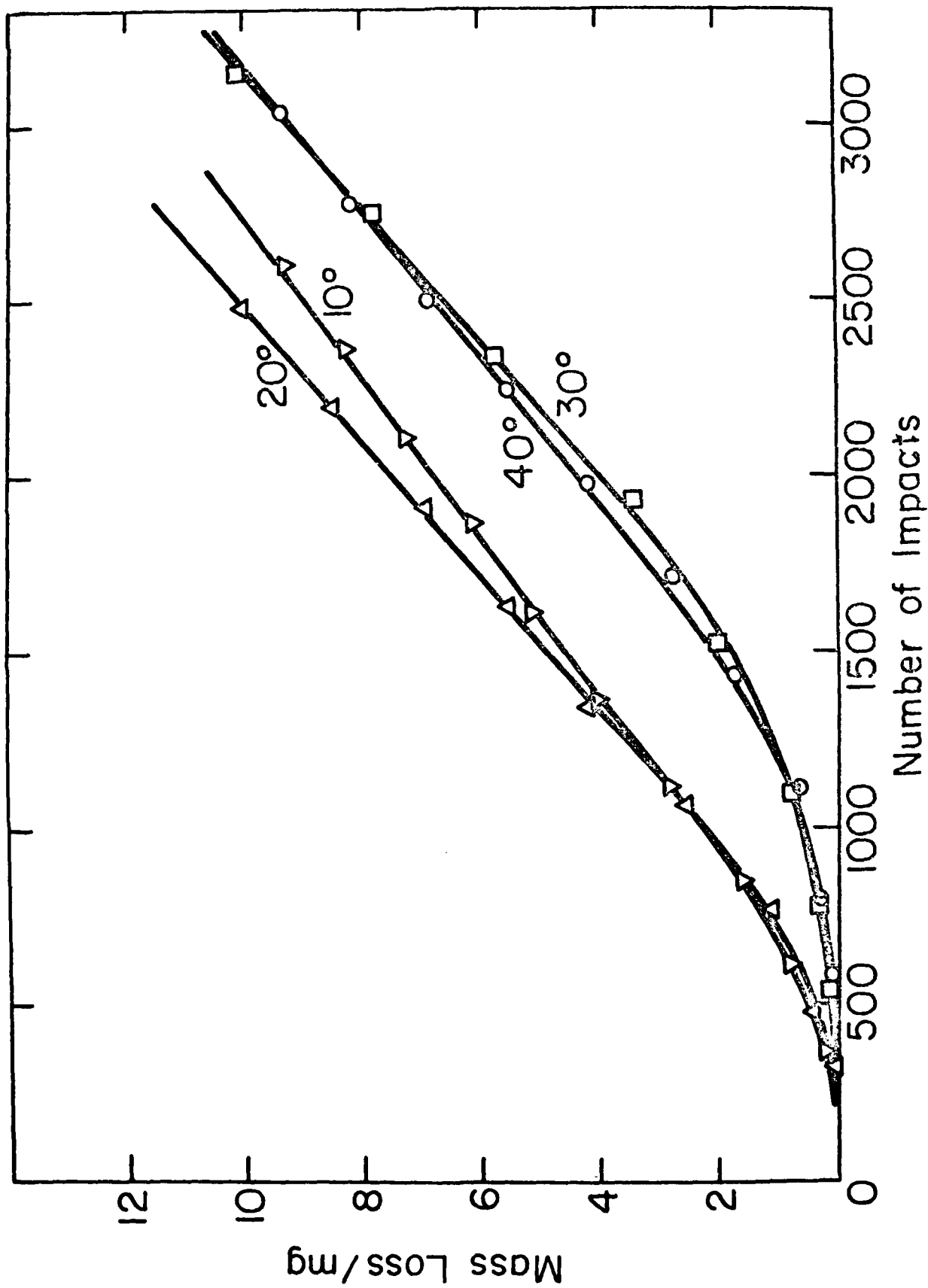


Figure 14 Mass loss versus number of impacts at various nominal impact angles and a nominal impact velocity of 50 m s^{-1} .

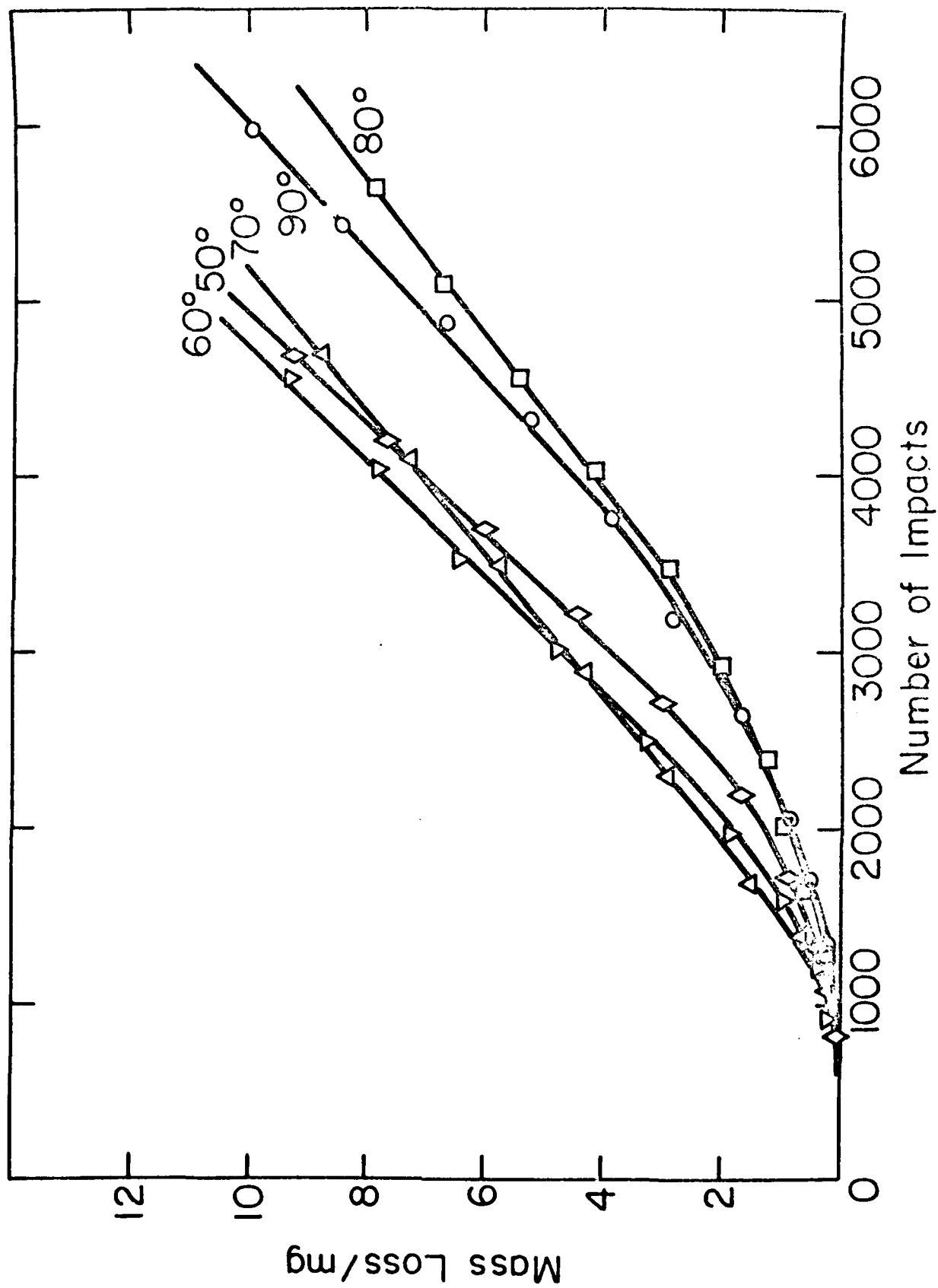


Figure 15 Mass loss versus number of impacts at various nominal impact angles and a nominal impact velocity of 50 m s^{-1} .

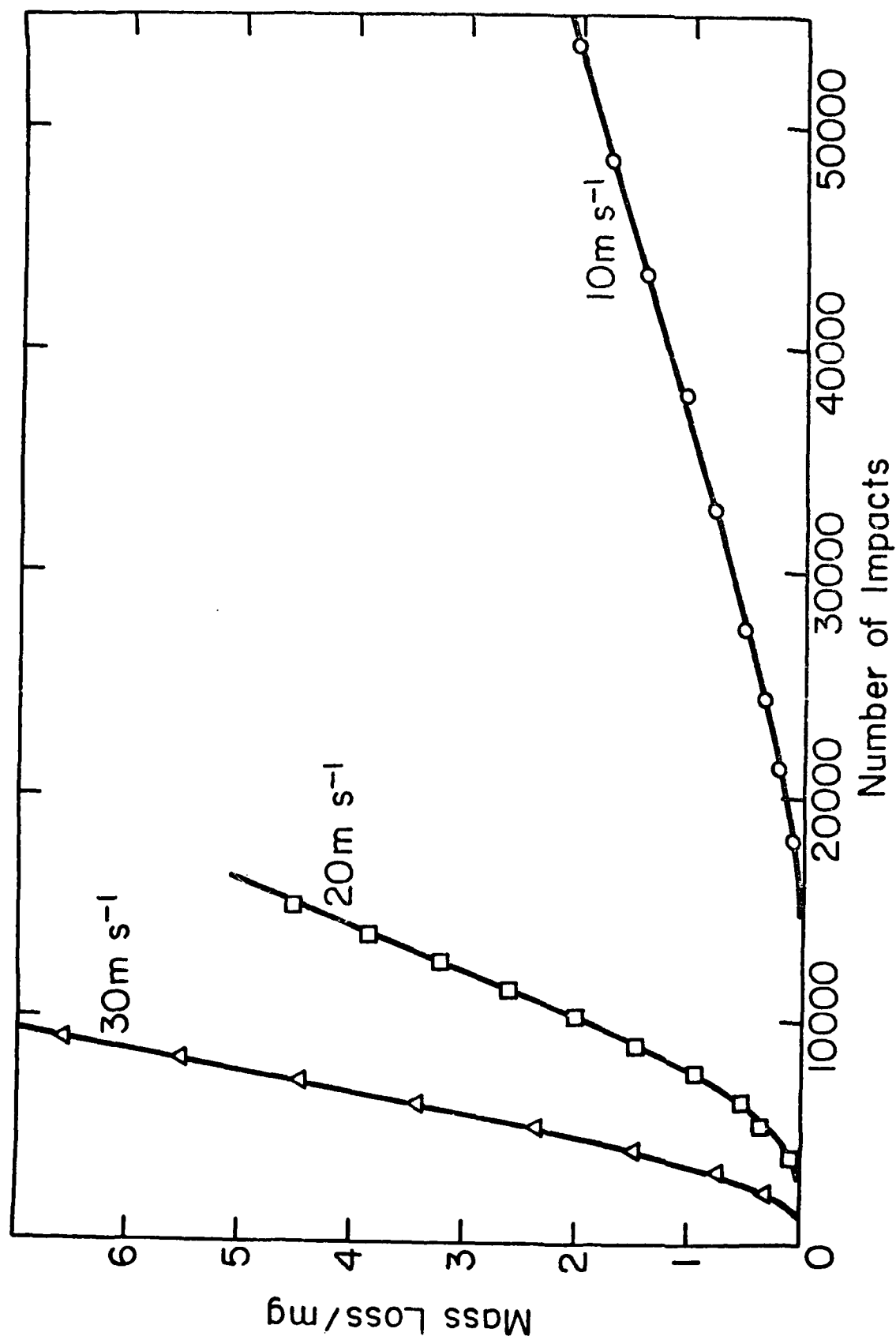


Figure 16 Mass loss versus number of impacts at various nominal impact velocities and a nominal impact angle of 30°.

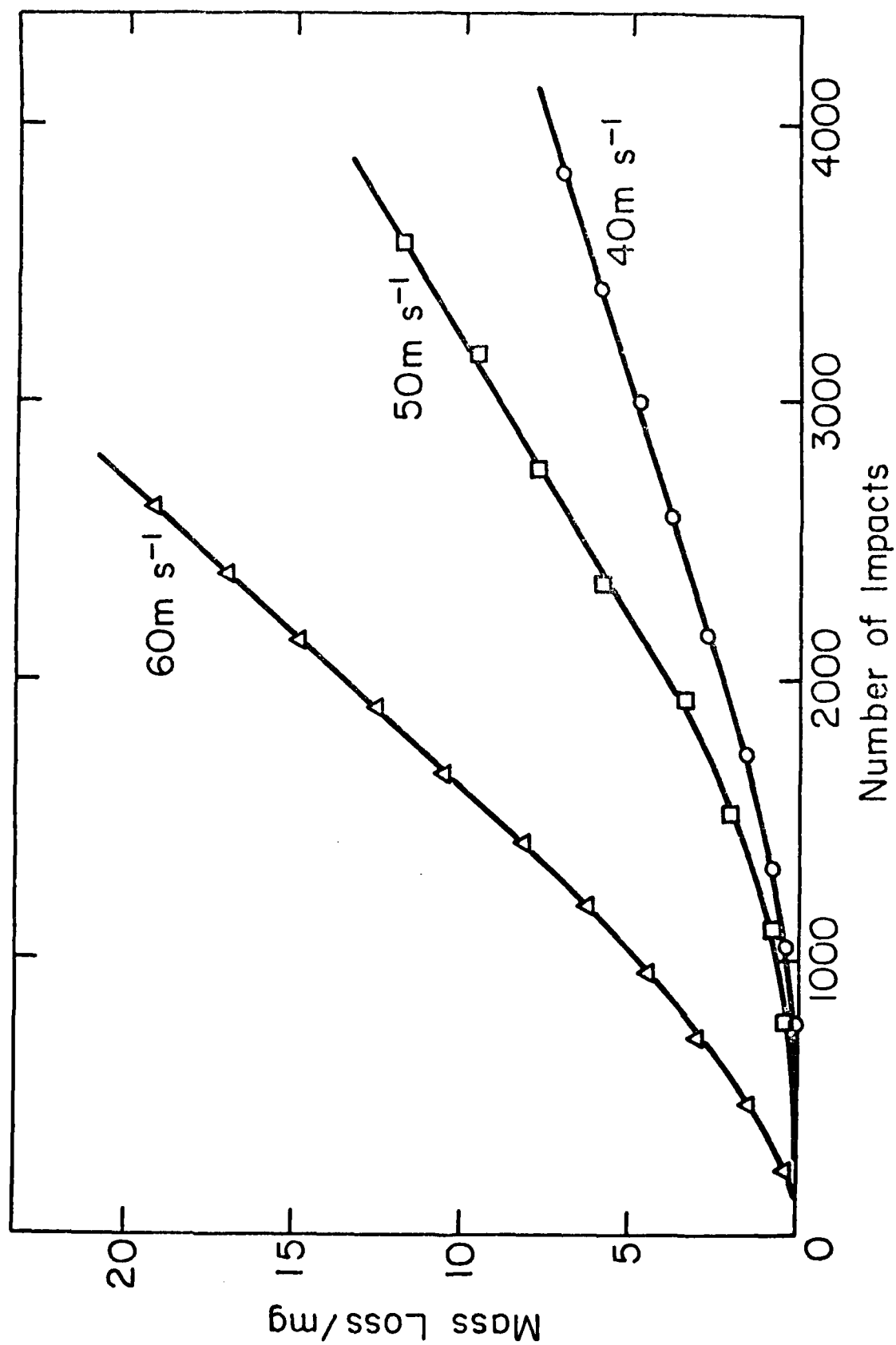


Figure 17 Mass loss versus number of impacts at various nominal impact velocities and a nominal impact angle of 30°.

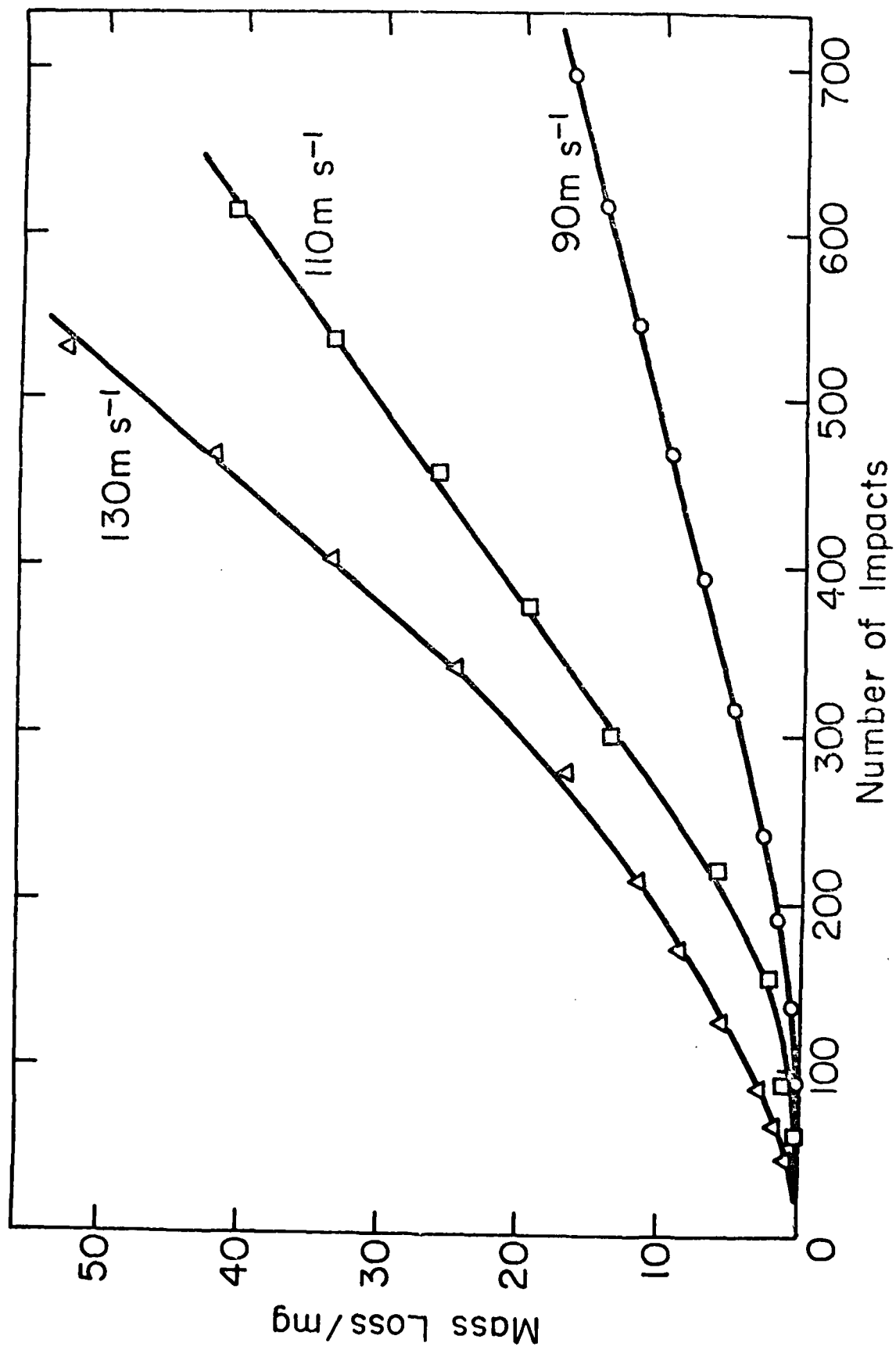


Figure 18 Mass loss versus number of impacts at various nominal impact velocities and a nominal impact angle of 30°.

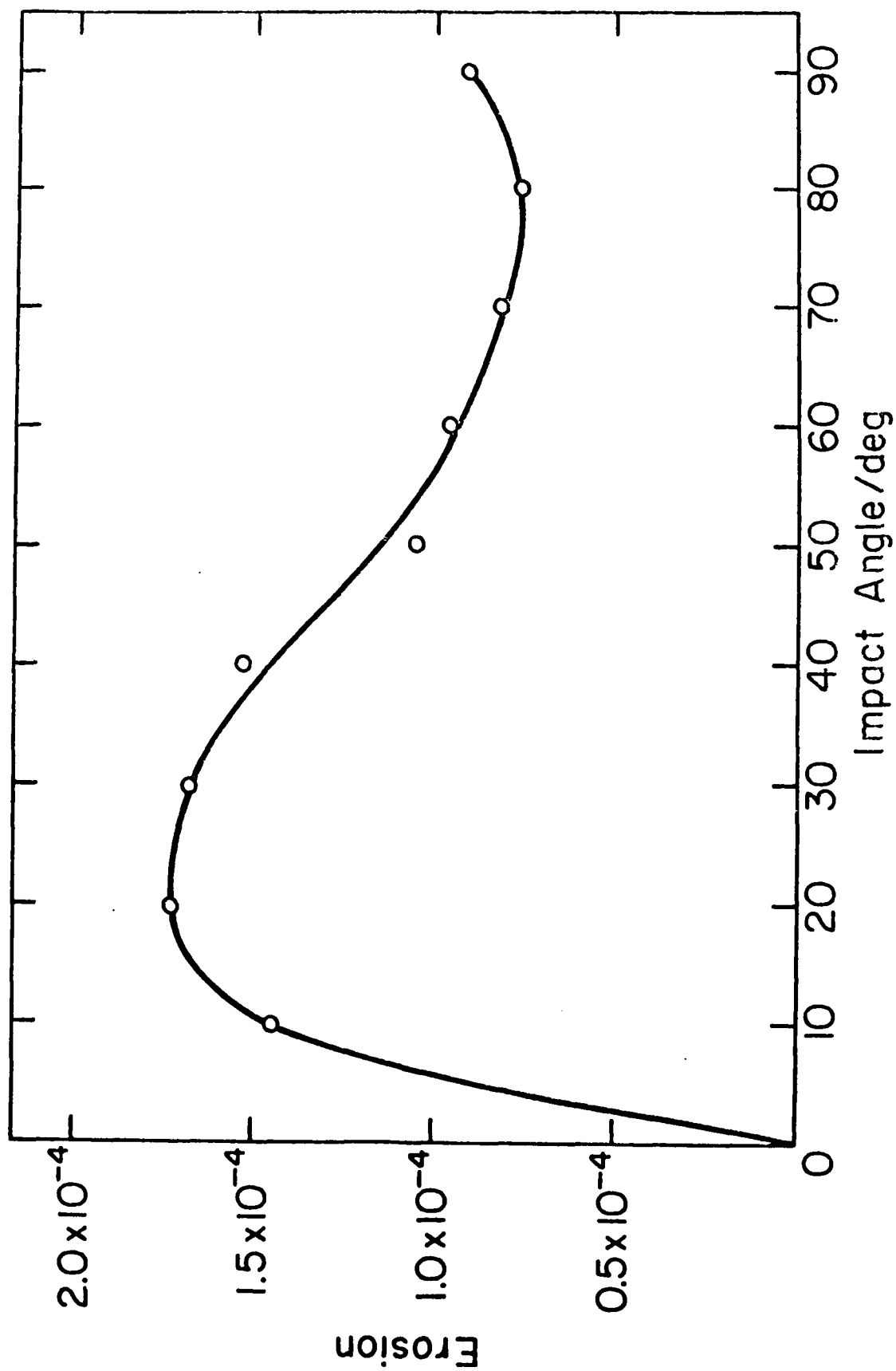


Figure 19 Steady-state erosion versus nominal impact angle at a nominal impact velocity of 50 m s^{-1} .

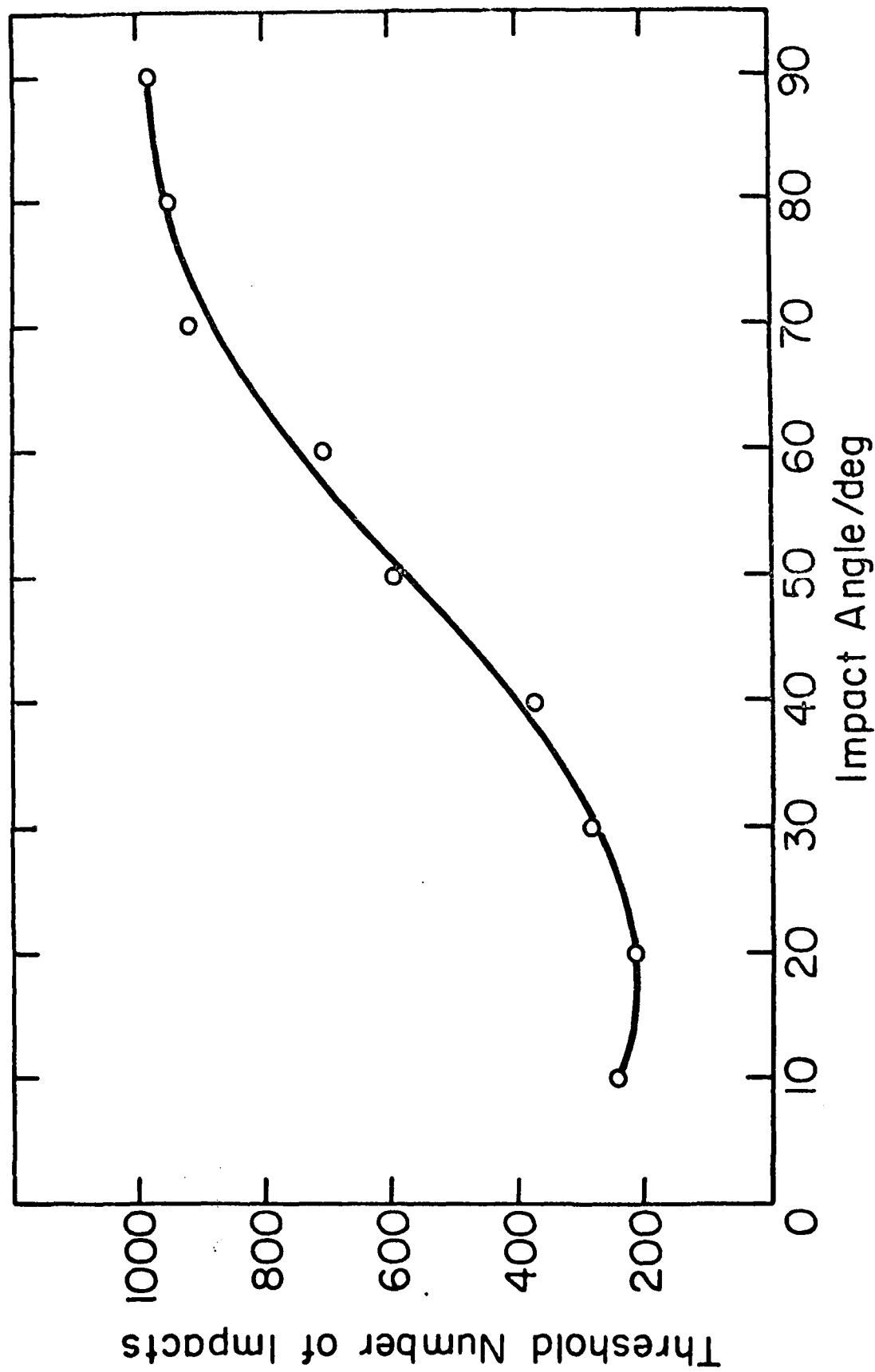


Figure 20 Threshold number of impacts versus nominal impact angle at a nominal impact velocity of 50 m s^{-1} .

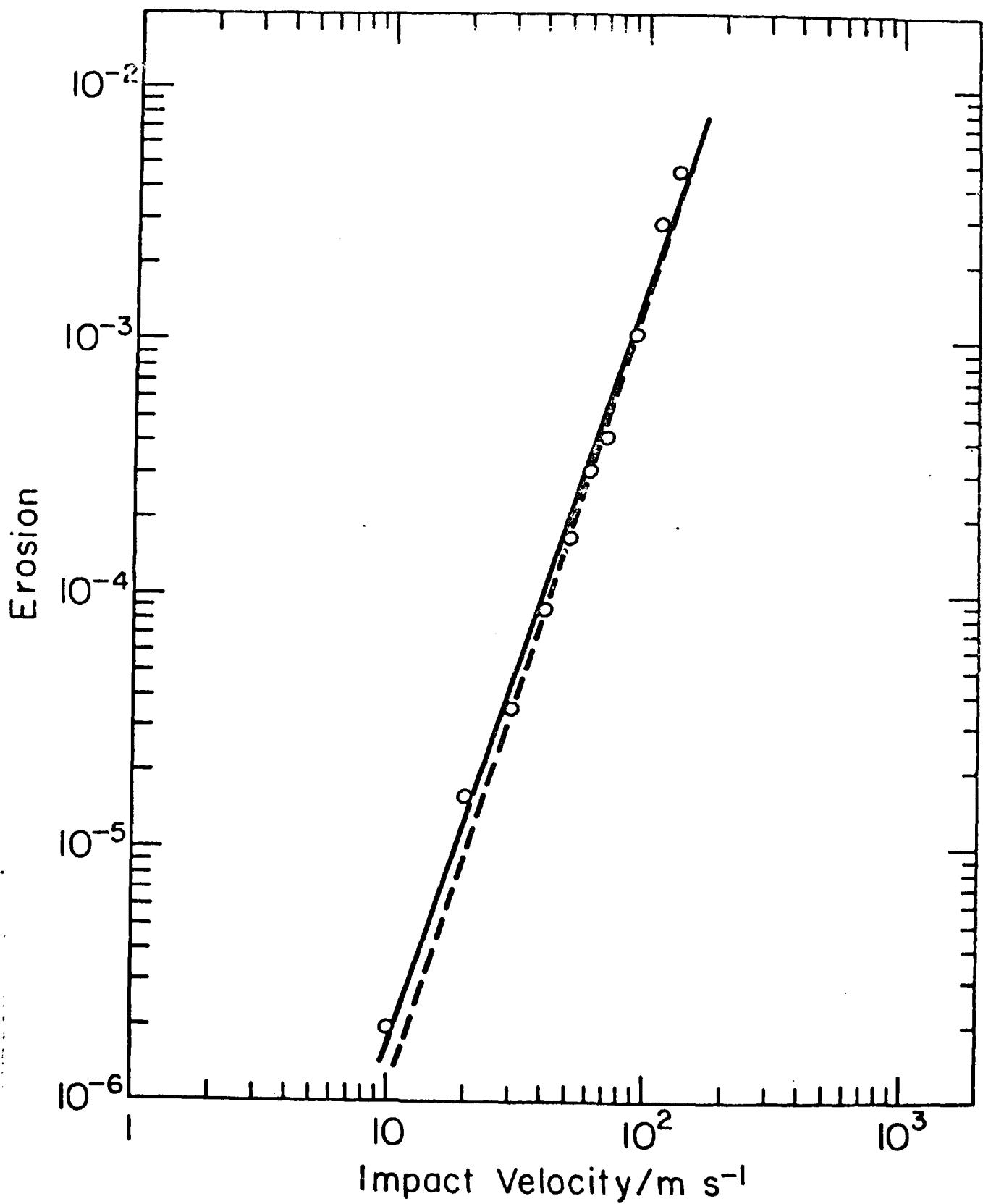


Figure 21 Steady-state erosion versus nominal impact velocity at nominal impact angles of 30° (data points and solid line) and 90° (dotted line).

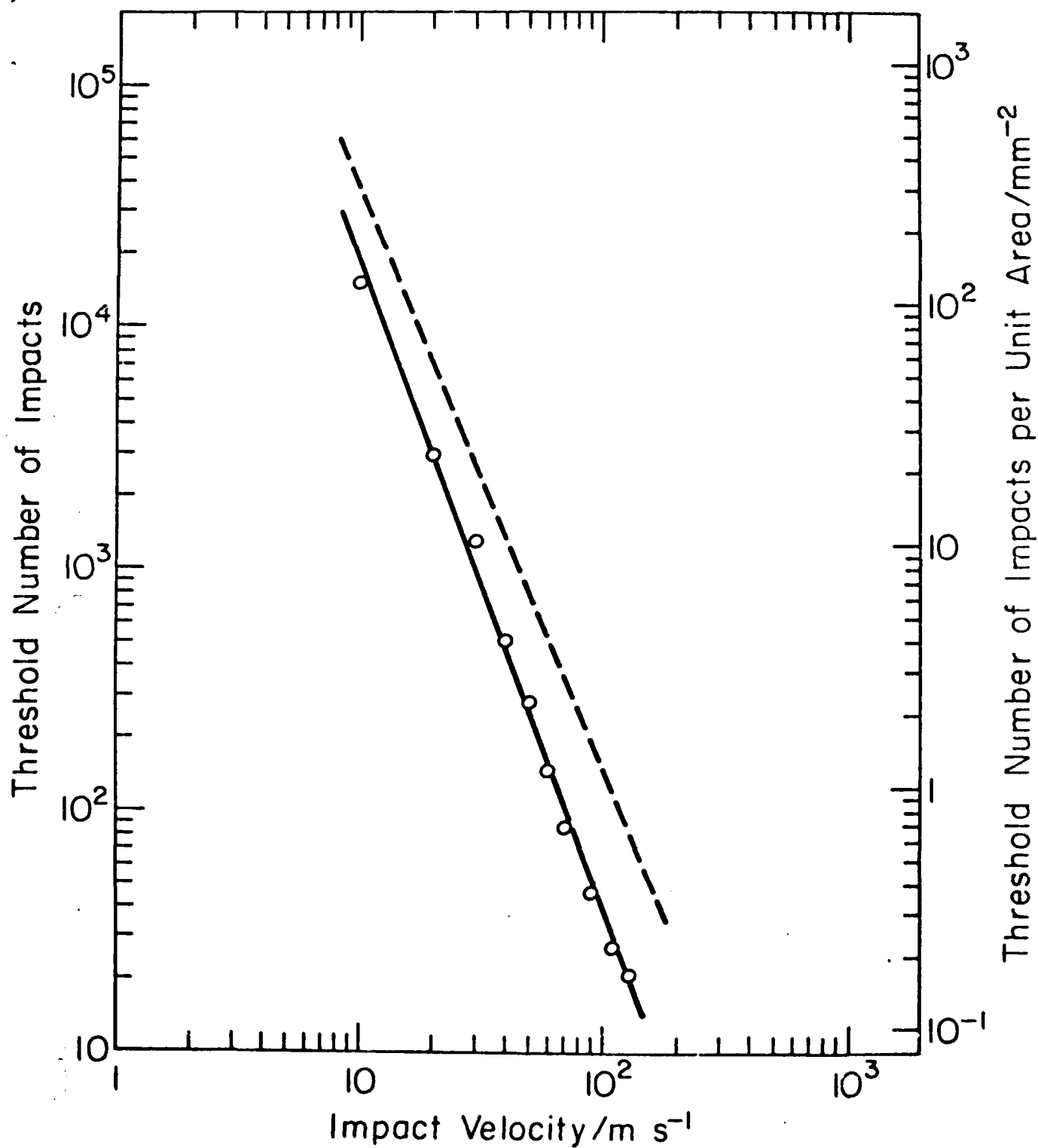


Figure 22 Threshold number of impacts versus nominal impact velocity at nominal impact angles of 30° (data points and solid line) and 90° (dotted line).

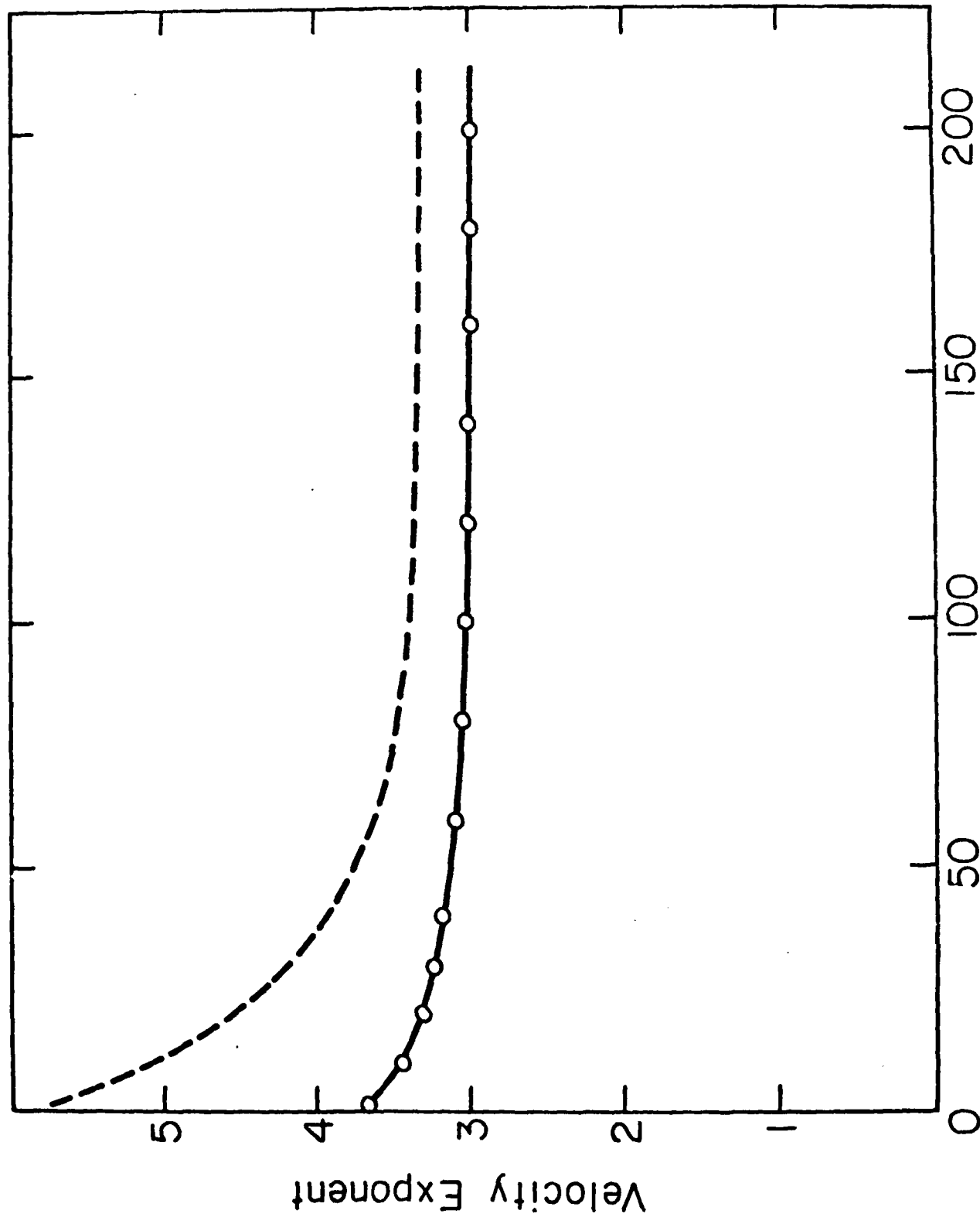


Figure 23 Exponent relating erosion to nominal impact velocity versus post-threshold number of impacts per unit area



Figure 26 Surface damage characteristic of steady-state erosion at various nominal impact angles and a nominal impact velocity of 50 m s^{-1} .



Figure 25 Surface damage characteristic of steady-state erosion at various nominal impact velocities and a nominal impact angle of 30° .

Appendix XII

Erosion of Aluminum and Magnesium Oxide by Spherical Particles

D. G. Rickerby and E. H. Macmillan
Materials Research Laboratory
The Pennsylvania State University
University Park, PA 16802, USA

Because the amount of material removed from any specimen by the impact of a single, irregularly shaped erosive particle can vary by several orders of magnitude, it is difficult to use such particles to investigate the early stages of erosion. A further complication in the case of ductile materials is that such particles tend to embed themselves in the specimen surface, sometimes in sufficient numbers that the specimen initially gains rather than loses weight. However, both of these difficulties can be overcome by using spherical particles. Accordingly, a rotating arm apparatus has been used to study the onset of erosion when 1.25 mm diameter WC-6% Co spheres impinge at normal incidence against coarse-grained aluminum and fine grained magnesium oxide specimens at velocities up to 350 and 100 ms^{-1} , respectively.

For aluminum, there was no detectable material removal until enough impacts had occurred to work harden the surface sufficiently that small platelets could be extruded from the highly deformed regions where impact craters had overlapped. In contrast, at velocities greater than about 25 ms^{-1} even a single impact produced sufficient cracking around the central crater to cause measurable material removal from magnesium oxide. Once material removal began, however, the erosion of both materials increased asymptotically to its steady state value as more and more particle impacts occurred. As a result of the type of erosive particles employed, these threshold and incubation phenomena occurred in a well-defined and highly reproducible manner, and thus it was possible to describe quantitatively, for the first time, the way in which they depend upon impact velocity and the elastic-plastic response of the specimen.